Protostellar jets: Numerical modeling and observational studies

A thesis submitted

in partial fulfillment for the award of the degree of

Doctor of Philosophy

by

SREELEKSHMI MOHAN

Department of Earth and Space Sciences
Indian Institute of Space Science and Technology
Thiruvananthapuram, India

July 2023

Certificate

This is to certify that the thesis titled ***Protostellar jets: Numerical modeling and observational studies*** submitted by **Sreelekshmi Mohan**, to the Indian Institute of Space Science and Technology, Thiruvananthapuram, in partial fulfillment for the award of the degree of **Doctor of Philosophy** is a bona fide record of the original work carried out by him/her under my supervision. The contents of this thesis, in full or in parts, have not been submitted to any other Institute or University for the award of any degree or diploma.

Dr. Sarita Vig
Professor
Dept. of Earth and Space sciences

Dr. Rama Rao Nidamanuri
Professor & Head
Dept. of Earth and Space Sciences

Place: Thiruvananthapuram
Date: July 2023

Declaration

I declare that this thesis titled ***Protostellar jets: Numerical modeling and observational studies*** submitted in partial fulfillment for the award of the degree of **Doctor of Philosophy** is a record of the original work carried out by me under the supervision of **Prof. Sarita Vig**, and has not formed the basis for the award of any degree, diploma, associateship, fellowship, or other titles in this or any other Institution or University of higher learning. In keeping with the ethical practice in reporting scientific information, due acknowledgments have been made wherever the findings of others have been cited.

Place: Thiruvananthapuram SREELEKSHMI MOHAN
Date: July 2023 (SC18D032)

This thesis is dedicated to my beloved parents…

Acknowledgements

First and foremost I would like to express my deepest gratitude to my research advisor, Prof. Sarita Vig, for the patient guidance, encouragement and advice she has provided throughout my time as her student. She has opened the doors for me to the area of star formation and is responsible for making this work a reality. Her outstanding feedback and unconditional guidance are invaluable and will benefit me throughout my life. She has kept me motivated throughout my PhD days, particularly during the most challenging times. For all this and much else besides, I am grateful to her.

I cannot overstate my gratitude to my collaborator, Prof. Samir Mandal (IIST), for the thought-provoking discussions and enlightening me with your insightful ideas. You always come up with brilliant solutions to any of my doubts and confusions, inspiring me throughout the challenges during my doctoral studies. Words are not enough to thank my collaborator, Dr. Watson P. Varricatt, for his time and patience in helping me with data reduction, in sharing your perspective during data analysis and helping me grow as a researcher.

I owe a great thanks to my doctoral committee members Prof. Anandmayee Tej, Prof. Anand Narayanan and Dr. Dinesh N. Naik for all their feedback and valuable suggestions, and the Astronomy and Astrophysics faculty members Dr. Resmi Lekshmi and Dr. Jagadheep D. Pandian for sharing your precious knowledge and expertise with me. I also thank my senior, Dr. Veena V S, for the help and guidance she has given.

A big thanks to our friendly lab tutor Mr. Sai Krishnan for keeping the astronomy lab lively and without whose hard-work the lab would not function smoothly.

I am forever indebted to my parents, Mr. Mohanachandran Nair and Mrs. Prameela Kumari, who raised me, educated me with all they have and wholeheartedly devoted their life for me. My father's critical thinking and reasoning skills in every aspect of life, especially in science, has always filled me with awe and curiosity, and he is the biggest motivation for me. The selfless love, understanding and sacrifices my mother has made for supporting me in following my passion is priceless. I cannot thank them enough for keeping aside their needs and being patient with me, and without them this would not have been possible. This is their thesis, as much as it is mine.

To Dr. Sunitha Joseph, my childhood friend who has ever since motivated me through her hard-work, passion and dedication towards studies and work, and showing me how to

be a successful woman. To Dr. Rashi Jain who has always comforted and supported me immensely during tough times, for never doubting my skills (even when I do), she never failed to reassure and encourage me. To Dr. Namitha Issac and Dr. Prabith Prabhakar for all the cheerful and fond memories, at the same time for giving me research advice, and has been there for me emotionally and intellectually. My warmest thanks to Ravishankar for your unlimited love and I cant thank you enough for the times you have helped me. To Swapnil, Sarwar, Bhagyasree and Prachi who has been great examples of motivation, determination and hard-work. A very special thanks to Pratyaksh for your unconditional care, your delightful over-appreciation of me, for believing in me no matter what, along with Srija for patiently listening to my ranting for hours and being my food, dance and travel companions. To Indu and Amulya for being my little stress busters. To Anindya, Amal and Arun for giving me a feel of how it is to have siblings, for being my daily dose of motivation, and for making our lab feel like home. I would also like to thank all the fellow PhD students Jyotirmoy, Geethu, Hafiz and all my dear friends who were always there to cheer me up during tough times: Sajith, Dr. James, Rahul, Abhishek, Swaliha, Sudev, Tillo, Resmi, Renjith, Sriram, Manu, Anju, Shiyas, Lekshmi, Saumya, Jerin, James, Nikhil and Dr. Farrah.

SREELEKSHMI MOHAN

Abstract

Protostellar phase is one of the earliest phases of star formation. The most important observational signature associated with this phase is the ejection of powerful bipolar jets/outflows. These jets are presumed to be the entities that enable protostellar accretion to proceed by removing excess angular momentum from the innermost radii of accretion disks. Since these jets are a by-product of accretion, various signatures of the protostellar accretion process are imprinted on the geometry, velocity structure, and symmetries of jets, which makes them powerful probes of various aspects of star formation. Large parsec-scale jets could also provide constraints on the mass-loss histories of their driving sources. Studying these jets could therefore open up an indirect window of knowledge into the evolutionary stages and activities of the protostar driving these jets.

Protostellar jets can be observed from radio to X-ray wavelengths both as continuum and spectral line emission which enable us to trace the dynamics as well as their physical and chemical conditions. However, since protostellar jets are associated with young forming stars which are enshrouded in vast amount of gas and dust, they have been extensively studied in the longer wavelengths most suitably in radio since the effect of extinction is minimal in this wavelength regime. In the first part of this thesis, our aim is to develop a numerical model to describe the radio spectra of protostellar jets. Radio continuum observations of ionized protostellar jets have shown the presence of thermal free-free emission and non-thermal synchrotron emission mechanism at play. We have therefore developed a model that incorporates both these emission mechanisms. The model flux densities include contribution from an inner thermal jet, and a combination of emission from thermal and non-thermal distributions along the edges and extremities, where the jet interacts with the interstellar medium.

We then characterize the model by carrying out a detailed investigation of the dependence of the model spectrum on the jet parameters. For each of these cases, we have calculated the turnover frequencies of the spectra and corresponding spectral indices between these turnovers, and we have carefully analyzed the behavior of these two features with variations in the model parameter values. We then discuss the potential of the model to explain the observed radio spectra of various protostellar jets and the model has been implemented to estimate physical and micro-physical parameters of these jets. The sample

of few protostellar jets to which we have applied the model are HH80-81 jet, jet driven by the young stellar object (YSO) G114.0835+02.856 and DG-Tau jet, and we have fitted the model to the observational data of these jets. For all these sources, the best fitting parameter values were estimated by χ^2 minimization.

In the second part of this thesis, we have carried out a detailed observational study of the largest known protostellar jet in the Galaxy, the HH80-81 jet, in the near-infrared (NIR) wavelengths. Here, we have explored the partially ionized and molecular regions of the jet for understanding the jet properties and estimation of its physical parameters. For this, we have utilized the emission from shocks generated by these supersonic jets. Shocks associated with jets can be best studied using emission lines in the NIR wavelength. We have, for the first time, carried out a combined 2.122 μm H_2 and 1.644 μm [Fe II] imaging followed by detailed qualitative and quantitative analysis of the HH80-81 jet. The observations were carried out using the Wide-Field Camera (WFCAM) mounted on the 3.8 m United Kingdom Infrared Telescope (UKIRT). In addition to the narrow-band filters, we have also imaged this region in the broad-band NIR J, H and K filters and the mid-infrared (MIR) L' and M' filters.

The morphology of emission in shock tracers can provide a resourceful gauge to examine the interaction of the jet with the ambient medium. Molecular H_2 emission is an indicator of low velocity weak C-shocks whereas, [Fe II] emission is widely used to understand fast and dissociative J-shocks caused by jets with velocities larger than 50-80 kms^{-1}. From the observed morphology of knots aligned along the jet, we segregated strong and weak shocks, and the prevalence of [Fe II] emission in the majority of knots suggests an overall dominance of strong dissociative J-shocks throughout the jet, even up to the farthest knots in the jet's southern arm. The measured H_2 and [Fe II] fluxes of the knots are in the range $0.4 - 5.2{\times}10^{-14}$ erg s^{-1} cm^{-2} and $3.1 - 13.6{\times}10^{-14}$ erg s^{-1} cm^{-2}, respectively. Following this, we used the [Fe II] luminosities to estimate mass-loss rates of the atomic component of the jet which is in the range $3.0 \times 10^{-7} - 5.2 \times 10^{-5}$ M$_\odot$ yr^{-1}. For the knots close to the central source, the values are consistent with those obtained from other tracers such as molecular gas using CO, and radio emission from ionized gas towards the central region of this jet system. The mass-loss rates of knots are also larger than those from jets of low mass YSOs ($10^{-10} - 10^{-7}$ M$_\odot$ yr^{-1}), but comparable to the [Fe II] mass-loss rate from few massive YSOs ($10^{-7} - 10^{-4}$ M$_\odot$ yr^{-1}). Additionally, the H_2 emission features identified in the central jet region include multiple groups of knots aligned linearly along outflows/jets previously identified as well as bow/arc shaped structures indicating the bow shocks arising from winds driven by two YSOs in the neighborhood of the driving source.

Contents

List of Figures

List of Tables

Chapter 1

Introduction

Since the dawn of time, humanity has treasured the sight of stars, whether in a clear night sky or in bright daylight, especially with the sun playing an irreplaceable role in maintaining life on the planet. We absolutely owe it to the stars for the origin as well as continuation of our existence. Despite advances in our knowledge about their birth, evolution, and eventual death, the intricate details of the formation of stars have been a mystery for ages. The key reason behind this is the fact that the birth sites of stars are embedded deep within dark, cold, and dense clouds, which are impervious to visible light. Star formation studies have been viable only in the past few decades due to a significant advancement in radio and infrared (IR) observational techniques and recent innovations in instrumental astronomy which have enabled probing the high extinction regions of star-forming clouds.

Stars are the fundamental constituents of galaxies. They begin their life cycle within dense molecular clouds comprised of gas and dust, where molecules can form, with hydrogen being the most prevalent. This makes hydrogen the predominant ingredient of stars, with lesser fractions of helium and other heavy elements such as carbon, nitrogen, oxygen, etc., depending on the star formation history of the parent cloud. During their evolution, stars manufacture heavy elements as well as inject these heavy elements along with energy and momentum into the cloud, thus altering the cloud structure and composition for the next generation of stars.

1.1 Observational overview of star formation

1.1.1 Interstellar medium

The interstellar medium (ISM) is the all pervasive inhomogenous medium that is present within the Galaxy and an essential ingredient for the formation of stars and planets. It is constantly undergoing interactions with radiation and winds from stars, gravitational and magnetic fields, turbulence, as well as accelerated charged particles. Hence the behavior of ISM is controlled by a number of complex physical processes. The ISM provides the raw ingredients, mainly hydrogen, helium and dust, required for the formation of stars. Stars then enrich the interstellar material with heavier elements via nuclear processing and as they reach the end of their lifetimes, this material is returned back, often violently. This cyclic movement of matter from ISM to the stars and vice-versa, is essential to the evolution of galaxies (Gnedin et al., 2016; Simon et al., 2019).

The ISM is mostly comprised of gas and dust with gas accounting for approximately 99% of the ISM's mass and dust constituting the remaining 1% (Draine, 2011). The ISM exists in different phases that exhibit large variations in temperature, ionization state, and density. These phases with different physical properties can be categorized as (i) Hot ionized medium, (ii) Warm neutral medium, (iii) Warm ionized medium, (iv) Cold neutral medium, (v) Molecular clouds and, (vi) HII region. Of these phases, the cold neutral medium which exists at temperature of $\sim$80K, having a typical number density and volume filling factor of 50 cm^{-3} and 1%, respectively, hosts giant molecular clouds (GMCs) that make up the majority of the galaxy's molecular component (Tielens, 2005). The ISM's average material density, which is just around one particle per cubic centimetre, is insufficient to cause the interstellar gas to gravitationally bind and give rise to stars and hence star formation occurs within these colder and denser GMCs.

Star formation commences in a nearly quiescent molecular cloud which then undergo a cascade of fragmentation processes, which ultimately gives birth to stars. The sequence of fragmentation of clouds were identified to exhibit a discernible pattern from the scale of the spiral arms of the Galaxy down to the star-disk system by Schulz (2005). These fragmentation scales can be classified as follows:

- 10 kpc scale: This represents the spiral arms of the Galaxy. The fragmentation begins with the compression initiated by the spiral waves in the arms.
- 1 kpc: This represent the scale of diffuse clouds of HI gas traced by 21 cm radio spectroscopic observations.
- 100 kpc: This represents the scale of GMCs.
- 10 pc: This corresponds to the scale of molecular clouds
- 0.1 pc: This scale is comparable to the size of molecular cores.
- 100 au: This corresponds to the scale of protostars.

1.1.1.1 GMCs

GMCs, which are distributed in the ISM, are considered to be the stellar factories within galaxies because all known star formation is believed to occur in these clouds. As the name suggests, they are composed mostly of molecular gas, the most common one being hydrogen. GMCs are typically found at scales of 100 pc within the galactic disk (Dame et al., 1986; Bronfman et al., 1988). Thousands of GMCs inhabit our Galaxy and they contribute to majority of the molecular mass within the Galaxy. Their typical sizes range from $\sim 40 - 100$ pc with masses of the order of 10^4–10^6 $M_\odot$ (Murdin, 2000). In these regions, the average number densities of ~100 cm^{-3} provides shielding from interstellar radiation that results in cooling such that low temperatures of ~10-20 K are typical of GMCs (Larson, 2003). GMCs serve as excellent tracers of the galaxy's large-scale structure and as the sites where the majority of the massive stars in the galactic disk are born. A notable example of a GMC is the neighboring star-forming region known as Orion, which is located ~410 pc away (Reid et al., 2009).

Although at first, the GMCs were believed to be stable against gravitational collapse, the origin of their stability is still hugely debated. While these dense and cold regions are thought to be supported by turbulence (Mac Low & Klessen, 2004) and magnetic fields (Shu et al., 1987), there are a few concerns regarding these assumptions. For instance, the dissipation timescale of turbulence is much shorter than the lifetime of molecular clouds (Blitz & Shu, 1980; Mac Low et al., 1998). Even though there is a lack of clarity regarding the large-scale stability of GMCs, the cloud's substructures that have densities well above average can cause them to collapse and give rise to stars. Therefore galactic star formation is a result of collapse of unstable regions within the GMCs (Dobbs et al., 2014) where the non-thermal motions resulting from turbulence are not sufficient to provide stability against collapse (McKee & Ostriker, 2007).

The high density substructures within GMCs are known as clumps and cores (Motte et al., 2018). Clumps are gravitationally bound objects, with typical densities of ~10^4 cm^{-3} extending upto ~0.5 pc scales, from which stellar clusters originate. These clumps are believed to be the condensations associated with cluster formation. Meanwhile, cores are denser and more compact regions with densities and sizes of the order of ~10^6 cm^{-3} and $\leq$0.1 pc. It is from these cores, the individual gravitationally bound systems consisting of single, binary or multiple stars are formed. Rather than being distributed randomly, these cores are often seen to be aligned along filamentary structures although very less is known about their origin. It is when self-gravity overcomes the thermal pressure and turbulence, clumps and cores begin to collapse (Hayashi & Nakano, 1965; Masunaga & ichiro Inutsuka, 2000). In this context, here we will briefly discuss the condition for the collapse of these high density substructures of GMCs. Consider a spherical cloud of molecular hydrogen gas having a uniform number density (n_{H_2}) which is supported by thermal pressure arising from a constant temperature (T). For simplicity, here we consider only the effects of thermal gas pressure and gravity. As long as gravitational pressure is higher than the thermal gas pressure, the cloud will continue to collapse. The minimum mass the cloud must posses for the collapse to occur is given by the equation below (Stahler & Palla, 2004).

$$M_J = 1.0 M_\odot \left(\frac{T}{10\ K} \right)^{3/2} \left(\frac{n_{H_2}}{10^4\ \mathrm{cm}^{-3}} \right)^{-1/2} \tag{1.1}$$

This follows from the Jeans criterion for the gravitational collapse of molecular clouds where M_J is called the Jeans mass. A mass greater than M_J would lose thermal support and start to collapse. The number density and temperature dependencies in the above equation show that the collapse is favored for clouds of high densities and low temperatures.

1.1.2 Low mass star formation

The majority of star-forming regions in the vicinity of the Solar System are typically not dense and massive enough to produce high mass stars. That being the case, the low mass (M $<$ 8 M$_\odot$) star-forming regions, which produce the vast majority of the Galaxy's stars, were the first to receive an extensive and in-depth research. Consequently, the overall picture of low mass star formation is clearer than massive star formation. Currently, it is widely accepted that low-mass star formation commences with the self-gravitational collapse and fragmentation of molecular clouds that leads to the formation of dense cores within the clouds. As these cores collapse further, one or more newborn protostars may be formed deeply embedded in dense envelopes of molecular gas and dust. The luminosity of protostars could arise from gravitational contraction, accretion or deuterium burning (Hosokawa & Omukai, 2009; Dunham et al., 2013). Most of this luminosity is absorbed and re-emitted in the IR by the vast amount of dust that surrounds the protostars, making them invisible in the optical wavelength (Stahler, 2015). A protostar is essentially a hydrostatic core surrounded by a circumstellar disk and is deeply embedded within an infalling envelope during their early phases. This makes them invisible at optical and NIR wavelengths, and they can only be identified with the help of radio and far-infrared (FIR) observations since these longer wavelength radiation can penetrate through regions of dust almost without being absorbed (Benaglia, 2011). Any stellar object that has evolved into or beyond the protostellar phase and has not yet reached the main-sequence phase can be considered to be a YSO. In the context of low mass star formation, a protostellar system involves five main elements that are either inherent to the protostellar system or are associated with it at specific phases in its evolution. These are given below.

1. Central YSO (Strom et al., 1975; Myers & Ladd, 1993; Saraceno et al., 1996; Casali & Eiroa, 1996; Liu et al., 1996; Gutermuth et al., 2011; Adams & Gregory, 2012): This is the main central object that is in the process of active accretion of circumstellar material. Most of the radiation emitted during its early stages result from accretion, despite the onset of deuterium burning at its center.

2. Circumstellar disk: These are disks of dust and gas which revolve around the central YSO and it is with the help of these disks that YSOs accrete majority of their masses. The total masses (dust + gas) and radii of disks typically range from $0.001 - 0.1$ M$_\odot$ and $500 - 800$ au, respectively.

3. Protostellar Jet/Bi-polar outflow (Bally et al., 2007; Anglada et al., 2018; Ray & Ferreira, 2021): Observations indicate that majority of protostars are associated with bipolar molecular outflows and jets. Such jets/outflows are essential to transport extra angular momentum out from the YSO driving it, in order to permit continued accretion.

4. Protostellar envelope (Yorke, 1979; Bonnell et al., 1996; Hogerheijde et al., 1999; Chandler & Richer, 2000; Rodgers & Charnley, 2003): This contributes to the bulk of the materials that could continue to be accreted onto the central YSO. The density and temperature of this region could roughly follow a power-law profile.

5. Surrounding parent cloud (Moriarty-Schieven et al., 1995; Arce, 2003): This could include nearby protostars or dense cloud regions whose radiation, energy, turbulence etc., can exert an influence on the structure of the protostellar envelope. The cloud's significant impact, however, is presumably on how YSOs appear to the observer because they redden the star's IR emission and contribute to processed emission following the absorption of stellar radiation.

   These components are detectable at wavelengths ranging from optical to millimetre and their sizes range from ~ 0.01 au to a few parsecs (Monnier & Millan-Gabet, 2002; Monnier et al., 2009; Masqué et al., 2012). Each of these components evolve with the age of the protostar. The envelope material will be either disseminated on the breakout of stellar winds and outflows or accreted by the central star. Outflows become significantly less energetic as accretion gradually ceases, but they would have already swept up a considerable amount of surrounding material and exhibit reduction in collimation. Meanwhile, the central disk expands and dust settle down at the disk mid-plane, setting up the initial conditions for formation of planets.

Three-dimensional magneto-hydrodynamic (MHD) simulations by Machida et al. (2009) have shown that outflows and jets could be arising from two different regions referred to as cores. In this scenario, the adiabatic core that drives low velocity outflows is considered as the first core and the protostar that drives high velocity jets is considered as the second core. A schematic diagram of such a protostellar-jet bearing system that also includes the components which are discussed above are shown in Fig. 1.1. Due to the shallow gravitational potential associated with the first core, the outflow arising close to this core is slower and is driven by magneto-centrifugal forces (Disk wind) compared to the jet arising close to the protostar which is faster and driven by magnetic pressure gradient forces.

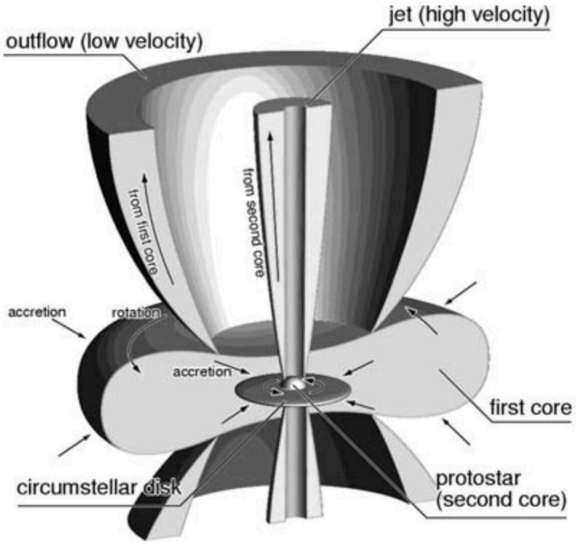

Figure 1.1: Schematic diagram illustrating the components of a protostellar-jet bearing system as adapted from Machida et al. (2009).

1.1.2.1 Early evolutionary stages

Theoretical and observational studies have shown that the process of low mass star formation occurs in distinct phases. It commences with a molecular cloud that undergoes collapse under self-gravity and concludes with the radiation pressure and outflows from the protostar clearing away the dusty natal cloud. In the course of the overall evolution, the spectral energy distribution (SED) of YSOs can be broadly classified into four main classes, that represents four different phases. Three of these classifications, as proposed by Lada (1987) and Adams et al. (1987), were based on the slope (α_{IR}) of the SED across the wavelength range of 2.2 μm to 10-25 μm, which is given by the equation below.

$$\alpha_{IR} = d\frac{log(\lambda F_\lambda)}{dlog\lambda} \tag{1.2}$$

Adding to this, Andre et al. (1993) established a new class, named Class 0, which is believed to be a phase that occurs before Class I. Prior to these stages, cold and dense cores inside molecular clouds undergo gradual collapse and are therefore essentially starless. The following are the principal attributes of these four classes.

(a) **Class 0**: This phase commences when a protostar with a mass of $\sim 10^{-3}$ M$_\odot$ and a radius of $\sim$2 R$_\odot$ is first created at the center of the core (Larson, 1969; Masunaga & Inutsuka, 2000) and the accretion process has proceeded far enough that the accretion disk begins to form. Hence, the protostar is actively accreting material while remaining highly embedded within the cold dusty envelope. In this stage, nearly all of the system's mass is still harbored in the disk gas and the temperature of the central core, which is less than 100 K, is still low. Observationally, the optical and NIR emission from these sources are weak, whereas they exhibit a significantly large luminosity in the sub-mm wavelength. The SED of these objects would correspond to that of a cold black-body with temperatures in the range of $\sim 10 - 30$ K. These properties imply that the cold, dusty envelope of the protostar is visible in this stage while the protostar remains deeply embedded continuing to acquire mass efficiently. This phase is expected to conclude after $\sim$10^5 years, when the envelope has shrunk to 10$\%$ of its initial mass (Evans et al., 2009).

(b) **Class I**: A positive value of α_{IR} ($\alpha_{IR} > 0$) characterizes this phase. This class indicates objects that are more evolved than Class 0 with SEDs broader than black-body due to the emission contributed by circumstellar dust. This includes a more flattened disk and as a result of the accretion of matter by the protostar over time, the core object has now significantly more matter accreted onto it, relative to the surrounding disk and ambient gas. However, the amount of dust and gas surrounding the YSO will still be significant enough to result in heavy extinction in optical band, making these objects visible predominantly in IR wavelengths.

(c) **Class II**: This class includes sources with $-1.5 \leq \alpha_{IR} \leq 0$. SEDs in this case are also broader than black-body due to additional IR excess. The negative α_{IR} of these sources result from the considerably less amount of circumstellar dust as compared to that of Class I sources. This is because the surrounding material is mostly blown off by the stellar winds. The temperatures will be as high as thousands of Kelvin. These sources are mostly seen in the optical and IR wavelengths. They are often referred to as Classical T-Tauri stars.

(d) **Class III**: This class includes sources with $-3 \leq \alpha_{IR} \leq -1.5$. Their SEDs resemble a black-body with a single temperature component, since only a small amount of circumstellar dust remains in this stage. Since they are associated with very less amount of circumstellar dust, they are visible in optical wavelength. In the pre-stellar phase, which lasts for $\sim 10^6 - 10^7$ years, this is the most evolved stage and are often identified as weak-line T-Tauri stars.

Aided with the knowledge of this classification scheme and the discovery of numerous sources that are seen to drive outflows, one can attempt to correlate the behavior of outflow properties and the evolutionary phase of the driving source. Bontemps et al. (1996) estimated the outflow strength from CO emission and age of the central object from the mass in the envelope of the protostar to show that Class 0 sources are associated with the most powerful, fast and collimated narrow jets whereas Class I and II sources display slower and wider jets. It can therefore be inferred that as the YSO evolves the strength and power of the outflow diminishes.

1.1.3 High mass star formation

Over cosmic time, massive stars (M $>$ 8 M$_\odot$) have molded the galactic environment around us by governing the evolution of the gas and stars in their vicinity. Understanding the exact formation mechanism of these stars remains as a long-standing challenge and is still inconclusive (Bally & Zinnecker, 2005; McKee & Ostriker, 2007; Zinnecker & Yorke, 2007). The significance of understanding the massive star formation is that their feedback mechanisms such as intense radiation, power-

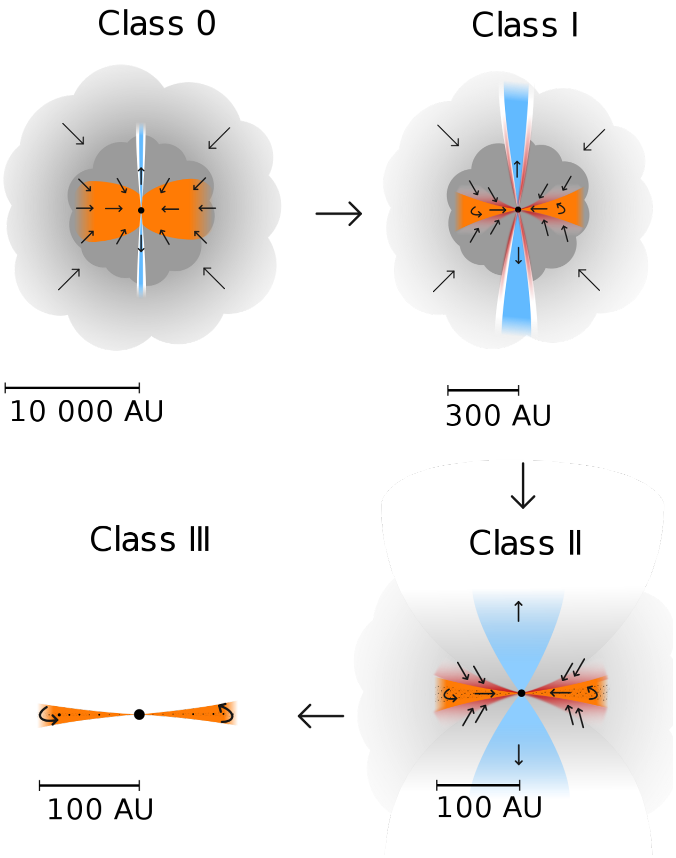

Figure 1.2: Schematic diagram illustrating the four main phases associated with the evolution of protostars as adopted from Persson (2014). The images are displayed in the order of increasing age as indicated by arrows. The circumstellar envelope is indicated in grey, the accretion in disk in orange and protostellar jets in blue.

ful jets/outflows/winds, energy and turbulence injected into the surroundings, and the release of heavy elements (metals) during their violent death dominate in determining the chemistry and physical properties of the natal cloud and of the galactic environment. They can also trigger the formation of new generation of low mass stars. Hence, the knowledge of massive star formation has a substantial impact in astrophysics.

The study of early phases of massive star formation has been drastically hampered by (i) the statistical rarity of massive stars (ii) large distances (kpc) associated (iii) high extinction due to deeply embedded conditions (iv) fast evolution/short lifetimes (v) formation in clusters with stars of all masses (vi) disruptive impact on their immediate environment. This poses challenges in the theoretical as well as observational study of high mass star formation (Zinnecker & Yorke, 2007; Tan et al., 2014). Given these challenges, three main observational strategies have provided us a wealth of information regarding the massive star-forming regions. These are based on the fact that (i) warm dust emission from embedded massive stars can be seen predominantly in FIR wavelengths (Sargent et al., 1981; Lightfoot et al., 1983; Leurini et al., 2015) (ii) these regions appear as IR absorption features when viewed against the bright Galactic background (Hennebelle et al., 2001; Ragan et al., 2009) (iii) strong shocks generated by supersonic jets/outflows can instigate maser emission (Beuther et al., 2002c; Ellingsen et al., 2010; Fontani et al., 2010). Observational surveys that utilize these features enable us to identify and study massive star-forming regions.

Two important timescales can explain the difference in formation timescales of low and high mass stars. These are the free-fall timescale (t_{ff}) and Kelvin Helmholtz (K-H) timescale (t_{KH}). t_{ff} is the timescale for the gravitational collapse of a molecular cloud. This collapse of the cloud results in the conversion of gravitational potential energy to thermal energy and the timescale on which this conversion occurs is t_{KH}. For high mass stars, $t_{ff} >> t_{KH}$, which implies that for these stars nuclear fusion begins while they are still collapsing. The ensuing luminosity induces an intense outward radiation pressure that prevents further accretion (Larson & Starrfield, 1971; Beuther et al., 2007b), thus giving rise to the radiation pressure problem. Several theoretical models for massive star formation (eg. Monolithic collapse, competitive accretion and stellar merger) have been proposed which address this issue besides other concerns such as overcoming the magnetic pressure, turbulence etc., during fragmentation.

1.1.3.1 Evolutionary stages

An embedded phase that lasts approximately 15$\%$ of a massive star's lifetime comes before the main-sequence life that is optically visible later in the star's evolution. Despite the lack of clarity regarding the scale and the processes involved in the formation of a massive star, the broad view is that high mass star formation must involve the same fundamental processes as low mass star formation (Zinnecker & Yorke, 2007) which are: (i) The creation of a dusty molecular cloud that endures turbulent fragmentation resulting in the formation of clumps and cores (ii) Collapse of these cores under the effect of self-gravity (iii) Accretion of matter by the central protostar (iv) Stellar activity that dissipates the parent cloud. Independent of the mechanism responsible for the collapse, the evolution of high mass stars up to the main-sequence phase has been attributed to a sequence of phases that are observationally distinct (Zinnecker & Yorke, 2007). These observational phases are given as follows:

- **Infrared dark clouds (IRDCs)**: These are the earliest observed phase of high mass star formation. IRDCs were discovered as dark high extinction ($>$2 mag at 8μm; Egan et al., 1998) features against the bright MIR background of the Galaxy with the Midcourse Space Experiment (MSX) and the Infrared Space Observatory (ISO) satellites (Perault et al., 1996; Egan et al., 1998; Omont et al., 2003). Millimetre and sub-mm studies of these objects have revealed masses in the range of $120 - 16,000$ M$_\odot$ (Rathborne et al., 2006), typical temperatures T $<$ 25 K (Carey et al., 1998; Pillai et al., 2006) and densities n$_H \sim 10^4 - 10^6$ cm^{-3} (Egan et al., 1998; Rathborne et al., 2006; Simon et al., 2006).
- **Hot Molecular Cores (HMCs)**: HMCs are compact ≤ 0.1 pc, warm ($100 - 300$ K) and dense ($10^6 - 10^8$ cm^{-3}) pockets of molecular gas, and they exhibit a rich chemistry that is detectable as molecular line emissions at sub-mm wavelengths. These young embedded objects are not detectable in the optical or NIR bands. HMCs are thought to be actively accreting material (Kurtz et al., 2000; Beuther et al., 2007a) so that these possess an equatorial accretion disk and massive bipolar outflow along the spin axis (Beuther et al., 2002a; Motte et al., 2007).
- **Hypercompact HII Regions (HC HII) and Ultracompact HII (UC HII) Regions**: These are the youngest stage of HII regions (Kurtz, 2005). HC HII regions are the earlier of the two phases, when compared to UC HII regions and has a typical size (diameter) ≤ 0.05 pc, electron density (n$_e$) $\geq 10^5$ cm^{-3}, emission measure (EM) $\geq 10^8$ pc cm^{-6} and radio recombination line width $\Delta V \geq 40$ km s^{-1} (Kurtz et al., 2000; Sewilo et al., 2004; Hoare et al., 2007; Murphy et al., 2010). The UC HII region is believed to represent the subsequent evolutionary stage following the HC HII region, and has a diameter ≤ 0.1 pc, n$_e \geq 10^4$ cm^{-3}, EM $\geq 10^7$ pc cm^{-6} and $\Delta V \sim 25 - 30$ km s^{-1} (Wood & Churchwell, 1989; Afflerbach et al., 1996; Hoare et al., 2007). Despite the fact that these HII regions are heavily obscured by a dense cocoon of molecular gas, it is nevertheless possible to study them at radio wavelengths. The radio continuum flux density of these HII regions arising from thermal bremsstrahlung (free-free emission) varies with frequency as S$_\nu \propto \nu^\alpha$ where α is the spectral

index such that -0.1 (optically thin) $\leq \alpha \leq$ +2 (optically thick).

- **Compact and Extended HII Regions**: Compact HII regions have more extended sizes of $\sim 0.06 - 0.4$ pc, n$_e$ $\sim 10^4$ cm^{-3} and are observed in more evolved cloud regions (Mezger et al., 1967). Extended HII regions can span several parsecs in size and indicate a more evolved state. They expand hydrodynamically and disrupts the parent molecular cloud, exposing the stellar population within them to optical and NIR observations (Zinnecker et al., 1993).

1.2 Protostellar jets

This thesis is devoted to the study of protostellar jets which are one of the five primary components of a protostellar system as already discussed in Sect. 1.1.2. In the following sections we will carry out an in-depth discussion on the most relevant aspects of protostellar jets.

Jets are the consequence of accretion of material in a rotating system. From ultra-relativistic/relativistic jets in high energy astrophysical phenomena (Mirabel & Rodríguez, 1999; Blandford et al., 2019) to non-relativistic jets in protostars (Reipurth et al., 2004; Lee et al., 2007) and brown dwarfs (Whelan et al., 2009; Palau et al., 2014), jets assist in accretion by carrying away excess angular momentum (Blandford & Payne, 1982; Pudritz & Norman, 1983). Since newly forming stars are embedded in large clouds of gas and dust, making them observationally challenging to probe, jets serve as an important tool in the indirect study of these embedded stages. This is because jets and the gas that they entrain in the form of outflows are easier to detect because of their kinematic signatures. Protostellar jets represent a significant signpost of ongoing star formation (Felli et al., 2006) as they influence the surrounding ISM by the transfer of momentum and energy. Protostellar jets can either augment or retard the star formation occurring in their vicinity (Li & Nakamura, 2006; Nakamura & Li, 2007; Shimajiri et al., 2008). The optical color composite image of two prominent protostellar jets as imaged by the Hubble Space Telescope (HST) are shown in Fig. 1.3.

The protostellar phase is when majority of the stellar mass is assembled via accretion. It is this phase when most of the angular momentum is believed to be lost, thereby favoring accretion. In terms of evolutionary age of the driving sources, protostellar jets are most likely to be observed during Class 0 to the early Class II phases when

Figure 1.3: Color composite image of the HH 901 and HH 902 jets in [SII] emission (red), Hα emission (green) and [OI] (blue) as imaged by the Wide Field Camera 3 of HST. Picture credit: NASA, ESA, Mario Livio (STScI), Hubble 20th Anniversary Team (STScI).

the central source is actively accreting matter. Detailed investigation of protostellar jets could provide indirect but significant insights into the accretion and mass-loss processes that regulate the birth of stars. Recent technical advancements have facilitated thorough observations of these jets from X-ray to radio wavelengths, thereby providing a comprehensive picture of protostellar jets and their associated outflows.

1.2.1 Observational aspects of protostellar jets

The interaction of jet with the ambient medium results in the formation of optically-visible spectacular emission nebulae known as Herbig-Haro (HH) objects (Reipurth & Bally, 2001). These were originally identified by Herbig (1951) and Haro (1950, 1952) in Hα-emission line. HH objects correspond to the emission from shock waves formed due to the impact of the supersonic protostellar jets on the ambient medium (Brugel, 1990; Böhm, 1995; Bjerkeli et al., 2011). These objects are excellent astrophysical laboratories for examining shock structures, shock physics and chemistry, hydrodynamics in collimated jets, as well as their interaction with their immediate surroundings. They enable us to retrace the accretion history since the shocks in the HH objects that are farthest from the driving source will trace to the oldest ejecta (Bally et al., 1996; Ellerbroek et al., 2013).

Shocks play a key role in the ionization of jet material (Hansen et al., 2017; del Valle et al., 2022). Based on the degree of ionization, protostellar jets can be broadly classified into two main components as given below:

- **(Partially) Ionized jet**: The ionized component of jets are detectable: as weak radio continuum sources at metre and centimetre wavelengths which mainly correspond to the base of the jet near its launching point (Anglada et al., 2018), or in the optical/NIR wavelength. The radio continuum emission is dominated by thermal free-free emission and recent investigations have also revealed the presence of non-thermal synchrotron emission in jets. The ionizing mechanism is believed to be associated with internal shocks within the flow or external shocks that result from the interaction between the jet and ISM. These jets have elongated morphologies and the observed sizes and flux densities are frequency dependent (Rodriguez et al., 1994; Reid et al., 1995; Wilner et al., 1999; Curiel et al., 2006). Due to the emission being weak and compact, sensitive radio interferometers with high angular resolution are necessary to detect and investigate the emission. Alternatively, excited shocks emit both permitted and forbidden emission lines in the optical and NIR wavelengths. These shocks offer emission lines with excellent diagnostic capabilities, e.g. Hα, [OI]λ630nm, [SII]λ λ671.6nm,673.1nm, [NII]λ658.3nm lines, [FeII]λ1644nm. These forbidden line emission enable us to probe regions even at distances of a few parsecs from the driving source and can be used to explore the morphology, kinematics and physical properties of jets, at high angular resolution.
- **Molecular jet**: The emission from this jet component is mainly contributed by highly excited molecular gas with temperatures, T ≥ 300 K, in the form of emission lines. The most commonly used molecular line tracers are the high-J rotational transitions of CO, SiO, SO etc., that emit in the sub-mm wavelengths and H_2 in the NIR (Hirano et al., 2005; Qiu et al., 2019; Lee, 2020). Hence, observations that rely on high excitation lines allow for the detection of this component. In most cases, molecular jets are contained within molecular out-

flows that have a lower velocity and a lower degree of collimation.

Another secondary feature associated with protostellar jets are molecular outflows. When jets propagate forward through the ISM, they entrain/sweep up and accelerate the cloud gas, which leads to the formation of molecular outflows around the jet axis (Arce et al., 2007). Evidence from recent observations have shown that these outflows could also be directly ejected in the form of non-collimated winds from an accretion disk (Bjerkeli et al., 2016; Lee et al., 2017; Güdel et al., 2018). The low-J rotational transitions of the CO molecule are the most widely employed tracers of molecular outflows (Fukui et al., 1993; Wu et al., 2004) and are detectable as broad emission lines in the millimetre wavelengths. These lines can be utilized for the estimation of total mass, momentum and energy contained in the cold, entrained molecular gas.

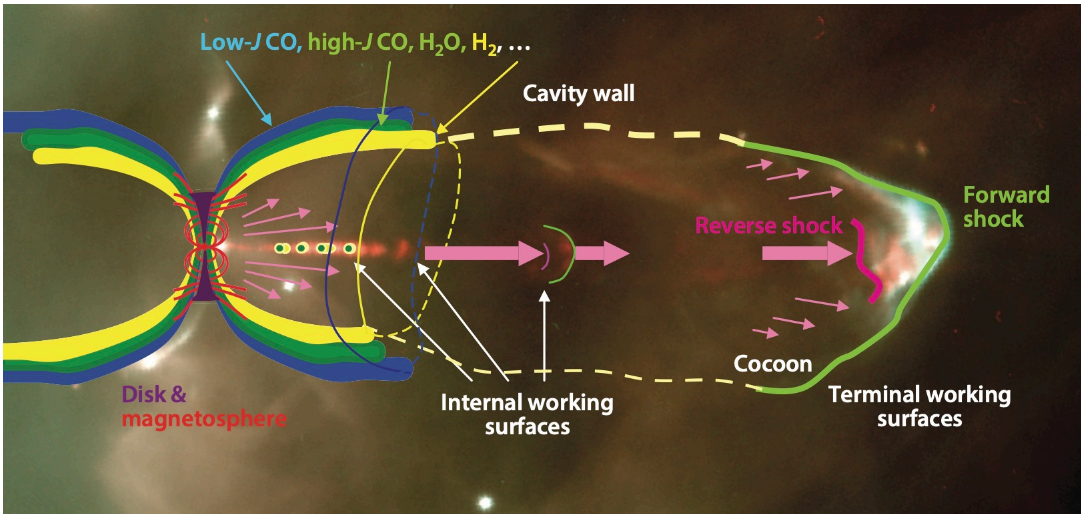

Figure 1.4: Schematic showing the effect of interaction of protostellar jet with the ambient medium, overlaid on the two-color image of HH 34 jet, with Hα emission shown in cyan and [S II] emission in red, as adapted from Bally (2016). The disk marked in purple and the poloidal component of magnetic fields (disk and magnetosphere) shown in red are blown up in scale. Bright green curve (see towards the right of the image) shows the shocks generated by the impact of the supersonic jet on the ambient medium that are traced by atomic or ionic emission in the resulting HH objects. The molecular emission traces both shocks in outflow cavity walls as well as the recently ejected jet material. The shocks along the cavity walls are marked by thick bands where low-J CO is shown in blue, high-J CO in green, and shock-heated H_2 in yellow. The atomic or ionized cavity wall is marked by a dashed yellow line.

The major components of protostellar jets as discussed above are shown in Fig. 1.4.

The figure shows a two-color composite image of HH 34 jet with Hα emission shown in cyan and [S II] emission in red, overlaid with the main observational features associated with these jets.

1.2.1.1 Physical parameters of jets

In order to determine the role that jets play in feedback, development of turbulence, and the disruption of the environment in which stars are forming, it is essential to characterize them through their velocities, masses and momentum injection rates. With a wealth of high-resolution spectral and imaging data, the morphology, kinematics, and microphysical conditions of the jets/outflows may be precisely traced. The presence of emission lines in jets also allows one to estimate various other physical parameters such as temperature, ionization fraction, electron density etc. The excitation states corresponding to these emission lines indicate typical temperatures of $\sim 10^4$ K, which corresponds to sound velocity of tens of km s^{-1}. This implies that these jets, being much faster, are highly supersonic, with Mach numbers in the range of 10 to 30. Line diagnostic studies of ionized jets from massive YSOs have indicated typical densities of protostellar jets to be $\sim 10^4$ cm^{-3} at a few hundreds of au from the driving source (Nisini et al., 2005; Giannini et al., 2013) and ionization fraction to be typically $2 - 15\%$ with the maximum value measured to be up to 40% (Bacciotti & Eislöffel, 1999; Bacciotti, 2002; Nisini et al., 2005; Giannini et al., 2013; Obonyo et al., 2019). In addition, it has been observed that ionization fractions decrease with radial distance away from the central source (Fedriani et al., 2019).

The majority of these protostellar jets are highly collimated with opening angles of less than 5° spanning distances of up to several pc (Mundt et al., 1990; Raga et al., 2001). These provide us estimates of typical width or radius of jets. With the knowledge of jet density, radius and its velocity, the mass loss rates can be estimated. Such studies indicate that the jet densities and mass loss rates decrease with increasing evolutionary phase for a young star of constant mass, but increase with the mass of the protostar (Purser et al., 2016). Further, mass-loss rates can be employed in the estimation of accretion rates using the correlation $\frac{\dot{M_{jet}}}{\dot{M_{acc}}} \sim 10 - 30\%$ (Codella et al., 2007; Antoniucci et al., 2008), depending on the mass of the central protostar.

1.2.2 Jet Launching mechanisms

The jet ejection and collimation mechanism has not yet been determined in its entirety. Even with the current generation of single-dish telescopes, it is challenging to get a clear picture of the small-scale processes that occur close to the central protostar. Although the jet launching mechanism is still debated, jets are believed to be closely linked to the magnetic field structure of the associated protostellar system. It is believed that the collimation of jets is achieved by the confining pressure of toroidal component of helical magnetic fields (Livio, 1997; Meier et al., 2001). This has been established by various hydromagnetic and MHD simulations (Lovelace et al., 1987; Ustyugova et al., 1995; Cerqueira & de Gouveia Dal Pino, 2001; Zanni et al., 2004; Bellan et al., 2005).

The MHD models are currently the focus of the majority of research. The two main widely accepted MHD models for protostellar jet launch are the Disk-wind and X-wind models. In this section, we will briefly discuss these models.

1.2.2.1 Disk-wind model

The idea of disk-wind model was originally conceived by Blandford & Payne (1982). The basic model envisions the entire accretion disk to be plasma-like as a result of heating by the protostar at the center. In this condition, the stellar magnetic field is able to pass through the disk unimpeded. A poloidal magnetic field predominates within the Alfvén radius, which is the radius at which the ratio of the flow velocity and Alfvén velocity in the poloidal direction attains a value of 1. Therefore, within this radius, the poloidal flow is sub-Alfvén and the magnetic field that passes through the disk co-rotates with the disk that rotates at the keplerian rate and drags the plasma along with it. When this happens, materials may be funneled from the disk out along the lines of the poloidal magnetic field as a result of the interaction between the centrifugal force of rotation and the poloidal magnetic field, akin to the analogy of beads-on-a-string. Based on the calculations carried out by Blandford & Payne (1982), in order for the centrifugal force on a packet of material at a certain point to be able to overcome the gravitational pull towards the protostar, the poloidal magnetic field component at that point must make an angle of at least 30° to the spin axis of the protostar. After crossing the Alfvén distance, the strength of the poloidal field diminishes and the inertia of the plasma that is in motion around the rotation axis

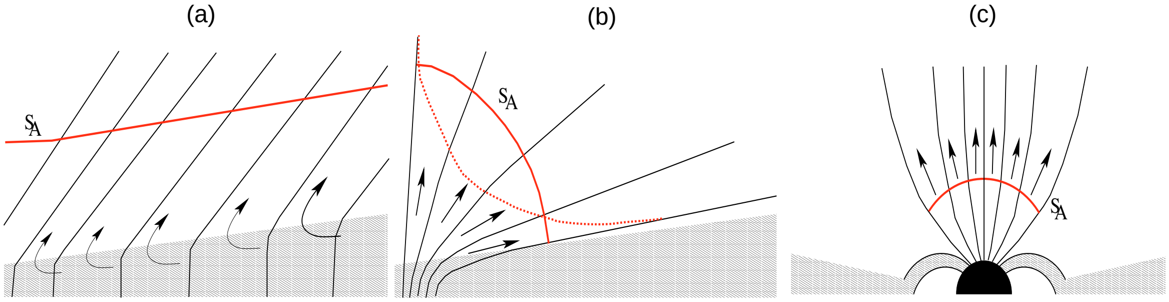

Figure 1.5: Schematic diagram illustrating (a) Disk winds, (b) X-winds and (c) Stellar winds as adapted from Ferreira et al. (2006). The black lines represent magnetic field lines and arrows indicate the direction of wind/jet that is launched. The respective Alfvén surfaces (S_A) have been sketched schematically (red lines) and the central YSO is shown in black.

starts to take over. The poloidal field is thus transformed into a robust toroidal field as a result of this motion. The magnetic hoops that follow from this process produce a helical structure that functions as a funnel to direct material along the rotation axis thereby generating a collimated jet (Brand, 2006). This scenario is represented in Fig. 1.5(a).

1.2.2.2 X-wind model

The X-wind model was initially developed by Shu et al. (1988). When compared to the disk-wind model, the primary distinction is that the magnetic field does not pass through the accretion disk in this case. Here, the magnetic field of the star is compressed and pushed through the disk's innermost radii. The inner edge of the disk is believed to be threaded by strong magnetic field lines associated with the stellar magnetosphere. The point on the inner disk where the angular velocity of the protostar and the disk are equal (co-rotating) is called the X-point. The material at the X-point has the potential to be either funneled along field lines right onto the surface of the star or hurled outward along field lines that are open. This scenario is represented in Fig. 1.5(b). Therefore X-wind model can only remove the residual angular momentum from the co-rotation radius, whereas the disk-wind model is able to remove extra angular momentum throughout several radii along the disk. As one moves away from the disk and closer to the poles of the star, the outflowing material becomes more powerful.

1.2.2.3 Stellar winds

Even though the exact mechanism that causes star winds is still not clearly known, one-dimensional models developed by Cranmer (2008, 2009) imply that MHD waves are caused by the energy that is released during the phenomenon of variable accretion. These waves advance from the accretion hot-spots on the surface of the star to the polar regions, resulting in an increase in MHD wave activity as well as stellar winds. This scenario is represented in Fig. 1.5(c). If the winds are powered by accretion, they are called accretion powered stellar winds (APSWs). APSWs require enormous large-scale magnetic fields to be effective (Zanni & Ferreira, 2011), however the observed fields barely reach the basic criteria of field strength required for their launch (Gregory et al., 2012). Therefore, even if APSWs are a realistic alternative for the launch of jets and spin-down of protostars, it is unlikely that they are the only mechanism involved.

1.2.2.4 Other mechanisms

In addition to the aforementioned mechanisms, there are a number of others that could work in the disk to remove angular momentum and produce outflows. These mechanisms include a magnetic tower flow in which the gas present in the disk can be elevated by the pressure of the toroidal magnetic field (Lynden-Bell, 1996, 2003), hot plasmoid ejection (Skinner et al., 2011) which are analogous to solar coronal mass ejections, or the magnetospheric ejections/reconnection X-wind (Ferreira et al., 2000) generated by the expansion and subsequent reconnection of magnetic field lines linking the star and disk. Besides the initial acceleration imparted to the jets during the magneto-centrifugal launch, a second acceleration process was observed in some jets at distances far away from the launch region (Hirano et al., 2006; Palau et al., 2006; Lee et al., 2022). To explain this, a magnetic acceleration mechanism has been recently proposed by Shang et al. (2023), where the acceleration is induced within a self-similar bubble driven by a wind with toroidal magnetic field orientation. This toroidal magnetic field is believed to increase the radial velocity of the jet up to two or three times its terminal velocity, thereby demonstrating the observed signatures of such long-range acceleration.

That being said, the X-wind and Disk wind models are the most prevalent and extensively utilized theoretical mechanisms. Jets launched under the influence of magneto-centrifugal force, as dictated by these models, are expected to be rotating such that they carry away angular momentum from the innermost disk radii, promoting materials to fall onto the central YSO. In order to corroborate the models for jet launch and to understand the role of jets in removing angular momentum from the disks, it is crucial to measure the jet rotation. Numerous observations have identified and estimated jet rotation towards different sources (Launhardt et al., 2009; Greenhill et al., 2013; Zapata et al., 2015; Lee et al., 2018a,b; de Valon et al., 2020). Jet rotation studies, through the detection of a slow wide-angle outflow, rotating with the disk, in SO and SO_2 emission, have found evidence of disk wind mechanism in the HH 212 jet (Tabone et al., 2017). This finding was further confirmed through higher resolution SO observations towards the same source by Lee et al. (2018a). In addition to the inner disk wind model, the X-wind model was also able to simulate the major characteristics of this jet, including radial flow, jet rotation, and structure (Lee et al., 2022). Therefore, observational evidences favor a magneto-centrifugal launch of jets via X-wind or Disk wind mechanisms.

1.2.3 Morphology of protostellar jets

Conventionally, a protostellar jet is believed to consist of two highly collimated, oppositely directed (bipolar) outflow lobes with numerous shocks and knots along their lengths. These jets terminate in bright bow shocks. The center of the bow shock is oriented perpendicular to the jet/outflow axis and with increase in distance from the axis, the shock surface becomes more oblique. Inhomogeneities in the pre-shock medium have the potential to cause asymmetries in observed bow shock shapes (Bally et al., 2007).

Protostellar jets can have a length scale of parsecs, with some reaching up to more than 10 pc and breaking out of their parent molecular clouds. These highly collimated protostellar jets exhibit morphologies that are comparable to those that originate from other astronomical objects, such as gamma ray bursts, X-ray binaries, and AGN. Owing to this reason and to the fact that all the types of jets share numerous other similarities, the process of jet launching is thought to be universal (Livio, 2011). In fact, collimated outflows occur in the vast majority of astrophysical systems because of the interaction between accretion, rotation, and magnetic fields. Therefore, a clear understanding of launching and collimation mechanisms of outflows of young stars has the potential to be applicable to all types of astrophysical jets.

Three-dimensional MHD models of protostellar outflows (Seifried et al., 2011, 2012) demonstrate that magnetically generated outflows can have a wide range of morphologies, from collimated, elongated outflows to nearly spherical bubbles. In all these scenarios, numerical simulations reveal that outflows have a complicated internal structure characterized by the formation of knots and other instabilities. Although these internal structures are frequently found in the jets of low mass stars (Ray et al., 2007), the outflow structure of intermediate and high mass stars needs to be explored.

1.2.3.1 Knot structure

Protostellar jets can be found in a wide variety of shapes and sizes, and they typically take the form of either linear or gently wiggling chains of compact knots with length-to-width ratios of 10:1 or higher (Reipurth & Bally, 2001). The specific nature of the mechanism that forms internal knots remains debatable. Most existing models are based on the concept that knots represent radiative shocks created within a jet flow.

A knot structure could be induced by Kelvin-Helmholtz (K-H) instabilities (Micono et al., 1998) or by time variability in the ejection velocity of the flow (Raga et al., 1990). Both of these scenarios might result in the production of internal working surfaces. These two scenarios are described below in detail:

(a) **Kelvin-Helmholtz (K-H) instabilities**: K-H instabilities occur at the boundary between the jet and the medium that surrounds it and have the potential to produce a pattern of oblique internal shocks (Ferrari et al., 1982; Birkinshaw, 1997). This process generates shocks that propagate at velocities considerably slower that the fluid and that are potential candidates for knot generation in jets for which the adiabatic treatment is applicable, such as relativistic extragalactic jets (e.g. AGN jets). On the other hand, if the jet is actively cooling via emission of radiation, this results in a decrease in the pressure of the cocoon which is believed to surround the jet. This lower pressure reduces the ability of the cocoon to produce K-H instabilities and as a consequence of this, it reflects internal shocks within the jet beam. Nevertheless, numerical simulations have shown that a wiggling chain of knots can be generated by K-H instabilities if the jet propagates into a medium in which density increases with radial distance from the driving source (de Gouveia dal Pino et al., 1996; de Gouveia dal Pino & Birkinshaw, 1996). In this scenario, the ambient ram pressure directed inward towards the jet axis will cause the cocoon to be compressed, and as a result, the beam will be significantly collimated. Following this, the compressing medium is responsible for inducing the formation of K-H instabilities.

(b) **Time variability in the ejection velocity**: It is now generally accepted that time variability in the ejection velocity of the flow is responsible for the generation of aligned knots in protostellar jets, which usually display a morphology similar to that of a bow shock (Reipurth & Bally, 2001). It essentially generates an ordered chain of radiative knots that are consistently spaced apart and have substantial proper motions. As they travel downstream, the knots undergo gradual expansion in the lateral directions and get weaker. In accordance with most observations, this process favors the creation of knots closer to the driving source of the flow. Theoretical investigations have given impetus for this assertion by demonstrating that propagating shocks generated in this way reproduce the basic properties of the observed knots (Raga et al., 1990; Raga & Kofman, 1992; Stone & Norman, 1993).

1.2.3.2 Onion-like velocity structure

Observations have revealed that the velocity structure of protostellar jets is such that the layers closest to the jet axis are the fastest and are surrounded by components moving at progressively slower velocities. The outer layers are most likely a result of magnetocentrifugally driven disk winds that are driven up to tens of astronomical units away from the central star and would most likely undergo photo-evaporation, but the origin of the innermost components is unknown. This onion-like velocity structure, which was initially observed in the DG Tau jet, has been identified by observations which could resolve the jet base in the lateral direction (Beck et al., 2007; Coffey et al., 2008; Agra-Amboage et al., 2011). As a result, it is possible that this structure is fairly general.

The onion-like velocity structure argues against the X-wind model in which the ejection velocities are similar at every angle. Instead, it mandates that the jet be closely surrounded by a wide angle wind component that is slower. A range of launch radii associated with an MHD disk wind (Agra-Amboage et al., 2011), or a magnetospheric wind that is encompassed by a disk wind (Pyo et al., 2009), can be a reasonable explanation for the progressive decrease in the transverse velocity. This low-velocity layer may also be caused by the presence of turbulent mixing layers as well as material that is expelled laterally from the main axis (Garcia Lopez et al., 2008) of the jet. Deeper understanding of the launch mechanism necessitates observations with high spectral and spatial resolutions.

1.2.3.3 Jet rotation

Observations and detailed studies of jet rotation can provide us with hints regarding the location from which a jet was launched. The detection of jet rotation and its magnitude are therefore essential for testing the currently accepted models for jet launch mechanism. The key distinction between the models is that the amount of angular momentum that is carried away from the system is a consequence of the launch radius i.e., winds released from larger radii typically carry more angular momentum than those launched from smaller radii. For instance, the X-wind model that assumes jet launch to occur at co-rotation radius imparts lesser angular momentum to the jet when compared to the disk wind model where the launch would occur at several au within the disk. Various jets/outflows have been observed to exhibit signs of jet rotation and these include DG Tau jet (Agra-Amboage et al., 2011), TMC 1A6 (Bjerkeli et al., 2016), HH30 (Louvet et al., 2018), CB 26 (Launhardt et al., 2009) and HH 212 (Lee et al., 2017), to cite a few prominent cases. The important factor that is relevant in observations of this kind is high angular resolution because, here one is attempting to identify variations in velocity laterally across a jet whose width is no more than a fraction of an arcsecond (Dougados et al., 2000).

1.2.4 Shocks generated by jets

Shock fronts are an inevitable result of the passage of supersonic jets/outflows through the protostellar envelope and the ambient molecular gas (Reipurth & Raga, 1999). Shocks occur whenever material propagates at velocities greater than the sound speed in the surrounding medium and the upstream material is unable to respond dynamically until the incoming material arrives (Draine & McKee, 1993). Following this, the shock compresses, heats and accelerates the medium. Elastic collisions of the ambient molecular gas entering the shock front with the previously shocked gas particles results in the heating and velocity randomization of these particles. In contrast, the grains in the interstellar medium are weakly coupled to the gas, making such collisional heating of grains infrequent. As a result, shocks are observed to be rich in line emission from cooling gas with relatively weak continuum emission from the grains (McKee et al., 1984; Hartigan et al., 1994; Gusdorf et al., 2008).

Collimated flows tend to generate shocks both along the flow and at the terminal edges where they slam into the slower ($\sim$ 1 km s^{-1}) or stationary cloud material. Shocks are a significant channel of stellar feedback in galaxies. Based on the physical properties such as ambient magnetic field strength, ionization fraction, shock velocity and the gas density, shocks can be broadly classified as (i) Jump shocks (J-shocks/J-type) (ii) Continuous shocks (C-shocks/C-type) and (iii) J-type with magnetic precursor (Draine, 1980; Flower et al., 2003).

1.2.4.1 J-shocks

A pressure disturbance that originates in cold interstellar medium where the sound speed can be assumed to be very small can result in a thermodynamically irreversible transition which will transform the energy of the bulk flow into the random thermal motion of particles. This results in the flow variables experiencing a discontinuous jump across the shock front, hence the label J-shock (Hollenbach, 1997). J-shocks are caused by jets with velocities larger than $50 - 80$ km s^{-1}. At these velocities, the temperature behind the shock front could rise up to 10^5 K (McCoey et al., 2004), as opposed to the pre-shock temperature of 10 K. The temperature profile of a typical J-shock is shown in Fig. 1.6(a). Across the discontinuity, there is a factor of 4 (at most) increase in the density of the gas, although the gas continues to be compressed in the cooling flow (Draine & McKee, 1993). Due to their high velocities, the ambient gas is abruptly halted, compressed and heated to high temperatures, and the shock front is much thinner than the post-shock cooling zone (Wilgenbus et al., 2000; Lehmann & Wardle, 2016). Thus, the mass, momentum, and energy conservation equations can be employed in terms of a set of straightforward "jump" conditions. The standard procedure followed when attempting to solve for the flow via J-type shock waves is to apply the Rankine-Hugoniot (RH) relations (Macquorn Rankine, 1870; Hugoniot, 1887, 1889) to the pre-shock gas and then numerically integrating the post-shock flow. The RH reations are a set of three equations that relate the state variables such as density, velocity and temperature of the preshock and the postshock gas to one another, as given below.

$$\boldsymbol{n_{post} = 4n_{pre}} \tag{1.3}$$

$$\boldsymbol{v_{post} = (1/4)v_s} \tag{1.4}$$

$$\boldsymbol{T_{post} = 31.8v_s^2 x_n^{-1} K} \tag{1.5}$$

Here, n_{pre} is the density of the ambient material (preshock), v_s is the shock velocity in km s^{-1} and x_n is the number of gas particles per hydrogen nucleus.

In a partially ionized medium, due to the presence of ion-neutral collisions and a well coupled magnetic field, disturbances undergo damping and propagate at the bulk Alfvén speed (v_A) given as (Hollenbach et al., 1989):

$$v_A = \left[\frac{B^2}{4\pi\rho}\right]^{1/2} \tag{1.6}$$

Here, B and ρ are the magnetic field strength and mass density of the medium. Shocks are possible in the medium if the disturbances propagate at velocities greater than v_A.

In a plasma with negligible ion-neutral collisions and in which magnetic field is well coupled to the ions, then Alfvén disturbances will propagate without damping at ion-Alfvén speed which is given as:

$$v_{i,A} = \left(\frac{\rho}{\rho_i}\right)^2 v_A \tag{1.7}$$

Here, ρ_i is the ion mass density. It can be noted that $v_{i,A}$ is always greater than v_A. If the compressive waves generated by the jet propagates at a velocity v_s, the shock structure is determined by whether $v_s > v_{i,A}$ or $v_s < v_{i,A}$. When B $= 0$, $v_s > v_{i,A}$ and $v_s > v_A$, it is no longer possible for information to travel upstream in the pre-shocked medium quickly enough to outrun the shock. This results in a discontinuous change in flow variables of both ions and neutrals across the shock front, thereby forming J-shocks.

J-shocks, being fast, dissociate the molecules and ionize the gas. Hence, they are mostly rich in hydrogen recombination lines and fine-structure lines from ions, such as [Ne II](12.8 μm), [Si II](35 μm), and [Fe II](26μm), and associated with high ionization levels and low magnetic field strength (Hollenbach & McKee, 1989).

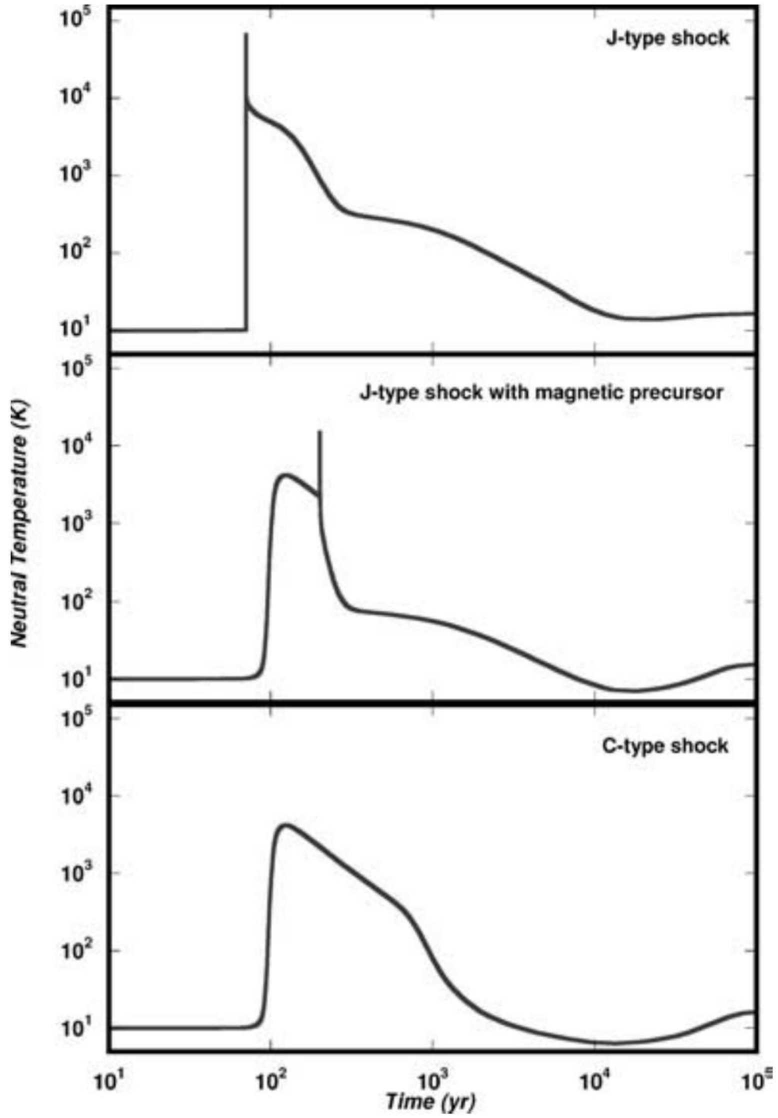

Figure 1.6: Temperature profiles of (top) J-shocks, (middle) Intermediate J-shocks and, (bottom) C-type shocks for a shock velocity, number density and magnetic field strength of 40 km s^{-1}, 10^4 cm^{-3} and 100 μG, respectively (McCoey et al., 2004).

1.2.4.2 Intermediate J-shocks

Younger shocks typically tend to be J-shocks (strong) and such shocks may eventually evolve into C-shocks (weak) in the presence of a strong magnetic field (Smith & Mac Low, 1997). A shock that has not attained thermal equilibrium could display the properties of both J- and C-shocks (Flower et al., 2003). The transitional stage in this evolution is called the intermediate J-type shock/J-shock with magnetic precursor.

For a medium with a relatively low ionization fraction, the presence of a sufficiently strong magnetic field results in the condition $v_{i,A} > v_s$ (Chernoff, 1987). The disturbances can now propagate through ions faster than the shock front and will begin to compress the ions and the coupled magnetic field in the upstream medium. This feature is known as a magnetic precursor. This precursor forces the upstream ions to stream through the neutral gas inducing ion-neutral collisions, thereby compressing the neutrals ahead of the arrival of the actual J-shock front (Draine, 1980). Even if the magnetic field is not particularly strong, when the fractional ionization is low, a shock is more likely to posses a magnetic precursor. An increase in magnetic field strength will enhance the influence of the precursor such that more ion-neutral collisions will be instigated, increasing the amount of energy and momentum imparted to the upstream neutral fluid. This causes the neutrals to be also strongly heated and compressed along with the ions and the field. In this scenario, the flow properties of both ions and neutrals do not undergo a sharp jump, but rather the height of the jump will reduce and the flow tends to be more continuous (McCoey et al., 2004). Compared to that of pure J-shocks, the presence of a precursor can result in a broadening of the shock front and a reduction in the peak temperature. The temperature profile of this scenario is shown in Fig. 1.6(b).

1.2.4.3 C-shocks

C-shocks are typically associated with velocities $\sim 40-50$ km s^{-1}, low ionization of molecular gas and strong magnetic fields (Wardle, 1990; Smith & Mac Low, 1997; Guillet et al., 2011). C-type shock waves can exist up to higher shock speed values than previously anticipated, according to new studies. For instance, when the pre-shock gas density is 10^4 cm^{-3}, the shock wave can continue to be of the C-type up to a velocity of 70 km s^{-1} (Le Bourlot et al., 2002; Flower & Pineau des Forêts, 2003). In a medium with low ion fraction, the influence of the magnetic precursor is strongly dependent on the strength of the magnetic field. If the magnetic field is stronger than a critical value such that $v_{i,A} >> v_s$, the influence of the magnetic precursor will result in the complete quenching of the J-shock front (Mullan, 1971). This indicates that the well coupled magnetic field and ions, along with the neutrals will not experience any jump but will instead display a smooth and continuous variation, hence the name C-shock (McCoey et al., 2004). In this case, the shocked neutral gas attains maximum temperatures of $3000 - 10^4$ K, depending on the density of the gas

(Hollenbach & McKee, 1989). The temperature profile of this scenario is shown in Fig. 1.6(c).

These shocks are rich in IR molecular emission lines (H_2, CO, H_2O, SiO etc.) (Noriega-Crespo, 2002; Gusdorf et al., 2008). Molecular emission is favored in these shocks because, by means of the ions, the magnetic field develops a magnetic precursor that broadens the shock front and offers a broad cushioning layer. The resultant absence of sharp jump across the shock front prevents dissociation of molecules (Draine & McKee, 1993).

1.3 Observations of protostellar jets

Observationally, protostellar jets have been probed at a wide range of wavelengths from radio band up to the X-ray regime (Güdel et al., 2007; Plunkett et al., 2015; Fedriani et al., 2019). In this thesis, we will focus on the radio and NIR wavelengths. These wavebands are advantageous as these suffer from minimal extinction compared to shorter wavelengths and also have the ability to trace different excitation conditions along the jet, traced by radio continuum emission, ionic emission and molecular gas. We will discuss this in detail in the following subsections.

1.3.1 Significance of radio observations

Radio continuum as well as spectroscopic studies have been extensively carried out towards protostellar jets since the effect of extinction is minimal in this wavelength regime (Reipurth et al., 2004; Shang et al., 2004; Obonyo et al., 2019). Radio spectroscopy can assist in imaging as well as kinematic studies of jets driven by highly embedded protostars which are inaccessible at other wavelengths. Aided by relatively less extinction and high angular resolution provided by radio interferometers, the advantages of radio continuum observations towards embedded YSOs are also manifold. Of these, the two key aspects relevant to this study are that it enables us to (i) Probe the base of ionized jets which is essential in understanding the jet acceleration and collimation mechanisms, (ii) Trace deeply embedded close protobinary systems which are useful to study their influence on jet's precession. This serves as a rationale for the fact that protostellar jets have been widely studied in the radio wavelengths (Bally, 2016; Girart et al., 2018).

Emission mechanisms

The radio emission from protostellar jets are typically considered to be thermal free-free emission (Girart et al., 2018) resulting from acceleration of electrons within the electric field of ions present in the partially/fully ionized jet material. It has been observed that, within radial distances of $\sim$1000 au from the driving source, the flux densities (S_ν) of radio jets were found to increase with increase in frequency as $S_\nu \propto \nu^\alpha$ (Sanna et al., 2018). In this case, the spectral index α will be positive indicating partially opaque emission with $0 < \alpha < 2$. However, a review of literature indicates that the radio spectral indices of protostellar jets are usually modeled as thermal free-free emission or synchrotron emission or a combination of both using simplistic considerations of uniform electron density, temperature, etc (Rodríguez, 2011; Purser et al., 2016; Anglada et al., 2018). This is in consequence of spectral indices of few radio jets being observed to be steeper than the optically thin limit of -0.1 for free-free emission, which is a manifestation of a non-thermal emission mechanism in addition to free-free emission (Rodríguez-Kamenetzky et al., 2016; Vig et al., 2018; Obonyo et al., 2019; Feeney-Johansson et al., 2019).

The most prominent example for the detection of non-thermal emission from protostellar jets is the HH80-81 jet system, driven by the massive protostar IRAS 18162-2048. High frequency radio observations of this jet had revealed negative spectral indices in the jet and its associated knots (Rodríguez & Reipurth, 1989; Curiel et al., 1993; Marti et al., 1993), and in addition, low frequency radio observations have enabled easier detection of the non-thermal emission (Vig et al., 2018). Among the lower mass counterparts, observations across a wide range of radio frequencies (Ainsworth et al., 2014; Purser et al., 2018; Feeney-Johansson et al., 2019) have shown that DG-Tau stands out in terms of non-thermal emission from protostellar jets. Furthermore, sensitive polarization observations towards the HH80-81 jet have found evidence for linearly polarized radio emission confirming that the observed negative spectral indices are arising from synchrotron emission (Carrasco-González et al., 2010).

1.3.2 Significance of NIR observations

As discussed earlier, the impact of these supersonic jets on the ambient medium results in the formation of shocks (Hollenbach, 1997; Suzuki-Vidal et al., 2015). The jet emission derives from the associated radiative shocks. Studies have shown that the shocked plasma is rich in forbidden line emission ([Fe II], [SiII], [NeII], [SII]) in the optical and IR wavelengths (Stapelfeldt et al., 1991; Nisini et al., 2005; Dionatos et al., 2009; Sacco et al., 2012). These lines can assist us in developing a better understanding of the physical parameters of the jet and its dynamics (Lavalley et al., 1997; Bacciotti & Eislöffel, 1999). Although high-velocity jets from YSOs produce shock-excited optical nebulae at large distances (HH objects), a search for jet signatures closer to the YSO could help us probe the inner regions of jets. This in turn is essential for the comprehension of jet launching and collimation mechanisms from protostars. Most YSOs are embedded within their molecular clouds causing these innermost regions to be highly obscured from our direct view in optical wavelengths. Although these driving sources remain highly obscured in the NIR wavelength, protostellar jets can be well probed in this regime and this can offer a wealth of information regarding the star-forming complex. The fact that protostellar jets provide a historical record of accretion, makes observations of these jets, particularly in the NIR, crucial in the study of embedded YSOs for which it is difficult to directly observe the process of accretion.

Embedded jets can be well probed at NIR wavelengths as they provide dual advantages of lower extinction and good spatial resolution. Numerous studies have been conducted in this domain over the past years (Whelan et al., 2004; Nisini et al., 2005; Davis et al., 2006; Podio et al., 2006; Varricatt et al., 2010). The NIR spectrum is rich in brightest atomic ([Fe II], [SII], [NI] etc.) as well as molecular (H_2) lines (Hartigan et al., 1994; Eislöffel et al., 2000; Nisini et al., 2002; Giannini et al., 2004) with the former tracing the inner ionized jet and the latter tracing the cold post-shocked molecular gas.

In the case of jets driven by high mass YSOs, observational studies are severely hampered due to high extinction ($A_V \lesssim 100$ mag) and large distances (several kpc) involved. In this scenario, it is challenging to isolate YSOs and their outflows due to confusion. In some instances, outflows could be driven by more than one object or even by YSOs with lower masses. One of the most unanswered questions in the area of understanding outflows from young stars of intermediate and high masses is the identification of the similarities and differences between the jets and surroundings of these young stars.

Emission from protostellar jets is typically characterized by line emission predominantly in the ultraviolet (UV) to sub-mm wavelength range. However, a review of literature shows that historically, these jets are widely observed in optical and NIR wavelengths. These wavelengths are very promising because the impact of these supersonic jets results in shock formation and cooling zones of the shocked plasma is rich in optical and IR emission lines. Since YSOs are highly embedded, the optical wavelength suffers from more extinction and therefore these shocks can be best studied in the NIR which undergoes lesser extinction. In general, massive outflows are commonly investigated through molecular outflow tracers (SiO, CO, HCO^+) at sub-mm and millimetre wavelengths (Beuther et al., 2002b; Wu et al., 2004; Duarte-Cabral et al., 2013). NIR also offers better resolution compared to most millimetre-wave observations, and this is essential for probing the collimated jet and individual compact knots.

We can observe a combination of permitted as well as forbidden emission lines from shocks associated with protostellar jets. The detection of forbidden emission lines can be perceived as the presence of low electron densities of the order of $10^4 - 10^5$ cm^{-3}. Imaging and spectroscopic studies of emission lines can assist us in probing the kinematics and in estimating fundamental physical parameters such as radial velocity, temperature, electron density etc. (Woitas et al., 2002; Nisini et al., 2005; Giannini et al., 2013). In addition, we can indirectly measure other relevant parameters, mainly, ionization fraction, mass loss rate, accretion rate etc. (Hartigan et al., 1994; Reiter et al., 2016).

1.3.2.1 Molecular H_2 and atomic [Fe II] emission

The most important NIR lines that have been employed to trace protostellar jets are the H_2 and [Fe II] emission lines (Stapelfeldt et al., 1991; Gredel et al., 1992; Smith, 1994; Davis & Eisloeffel, 1995; Reipurth et al., 2000). H_2 is a homonuclear diatomic molecule and for this molecule, only electric quadrupole radiative transitions are allowed between its ro-vibrational levels. The ro-vibrational lines of H_2 in the NIR spectrum, which are typically optically thin, serve as excellent tracers of the physical conditions that prevail in the inner circumstellar discs and winds that are located close to protostars. Using the line intensities corresponding to various H_2 transitions between different ro-vibrational levels, the temperature, column density and visual extinction can be derived. The possible mechanisms that could be responsible for the creation of NIR H_2 emission lines include (i) shocks resulting from the interaction of jets or winds with the ambient medium (Burton, 1987; Fernandes & Brand, 1998), (ii) UV fluorescence (Beckwith et al., 1978; Gatley et al., 1987), (iii) heating by X-rays (Draine & Woods, 1989) and, (iv) molecular formation pumping (Hollenbach & McKee, 1989). In general, in the scenario of shock excitation, collisions between the molecules populates the ro-vibrational levels of the ground electronic states. This occurs behind the shock front. Therefore the emission traces the location of the shock waves generated by a supersonic jet, and delineate where the kinetic energy of the jet is transformed to thermal energy in the molecules and subsequently radiated as line emission. The line-width of shocked H_2 lines typically have widths larger than that of fluorescent H_2 lines. In addition, higher excitation lines ($\nu \geq 5$) arise from florescent emission as opposed to collisional excitation. In the case of protostars, shock excitation has been the most commonly observed excitation mechanism for NIR H_2 emission (Davis et al., 2010). The 2.12μm line which is utilized in this study is the $\nu = 1 - 0$ S(1) line that corresponds to the transition from $\nu = 1$ to $\nu = 0$ and from $J = 3$ to $J = 1$.

Another important tracer, which is very useful in the study of shock properties, is the NIR [Fe II] emission lines (Dinerstein, 1995; Nisini et al., 2002; Nisini, 2008). These lines are stronger when generated by shocks as compared to that of photoionized regions. The reasons for this are: (i) the Fe^+ ion has 16 levels with low excitation energies such that shocks can easily excite these levels and the subsequent transitions among them result in numerous emission lines, particularly in the NIR band, (ii) Fe atom has low ionization potential (7.9 eV) such that the far-UV radiation from the shock front will be able to ionize Fe atoms in the post-shock region to Fe^+ ions, even while hydrogen atoms with higher ionization potential (13.6 eV) remains neutral and, (iii) Shocks can induce grain destruction which will release the Fe that is locked within these grains and this will increase the Fe abundance resulting in stronger emission (McKee et al., 1984; Hollenbach et al., 1989; Oliva et al., 1989; Mouri et al., 2000; KOO & LEE, 2015). The [Fe II] emission line at 1.644μm, which is utilized in this study corresponds to the transition from $3d^6 4s$ to $3d^7$ configuration of the Fe^+ ion.

High resolution observations have shown that the structure of jets/outflows can be divided into two main regions: (i) inner high-velocity material close to the jet axis, and (ii) low velocity less ionized gas near the limb of the jet/outflow (Moriarty-Schieven & Snell, 1988; Schmid-Burgk et al., 1990). The NIR H_2 and [Fe II] emission lines trace distinct regions along the same jet, and provide information complementary to that of optical and radio observations. Generally, [Fe II] emission arises from strong shocks in the inner regions close to the jet axis, while H_2 is typically associated with the boundary between the jet and the ambient medium (Davis et al., 2003). Therefore, a combination of H_2 and [Fe II] imaging of a jet can provide a unique insight into the jet propagation in the molecular cloud.

It is noteworthy that there have been large scale surveys targeted on these lines (Lee et al., 2014; Davis et al., 2008, 2009, 2008, 2009; Froebrich et al., 2011). Recent NIR surveys that utilize the $2.12\mu m$ H_2 emission, have shown a considerable increase in the number of candidate massive protostellar jets (Stecklum et al., 2009; Varricatt et al., 2010; Lee et al., 2012).

1.4 Motivation of this thesis

The primary motive of this research is to improve our understanding of various physical properties of protostellar jets. For this, we adopted a two-pronged approach. In the first case, we have developed a model that can help elucidate the properties of radio emission from ionized protostellar jets. This work was motivated by observations that have revealed the signatures of non-thermal emission in protostellar jets, followed by the confirmation of its synchrotron origin. An exhaustive assimilation of the model and available radio observational data can help in a comprehensive understanding of jets. The geometry of our model is such that the regions close to the jet axis, which are highly ionized, contribute to the majority of free-free emission and the outer edges that impact on the ambient medium result in the formation of astrophysical shocks where the conditions are suitable for the generation of synchrotron radiation along with free-free emission. We have studied the influence of each parameter on the characteristics of the model spectra and this has enabled us in estimating the parameters associated with the jets for which non-thermal emission was detected. This work lies in a relatively unexplored arena of understanding radio emission from protostellar jets. In the second part of the research, our objective was to investigate the partially ionized and molecular regions of protostellar jets in the NIR regime. This was motivated by the fact that NIR imaging and shock analysis of massive protostellar jets/knots using emission line tracers, H_2 and [Fe II] lines in particular, are very sparse. The properties of these lines can provide a wealth of information regarding the strength and nature of shocks associated with each knot of the jet. This, in turn, could provide valuable information regarding the jet dynamics and other important physical parameters associated with the jet and the central protostar. This can also be used as a diagnostic tool to indirectly examine few properties of the driving source of the jet. With this aim, we carry out a case study of the prominent protostellar jet, HH80-81, in which the jet is imaged in the NIR H_2 and [Fe II] filters for the first time.

Thus, the major objectives of the study can be summarized as follows:

(a) Numerical modeling of radio emission from protostellar jets:
   i. Develop a model which incorporates thermal and non-thermal radio emission mechanisms in a jet geometry consistent with previous observations and also overcome all the limitations of the existing widely used model, i.e., model by (Reynolds, 1986).
   ii. Characterization of radio spectra generated by the model by analyzing the effect and interdependence of various jet parameters on the model spectra.
   iii. Application of the model to the observational data of relevant protostellar jets to estimate the physical and micro-physical parameters associated with the jet and its environment.

(b) NIR narrow-band imaging of massive protostellar jets:
   i. Tracing the NIR H_2 and [Fe II] emission lines associated with a massive protostellar jet. HH80-81 jet was chosen as the target source for this case study.
   ii. Morphological analysis of the jet knots to gather clues regarding the nature of shocks that give rise to these emission.
   iii. Utilization of the observed emission in the estimation of physical parameters of the jet and the driving source.

These objectives have been adequately met through this study and will be discussed in detail in the following chapters.

1.5 Thesis outline

The thesis is structured in the following way:

Chapter 1: Introduction

In this chapter (the current chapter), we give a brief overview of star formation and a few observational aspects of high mass star formation and its early evolutionary stages. Since our focus is on the protostellar phase which is accompanied by protostellar jets, the jet launching mechanisms, the morphology of the jets and shocks are discussed in detail.

Chapter 2: Radio spectra of protostellar jets: Model description

In this chapter we discuss the important attributes of radio observations of protostellar jets. We first introduce the existing model for protostellar jets and its limitations. We then describe in detail the numerical model which we have developed. We highlight the geometrical features of the jet, followed by discussion about the emission mechanisms; thermal free-free and non-thermal synchrotron emission within the jet geometry. We then compare our model with the existing model to discuss the improvements and novelty of our new model over the existing one.

Chapter 3: Radio spectra of protostellar jets: Results from the model

In this chapter we demonstrate and interpret the model results. We explore the spectra generated by our model for various cases considered for the input parameters. We discuss the spectral properties of thermal and non-thermal spectra generated by our model to study the effects of different jet parameters on the spectra and the behavior of emission at different regions within the jet structure.

Chapter 4: Radio spectra of protostellar jets: Applications of the model

In this chapter we apply the model to observational data of protostellar jets with non-thermal emission in addition to thermal emission in their radio emission. For this, we have utilized the knowledge of the dependence of the jet spectrum on various model parameters. The sources to which we have applied the model include HH80-81 jet, jet driven by the massive YSO G114.0835+02.8568 and DG-Tau jet.

Chapter 5: Understanding of the massive protostellar jet HH80-81 in NIR shock tracers

In this chapter, we first present the details of the NIR observational data obtained for the HH80-81 jet system. We also elaborate the data reduction procedure that is followed for generating the narrow-band emission line images. We then give a brief introduction of the HH80-81 jet. We then proceed towards the discussion and interpretation of the images obtained from the analysis of the NIR data. This involves a discussion on NIR molecular H_2 and [Fe II] emission, utilization of these tracers to identify the nature of shocks in the HH80-81 jet knots and estimation of various physical parameters of the jet including luminosities, mass-loss and accretion rates. In addition to this, we also look into the imaging of the central region towards the driving source in broad-band and narrow-band emission. This primarily includes the molecular H_2 emission features identified here and its correlation with various outflows and YSOs in the neighborhood.

Chapter 6: Conclusions and future scope

Here we give a brief summary on the findings and inferences of this study. We discuss the alternative methods and strategies that can be followed for the robust application of the numerical model that we have developed. We also discuss the possibility of extending the observational techniques and procedure for estimation of jet parameters which we have followed here to various samples of other high mass YSO jets, given the paucity of studies on this topic.

Chapter 2

Radio spectra of protostellar jets: Model description

When on the pursuit of determining the physical and micro-physical parameters of protostellar jets, observations often battle against various limitations due to technical constraints thereby limiting the knowledge that can be achieved. The major challenges faced by astronomical observations include either of the following depending whether it is space- or ground-based: limited size of the telescope and field of view, artificial satellite contamination, atmospheric turbulence and poor weather conditions, scintillation, light pollution, extinction suffered by embedded sources, optical effects of instruments etc. In these scenarios, astrophysical models are essential for the complete exploitation of the limited information that can be extracted from available observational data and for understanding the underlying physical mechanism. Therefore, astrophysical models that assist in the complete interpretation of the observational data are complementary tools that are crucial in the present day research.

In this study, we develop and employ a numerical model to improve our understanding of protostellar jets and their emission mechanisms. This thesis is primarily focused on the characterization of the observed radio spectra of protostellar jets with the help of our toy model. As discussed in Chapter 1, the radio emission from protostellar jets results from either thermal free-free emission or synchrotron emission or a combination of both. Free-free emission from these jets is completely understood and has been well characterized, whereas the synchrotron emission properties are less explored. Non-thermal synchrotron emission has been observed toward several radio knots, associated with jets driven by YSOs, that show negative spectral indices. For example, a sample of few such jets show spectral indices in the range -0.3 to -

1.3 (Rodríguez-Kamenetzky et al., 2016; Purser et al., 2016; Osorio et al., 2017; Vig et al., 2018; Tychoniec et al., 2018; Obonyo et al., 2019). Such high negative spectral index values (α < -0.1) cannot be modeled by the Reynolds model as it considers only free-free emission, and these values can be explained through synchrotron emission. This emphasizes the need to develop a model that also incorporates synchrotron emission in addition to free-free emission. We have therefore incorporated both thermal free-free and non-thermal synchrotron emission mechanisms in our model.

2.1 Synchrotron emission in protostellar jets

Synchrotron radiation in radio wavelengths is typically observed in relativistic jets from AGN, micro-quasars etc. The theory of synchrotron emission from high energy phenomena related to these extragalactic jets is well established (Reynolds, 1982; Biermann & Strittmatter, 1987; Sari et al., 1998) because of the large volume of observational evidence that is available (Wijers & Galama, 1999; Dhawan et al., 2000; Harris & Krawczynski, 2006). However, there is lack of clarity regarding the origin of synchrotron emission from protostellar jets. This is mainly owing to the fact that there are fewer detection of synchrotron emission from protostellar jets, which in turn is related to their lower energies.

The presence of synchrotron emission in protostellar jets is a direct indication of the presence of relativistic or mildly-relativistic electron population within the jet material, implying that some acceleration mechanism is present. Evidence from relativistic extragalactic jets show that such relativistic electrons are generated via diffusive shock acceleration (DSA) which accelerates the originally thermal and supra-thermal electrons in the presence of shock waves (Fermi, 1949; Blandford & Eichler, 1987; Bosch-Ramon et al., 2010). Shocks are the outcome of such supersonic jet-ISM interaction. Protostellar jets propagate at velocities of few hundreds to thousands of km s^{-1} which is much larger than the typical speed of sound in the ISM, thereby generating shocks. As a result of magnetic turbulence in the shocked plasma, the electrons gain energy by diffusing back and forth across the shock front (Axford et al., 1977; Blandford & Ostriker, 1978). The upper limit of the energy gained by these electrons, on acceleration across the non-relativistic plane parallel shock fronts, is dependent on the amount of energy lost in the form of radiation and the number of particles that are advected away from the acceleration region. It is seen that in a fast and fully ionized protostellar jet, the particles could be accelerated up to energies of the order of TeV (Araudo et al., 2007), although this could be lower in the case of a partially ionized medium due to damping of Alfv́en waves by ion-neutral collisions (Padovani et al., 2015, 2016). Energies of the order of TeV imply Lorentz factors (γ) of the order of 10^6. Assuming that this energy is also dissipated by radiative losses such as relativistic bremsstrahlung etc., the remnant energy is sufficient to produce non-thermal synchrotron emission ($\sim$GeV) by acceleration of these relativistic electrons across the shock amplified magnetic field.

It is now clear that shocks are essential for the generation of relativistic particles. In general, a two-shock system is believed to exist at the region of interaction between the supersonic jet and the ambient medium, which consists of an adiabatic and a radiative component. Adiabatic shocks develop when the thermal timescale is longer than the shock timescale and radiative shocks develop in systems with high densities. Theoretical models have shown that relativistic particles originate via DSA within strong and fast adiabatic shocks in protostellar jets (Araudo et al., 2007; Bosch-Ramon et al., 2010) and this is hampered by slow shocks moving in dense medium. DSA is not possible in radiative shocks because in these shocks, the resultant entropy in the shocked material will be considerably high as a result of heating. This will result in the loss of order due to which inhomogenities arise in the magnetic field thereby hampering particle acceleration. High sensitivity and high angular resolution observations in radio wavelengths towards the HH80-81 jet had revealed that the synchrotron emission arises from the edges and termination points of the jet (Rodríguez-Kamenetzky et al., 2017). This can be attributed to the fact that strong adiabatic shocks are generated at the region of interaction between supersonic jet material and the relatively stationary ambient molecular cloud, thereby resulting in synchrotron emission in these regions within the jet geometry.

The thermal emission which is well studied in protostellar jets is a result of internal shocks due to variabilities in the flow velocity whereas synchrotron emission arises from stronger shocks at the lateral and terminal edges of the jet. Studying synchrotron emission from these jets could open up a new avenue of research to study the mechanism of DSA in slow-moving non-relativistic and dense plasma as opposed to relativistic strong shocks which are well studied in the case of high energy astrophysical phenomena. Hence, we are interested in constructing a model of the radio jet that can encompass both the thermal as well as non-thermal emission as a function of various model parameters.

2.1.1 Magnetic field information

As discussed in Chapter 1, the protostellar jets and magnetic field are closely associated in in various aspects including jet launching, acceleration and collimation even up to large distances. The well studied thermal free-free emission from protostellar jets, however, does not provide direct information about their magnetic field. Thus, the magnetic field is one of the least known physical parameters in protostellar jets. Synchrotron emission, on the other hand, can be used to gauge the direction and strength of magnetic field. It is also interesting to note that theories predict similar morphologies for jet magnetic fields, irrespective of whether they are of protostellar or AGN origin (Koenigl, 1986; Livio, 2000). Therefore, the identification of synchrotron emission from protostellar jets is indispensable and could provide valuable hints regarding the associated magnetic fields.

The major significance of studying sychrotron emission in protostellar jets is that the properties of synchrotron emission allows us to better analyze the associated magnetic field, using the same techniques followed in the case of relativistic jets. The magnetic field strength can be determined based on the SED at cm wavelengths and the field orientation and morphology can be derived from the linear polarization properties which include polarization angle, polarization degree and Faraday rotation. It is then possible to infer the 3-D morphology of the magnetic field by assimilating the observational results with theoretical models.

2.2 The Reynolds (1986) model

For thermal jets, the most widely employed model is that of Reynolds (1986), hereafter Reynolds model, which analytically calculates the radio emission and spectral indices using thermal free-free emission for various jet geometries. This model estimates thermal continuum emission from narrow, ionized jets as a function of jet parameters such as its width, ionization fraction, velocity and temperature which follow power-law radial profiles. The partially opaque spectral index of spherical, isothermal, constant-velocity jet estimated by the model is +0.6 and this model also delineate the conditions under which the spectral indices can be steeper or flatter than this value. This model assumes that the jet becomes sufficiently ionized at the injection radius given by r_0 and has a half-width of w_0 at r_0. The width of the jet is assumed to display a power-law gradient as a function of radial distance r from the driving source, such that the half-width w at any r is given by,

$$w = w_0 \left(\frac{r}{r_0} \right)^{\epsilon} \tag{2.1}$$

Here, ϵ is the power-law index of the radial profile of jet width. For an isothermal jet with constant velocity and ionization fraction, the free-free flux density ($S_{ff,\nu}$) increases with frequency (ν) as $S_{ff,\nu} \propto \nu^{\alpha}$. Here, α is the spectral index and its dependence on the jet geometry is given by,

$$\alpha = 1.3 - \frac{0.7}{\epsilon} \tag{2.2}$$

Although this model can be employed to explain the observed spectral indices from thermal jets in general, it suffers from various limitations which we have listed below.

(a) The Reynolds model has considered only thermal free-free emission in the estimation of spectral indices of radio jets

(b) The flux densities are calculated under the assumption that the jet is optically thick ($\tau >> 1$) towards the base and optically thin ($\tau << 1$) at farther radial distances. In other words, the Reynolds model assumes that the total flux density at a given frequency from the full length of the jet is the sum of fully optically thin and fully optically thick flux densities at that frequency.

(c) This model has adopted small angle approximation in its geometry, therefore, it is only applicable to narrow collimated jets.

2.3 Our toy model

We have formulated a numerical model to demonstrate the observed radio spectral indices using thermal and non-thermal emission mechanisms, simultaneously attempting to overcome the drawbacks of the Reynolds model. The geometrical considerations and emission mechanisms of our new model are described in detail in the following sections.

2.3.1 Jet model description

We have adopted a basic geometry that is identical to that of the Reynolds model but with multiple modifications applied. The geometry and orientation of the jet with respect to the observer is shown in Fig. 2.1. We assume the injection of jet at radius r_0, with an opening angle θ_0, and having a half-width w_0 at r_0. r_0 represents the distance from the central source where the jet is sufficiently ionized for free-free emission to be detectable. In addition, a thin outer shell (shaded region in Fig. 2.1) of material that emits a combination of thermal free-free and non-thermal synchrotron emission is incorporated. The maximum length of the jet as measured along the axis is $\mathrm{R_{jet}}$. The jet is inclined at an angle i with respect to the line-of-sight (LOS) direction of the observer. The jet model shown in the figure and discussed throughout this paper considers a single lobe of a bipolar jet that is blue-shifted. The analysis and results are similar for the red-lobe.

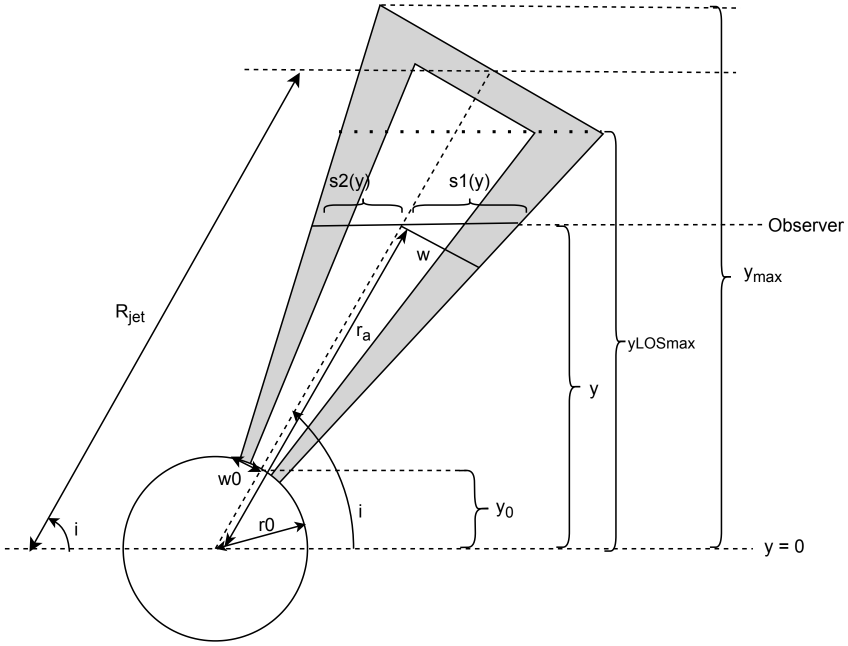

Figure 2.1: Schematic diagram of a jet with constant opening angle, following the schematic of Reynolds (1986). The unshaded jet region represents the inner (near the jet-axis) fully thermal jet. The shaded area represents the geometrically thin region with shocked material that contributes to a combination of thermal and non-thermal emission. The projected distance corresponding to the jet injection radius is marked as y_0.

We define the radial distance measured along the axis of the jet as r_a. The length of the jet projected in the plane of the sky, y, and the half-width of the jet (w) at any radial distance r_a, are given by the following relations.

$$y = r_a \sin i \tag{2.3}$$

$$w(y) = w_0 \left(\frac{r_a}{r_0}\right)^{\epsilon} = w_0 \left(\frac{y}{y_0}\right)^{\epsilon} \tag{2.4}$$

For a given y, in addition to w, another important parameter is the LOS jet cross-section. In Fig. 2.1, $\mathcal{S} = s_1(y) + s_2(y)$ represents the LOS cross-section across the center of a jet. As evident from the figure, $s_1(y)$ and $s_2(y)$ represent the widths of the jet on the front and rear side of the jet long axis (with respect to the observer), respectively. The dotted line in the figure shows the maximum LOS distance to the observer through the jet material, perpendicular to the sky plane. This means that the column of jet material contributing to the emission is the maximum at the projected distance $y_{\mathrm{LOS}_{\mathrm{max}}}$. The length y_{max} shown in the figure corresponds to the farthest tip of the projected jet, and is given by the following equation.

$$y_{max} = \mathrm{Y}_{\mathrm{jet}} + w(\mathrm{Y}_{\mathrm{jet}}) \cos i \tag{2.5}$$

where, $\mathrm{Y}_{\mathrm{jet}} = \mathrm{R}_{\mathrm{jet}} \sin i$.

2.3.1.1 Jet geometry

The jet geometry is dictated by the nature of evolution of the jet width (w) with the jet-axis radial distance r_a from the injection distance r_0. This is determined by the power-law index ϵ defined in Eqn. (2.4). The evolution of the jet width as a function of radial distance from the driving source of the jet is illustrated in Fig. 2.2. Here, we have considered a protostellar jet with $r_0 = 10$ au, which is reasonable since high resolution observations have probed jets very close to the exciting source (Greenhill et al., 1998; Launhardt et al., 2009; Matthews et al., 2010; Lee et al., 2017; Bjerkeli et al., 2019). Further, we assume $\mathrm{R}_{\mathrm{jet}} = 1000$ au measured along the axis and inclination $i = 90°$.

The following are the inferences from Fig. 2.2,

(a) $\epsilon = -1$: The jet width decreases with increase in radial distance.

(b) $\epsilon = 0$: Constant collimation throughout the jet length.

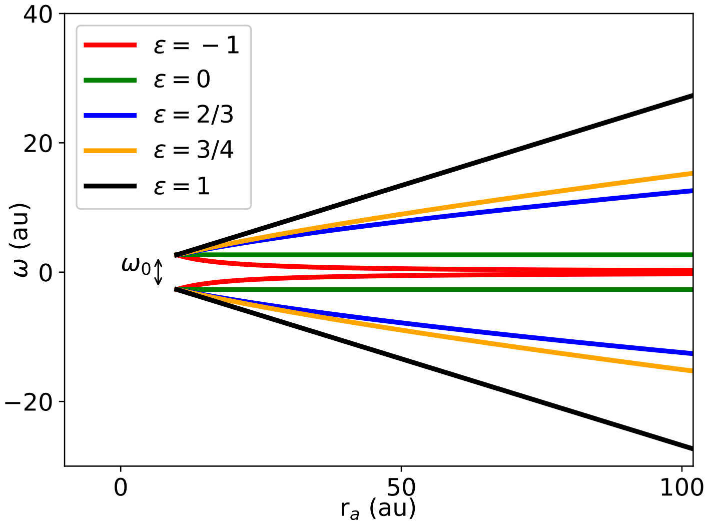

Figure 2.2: Jet width, ω, as a function of power-law index of jet width (ϵ) and jet-axis radial distance (r_a).

(c) $\epsilon = 2/3$: Opening angle decreases as a function of radial distance.

(d) $\epsilon = 3/4$: Opening angle decreases (at a faster rate compared to that of $\epsilon = 2/3$) as a function of radial distance.

(e) $\epsilon = 1$: Conical jet with a constant opening angle.

To further understand the effect of ϵ on the jet collimation, we also demonstrate the variation of jet opening angle (θ) as a function of jet-axis radial distance r_a for different values of ϵ. This is given by the following expression.

$$\tan(\theta/2) = \frac{w}{r_a} = \frac{w_o}{r_a}\left(\frac{r_a}{r_0}\right)^{\epsilon} = \tan(\theta_0/2)\left(\frac{y}{y_0}\right)^{\epsilon-1} \tag{2.6}$$

The jet collimation as a function of ϵ along the jet-axis radial distance r_a is displayed in Fig. 2.3. It can be seen that negative values of ϵ imply the contraction of jet width at outer radial distances i.e. to higher values of y. The conical case of constant opening angle for $\epsilon = 1$ can be clearly visualized.

2.3.1.2 Number densities along the LOS

In our calculations, we assume that, for any point considered within the jet, the distance from that point to the central star is given by r and the points with the same

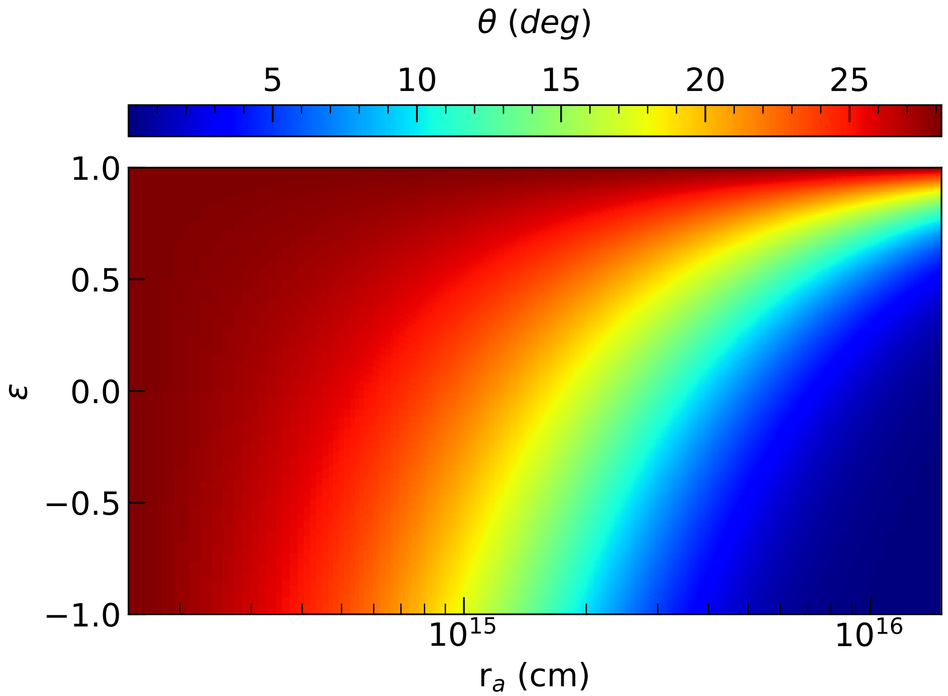

Figure 2.3: Jet opening angle, θ, as a function of power-law index of jet width (ϵ) and jet-axis radial distance (r_a).

r are located on a spherical surface, centered on the star. In Fig. 2.4, shown on the left is the schematic diagram of two jets, one of which is highly collimated and has an opening angle of 1° (grey shaded conical area) and the other with a much wider opening angle of 30° (outer unshaded cone). Here we compare the number density profile across the width (LOS) of these two jets for a particular y. The figure on the right shows the number density vs LOS distance across the width of both the jets, for the same y. The green horizontal line shows the number density profile of Reynolds model at that y for both the opening angles considered here. The red and yellow curves show the number density profile for jets with opening angles 30° and 1°, respectively, both for q_n = -2. The shaded blue region in this figure shows the width of the narrow jet with opening angle 1°.

Here, we assume a parameter s that varies along the LOS such that the point $s = 0$ represents the axis and s increases towards either side of the jet. In Fig. 2.4, as marked in the figure on the left, $s = s_1$ and $s = s_2$ corresponds to the the front and behind edges, respectively, of the jet with opening angle of 30°. Correspondingly, in the figure on the right, the loci of $s = 0$ for every y which is shown as black dashed

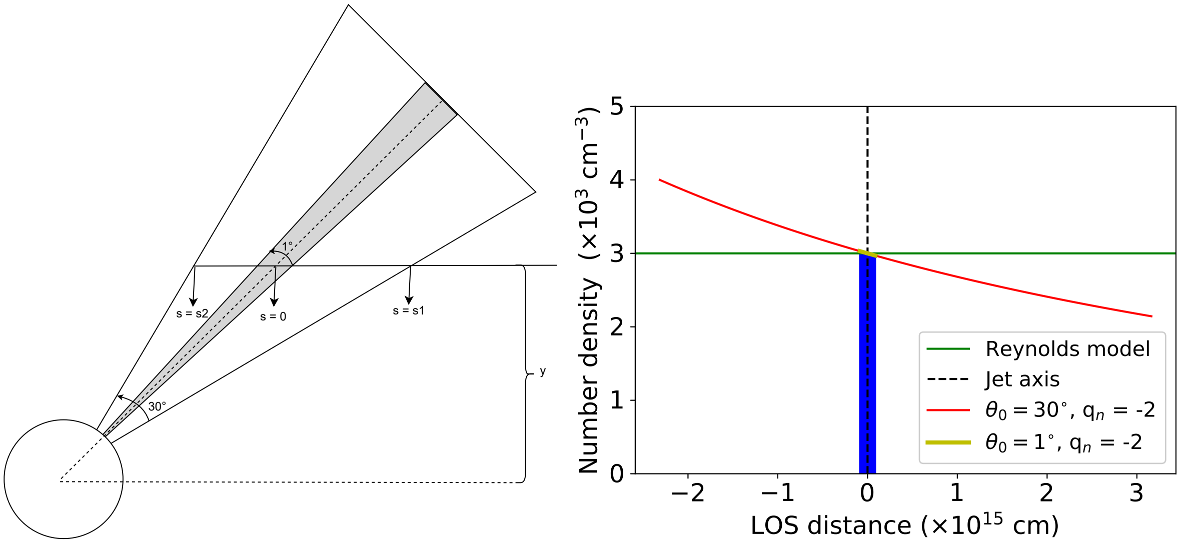

Figure 2.4: [Left] Schematic diagram of jets with opening angle 30° and 1° (shaded) showing the LOS along a given y. [Right] The number density profiles for both the jets as a function of the LOS distance across the jet, for a particular y along the jet length.

line, represents the jet axis and s increases on either side such that the negative s on the plot indicates the rear half and the positive s indicates the front half of the jet.

For a given LOS, Reynolds model assumes same value for the parameters that vary radially, while for the numerical model this varies along each point along the LOS. This means that for a given LOS, the number density which is contributing to the emission in Reynolds model is different from that of the numerical model. For instance, the total LOS length in the Reynolds model (represented as s) is modified as s_1 + s_2 in our numerical model, where $s_1 > s_2$ for a jet inclined towards the observer direction. It is evident from the plot on the right that, all the materials along s_1 corresponds to a lower number density and those along s_2 corresponds to a higher number density than that of the corresponding regions in the Reynolds model geometry. However, the flux difference contributed by the difference in number densities on either half of the jet averages out and will be comparable to that estimated by the Reynolds model. Therefore it is to be noted that, irrespective of whether the opening angle of the jet is small or large, this effect does not affect the overall flux densities considerably. Nevertheless, we incorporate this feature into our jet geometry to make our calculations more representational of wider jets.

2.4 Emission from the jet model

2.4.1 Free-Free emission

Here, we first present a description of the calculations involved in the free-free emission model. We have already introduced the initial jet injection radius r_0, initial jet half-width w_0 and the opening angle θ_0. The other physical quantities such as jet velocity (v), temperature (T), electron number density in the jet material (n) and ionization fraction (x) have radial power-law indices given by q_v, q_T, q_n and q_x, respectively. Note that q_v is related to q_n by the mass conservation equation.

$$q_v + q_n + 2\epsilon = 0 \tag{2.7}$$

The free-free emission and absorption coefficients are given by the following expressions.

$$j_\nu^{ff} = a_j\, n^2\, x^2\, T^{-0.35}\, \nu^{-0.1} \tag{2.8}$$

$$\alpha_\nu^{ff} = a_k\, n^2\, x^2\, T^{-1.35}\, \nu^{-2.1} \tag{2.9}$$

Here, $a_j = 6.50\times10^{-38}$ ergs cm^3 Hz$^{-0.9}$ K$^{0.35}$ s^{-1} sr^{-1} and $a_k = 0.212$ cm^5 K$^{1.35}$ Hz$^{2.1}$ are the proportionality constants of emission and absorption coefficients, respectively, in cgs units. From Eqns. (2.8) and (2.9), it is evident that j_ν^{ff} and α_ν^{ff} are functions of number density and temperature. Therefore, a radially varying density or temperature profile results in a variation of emission and absorption coefficients along a LOS. Assuming a LOS variable s, the source function of the jet material is given by $\frac{j_\nu^{ff}(s)}{\alpha_\nu^{ff}(s)}$. The flux density from a LOS of the jet that subtends an incremental solid angle dΩ at the observer's location, is given by the following expression.

$$S_\nu = \int_{y_0}^{y_{max}} d\Omega \int_0^{\tau_\nu} \frac{j_\nu^{ff}(s)}{\alpha_\nu^{ff}(s)} \left(e^{-(\tau_\nu^{ff} - \tau(s))}\right) d\tau \tag{2.10}$$

Here, $\tau_\nu^{ff} = \int \alpha_\nu(s)\, ds$ and $\tau(s)$ are the total LOS optical depth and the optical depth corresponding to any s along a LOS, respectively. The second integral in Eqn. (2.10) incorporates the radial dependence of physical parameters in the volume element along a LOS. This model accommodates a large opening angle in contrast with the Reynolds model which deals with narrow jets and to allow for this, we integrate at each location along the width of the jet (on the plane of the sky). This implies an integration along the LOS of $\mathcal{S}$ which is maximum along the jet axis to zero at the edges.

The integration over y is carried out to estimate the flux density from the entire length of the jet.

$$S_\nu = \int_{y_0}^{y_{max}} \int_0^{w(y)} \frac{2\, dw\, dy}{d^2} \frac{a_j}{a_k}\, \nu^2 \int_0^{\tau_\nu} T(s)(e^{-[\tau_\nu^{ff} - \tau(s)]})\, d\tau \qquad (2.11)$$

Here, y_{max} is the full extent of the jet. For low values of base density, n_0, the jet can be optically thin throughout its extent.

2.4.1.1 LOS for an inclined jet

An additional consideration that we include is the effect of inclination on the thickness of the jet. Assuming that the jet is spatially resolved, the inclination of the jet with respect to the sky plane will give rise to the jet having unequal LOS distances on front ($s_1(y)$) and rear ($s_2(y)$) sides of the long central jet axis. Thus the total LOS is $\mathcal{S} = s_1(y) + s_2(y)$ (as shown in Fig. 2.1), rather than $2w/\sin i$ as assumed in the Reynolds model. In this section, we will discuss the calculation of $\mathcal{S}$. As an example, let us assume the case of a collimated jet with $\epsilon < 1$. Fig. 2.5 shows the schematic diagram of such a jet ($\epsilon < 1$) and represented here is the LOS passing through the long axis of the jet at an arbitrary projected length y. At any y, the distances $s_1(y)$ and $s_2(y)$ can be calculated directly from the jet geometry using the opening angle of the jet. However, owing to the inclination with respect to the plane of the sky, for any jet with $\epsilon \neq 1$, the opening angles of the jet corresponding to the front and rear edges of the jet will be different. As evident from the figure, the opening angles where the LOS crosses the front and rear edges of the jet are $\frac{\theta_1}{2}$ and $\frac{\theta_2}{2}$, respectively. θ_1 is smaller and θ_2 is larger than θ. In this case, the jet opening angles corresponding to $s_1(y)$ and $s_2(y)$ are $\frac{\theta_1(y)}{2}$ and $\frac{\theta_2(y)}{2}$, respectively.

In order to calculate the two opening angles we first look into the geometry of the jet. In the figure, the base of the jet is represented by A, while B and D represents the intersection of LOS with the long axis and front edge of the jet, respectively. C is the base of the perpendicular from D to the axis and the arc DE represents all the material within the jet located at the same radial distance from the central source. For any y, we define y_C and y' as the projected length of AC and AE on the sky plane,

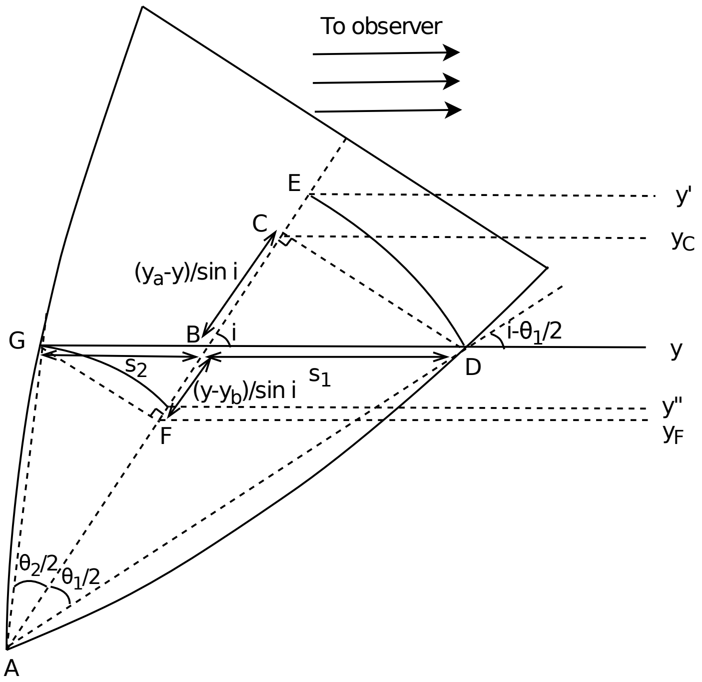

Figure 2.5: Schematic diagram of a jet for which the opening angle decreases with y ($\epsilon < 1$). Shown here is a LOS at y passing through the main axis of the jet. Here $\frac{\theta_1}{2}$ and $\frac{\theta_2}{2}$ are the opening angles corresponding to the jet front and rear edges, respectively.

respectively. From Eqn. (2.6), we know that any arbitrary y' can be written as,

$$y' = y\left[\frac{\tan(\theta_1/2)}{\tan(\theta/2)}\right]^{1/\epsilon\,-\,1} \tag{2.12}$$

Similar to y_C and y', y_F and y" are defined for the rear edge of the jet. From the triangles ABD and CBD, it is clear that the side BD (=$s_1(y)$) can be evaluated separately and then equated to obtain θ_1 as follows.

$$\left[\left(\frac{\tan(\theta_1/2)}{\tan(\theta/2)}\right)^{1/\epsilon\,-\,1} - 1\right] - \frac{\sin(\theta_1/2)}{\sin(i-\theta_1/2)}\cos(i) = 0 \tag{2.13}$$

Similar calculations for the rear half of the jet using triangles ABG and FBG, and equating BG (=$s_2(y)$) gives θ_2 as follows.

$$\left[1 - \left(\frac{\tan(\theta_2/2)}{\tan(\theta/2)}\right)^{1/\epsilon\,-\,1}\right] - \frac{\sin(\theta_2/2)}{\sin(i-\theta_2/2)}\cos(i) = 0 \tag{2.14}$$

With the knowledge of the opening angles, the inclined widths of the front and behind half of the jet, $s_1(y)$ and $s_2(y)$ can be calculated in the following way.

$$s_1(y) = \frac{y\,\sin(\theta_1/2)}{\sin(i-\theta_1/2)\,\sin(i)} \tag{2.15}$$

$$s_2(y) = \frac{y\,\sin(\theta_2/2)}{\sin(i+\theta_2/2)\,\sin(i)} \tag{2.16}$$

The above equations are applicable for any value of $\epsilon < 1$ and a similar approach can be considered for the case of any $\epsilon \geq 1$ as well. For simplicity, here we will consider the specific case of a jet with $\epsilon = 1$ (constant opening angle) as displayed in Fig. 2.1. For this case, at any y, $s_1(y)$ and $s_2(y)$ are given as follows.

$$s_1(y) = w(y)\,\frac{\cos{(\theta/2)}}{\sin{(i-\theta/2)}}, \quad s_2(y) = w(y)\,\frac{\cos{(\theta/2)}}{\sin{(i+\theta/2)}} \tag{2.17}$$

The total flux density is calculated by taking this geometrical factor into consideration.

2.4.2 Combination of Free-Free and Synchrotron emission

As discussed in the previous section, the discovery of negative spectral indices steeper than -0.1 across radio frequencies for a few protostellar jets (Marti et al., 1993; Curiel et al., 1993; Garay et al., 1996; Wilner et al., 1999; Rodríguez-Kamenetzky et al., 2016; Purser et al., 2016; Vig et al., 2018) indicates the presence of synchrotron emission. In a few cases, towards higher frequencies, the spectral indices are flatter than what is expected from synchrotron emission (Marti et al., 1993; Vig et al., 2018) suggesting the co-existence of thermal free-free emission and non-thermal synchrotron emission. Motivated by the fact that non-thermal emission is produced at the edges of the jet (Rodríguez-Kamenetzky et al., 2017), we explore the possibility of combining thermal and non-thermal emission from protostellar jets and we model it using this consideration.

2.4.2.1 Synchrotron emission

We have already discussed the case of thermal free-free emission in Sect. 2.4.1, hence we discuss the case of synchrotron emission here. For a relativistic electron of mass m and charge e, traveling at velocity $\vec{v}$ in a magnetic field $\vec{B}$, a Lorentz force $\vec{v} \times \vec{B}$

is exerted on the electron. This force accelerates the electron resulting in a radiative power loss which in turn depends on the electron energy and magnetic field strength. For a relativistic electron emitting synchrotron radiation at a characteristic frequency of ν_{pk}, the corresponding Lorentz factor γ_{pk} is given by the following equation (Rybicki & Lightman, 2008).

$$\gamma_{pk} = \sqrt{\frac{4\pi\, m\, c\, \nu_{pk}}{3\, e\, B}} \tag{2.18}$$

This assumes an equi-partition of total energy into energy of relativistic electrons and energy due to the magnetic field (of magnitude B) in the shocked plasma in order to achieve a condition of minimum energy state (Pacholczyk, 1970; Govoni & Feretti, 2004). We consider a population of relativistic electrons in the shocked region, having a power-law number density distribution with an index p in energy space, or the equivalent γ-space where γ is the Lorentz factor. The kinetic energy E of the electrons is related to their Lorentz factor as $E = \gamma\, m\, c^2$.

The number density of relativistic electrons, $n(\gamma)d\gamma$ between γ and $\gamma + d\gamma$ is, therefore, given by the following equation.

$$n(\gamma)\, d\gamma = n_k\, \gamma^{-p}\, d\gamma \tag{2.19}$$

Here n_k represents the proportionality constant for the number density of electrons in γ-space. For the given distribution of electrons, the synchrotron emission coefficient, j_ν^{syn}, is given by the following expression (Rybicki & Lightman, 2008).

$$\begin{aligned} j_\nu^{syn} = \frac{1}{4\pi} \frac{\sqrt{3}\, e^3\, n_k\, B\, \sin\alpha_{\text{pa}}}{2\pi\, m\, c^2\, (1+p)}\, \Gamma\left(\frac{p}{4} + \frac{19}{12}\right) \Gamma\left(\frac{p}{4} - \frac{1}{12}\right) \times \\ \left(\frac{2\pi\, \nu\, m\, c}{3e\, B\, \sin\alpha_{\text{pa}}}\right)^{-(p-1)/2} \end{aligned} \tag{2.20}$$

Here $\Gamma(x)$ is the gamma function for an argument x and α_{pa}, termed as pitch angle, is the angle between the magnetic field and the velocity of electrons accelerated in the field. The synchrotron emission spectrum peaks at a critical frequency (ν_{pk}) which corresponds to the turnover frequency at which the electrons emit the maximum power.

It is also possible for the same population of relativistic electrons to absorb the synchrotron emission. This is expressed through the absorption coefficient, α_ν^{syn}, which is given by the following expression.

$$\begin{aligned}\alpha_\nu^{syn} = & \frac{\sqrt{3}e^3}{8\pi\, m}\left(\frac{3e}{2\pi m^3 c^5}\right)^{p/2} n_k\,(B\,\sin\alpha_{\rm pa})^{(p+2)/2}\,\Gamma\left(\frac{3p+2}{12}\right) \\ & \times\Gamma\left(\frac{3p+22}{12}\right)\,\nu^{-(p+4)/2}\end{aligned} \tag{2.21}$$

We assume an isotropic distribution of electron velocities. Therefore, the average of terms involving sin($\alpha_{\rm pa}$) over all directions around the field is of the order of unity in Eqns. (5.1) and (2.21). The absorption coefficient is used to determine the optical depth, and the frequency where the synchrotron optical depth $\tau_{syn} = 1$ defines the self-absorption frequency (ν_a). This is determined by the microscopic parameters and the power-law index p. Depending on the parameters of the jet, ν_a can lie on either side of ν_{pk}. Another feature of the spectrum is that, as the system ages, the energy of the electrons reduces due to radiative losses, resulting in lowering of Lorentz factors of the emitting electrons. With time, electrons with higher energies lose their energy faster, also known as spectral aging. Consequently, the higher energy tail of the spectrum breaks at a frequency (cooling frequency, ν_c) where the cooling of those electrons becomes dominant. Thus, ν_c can be taken to be the upper frequency limit for our analysis as it is relatively large $\nu_c = 100$ GHz (Govoni & Feretti, 2004).

For a distribution of electrons of density $n(\gamma)$ emitting between frequencies ν_{pk} and ν_c, the constant n_k in Eqn. (2.19) can be estimated by integrating $n(\gamma)d\gamma$ from γ_{pk} to γ_c. This results in the following expression.

$$n_k = \frac{n\,(p-1)}{\gamma_{pk}^{-(p-1)}} \tag{2.22}$$

2.4.2.2 Nature of Synchrotron spectrum

Here we will briefly discuss the calculation of a synchrotron spectrum. The source function and optical depth at the synchrotron characteristic frequency ν_{pk} are,

$$I_{\nu_{pk}} = \frac{j_{\nu_{pk}}}{\alpha_{\nu_{pk}}}$$

$$\tau_{\nu_{pk}} = \int_0^S \alpha_{\nu_{pk}} ds$$

where $\mathcal{S}$ represents the LOS through the jet cross-section. The flux density at any observing frequency ν is given by:

For $\nu \leq \nu_c$:

$$\tau_\nu = \tau_{\nu_{pk}} \left(\frac{\nu}{\nu_{pk}}\right)^{-(p+4)/2}$$

$$S_\nu = \int_{y_0}^{y_{max}} \int_0^{w(y)} \frac{2\,dw\,dy}{d^2}\, I_{\nu_{pk}}\, (\tfrac{\nu}{\nu_{pk}})^{5/2}\, (1 - e^{-\tau_\nu})$$

For $\nu > \nu_c$:

$$\tau_\nu = \tau_{\nu_{pk}} \left(\frac{\nu_c}{\nu_{pk}}\right)^{-(p+4)/2} \left(\frac{\nu}{\nu_c}\right)^{-(p+5)/2}$$

$$S_\nu = \int_{y_0}^{y_{max}} \int_0^{w(y)} \frac{2\,dw\,dy}{d^2}\, I_{\nu_{pk}}\, (\tfrac{\nu}{\nu_{pk}})^{5/2}\, (1 - e^{-\tau_\nu})$$

We note that for a given distribution of electrons of constant number density, the spectral indices (β) across the spectrum due to synchrotron emission varies as follows:

For $\nu_a < \nu_{pk}$:

$\nu < \nu_a, \beta = 2$

$\nu_a < \nu < \nu_{pk}, \beta = 1/3$

$\nu_{pk} < \nu < \nu_c, \beta = -(p-1)/2$

$\nu > \nu_c, \beta = -p/2$

For $\nu_a > \nu_{pk}$:

$\nu < \nu_{pk}, \beta = 2$

$\nu_{pk} < \nu < \nu_a, \beta = 5/2$

$\nu_a < \nu < \nu_c, \beta = -(p-1)/2$

$\nu > \nu_c, \beta = -p/2$

In our model we do not encounter a case of $\nu_a < \nu_{pk}$ due to the range of energies involved, hence we ignore this part of the spectrum calculation for the present.

2.5 Overall flux densities

Armed with the knowledge about both free-free and synchrotron emission mechanisms discussed so far, we proceed towards the methods by which these mechanisms can be incorporated in the geometry to find the radio flux densities generated by the jet. It is to be noted that the total flux densities are highly sensitive to the degree of ionization of the jet material. Therefore, in this section, we first discuss the nature of ionization fraction profile within the jet geometry. We will then proceed into calculation of total radiative emission from the jet material.

2.5.1 Lateral variation of ionization fraction

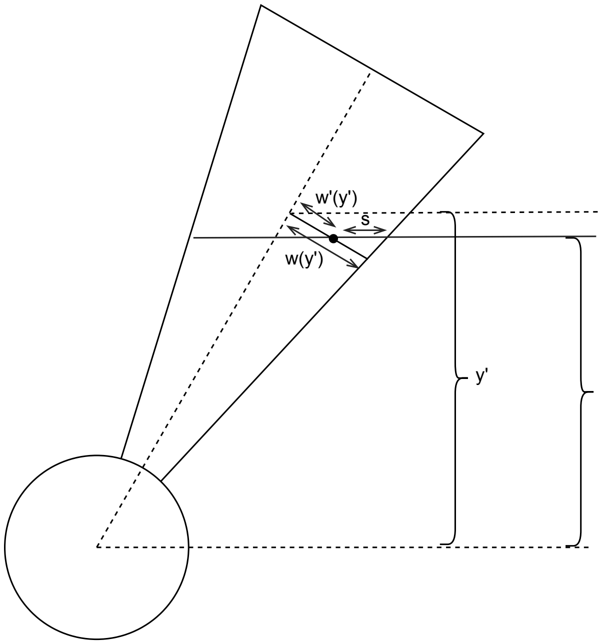

Figure 2.6: Schematic diagram of the jet representing the distance of any point s along the LOS from the long axis $[w'(y')]$, and the corresponding jet width $[w(y')]$.

The ionization fraction or the degree of ionization plays an important role in quantifying the coupling of the gas to the magnetic field. The distribution of ionized gas in the jet is important as theories predict that the centrifugal launch of jet occurs along the magnetic field lines (Goodson & Winglee, 1999; Zanni, 2014).

Observationally, studies of ionized jets from massive YSOs have indicated ionization fraction to be typically $2 - 15\%$ with the maximum value measured to be up to

40% (Bacciotti & Eislöffel, 1999; Bacciotti, 2002; Nisini et al., 2005; Giannini et al., 2013; Obonyo et al., 2019). In addition, it has been observed that ionization fractions decrease with radial distance away from the central source as expected (Fedriani et al., 2019), lending credence to the introduction of the parameter q_x in the models, which has the following form.

$$x_a(r) = x_0 \left(\frac{r_a}{r_0}\right)^{q_x} \quad \Rightarrow \quad x_a(y) = x_0 \left(\frac{y}{y_0}\right)^{q_x} \tag{2.23}$$

Here, the subscript a implies that it is axial and x_0 represents the base ionization fraction at r_0.

The model discussed so far allows for a variation of ionization fraction along the radial direction only, through q_x. We believe it is more realistic to incorporate an ionization fraction that decreases across the jet cross-section, away from the central axis towards the edge of the jet. This is expected because theories predict a decrease in the velocity structure laterally across jets (Machida, 2014). This suggests that the inner regions of the jet would be highly ionized and the ionization fraction decreases to 0 towards the lateral edges. The presence of synchrotron emission from shocks at the edges of jets is another inducement for introducing the lateral variation in ionization fraction as it has been found from line ratios investigated in shocks from jets that the ionization fractions are found to be relatively low, $\sim 1-10\%$ (Hartigan et al., 1994; Bacciotti et al., 1995; Dionatos et al., 2010).

In order to establish the effect of ionization fraction across the lateral direction of the jet, we consider the following modifications to the equations discussed in Sect. 2.4.1 and 2.4.2. The variation of ionization fraction across a given LOS of the jet can be introduced through a power-law with index q_x' as follows.

$$x(s) = x_a(y') \left[\frac{w(y')}{w(y') - w'(y')}\right]^{q_x'} \tag{2.24}$$

Here, y' is a function of s, $x_a(y')$ is the ionization fraction along the long axis of the jet at y', $w'(y')$ represents the shortest distance of any point s along a given LOS, from the central long axis of the jet, while $w(y')$ is the half-width of the jet that intersects the point s, shown schematically for clarity in Fig. 2.6. We consider $q_x' \leq 0$ as ionization diminishes towards the edges. For a jet with $q_x = 0$ and $q_x' = 0$ we take $x(s) = 1$ throughout, even though a singularity appears at the outer edges, i.e. at $w = w'$.

These modifications are incorporated to calculate the number density of electrons in Regions 1, 2 and 3 (see Fig. 2.7) which are discussed in the following section.

2.5.2 Total emission from the jet

For a given LOS, we can divide the jet into three regions R1, R2 and R3 as shown in Fig. 2.7. Regions 1 and 3 (also R1 and R3) represent the outer shocked material which are the front and rear layers, respectively, while viewing along $\mathcal{S}$. These regions contribute to the flux densities through (i) synchrotron radiation emitted by a fraction of electrons that are relativistic (η_e^{rel}), and (ii) free-free emission from the rest of the non-relativistic fraction of electrons.

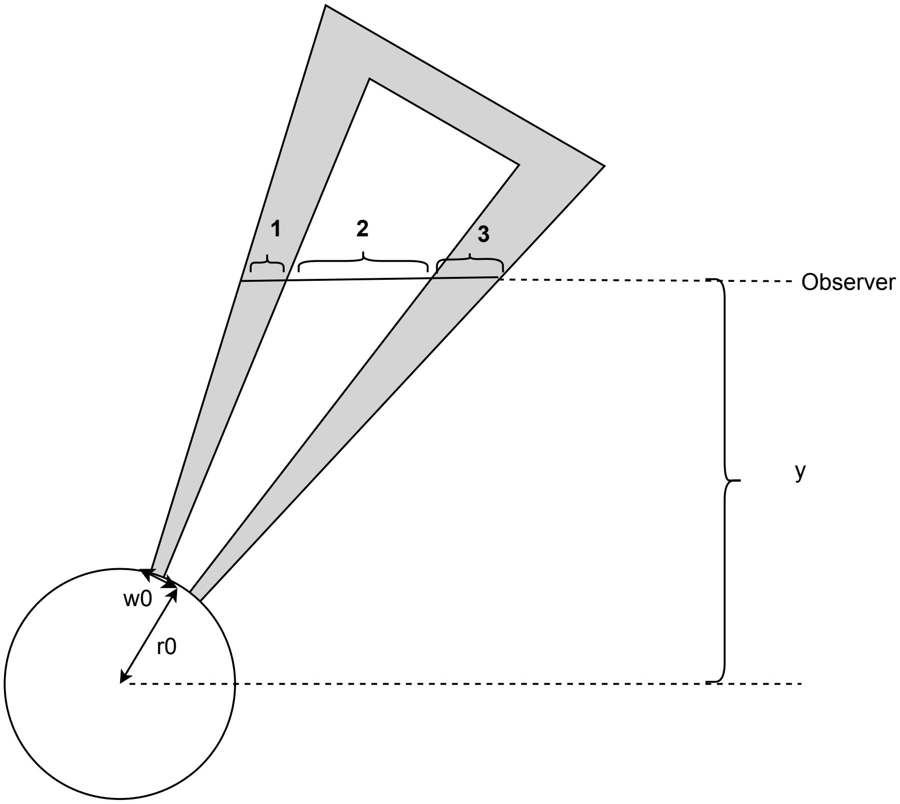

Figure 2.7: Schematic diagram of the jet representing the different layers of particle distribution along a particular LOS at y. Regions 1 and 3 give rise to a combination of thermal and non-thermal emission, while Region 2 solely contributes to thermal emission.

For an infinitesimal volume of material located in the shocked region at a distance s along any LOS having a number density n, ionization fraction x and fraction of relativistic electrons η_e^{rel}, the number density of electrons capable of emitting free-free radiation are given by,

$$\begin{aligned} n^{ff} &= n\,x\,(1-\eta_e^{rel}) \\ &= n_0\,x_0\left(\frac{y'}{y_0}\right)^{q_n}\left(\frac{y'}{y_0}\right)^{q_x}\left[\frac{w(y')-w'(y')}{w(y')}\right]^{q'_x}(1-\eta_e^{rel}) \end{aligned} \tag{2.25}$$

On the other hand, the number density of electrons capable of emitting synchrotron are given by,

$$\begin{aligned} n^{syn} &= n\,x\,\eta_e^{rel} \\ &= n_0\,x_0\left(\frac{y'}{y_0}\right)^{q_n}\left(\frac{y'}{y_0}\right)^{q_x}\left[\frac{w(y')-w'(y')}{w(y')}\right]^{q'_x}\eta_e^{rel} \end{aligned} \tag{2.26}$$

Note that the number density of free-free emitters from the fully thermal jet would correspond to $\eta_e^{rel} = 0$ in Eqn. (2.25). From Eqns. (2.8), (2.9), (5.1) and (2.21) it is clear that for the shocked region, the emission and absorption coefficients are given by the following.

$$j_\nu^{ff+syn} = A_{\nu,1}(n^{ff})^2 + A_{\nu,2}n^{syn} \tag{2.27}$$

$$\alpha_\nu^{ff+syn} = B_{\nu,1}(n^{ff})^2 + B_{\nu,2}n^{syn} \tag{2.28}$$

Here, $A_{\nu,1}$, $B_{\nu,1}$ and $A_{\nu,2}$, $B_{\nu,2}$ are constants associated with free-free and synchrotron mechanisms whereas for the case of a thermal jet both j_ν^{ff} and α_ν^{ff} are $\propto (n^{ff})^2$. This means that the source function for the shocked region will be different for any infinitesimal volume of material at different locations within the jet volume. As the distributions of populations generating (i) and (ii) are independent in a given volume, the overall emission and absorption coefficients for the combination of the processes are given by the individual sums of the coefficients of the two processes. These are given by the following expressions.

$$j_\nu^{ff+syn}(s,y) = j_\nu^{ff}(s,y) + j_\nu^{syn}(s,y) \tag{2.29}$$

$$\alpha_\nu^{ff+syn}(s,y) = \alpha_\nu^{ff}(s,y) + \alpha_\nu^{syn}(s,y) \tag{2.30}$$

Region 2 (also R2) is the inner highly ionized jet (near the jet-axis) which solely emits free-free radiation, and therefore has emission and absorption coefficients j_ν^{ff} and α_ν^{ff}, as discussed earlier.

For a LOS along $\mathbb{S}$ intersects with different particle distributions and the intensities contributed by each of these regions for a given y are given by the following expressions.

$$I_{\nu,R1}^{ff+syn} = \int_0^{\tau_{\nu,R1}^{ff+syn}} \frac{j_{\nu,R1}^{ff+syn}}{\alpha_{\nu,R1}^{ff+syn}} e^{-(\tau_{\nu,R1}^{ff+syn}-\tau)}\, d\tau \tag{2.31}$$

$$I_{\nu,R2}^{ff} = \int_0^{\tau_{\nu,R2}^{ff}} \frac{j_{\nu,R2}^{ff}}{\alpha_{\nu,R2}^{ff}}\, e^{-(\tau_{\nu,R2}^{ff}-\tau)}\, d\tau \tag{2.32}$$

$$I_{\nu,R3}^{ff+syn} = \int_0^{\tau_{\nu,R3}^{ff+syn}} \frac{j_{\nu,R3}^{ff+syn}}{\alpha_{\nu,R3}^{ff+syn}} e^{-(\tau_{\nu,R3}^{ff+syn}-\tau)}\, d\tau \tag{2.33}$$

Here, $I_{\nu,Rn}$ and $\tau_{\nu,Rn}$ represent the total intensity and optical depth for each region given by subscript n, where $n = 1,\ 2,\ 3$. Note that the limits of the integration are dependent on the region under consideration and the projected length y. The total radiation intensity from a LOS at y can be calculated by adding the contribution of each of these regions after considering absorption from the layers in front of it. This is given as follows.

$$I_\nu(y) = I_{\nu,R1}^{ff+syn}\, e^{-(\tau_{R2}^{ff}+\tau_{R3}^{ff+syn})} + I_{\nu,R2}^{ff}\, e^{-\tau_{R3}^{ff+syn}} + I_{\nu,R3}^{ff+syn} \tag{2.34}$$

The above intensity is integrated along the width (in the sky plane) and the projected length of the jet to give the total flux density emitted by the jet.

$$S_\nu = \int_{y_0}^{y_{max}} \int_0^{w(y)} \frac{2\, dw\, dy}{d^2} I_\nu(y) \tag{2.35}$$

It should be noted that $I_\nu(y) \equiv I_\nu(w, y)$. This is because so far we have discussed only about the LOS which crosses the main axis of the jet but, the LOS through the jet decreases as one moves from the axis along the width of the jet in the plane of the sky. Here we will discuss the calculations associated with any arbitrary LOS that is away from the jet axis.

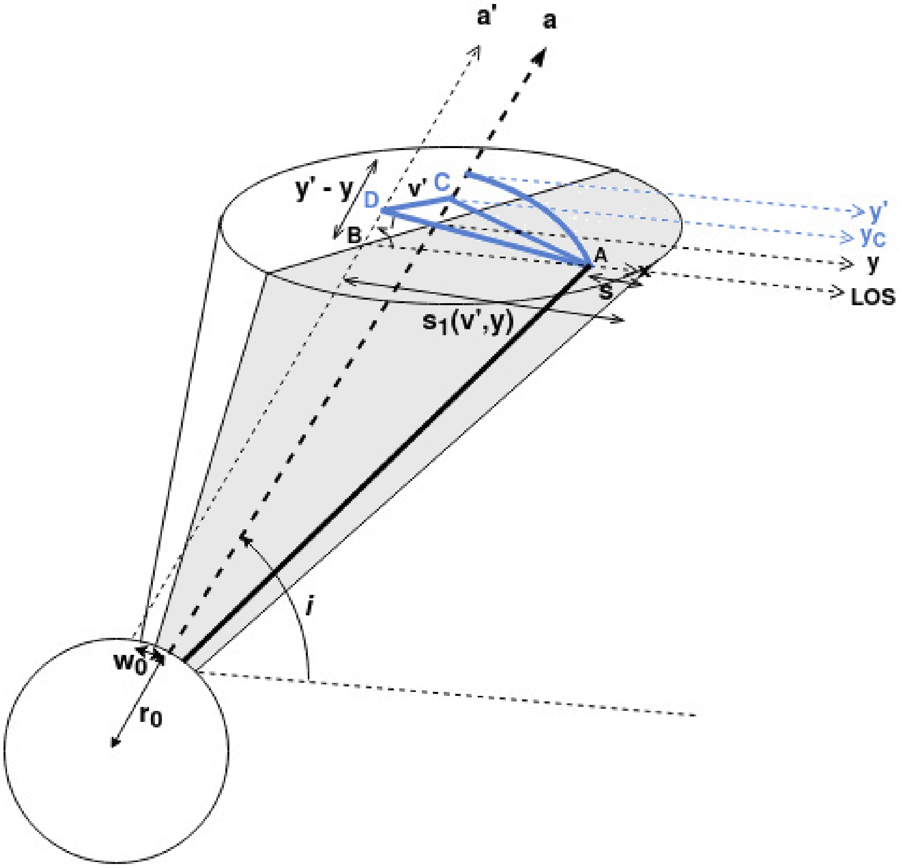

Figure 2.8: Side view of the jet, inclined at an angle i, slightly offset from the direction of the observer aligned at a length y on the main axis. An arbitrary LOS located at v' from the main axis along the sky plane is shown. The grey region represents the front half of the jet cross-section where the plane containing all the LOSs at y cuts the jet. The blue lines (solid and dashed) are located above the LOS plane. y_C is the projected length corresponding to the radial distance from $r_a = 0$ along the jet axis upto C. s and $s_1(v',y)$ are the variable along the LOS and the full LOS distance for the front half of the jet at v', respectively.

It is evident from Eqns. (2.25) and (2.26) that for any infinitesimal volume of material located at a distance s along a LOS, the knowledge of y', $w(y')$ and $w'(y')$ corresponding to its location are required to calculate its flux contribution. These elemental contributions can then be integrated first along each LOS, then the width and finally over the projected length to get the overall flux from the jet. Consider a jet as shown in Fig. 2.8 with a constant opening angle ($\epsilon = 1$) whose main axis is $\vec{a}$ and the observer is located at a projected distance y on the axis. Assume the plane formed by all the LOSs at y which chops the jet at y, to be the LOS plane. The front half of this cross-section is represented as grey and all the regions above the LOS plane are represented as blue lines in the figure. Let us begin by assuming an arbitrary LOS in the LOS plane at a distance of v' from the main axis such that v' ranges from 0 to $w(y)$ on either side of the axis. Note that v' is the distance measured in the plane of the sky on either side of the axis, so the limits are slightly different for the top portion of the jet, where the curved edges of the jet dictate the projected width of the jet. Since the remaining calculations are the same, we do not consider the top portion for now. We know that the actual half-width corresponding to y is $w(y)$. This is the half-width of the jet at y when it is not inclined. The half-width of the jet at v' is the half-chord at distance v' from the axis given by,

$$w(v', y) = \sqrt{w(y)^2 - v'^2} \tag{2.36}$$

Using the relationship shown in Eqn. (2.17), the actual half width $w(v', y)$ can be used to calculate the projected widths on the front side and back side of the jet at v' as,

$$s_1(v', y) = w(v', y)\,\frac{\cos(\theta/2)}{\sin(i - \theta/2)} \tag{2.37}$$

$$s_2(v', y) = w(v', y)\,\frac{\cos(\theta/2)}{\sin(i + \theta/2)} \tag{2.38}$$

Next, assume an infinitesimal volume of material located at A on the LOS at an arbitrary distance s from the jet edge such that s can vary from 0 to $s_1(v', y)$. Here $s = s_1(v', y)$ corresponds to the point marked B in Fig. 2.8. In order to make the calculations simpler we project the axis $\vec{a}$, into the plane containing the points A, B and D, as axis $\vec{a'}$. AC and AD represent the distance of A from $\vec{a}$ and $\vec{a'}$, respectively, where C and D are separated by a distance of v'. The projected length of the jet axis upto C (y_C) can be calculated as,

$$\begin{aligned} y_C - y &= (s_1(v', y) \;-\; s)\cos(i)\,\sin(i) \\ \Rightarrow y_C &= y \;+\; (s_1(v', y) \;-\; s)\cos(i)\,\sin(i) \end{aligned} \tag{2.39}$$

The distance of A from the axis, $w'(s, v', y)$ ($\equiv$ AC) can be calculated from the geometry as,

$$w'(s, v', y) = \sqrt{((s_1(v', y) \;-\; s)\sin(i))^2 + v'^2} \tag{2.40}$$

From Eqns 2.39 and 2.40, the projected length of the jet corresponding to A can be calculated as,

$$y' = \sqrt{y_C^2 + [w'(s, v', y)\sin(i)]^2} \tag{2.41}$$

Similar calculations can be done for the behind half of the jet. These quantities can then be substituted in Eqns. (2.25) and (2.26) to find the number density of the electrons emitting the radiation. This helps in calculating the emission, absorption coefficients and optical depth which are required to obtain its flux contribution. Hence, the total radiation intensity for any LOS at v' can be calculated as (similar to Eqn. (2.34)),

$$\begin{aligned} I_\nu(v', y) = I_{\nu,R1}(v', y)\, e^{-(\tau_{\nu,R2}^{ff}(v',y) + \tau_{\nu,R3}^{ff+syn}(v',y))} \\ +\ I_{\nu,R2}(v', y)\, e^{-\tau_{\nu,R3}^{ff+syn}(v',y)}\ +\ I_{\nu,R3}(v', y) \end{aligned} \tag{2.42}$$

For a jet with varying opening angle ($\epsilon < 1$), the above calculations are similar except that for a given LOS, the opening angle corresponding to the front edge and the behind edge will be different as described in Sect. 2.4.1.1, hence $s_1(v', y)$ and $s_2(v', y)$ are given by the Eqns. (2.15) and (2.16).

This is extended to the top portion of the jet, from $y_{\mathrm{LOS_{max}}}$ to y_{max}, with appropriate limits for v' obtained from the geometrical calculations. Here, s_1 and s_2 are represented as s_1^{top} and s_2^{top}, respectively. These are given by the following equations.

$$s_1^{top}(v', y) = \frac{(\mathrm{Y_{jet}} - y)}{\sin(i)\cos(i)} s_2^{top}(v', y) = s_2(v', y) y_{\mathrm{LOS_{max}}} \leq y < \mathrm{Y_{jet}} \tag{2.43}$$

$$s_1^{top}(v', y) = 0 s_2^{top}(v', y) = s_2(v', y) - \frac{(y - \mathrm{Y_{jet}})}{\sin(i)\cos(i)} \mathrm{Y_{jet}} \leq y < y_{max} \tag{2.44}$$

We use these values to integrate the intensity along every LOS in the top portion.

In addition to the inner region and outer shell, we also consider the interaction of the jet with the ambient medium at the terminal region and for simplicity assume a flat thin interaction region instead of bow-shock like curvature seen towards terminal edges of many jets and HH objects. This region produces synchrotron emission, in addition to thermal emission. The LOS through the extreme end of the jet, therefore, gradually tapers down due to its inclination with respect to the plane of the sky. Hence, at the extreme top end of the jet, only the shocked region contributes to the total flux, identical to R1 and R3.

2.6 Summary

In this chapter we have presented the details of the model which we have formulated to explain the observed radio spectral indices of protostellar jets using thermal and non-thermal emissions. We have discussed the flux calculation of free-free emission, synchrotron emission and the combined contribution of both these mechanisms to the overall jet spectrum. The calculations described here are for a single blue-shifted lobe of the bipolar jet. The analysis and results are similar for the red-lobe.

Chapter 3

Radio spectra of protostellar jets: Results from the model

In this chapter, we characterize the numerical model and our aim is to achieve a better understanding of the behavior of the jet model in different plausible scenarios. Such a characterization would enable the application of the model to observations of various jets in order to derive fundamental parameters that are otherwise difficult to be obtained directly from observations. In this context, our model has a two-fold application. This can be employed to model radio emission from (i) thermal jets at smaller distances (i.e $r_0 \simeq 10$ au), as well as (ii) knots observed farther away from YSOs. We bring to attention the fact that this model does not include the effects of dust emission and for higher radio frequencies ($\gtrsim 50$ GHz), this contribution may need to be included.

3.1 Comparison of our thermal model with Reynolds model

In this section, we compare the radio spectrum of fully thermal emission in our model with intermediate ranges of optical depth to that generated using Reynolds model. This is to gain an insight into the impact of modifications incorporated into the geometry of our model. The model parameters used to generate the spectra are $r_0 = 10$ au, opening angle $\theta_0 = 30°$, a typical jet base density $n_0 = 5 \times 10^7$ cm^{-3} which is estimated by the interpolation of typical values found in literature (Marti et al., 1995; Bacciotti & Eislöffel, 1999; Anglada et al., 2018) with a power-law index of q_n = -2.

The ionization fraction at the base of jet is $x_0 = 0.2$ (Cesaroni et al., 2018; Fedriani et al., 2019), temperature at base of jet is $T_0 = 10^4$ K, constant opening angle $\epsilon = 1$, the jet is isothermal $q_T = 0$, constant ionization fraction $q_x = 0$, extent of the jet $y_{max} = 1000$ au, for inclination $i = 60°$, at a distance $d = 1$ kpc. We compare the Reynolds model with three different cases of our model: (i) our model with intermediate optical depth effects and geometrical generalizations included (blue curve), (ii) our model with intermediate optical depth effects and geometrical generalizations included (i.e geometry identical to that of the Reynolds model; green curve) (iii) same as (i) but for a fully optically thin jet (cyan), which is attained at lower number densities, n_0 = 10^6 cm^{-3}, with the other parameters remaining the same.

The radio spectra for the three cases are displayed in Fig. 3.1. The frequency ν_m (35.8 GHz, blue curve) in the figure represents the turnover frequency where the full jet becomes optically thin ($\tau \leq 1$). Hence, for frequencies below ν_m, the spectral index is $+0.6$ as expected and above ν_m, the spectral index is -0.1 which is characteristic of optically thin free-free emission. In the figure, for the purpose of comparison with this spectrum, the resulting flux densities for case (iii) are scaled up by a factor of 2500, as the flux density is proportional to the square of number density, and we obtain the optically thin spectral index of -0.1. For case (ii), we find a flux difference of $11 - 13\%$ as expected from the calculations of Anglada et al. (2018), which is solely due to optical depth effects.

The spectra in Fig. 3.1 show a single turnover in the frequency range of interest. However, in general, a thermal jet could exhibit two turnover frequencies which separates a low frequency regime having a spectral index of $+2$ (fully optically thick), an intermediate frequency regime with spectral index close to $+0.6$ (part of the jet is optically thick and part is optically thin) depending on the geometrical parameters, and a high frequency regime with a spectral index of -0.1 (fully optically thin). The high frequency turnover is dictated by the ionized density at r_0, while the low frequency turnover depends on the density close to $y_{\mathrm{LOS}_{\mathrm{max}}}$.

For our numerical model, the overall behavior is similar to the spectrum from Reynolds model. However, the Reynolds approximation is an overestimate by $24 - 32\%$, as expected. There are two factors that contribute to this discrepancy, which are as follows: (i) geometrical effects due to the large opening angle, and (ii) effect of intermediate optical depths. In our model each slice of the jet at any y has an elliptical

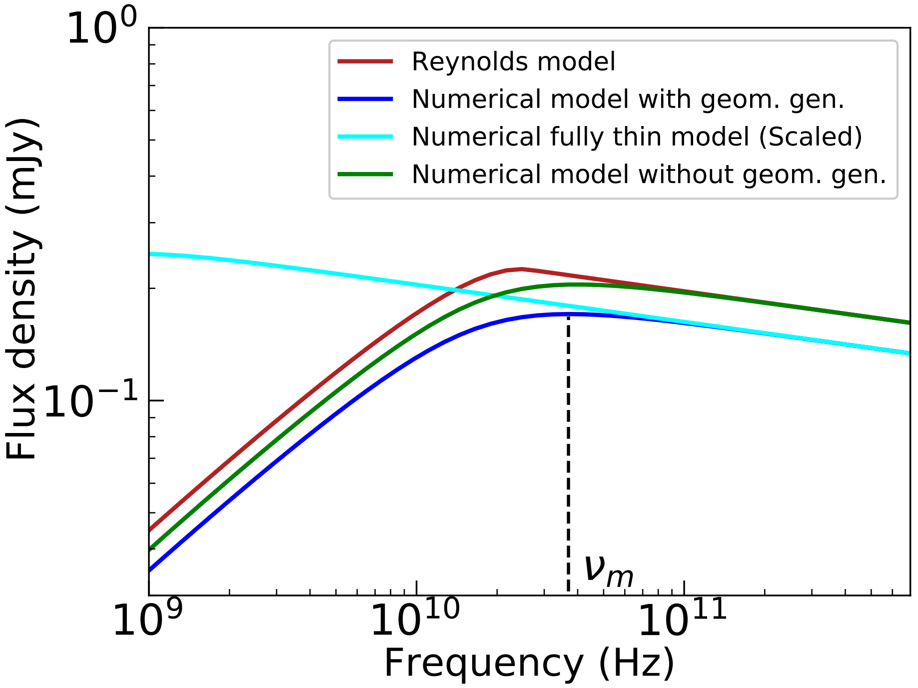

Figure 3.1: Comparison of thermal free-free spectrum calculated analytically (Reynolds, 1986) with that calculated numerically for a jet at a distance of 1 kpc. The parameters of the jet are n_0 = 5 × 10^7 cm^{-3}, x_0 = 0.2, q_n = -2, q_x = 0, r$_0$ = 10 au, θ_0 = 30°, ϵ = 1, i = 60°, T$_0$ = 10^4 K, q_T= 0, y_{max} = 1000 au, see text for more details. A lower n_0 of 10^6 cm^{-3} results in a fully optically thin jet shown in cyan (scaled up by a factor of 2500).

or circular cross-section depending on the jet inclination. In Reynolds model, on the other hand, a similar slice of the jet has rectangular cross-section. Due to the accommodation of larger opening angles in our model, the calculation of radial variation of the parameters are considered for a given LOS whereas the same has been ignored in the Reynolds model. The secondary factor for the difference in flux density is due to the inclusion of intermediate optical depths in the flux density estimation. The effect of intermediate optical depths is visible from the figure, where our model shows a relatively gradual turnover unlike the Reynolds case.

3.2 Jet spectrum for a combination of thermal and non-thermal emission mechanisms

We will now proceed to discuss the case of a jet which is representative of a knot located farther away from the driving source with non-thermal emission dominating its spectrum. An example of such a jet spectrum with thermal and non-thermal emission is shown by the solid black curve in Fig. 3.2. Here, we have assumed the jet to have a constant opening angle of $\theta_0 = 30°$, of which the outer region $\delta\theta = 0.5°$ contributes to the synchrotron emission, and for this we have taken $\eta_e^{rel} = 10^{-5}$. Due to episodic ejection of materials by the driving source, jets are usually observed as knots/lobes. Since non-thermal emission is seen in jet knots which are observed to be farther away from the central source (Vig et al., 2018), we have assumed an r_0 = 3000 au and the size of the lobe to be 800 au. We have considered an electron distribution with $p = 2.3$ accelerated in a $\vec{B}$ field of 0.3 mG. The base number density is taken as $n_0 = 500$ cm^{-3} with number density falling off as r^{-2}, and the jet is isothermal with a temperature $T = 10^4$ K. The ionization fraction at the jet base $x_0 = 0.2$ with its radial variation given by $q_x = -0.5$. We have considered a value of $\nu_{pk} = 10$ MHz and $\nu_c = 100$ GHz. The other parameters are the same as those used earlier to generate the free-free emission in Fig. 3.1. The radio spectrum seen in Fig. 3.2 (solid black curve) displays dominant synchrotron contribution, with a turnover at $\nu_t = 1.4$ GHz. This turnover represents the frequency at which the flux density is maximum and is a sort of average over the entire jet, determined by the combined properties of free-free and synchrotron emission. The spectral indices are $+2.5$ below ν_t, and -0.64 above ν_t. There is a break in the spectrum at higher frequency that occurs at ν_c, corresponding to the synchrotron cooling frequency as discussed earlier.

The spectrum generated with $q'_x < 0$ is expected to have lower flux densities compared to the case of $q'_x = 0$ because this would imply a decrease in ionization fraction with lateral distance from the jet axis. This will result in a decrease in the number density of particles that are capable of contributing to the radiative emission. This effect could be more pronounced in the case of a knot with dominant synchrotron emission. This is because our model assumes that synchrotron emission originates from the shocked lateral edges of the jet and in the presence of a descending ionization fraction profile, the ionized number density at these edges would be low resulting in the overall reduction of flux densities. This is evident from the spectrum of a jet with $q'_x = -1$ (grey dashed curve), and shown in Fig. 3.2 for comparison. All the other parameters are kept the same as that for the solid black curve described in Sect. 2.4.2. The turnover frequency in this case is $\nu_t = 750$ MHz, which is lower than that for $q'_x = 0$.

In general, one could encounter different types of turnovers in a spectrum that in-

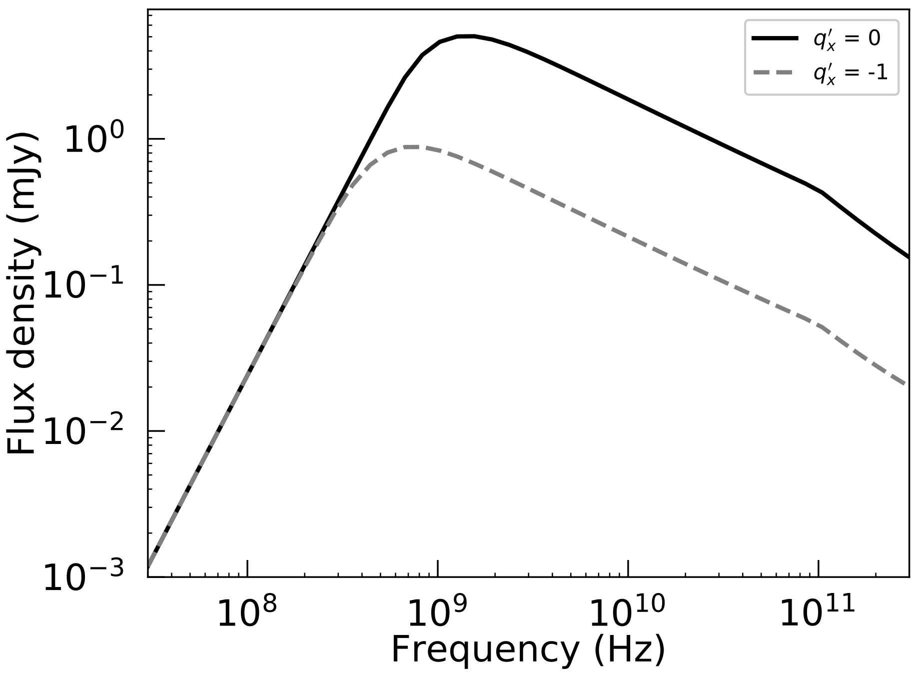

Figure 3.2: The spectra of jet models which incorporate both free-free and synchrotron emission. The parameters of the jet models are n_0 = 500 cm^{-3}, q_n = -2, T_0 = 10^4 K, r_0 = 3000 au, θ_0 = 30°, x_0 = 0.2, y$_{max}$ = 4500 au, ϵ = 1, i = 60° and d = 1 kpc. The synchrotron radiation is assumed to be generated from a shell of thickness 0.5° having an electron distribution with $p = 2.3$ accelerated in a $\vec{B}$ field of 0.3 mG, generating $\eta_e^{rel} = 10^{-5}$ in both the cases shown. The power-law index of radial variation in ionization fraction q_x = -0.5. The power-law index of the lateral variation in ionization fraction is represented as q'_x; two cases of which are shown in the plot.

corporates both thermal free-free and synchrotron emission. In frequency ranges where either thermal or non-thermal emission mechanism dominates, there could be frequency turnovers corresponding to a fully optically thick jet to a regime where a part of the jet is optically thick (change of spectral index from 2 to $\sim$0.6), from this regime to a fully thin thermal jet ($\sim$0.6 to -0.1), and from optically thick to thin regime for the non-thermal emission (2.5 to -0.6). In addition, the combination of the thermal and non-thermal contributions can result in more turnovers depending on the frequency sub-ranges in which alternate emission mechanisms dominate. This could include the transition from fully optically thick thermal emission to optically thin non-thermal emission (2 to -0.6), from fully optically thick thermal emission to optically thick non-thermal emission (2 to 2.5), from optically thick non-thermal emission to a regime where a part of the jet is optically thick thermal emission (2.5 to

$\sim$0.6), from optically thin non-thermal emission to fully thin thermal emission (-0.6 to -0.1), etc. It is important to bear in mind that the above mentioned spectral indices are indicative and the exact values will depend on the relative contributions of the emission from the two mechanisms.

3.3 Nature of emission across jet length

It is instructive to note the variation in flux densities across the length of the protostellar jet. For the model parameters considered in Sect. 3.2 and $q'_x = -1$, we present the total flux densities as a function of the projected length along the y-axis and frequency along the x-axis, in Fig. 3.3 (left). At this aim, the jet is divided into segments with width equal to the width of the jet at any y and height $\Delta y = 3$ au. The flux densities from each of these segments is then calculated separately. The jet spectrum at any arbitrary y can be analyzed by noting the behavior across the frequency axis. l_1, l_2 and l_3 marked in white represent three different locations along the jet projected length y. The spectra for the three different positions are shown in Fig. 3.3 (right). Blue and green in Fig. 3.3 (right) show that for l_1 and l_2, the total flux is dominated by free-free emission. Here, the major contribution of the flux density is from the inner thermal jet. On the other hand as one moves farther out to larger y, the flux contribution is dominated by synchrotron (red). Whether the dominant flux contribution to a spectrum is from thermal free-free or non-thermal synchrotron emission can be established from the spectral indices. In the sample spectra shown in Fig. 3.3 (right), the optically thin spectral index along l_1 is -0.07 implying dominant thermal free-free emission, and those along l_2 and l_3 are -0.40 and -0.60, respectively, upto 100 GHz (ν_c). From this, we conclude that non-thermal synchrotron emission is dominant in the higher frequency range along these two lines-of-sight.

In each of these spectra, one can identify a turnover frequency that corresponds to the combined (free-free and synchrotron) emission of the jet element towards this position becoming fully optically thin. We observe that the turnover shifts to lower frequencies as one moves away from the jet base. From Fig. 3.3 (left), it can also be seen that the rate of change in turnover frequency with maximum emission (black) becomes lower in the synchrotron dominated region of the jet, implying that the synchrotron turnover frequency is less sensitive to radial variation in parameters such as jet width $w(y)$, number density n and ionization fraction x as compared to free-free

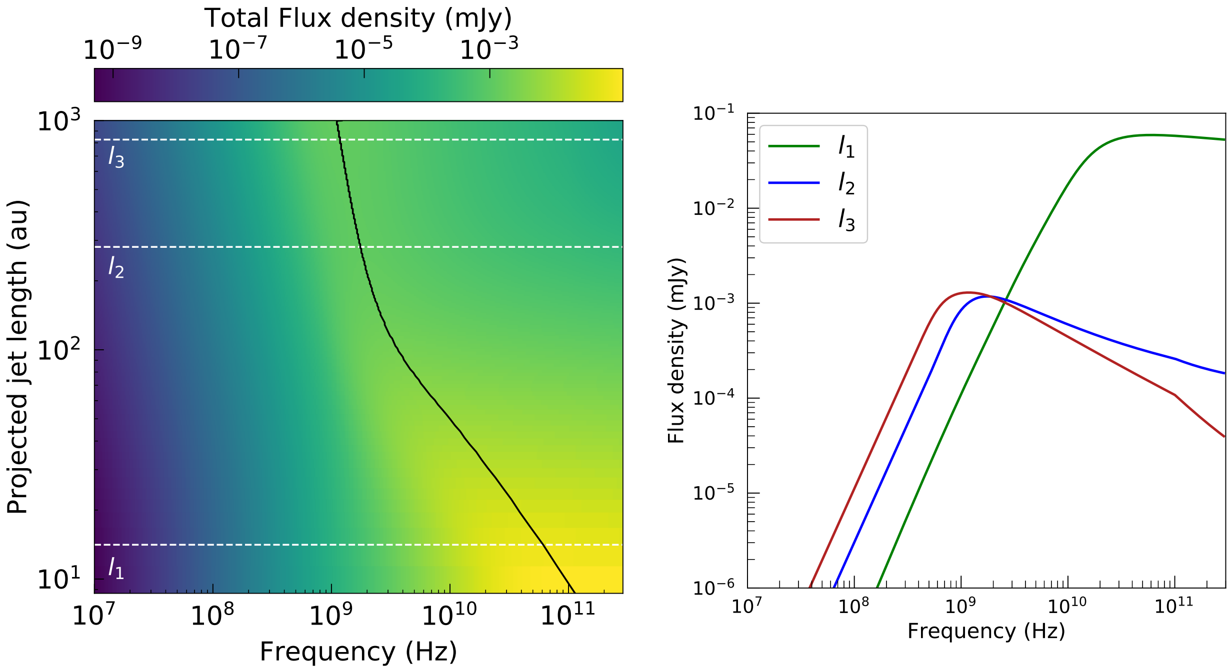

Figure 3.3: [Left] The flux density distribution (combined free-free and synchrotron) as a function of frequency (ν) and projected length of the jet (y) plotted in logarithmic space. At each y along the jet, the flux densities are calculated for segments with width equal to the width of the jet, and Δy = 3 au. The black curve represents the variation of the turnover frequency ν_t where emission is maximum. l_1, l_2 and l_3 marked in white are three different positions along y, whose spectra are shown in [right]. The jet model parameters $n_0 = 10^8$ cm^{-3}, r_0 = 10 au, $y_{max} = 1000$ au, $q_x = q'_x = 0$; the remaining parameters are same as in Fig. 3.2.

emission. This is easily understood since we know that synchrotron and free-free optical depths vary with the density of electrons as $\tau_\nu^{syn} \propto n\,x$ and $\tau_\nu^{ff} \propto n^2\,x^2$. As we move outwards to larger y, $w(y)$ increases but n and x decrease, thereby exhibiting more influence on the free-free optical depth and hence its turnover frequency. These spectra clearly exhibit the transition from free-free to synchrotron dominated flux as one moves from the jet base to the top of the jet.

3.4 Dependence of radio spectrum on model parameters

The dependence of the model spectrum on various parameters is illustrated here, both for (i) free-free emission analogous to thermal jets, and (ii) a combination of free-free and synchrotron emission. We characterize the spectrum in terms of the turnover frequencies. The full spectrum is divided into frequency windows based on the turnover frequencies and the spectral indices are determined accordingly in these windows.

3.4.1 Thermal jet

We first consider cases corresponding to a fully thermal jet. For all the thermal spectra shown in this section, the high frequency turnover corresponds to the frequency above which r_0 becomes optically thin and the low frequency turnover corresponds to the frequency below which the emission towards $y_{\mathrm{LOS}_{\mathrm{max}}}$ becomes optically thick. We consider a jet located close to the YSO at $r_0 = 50$ au with $y_{max} \sim 1300$ au, inclined at an angle $i = 60°$, and located a distance $d = 1$ kpc. We assume the parameters at r_0 as follows: jet opening angle $\theta_0 = 30°$, ionization fraction $x_0 = 0.2$ and electron temperature $T_0 = 10^4$ K. The remaining parameters are $\epsilon = 1$, the power-law indices of radial ionization fraction profile $q_x = -0.5$, and lateral ionization fraction profile $q'_x = -1$.

3.4.1.1 Number density profile

Fig. 3.4 (a) shows the spectrum of this knot for various number densities n_0 at r_0, assuming $q_n = -2$ (Case I). An increase in n_0 would lead to an overall increase in the number of particles contributing to the emission and consequently, the flux densities would increase. It can be seen from the figure that with an increase in number density by a certain factor, the flux density increases roughly by the same factor. It is instructive to compare our results with the predictions of the analytical Reynolds model, although the latter makes geometrical approximations and does not consider lateral variation in ionization fraction. We emphasize that the absolute values of flux densities in our model are expected to be different from that of Reynolds due to these generalizations. The flux densities estimated from our model are about $65 - 86\%$ lower than the values from the corresponding Reynolds model. This can be attributed to contributions from (i) optical depth generalization, (ii) geometrical generalization that includes the (a) jet cross-section and (b) opening angle generalization, and (iii) introduction of lateral variation in ionization fraction. We find that a flux difference of about 24-32% can be accounted due to (i) and (ii), while the rest is attributed to (iii). Of the 24-32$\%$ flux difference, $\sim 8-12\%$ is due to the effect of intermediate optical depths, about 7-9$\%$ is due to opening angle generalization, and $\sim 9-12\%$ is due to the modification of the jet cross-section (from rectangular cross-section in Reynolds model to circular cross-section in our model). If we consider a relatively low frequency of 270 MHz (arbitrary), the ratio of flux densities for $n_0 = 10^7$, 5×10^7 and 10^8 cm^{-3} with respect to $n_0 = 10^6$ cm^{-3} are 13, 62 and 115 in our model. According to the Reynolds model, the flux densities are directly proportional to n_0, and hence the corresponding ratios are 10, 50 and 100. This implies an agreement between the two models at low frequencies. In Fig. 3.4(a), we also note that as the number density increases, both the high and low frequency turnovers shift to higher values. With an increase in the number density of the particles contributing to the emission, the overall optical depth within the jet increases. As a result of this, the farther region of the jet with the largest LOS distance (that determines the low frequency turnover) will remain optically thick even at higher frequencies compared to the cases with lower number densities. Similarly, r_0 remains optically thick up to higher frequencies, thereby resulting in an increase in the high frequency turnover. The Reynolds model predicts that the transition to a fully optically thin jet (high frequency turnover) is dependent on n_0 as $n_0^{2/2.1}$. This means that a variation of n_0 by a factor of 10 should result in a variation of turnover frequency by a factor of ~ 9. The corresponding factor obtained from our model is ~ 10. The dependence of turnover frequencies on n_0 can be observed from Table 3.1 (Case I).

In Fig. 3.4 (b), we demonstrate the effect of varying q_n on the spectral properties for $n_0 = 5\times10^7$ cm^{-3} (Case II). The remaining parameters are the same as Case I. The figure shows that the flux densities decrease with an increase in $|q_n|$. This is because a larger $|q_n|$ results in a lower number density of electrons as we move away from r_0 that contribute to the overall flux. To understand this better, we take the ratio of flux densities between q_n = -2 and -2.5 at a frequency of 500 MHz suitable for comparison with the Reynolds model. The ratio is 2.6 for our model and the corresponding ratio for Reynolds model is 2.9. The values are similar, but not identical. The difference can be attributed to geometrical generalization and lateral variation of ionization fraction included in our model. In the figure, the spectral indices in the frequency range between the two turnover frequencies are 0.36, 0.81 and 1.04 for q_n = -1, -2 and -2.5, respectively. This implies that a larger $|q_n|$ results in a steeper spectrum. This is because an increase in $|q_n|$ results in a larger decline in overall jet density. As number density decreases, the portion of the jet that is optically thick

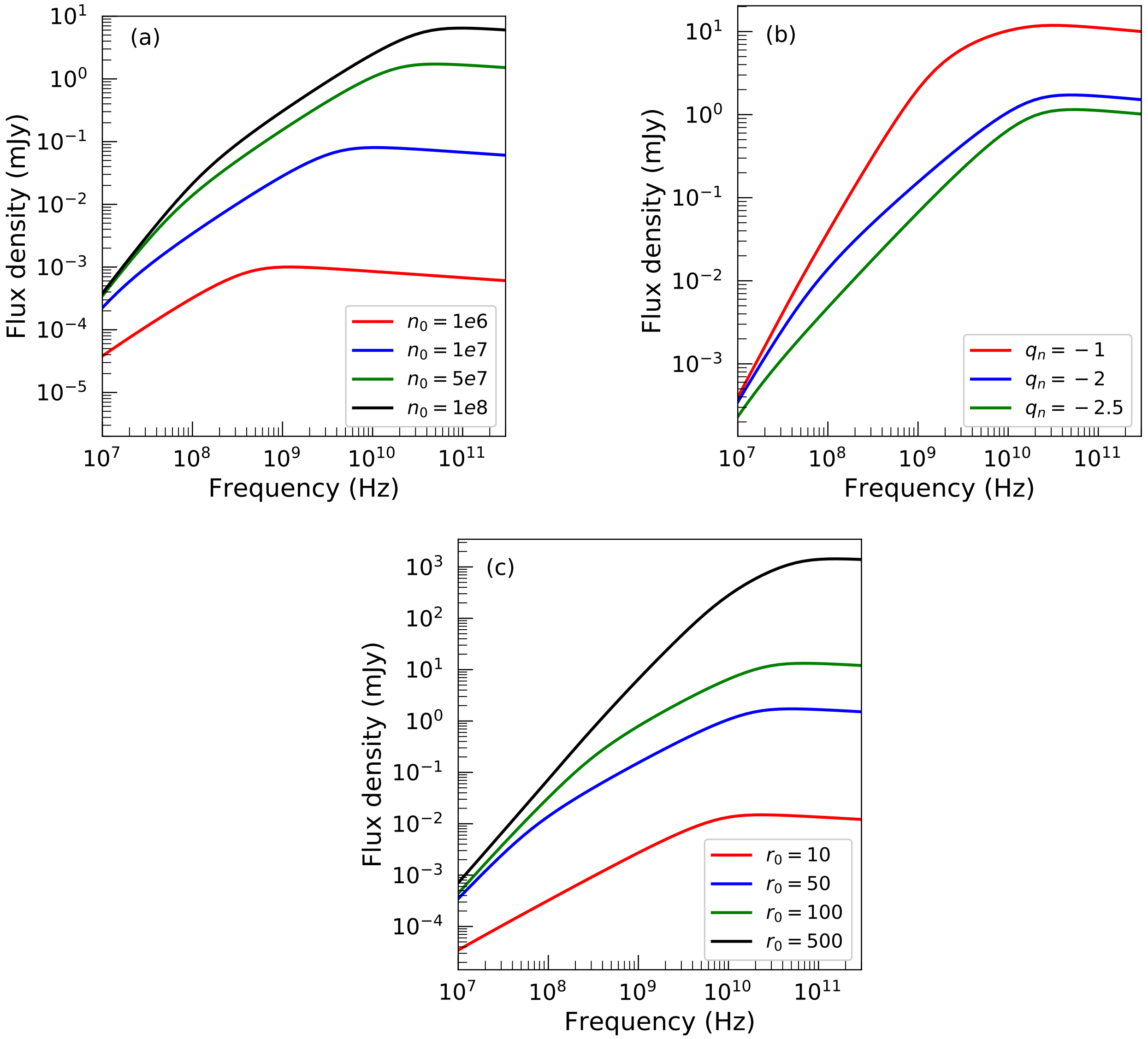

Figure 3.4: Dependence of the radio spectrum of a fully thermal jet on (a) $n_0(cm^{-3})$, (b) q_n, and (c) r_0 (au). Other than the parameter which is varied in each case, the remaining jet parameters are r_0 = 50 au, n_0 = 5×10^7 cm^{-3}, $\theta_0 = 30°$, x_0 = 0.2, T_0 = 10^4 K, q_n = -2, q_x = -0.5, q'_x = -1, ϵ = 1, $y_{max} \sim 1300$ au, $i = 60°$ and d = 1 kpc. The details of the spectra shown in (a), (b) and (c) are listed in Table 3.1 as Cases I, II and III, respectively.

gradually reduces and as a result, the flux contribution from optically thick region will be lower resulting in a steeper spectral index. The spectral indices and turnover frequencies corresponding to these plots are listed as Case II in Table 3.1.

In this context, we consider the case of varying r_0 (Case III). Fig. 3.4 (c) shows the dependence of the spectrum on the parameter r_0 for a constant $n_0 = 5 \times 10^7$ cm^{-3}.

The remaining parameters are the same as Case I. It is to be noted that this case represents spectra of different jets with different number densities although n_0 at r_0 for each jet is the same. This implies that a jet with larger r_0 has a higher number density at any radial length r as compared to the number density of a jet with a lower r_0. This means that the number density at each r that is contributing to the emission will be different for each jet since the number densities are scaled by the factor $\left(\frac{r}{r_0}\right)^{q_n}$. This produces an indirect effect on the observed spectrum as r_0 is varied. To understand this in detail, we consider Eq. (16) of the Reynolds model which states that the flux densities are proportional to $r_0^{2.5}$ for the assumed parameters. We again select a low frequency for comparison with the Reynolds model. At a frequency of 600 MHz, the ratio of flux densities for the cases of r_0 = 50 and 100 au with respect to $r_0 = 10$ au as obtained from the our model are 54 and 259, respectively, whereas the corresponding values predicted by the Reynolds model are 55 and 316. This conveys the agreement between the two models. For $r_0 = 500$ au, a comparison with the Reynolds model is difficult since this spectrum is dominated by fully optically thick and fully optically thin regimes only, without a perceptible intermediate regime. This is because in this case, r_0 and r_{max} are rather close, so that the low and high frequency turnovers are quite similar. We again find that for these parameters, our model flux densities are lower by $67 - 86\%$ as compared to the Reynolds model across the spectrum, and we attribute this difference to the effect of geometrical generalization and introduction of lateral variation in ionization fraction. The turnover frequencies for this case are given in Table 3.1 (Case III).

3.4.1.2 Ionization fraction profile

Fig. 3.5 (a) displays the jet spectra for different ionization fractions x_0 at r_0 (Case IV). The jet parameters are $n_0 = 5 \times 10^7$ cm^{-3} and the remaining parameters are same as that of Case I. Since x_0 determines the ionized fraction of particles in the jet material that contribute to the emission, the flux densities increase with increase in x_0 as shown in the figure. The same reasoning is applicable to an increase in turnover frequencies with increase in x_0. We note that the Reynolds model predicts that the transition to a fully optically thin jet (high frequency turnover) is dependent on x_0 as $x_0^{2/2.1}$ suggesting an increase in turnover frequency with x_0. The spectral indices and turnover frequencies corresponding to the case explored here are listed as Case IV in Table 3.1.

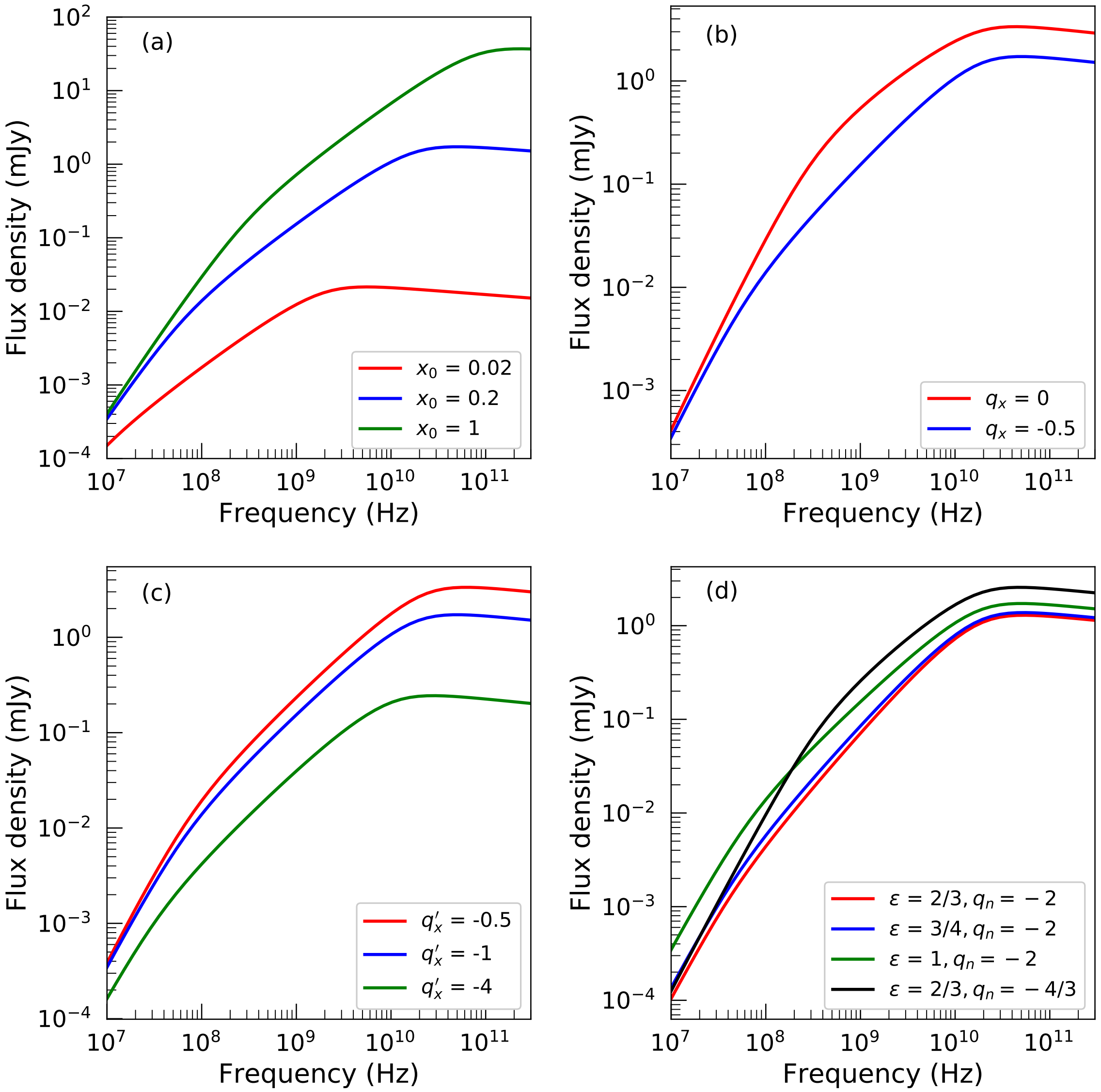

Figure 3.5: Dependence of the radio spectrum of a fully thermal jet on (a) x_0, (b) q_x, (c) q'_x, (d) combination of ϵ and q_n. The parameters other than the ones varied here are same as that of Fig. 3.4. The details of the spectra shown in (a), (b), (c) and (d) are listed in Table 3.1 as Cases IV, V, VI and VII, respectively.

In Fig. 3.5 (b) and (c), we have shown the dependence of the spectrum on the power-law indices q_x and q'_x (Cases V and VI, respectively). The jet parameters are $n_0 = 5 \times 10^7$ cm^{-3} and the remaining parameters other than the ones varied here are same as Case I. From the plots, it is evident that flux densities decrease with increase in the value of $|q_x|$ and $|q'_x|$ as this results in the lowering of the number density of particles

Table 3.1: Turnover frequencies and associated spectral indices of a fully thermal jet close to the YSO, for various jet parameters. The corresponding spectra are plotted in Figs 3.4 and 3.5.

THERMAL FREE-FREE EMISSION

Variable Parameter	Value	Turnover frequencies (GHz)	Spectral indices
Case I [Fig. 3.4(a)]			
n_0	10^6	0.76	0.80; -0.09
	10^7	0.04; 6.87	1.30; 0.83; -0.09
(cm^{-3})	5×10^7	0.18; 31.17	1.57; 0.83; -0.06
	10^8	0.35; 60.59	1.65; 0.84; -0.04
Case II [Fig. 3.4(b)]			
q_n	-1	1.67; 32.70	1.86; 0.36; -0.08
	-2	0.18; 31.17	1.57; 0.83; -0.06
	-2.5	0.03; 30.58	1.43; 1.04; -0.06
Case III [Fig. 3.4(c)]			
r_0	10	14.92	0.88; -0.07
	50	0.18; 31.17	1.57; 0.83; -0.06
(au)	100	0.86; 45.52	1.72; 0.76; -0.06
	500	101.35	1.71; -0.01
Case IV [Fig. 3.5(a)]			
x_0	0.02	3.61	0.89; -0.08
	0.2	0.18; 31.17	1.57; 0.83; -0.06
	1	0.84; 146.27	1.71; 0.83; -0.01
Case V [Fig. 3.5(b)]			
q_x	0	1.81; 31.79	1.57; 0.49; -0.07
	-0.5	0.18; 31.17	1.57; 0.83; -0.06
Case VI [Fig. 3.5(c)]			
q'_x	-0.5	0.23; 38.18	1.64; 0.85; -0.06
	-1	0.18; 31.17	1.57; 0.83; -0.06
	-4	0.09; 18.73	1.44; 0.82; -0.07
Case VII [Fig. 3.5(d)]			
ϵ, q_n	2/3, -2	0.07; 30.87	1.70; 1.05; -0.06
	3/4, -2	0.08; 30.87	1.68; 0.99; -0.06
	1, -2	0.18; 31.17	1.57; 0.83; -0.06
	2/3, -4/3	0.69; 31.77	1.78; 0.71; -0.07

that are contributing to the emission. To understand this better, we first consider the case of varying q_x. For this, we choose an arbitrary frequency of 1.5 GHz where our model is comparable with that of Reynolds. At this frequency, the ratio of flux densities for the Reynolds model between $q_x = 0$ and $q_x = -0.5$ is 3.6, whereas for our model the corresponding ratio is 3.3. This shows the agreement with the model of Reynolds at low frequency. The influence of q'_x on the spectrum, shown in Fig. 3.5(c), is expected to be such that the regions of the jet farther away from the axis will have lower number density of particles contributing to the emission, thereby reducing the overall flux density. The spectra agree with this prediction.

3.4.1.3 Combination of geometry and number density profile

The next power-law index that we are interested in studying is ϵ which plays a role in deciding the jet geometry. In Fig. 3.5 (d), we have shown the dependence of the spectrum on a combination of ϵ and q_n (Cases VII). In this figure, the red, blue and green curves represent a case of constant q_n but varying ϵ. The observed trend implies that the flux densities increase with an increase in the value of ϵ due to the jet becoming wider, and therefore assimilating more material that can contribute to the overall emission. At a frequency of 500 MHz, the ratio of flux densities for ϵ = 1 and 3/4 with respect to ϵ = 2/3 are 2.5 and 1.2, respectively. The corresponding values for Reynolds model are 2.9 and 1.3, respectively.

Additionally, we have included a scenario in which both ϵ and q_n are varied (black curve) in Fig. 3.5 (d). A comparison with the other combinations in the figure shows that the low frequency turnover in this case occurs at a higher frequency while the high frequency turnover is similar to the other cases. From the red, blue and green curves in this figure, we note that increasing ϵ leads to an increase in flux densities, while for $|q_n|$ the effect is opposite (see Case II). In Case II, the flux densities at low frequencies where the full jet is optically thick do not vary significantly with a change in q_n, but vary considerably at high frequencies. Varying ϵ and q_n simultaneously (black curve versus the others), the effect of varying q_n is minimal and the ϵ factor appears to dominate at low frequencies as a wider jet contributes to larger flux densities. At higher frequencies, a narrower jet with a flatter q_n profile contributes to higher flux densities than a wider jet with similar or larger value of $|q_n|$ suggesting that q_n appears to be the dominant parameter compared to ϵ here. The spectral indices and the associated turnover frequencies are listed as Case V, VI and VII in

Table 3.1.

3.4.2 Jet with combination of thermal and non-thermal emission

As we move farther away from the central YSO, the densities are expected to decrease thereby reducing the thermal contribution in the jet spectrum, and resulting in the increased contribution of non-thermal emission. To describe this evolution, we have considered a jet with parameters $r_0 = 50$ au, $y_{max} = 1300$ au, $n_0 = 10^8$ cm^{-3}, $q_n = -2$, $\theta_0 = 30°$, $\epsilon = 1$, $i = 60°$, $x_0 = 0.2$, $q_x = -0.5$, $q'_x = -1$, $T_0 = 10^4$ K at a distance $d =$ 1 kpc. We have included the effects of synchrotron emission in the outer edges of the jet with an angular thickness of $\delta\theta = 0.5$. The values of parameters related to the synchrotron emission are $p = 2.3$ and $B_0 = 0.3$ mG.

The radiative power released by the electrons in the form of synchrotron emission is a function of the efficiency of converting the power contained within the shock to non-thermal particles and, the fraction out of this that will be transferred to the electrons. This is expressed through the parameter η_e^{rel} which is the efficiency with which shock energy is transferred to the electrons. We therefore illustrate the evolution of jet spectrum from dominating thermal emission to dominating synchrotron emission by varying the parameter η_e^{rel} (Case VIII). It can be seen from Fig. 3.6 that as η_e^{rel} increases, non-thermal emission gradually dominates over thermal emission. During the course of this evolution, we observe a few turnover frequencies relating the optically thick/thin emission from the thermal/synchrotron mechanisms, as described in Sect.2.4.2. The spectral indices and turnover frequencies for this case are listed in Table 3.2 as Case VIII.

3.4.2.1 Dependence of spectrum on synchrotron emission parameters

We next consider the case of a knot located farther away from the exciting YSO to elucidate the effect of the parameters of synchrotron mechanism on the jet spectrum. In this case, we take parameters characteristic of a farther knot with $r_0 = 3000$ au, $y_{max} \sim 4500$ au, $n_0 = 500$ cm^{-3}, q_n = -2, $\theta_0 = 30°$, $\epsilon = 1$, $i = 60°$, $x_0 = 0.2$, $q_x = -0.5$, $q'_x = -1$, $T_0 = 10^4$ K at a distance $d =$ 1 kpc. We take $\delta\theta = 0.5$, $p = 2.3$, $B_0 = 0.3$ mG and $\eta_e^{rel} = 10^{-5}$. We first study the effect of number density on the jet spectrum. This is shown in Fig. 3.7 (a) (Case IX). Similar to what was observed in the thermal jet case, with an increase in n_0 at r_0, we find

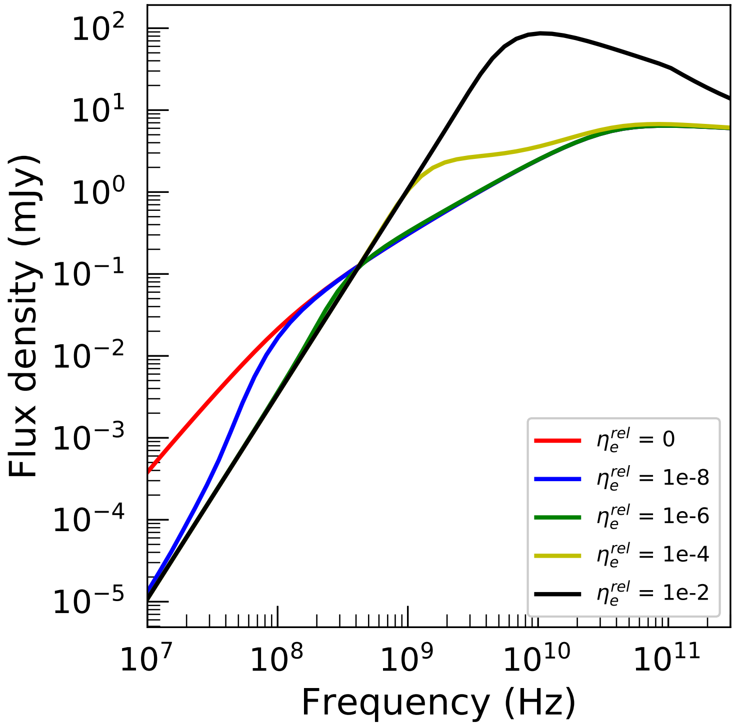

Figure 3.6: Evolution of the radio spectrum of a knot with inner thermal region and outer non-thermal shell as a function of relativistic electron fraction (η_e^{rel}). The jet number density at r_0 is $n_0 = 10^8$ cm^{-3}, $\epsilon = 1$, $q_n = -2$, and the remaining parameters of the thermal emission are same as those that remain fixed in the plots shown in Fig. 3.4. The parameters of the non-thermal emission are p = 2.3, $\delta\theta$ = 0.5 and $B_0 = 0.3$ mG. The details of the spectra are listed in Table 3.2 as case VIII.

that the flux densities increase, due to increase in the number density of particles contributing to the overall emission. We also note that with a decrease in n_0 (i) the low frequency turnovers shift to lower values due to the jet becoming more optically thin overall, and (ii) the optically thin spectral index becomes steeper due to the gradual domination of synchrotron emission over thermal emission. Note that the variation of flux density with number density is not the same in the two cases; it varies as n_0^2 and n_0 for thermal and non-thermal emission, respectively. The details of the spectra are listed in Table 3.2. The other panels of the figure encapsulate the effect of the synchrotron parameters B_0 (Case X), p (Case XI) and $\delta\theta$ (Case XII) on the spectrum of the knot. From the figure it is observed that, the flux densities increase with increase in the values of B_0 and $\delta\theta$. The strength of B_0 determines the degree of acceleration imparted to the electrons through the Lorentz force. This in turn dictates the amount of energy delivered to them which will eventually be emitted in the form of synchrotron radiation. Likewise, an increase in $\delta\theta$ implies an increase in the angular thickness of the region from which synchrotron emission arises, thereby contributing to higher synchrotron flux densities. On the contrary, an increase in p leads to a reduction in flux densities, and the optically thin spectral index is strongly dependent on the value of p. This is because as p increases, the number of electrons in the higher energy regime decreases, thereby lowering the corresponding emission by these electrons. The plots shown in the figure support the above arguments. The spectral index values and turnover frequencies are listed in Table 3.2 as Case IX, X, XI and XII.

3.4.3 Emission across the jet length

To understand the relative contributions of different regions within the jet to the overall spectrum, we divide the jet into three regions of equal volume along its length. For simplicity, we assume the jet to be in the plane of the sky i.e with an inclination angle $i = 90°$.

3.4.3.1 Fully thermal jet

The first region which we consider is close to the injection radius where the number densities and optical depths are very high. We then take the intermediate and farther regions along the jet length where the number densities gradually decrease according to the radial power-law index q_n. Fig. 3.8 (a) displays the spectra of the three regions in the case of a fully thermal jet with parameters $r_0 = 50$ au, $\theta_0 = 30°$, $n_0 = 5 \times 10^7$ cm^{-3}, $q_n = -2$, $x_0 = 0.2$, $q_x = -0.5$, $q'_x = -1$, $T_0 = 10^4$ K, $q_T = 0$, $\epsilon = 1$ and $y_{max} = 700$ au at a distance d = 1 kpc (Case XIII). For this fully thermal jet, the region close to the YSO being highly optically thick, displays two turnover frequencies in the frequency window of interest. On the other hand, as we move farther away, due to decrease in number density and optical depth, both the turnover frequencies shift to lower values. In both cases, the low frequency turnover goes below the frequency range displayed and the total flux contributions also reduce. The spectral indices and turnover frequencies associated with this case are listed in Table 3.3 as Case XIII.

Table 3.2: Turnover frequencies and associated spectral indices of knots emitting combined thermal and non-thermal emission located farther away from the exciting YSO, for various jet parameters. The corresponding spectra are plotted in Figs 3.6 and 3.7.

THERMAL FREE-FREE AND NON-THERMAL SYNCHROTRON EMISSION

Variable Parameter	Value	Turnover frequencies (GHz)	Spectral indices
Case VIII [Fig. 3.6]			
η_e^{rel}	0	0.10; 95.46	1.82; 0.87; -0.07
	10^{-8}	0.16; 95.28	3.14; 0.83; -0.07
	10^{-6}	0.36; 95.15	2.55; 0.78; -0.07
	10^{-4}	1.92; 85.02	2.44; 0.36; -0.09
	10^{-2}	10.69; 100	2.40; -0.43; -0.76
Case IX [Fig. 3.7(a)]			
n_0	500	0.29; 100	2.31; -0.63; -1.13
	10^3	0.36; 100	2.26; -0.64; -1.12
(cm^{-3})	10^4	0.75; 100	2.36; -0.61; -0.89
	10^5	1.63; 100	2.39; -0.43; -0.35
Case X [Fig. 3.7(b)]			
B_0	0.1	0.17; 100	2.20; -0.64; -1.10
	0.2	0.24; 100	2.20; -0.64; -1.1
(mG)	0.3	0.29; 100	2.31; -0.63; -1.13
Case XI [Fig. 3.7(c)]			
p	1.8	0.03; 100	1.18; -0.40; -0.90
	2.3	0.29; 100	2.31; -0.63; -1.13
	2.6	0.90; 100	2.39; -0.77; -1.23
Case XII [Fig. 3.7(d)]			
$\delta\theta$	0.1	0.17; 100	2.19; -0.63; -1.06
	0.5	0.29; 100	2.31; -0.63; -1.13
()	1	0.37; 100	2.26; -0.64; -1.14

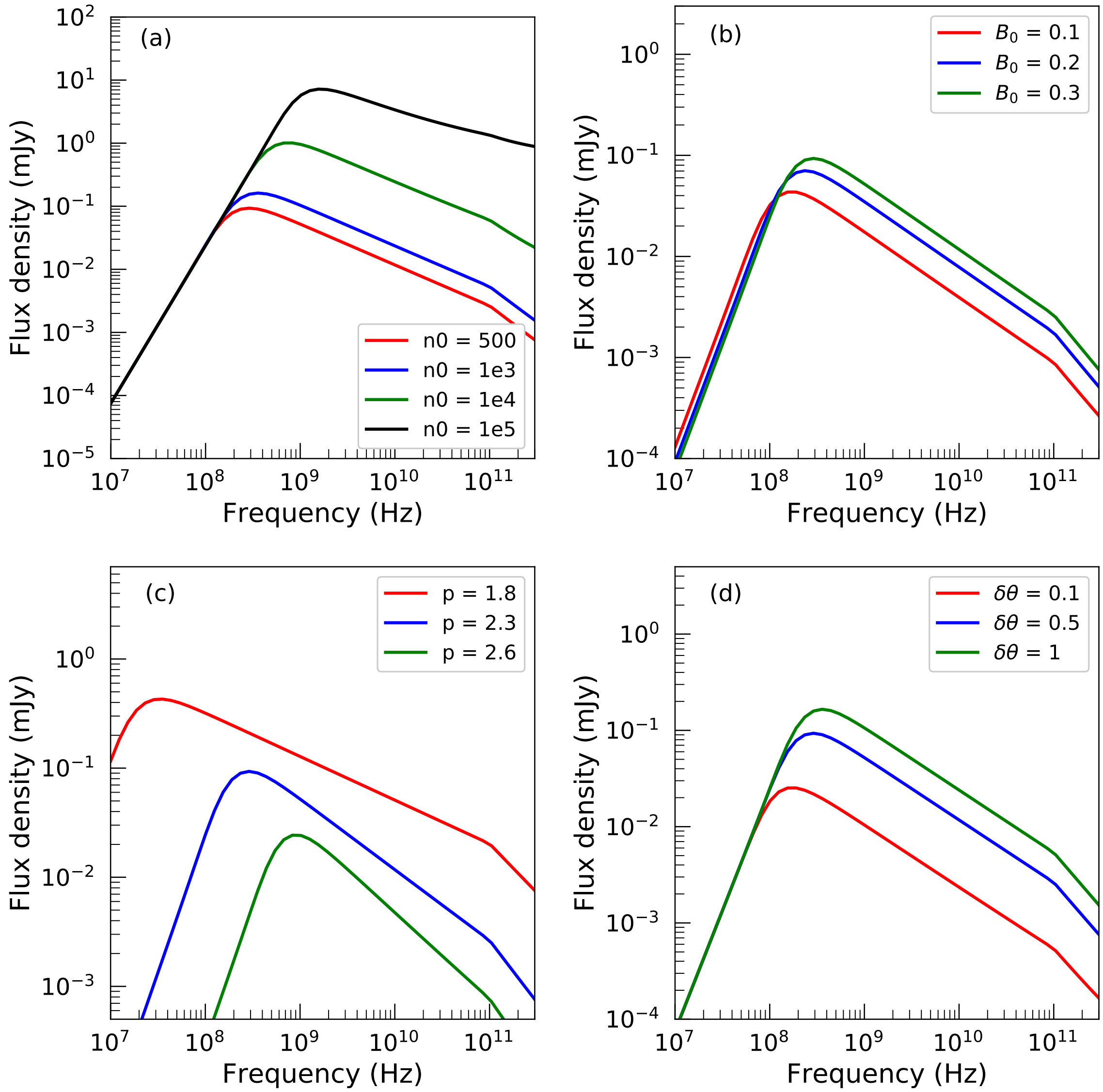

Figure 3.7: Dependence of the radio spectrum of a knot with inner thermal region and an outer non-thermal shell on (a) n_0 (cm^{-3}) , (b) B_0 (mG), (c) p, and (d) $\delta\theta()$. We have used $r_0 = 3000$ au and $y_{max} \sim 4500$ au. The remaining parameters other than the ones varied here are same as that of Fig. 3.4. The parameters of synchrotron emission are $\delta\theta = 0.5$, $p = 2.3$, $B_0 = 0.3$ mG and $\eta_e^{rel} = 10^{-5}$. The details of the spectra shown in (a), (b), (c) and (d) are listed in Table 3.2 as Cases IX, X, XI and XII, respectively.

3.4.3.2 Jet with a combination of thermal and non-thermal emission

We next consider a jet that includes a combination of thermal and non-thermal emission and Fig. 3.8 (b) shows the spectra of the three regions of the jet (Case XIV). In

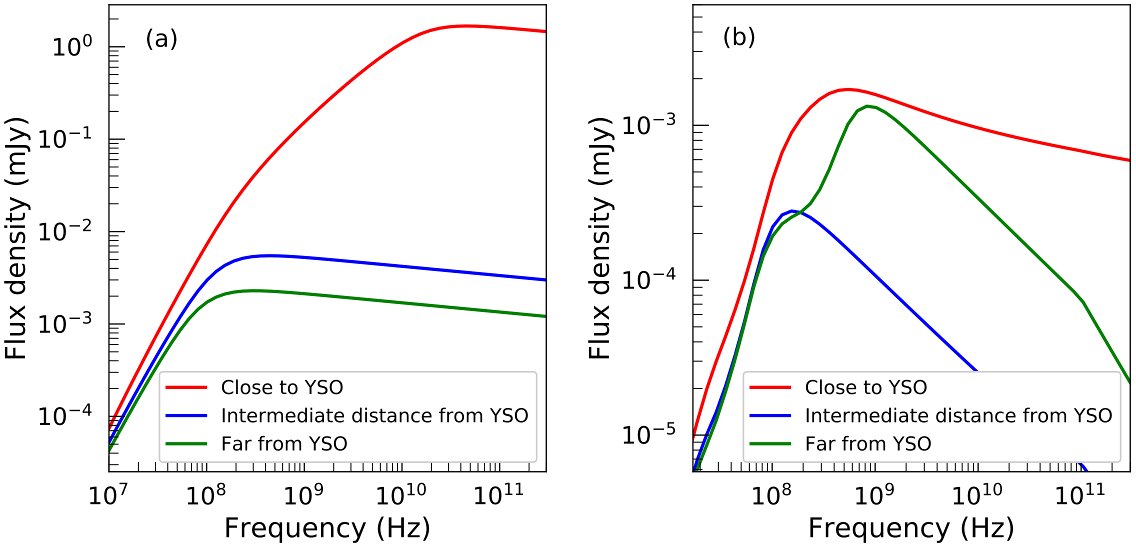

Figure 3.8: Radio spectrum of (a) a fully thermal jet, and (b) a jet with with inner thermal region and an outer non-thermal shell, showing emissions from three different regions of equal volume along the jet length. The inclination angle of the jets are $i = 90°$. The remaining parameters of the jets in (a) and (b) are listed in the text where this is discussed. The details of the spectra shown in (a) and (b) are listed in Table 3.3 as Cases XIII and XIV, respectively.

this case, we assume a jet located at $r_0 = 100$ au and $y_{max} = 450$ au with a density $n_0 = 10^6$ cm^{-3} and the remaining parameters are the same as that of Case XIII. This jet includes shocked edges of thickness $\delta\theta = 0.5°$, where the parameters for synchrotron emission are $B_0 = 0.3$ mG, $\eta_{rel} = 10^{-5}$ and $p = 2.3$. It is evident from the figure that the region close to the YSO is dominated by thermal free-free emission, the intermediate region shows competing contributions from both thermal and non-thermal mechanisms while the farthest region in the jet shows dominant non-thermal emission. As we move from the region close to the YSO to the intermediate region, the number density declines and this manifests as a decrease in flux densities and turnover frequencies. This can be seen from the figure. In both these regions, the contribution to synchrotron emission arises from the shocked regions at lateral edges of the jet. On the other hand, in the region of the jet farthest from the central YSO, apart from the lateral edges, there is an additional contribution of synchrotron emission from the top terminal edge. As a result, the flux densities and turnover frequencies increase compared to the intermediate region of the jet. The figure emulates

Table 3.3: Turnover frequencies and associated spectral indices for fully thermal jet close to the YSO, and a jet emitting combined thermal and non-thermal emission located farther away from the exciting YSO, i.e. Cases XIII and XIV. The corresponding spectra are plotted in Fig. 3.8.

THERMAL FREE-FREE EMISSION		
Case XIII [Fig. 3.8(a)]		
Jet region	Turnover frequencies (GHz)	Spectral indices
Close to YSO	0.23; 46.03	1.91; 0.81; -0.08
Intermediate distance from YSO	0.44	1.29; -0.09
Farther from YSO	0.31	1.24; -0.09
THERMAL FREE-FREE AND NON-THERMAL SYNCHROTRON EMISSION		
Case XIV [Fig. 3.8(b)]		
Close to YSO	0.48	1.81; -0.17
Intermediate distance from YSO	0.20; 100.00	1.90; -0.62; -0.83
Farther from YSO	0.19; 0.83; 100.00	2.01; −*; -0.64; -1.14

*The spectral index is not well-defined in this region due to the close proximity of two turnover frequencies.

this behavior. The spectral indices and turnover frequencies associated with this case are listed in Table 3.3 as Case XIV.

3.5 Summary

In this chapter we have compared our model to the Reynolds model and we conclude that as a consequence of the approximations assumed in the calculation of geometry and emission mechanisms, the Reynolds model over-estimates the flux densities of jets. Our generalized model can therefore predict the spectra of protostellar jets more accurately and can be applied to jets with wide as well as narrow opening angles.

Having demonstrated the better applicability and robustness of our model compared to the existing one, we have explored the effect of various model parameters on the radio spectra of jets. Here, we have characterized the numerical model by carefully analyzing the nature of the resultant spectra under different cases of input model parameters. This is essential for employing the model for the purpose of estimation of physical parameters of jets, which are otherwise difficult to be constrained by observations. In this context, the two-fold application of the model has aided in the study of jets/knots which are both close and far away from the exciting YSO.

Chapter 4

Radio spectra of protostellar jets: Applications of the model

In this chapter, we employ our model to understand the radio spectra of few prominent protostellar jets, which exhibit the characteristics of non-thermal emission. In order to do this, we have taken the available observational data of few protostellar jets at radio frequencies and generated model spectra that could reproduce the observed flux densities and spectral indices. This is assisted by the knowledge of dependence of the spectrum on the jet model parameters as discussed in the previous chapter. Observations indicate the presence of non-thermal emission from knots/lobes of few YSO jets, while in some cases the emission can be explained due to thermal free-free mechanism. While modeling, few parameters are taken from observations, and for the other parameters, we have employed a range of values which are typical of jets.

4.1 Comparison of model with observations

The observational data of three protostellar jets that are considered here include HH 80-81, G114.0835+02.8568 and DG-Tau. The references for these data sets are given in Table. 4.1. These references for the observed radio flux densities of the knots are also given in Figs. 4.2, 4.6 and 4.8. The sizes and locations of jet lobes, the jet opening angles, and other properties such as estimates of magnetic field which are taken from previous studies in literature, where available, are represented in Table. 4.2 along with the relevant references. These physical parameters are incorporated into the models to generate the radio spectra and more details about the parameters are given the subsequent subsections.

Table 4.1: References for observational radio data of jet sources.

Source name	References
IRAS 18162-2048	1,2,3,4,5,6,7
HH 80	1,2,3,4
HH 81	1,2,3,4
G114.0835+02.8568	8
DG-Tau	9

† (1) Vig et al. (2018) (2) Masqué et al. (2012) (3) Marti et al. (1993) (4) Masqué et al. (2015) (5) Gomez et al. (1995) (6) Carrasco-González et al. (2012) (7) Rodriguez et al. (1989a) (8) Obonyo et al. (2019) (9) Feeney-Johansson et al. (2019)

Table 4.2: Physical parameters of the jet knots based on observations.

Object	r_0^a (au)	r_{max}^b (au)	θ_0^c (°)	T_0^d (K)	B_0^e (μG)	i^f (°)	$\boldsymbol{d}^g$ (pc)	References†
IRAS 18162-2048	250	826	38.5	10^4	200	34	1400	1,2,3,4,5,6,7
HH 80	657741	675672	2.4	10^4	132	34	1400	1,2,7,8,9
HH 81	553636	562004	2.5	10^4	160	34	1400	1,2,7,8,9
Lobe G114.0835+02.8568-B	7974	20100	23.4	10^4	200*	60*	4200	10
DG-Tau A, Knot C	2485	3532	20.6	5×10^3	110	37.7	120	11,12,13,14,15

† (1) Vig et al. (2018) (2) Marti et al. (1993) (3) Carrasco-González et al. (2010) (4) Carrasco-González et al. (2012) (5) Masqué et al. (2012) (6) Rodriguez et al. (1989a) (7) Añez-López et al. (2020) (8) Bosch-Ramon et al. (2010) (9) Heathcote et al. (1998) (10) Obonyo et al. (2019) (11) Feeney-Johansson et al. (2019) (12) Vorobyov et al. (2018) (13) Oh et al. (2015) (14) Eislöffel & Mundt (1998) (15) (Purser et al., 2018)

* assumed values

[a] The projected distance of the knot from the central source that corresponds to the injection radius for continuous jet given in angular units

[b] The projected distance of the farther end of the knot

[c] The jet opening angle at r_0

[d] The electron temperature of the jet material at r_0

[e] Jet magnetic field at r_0

[f] Inclination angle

[g] distance of the source from the observer in pc

The physical parameters that are not constrained by the observations are decided based on a grid of values that are either generally observed in jets or expected from physical models of jets. These include q_n, q_x, q'_x, $\delta\theta$, p, η_e^{rel} and in some cases n_0, if it is unavailable from observations. Since the jets considered here are collimated, we assume that the jet opening angle continues to decrease as it moves out radially and therefore, for each knot ϵ is kept constant. In the case of HH80-81 jet, since all the knots belong to the same jet, we have assumed the same value of ϵ for all these knots. We also assume a temperature of 10^4 K, typical of ionized gas, for all the jet knots, wherever not available. The parameters n_0 and x_0 are combined to a single parameter corresponding the ionized number density ($n_0 \times x_0$) and typical values as obtained from observations are used in the models. The rest of the parameters are explored in a range typical to jets through a coarse grid, and the best fitting parameter set is chosen through the chi-square statistic. A finer grid around this set was explored to choose the best fitting model based on chi-square value. The set of values explored for each parameter in the coarse grid are listed in Table. 4.3. As the observational data is limited and we are interested in obtaining typical model parameters, the grid step-size can be considered as representative of the parameter uncertainties. The observational data for the selected knots and their corresponding best fit models are shown in Fig. 4.2 and each case is discussed below.

Table 4.3: Range of parameters explored in the grid of models.

Parameters	Range Explored and Grid spacing
Number density at jet base (n_0 [cm^{-3}])	100 to 10^6 by a factor of 10
Power-law index of radial number density variation (q_n)	-3 to -1 in steps of 0.5
Power-law index of radial ionization fraction variation (q_x)	-5 to 0 in steps of 0.1
Power-law index of lateral ionization fraction variation (q'_x)	-5 to 0 in steps of 0.1
Angular thickness of shocked region ($\delta\theta$ [°])	0.01 to 0.5 in steps of 0.01
Power-law index of non-thermal electron population (p)	1.7 to 2.6 in steps of 0.05
Fraction of relativistic electrons (η_e^{rel})	10^{-7} to 10^{-4} by a factor of 10

4.1.1 HH80-81 Jet

The HH80-81 protostellar jet is the largest known and most luminous HH system in the Galaxy. It is powered by the massive protostar GGD 27-MM1 (Fernández-López et al., 2011; Girart et al., 2017) which is located at a distance of 1.4 kpc (Añez-López et al., 2020). The HH80-81 jet is highly collimated with an approximate size of 18.7 pc (Masqué et al., 2012; Vig et al., 2018). The inclination angle of the jet with respect to the observer's direction was observed to be 34° (Heathcote et al., 1998). The jet consists of numerous knots of which the most prominent ones include HH80, HH81 towards the south and HH80N in the north (Rodríguez & Reipurth, 1989; Girart et al., 2001). Radio and optical measurements show velocities of $600 - 1000$ km/s for these knots (Marti et al., 1995; Heathcote et al., 1998). The radio continuum image of the HH80-81 jet at 610 MHz, originally published by Vig et al. (2018), is presented in Fig. 4.1. Here, have only show the region of interest for our investigation, comprising of the central jet along with the HH80 and HH81 knots, which are marked with cyan crosses and labeled accordingly in the figure.

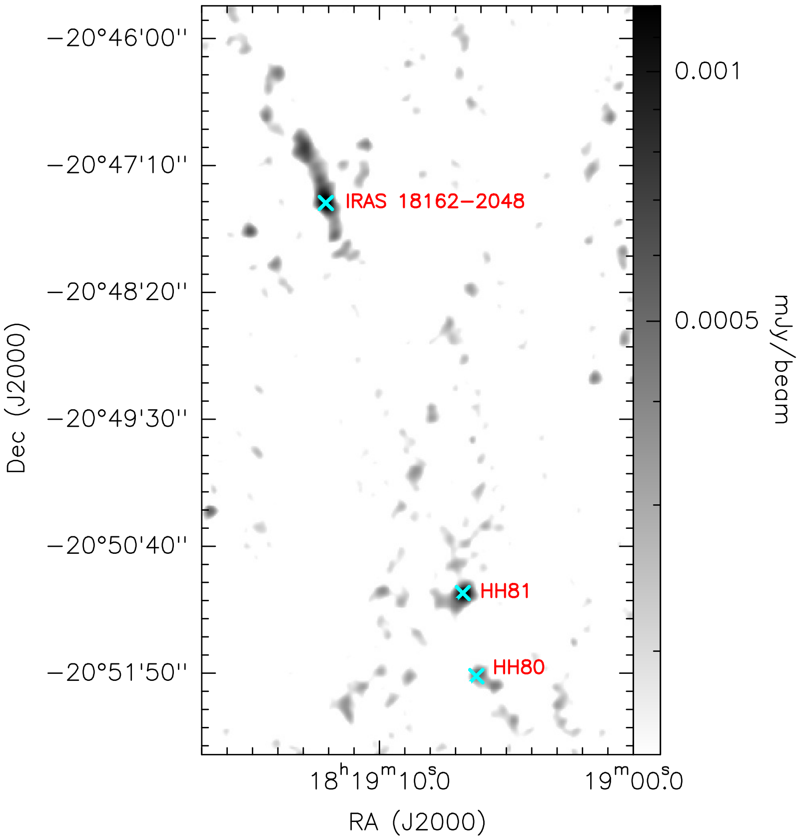

Figure 4.1: 610 MHz radio continuum image of IRAS 18162-2048 region showing the HH80-81 jet, adopted from Vig et al. (2018). The central region of the jet (IRAS 18162-2048) and the knots HH80 and HH81, which are investigated in this study, are marked in cyan crosses.

In the immediate vicinity of the exciting source, thermal emission is observed and synchrotron emission has been confirmed farther out, up to a distance of ~ 0.5 pc through the detection of linearly polarized emission (Carrasco-González et al., 2010).

The outer lobes along the jet have also been observed to show non-thermal nature. Non-thermal emission at lower frequencies of 325, 610 and 1300 MHz was detected by Vig et al. (2018), being the first case of detection of non-thermal emission from this jet at such low frequencies. In addition, variability of non-thermal emission was also demonstrated by the authors. The measured spectral indices of most of the knots are as steep as ~ -0.7. Both polarization observations (Carrasco-González et al., 2010) and non-thermal spectral indices (Vig et al., 2018) have provided estimates of the strength of magnetic field to be $\sim 200\ \mu$G.

As a case study, we choose to investigate three prominent lobes of this jet system: the central region IRAS 18162-2048, as well as the knots HH80 and HH81 using the radio measurements, where flux densities have been measured at similar epochs. These sources are labeled by their respective names in Fig. 4.1.

4.1.1.1 IRAS 18162-2048

This is the central region of the protostellar jet, and in radio wavelengths, the spectrum could include thermal free-free emission from the HII region ionized by stellar UV photons emitted by the YSO. Recently, it has been demonstrated that the HII region is likely to be in an early stage (Añez-López et al., 2020). We therefore proceed with the assumption that the free-free contribution to the spectrum of this source is solely due to the jet. Carrasco-González et al. (2012) conducted high resolution observation of the region at a wavelength of 1.3 cm. We assume that the resolution of this observation ($0.1''$) corresponds to the projected distance of the base of the jet from the central source. The major axis of the central jet is $0.23''$, which we assume as the size (length) of the knot. It is possible to estimate the opening angle of the knot from its angular size (width) and radial distance using the formula, $\theta_0 = 2\tan^{-1}(\frac{\theta_{min}}{2r_0})$ radians $= 38.5°$, for θ_{min} = $0.07''$. Here, θ_{min} represents the minor axis of the projected jet (perpendicular to the jet axis) as obtained from observations. We take this to be the width of the knot. Millimetre and sub-mm observations towards the central region of the jet have shown that the number density observed here is approximately in the range $10^4 - 10^5$ cm^{-3} (Hunter et al., 2000; Qiu et al., 2019; Cheng et al., 2019).

Multiple epochs of observational data were available for this source. Of these, we have chosen only two epochs (2009 and 2016) of data for fitting the model. As these two datasets showed a variability in flux densities, the fitting was carried out

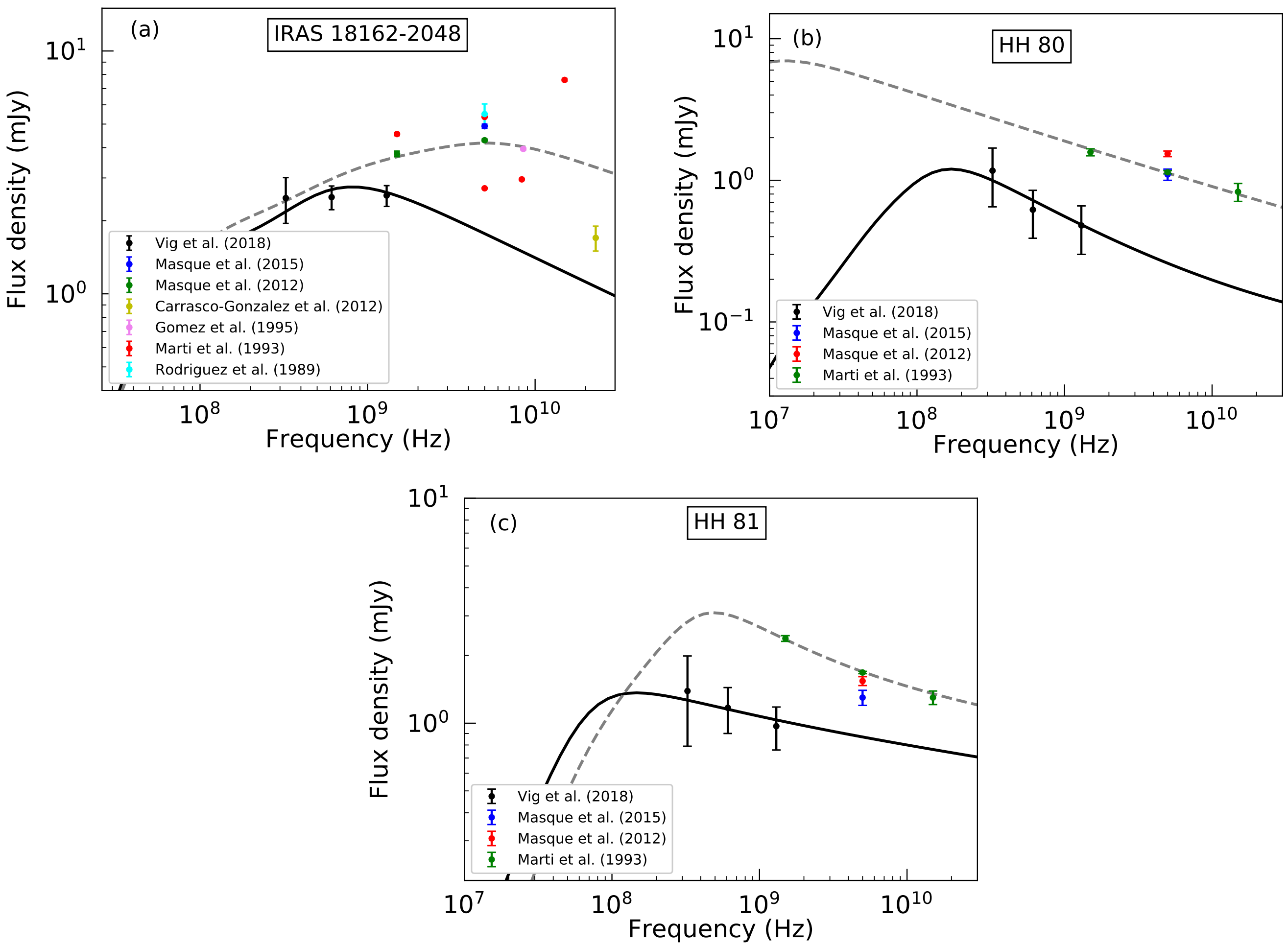

Figure 4.2: Comparison of best fit-model spectra with observational data for (a) IRAS 18162-2048, (b) HH80, and (c) HH81. The data points shown in black and green are used for fitting and the remaining data are plotted only for representation. The solid black curves in (a), (b) and (c) represent models 18162/2016, HH80/2016 and HH81/2016, respectively. The dashed gray curves in (a), (b) and (c) represent models 18162/2009, HH80/1989 and HH81/1989, respectively.

separately for each epoch. The data from other epochs were not considered due to the following: (i) unavailability of multifrequency data which are coeval (ii) lack of similar uv coverage as the data in other epochs (iii) large variations in flux densities between the multifrequency data corresponding to the same epoch.

We first model the observations for data from the most recent epoch (2016) at low frequencies from Vig et al. (2018). The best-fit model, designated as 18162/2016, is shown in Fig. 4.2 (a) as the solid black curve, along with the all the observational data available for this source. The datapoints used for the fitting are shown in

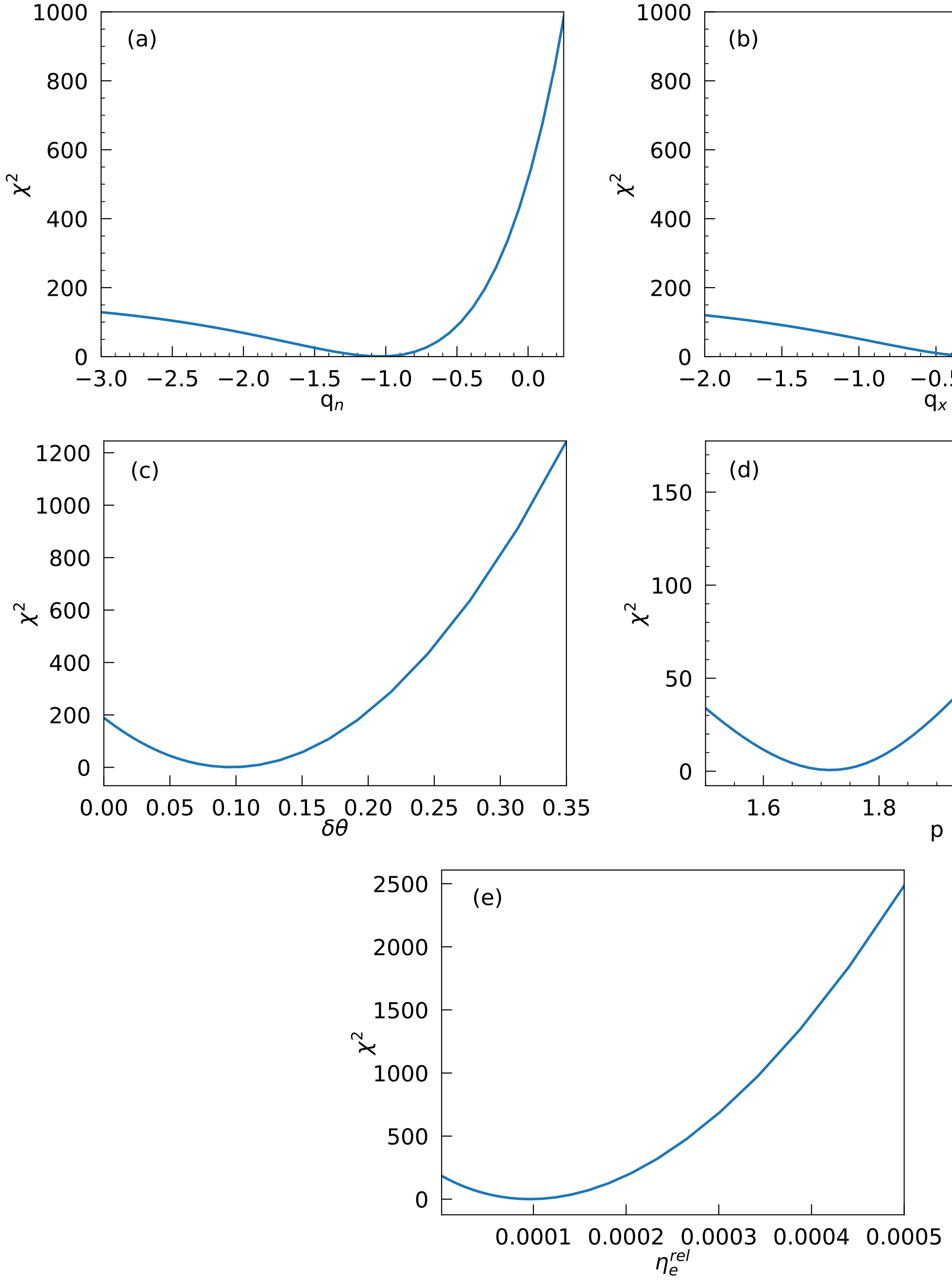

Figure 4.3: χ^2 value plots of the model 18162/2016 for parameters (a) q$_n$, (b) q$_x$, (c) $\delta\theta$, (d) p, and (e) η_e^{rel}, calculated by varying each parameter while the other best-fitting parameters are held constant.

black and the remaining data are shown only for representation. This model reproduces the flat spectral index observed at low radio frequencies, which is explicable by a combination of thermal and non-thermal emission. The spectrum peaks at a frequency of 762 MHz with a flux density of 2.75 mJy. The spectral index of the model between $0.3 - 1.3$ GHz is $+0.13$. In order to demonstrate the fidelity of the determination method of the best-fitting parameters, we display the χ^2 values of the parameter space that we have explored in the fitting procedure in Fig. 4.3. For this, we have varied each parameter while keeping the other parameters fixed to their best-fit values. The parameters under consideration for this knot include q$_n$, q$_x$, $\delta\theta$, p and η_e^{rel}.

We also model the higher frequency VLA data corresponding to the observational epoch of 2009 (Masqué et al., 2012). The best-fit model, designated as 18162/2009, is shown in Fig. 4.2 (a) as dashed grey curve, along with the observational data. The datapoints used for the fitting are shown in green. For this model, we have assumed the same thickness of shocked shell ($\delta\theta = 0.1^\circ$) as obtained for the low frequency case. This spectrum peaks at a frequency of 5.3 GHz with a flux density of 4.18 mJy. The spectral index of the model calculated between $1.5 - 5.0$ GHz is $+0.11$.

The best-fit parameters for the models 18162/2016 and 18162/2009 are listed in Table. 4.4. It can be seen that the change in the values of best-fit parameters between the two models is minor. The best fit values for $\delta\theta$, p and η_e^{rel} are same, whereas, q_n varies in the range -1 to -2 and q_x varies from -0.2 to -0.5 between the two models. This suggests a minor change in the density and ionization fraction structure. The best fit value of $\delta\theta$ shows that the shocked region comprises 0.8$\%$ of the jet opening angle.

4.1.1.2 HH80

The HH80 knot is located at a projected distance of $4.4'$ from the central source. High angular resolution observation by Heathcote et al. (1998) has identified a large bright knot HH80A in this region with a projected linear size to be 1.5×10^{17} cm (0.05 pc). We take this to be approximately the size of the whole HH80 region that we are considering here. For the knot, we calculate an opening angle of 2.4° using the opening angle of the central knot IRAS 18162-2048. The electron density in HH80 region is determined to be 200 cm^{-3} based on the [SII] line ratios (Heathcote et al., 1998). Since there are multiple epochs of observations at different frequencies and the jet is variable, we estimate the parameters for models corresponding to two observational epochs separated by nearly three decades: 2016 (Vig et al., 2018) and 1989 (Marti et al., 1993).

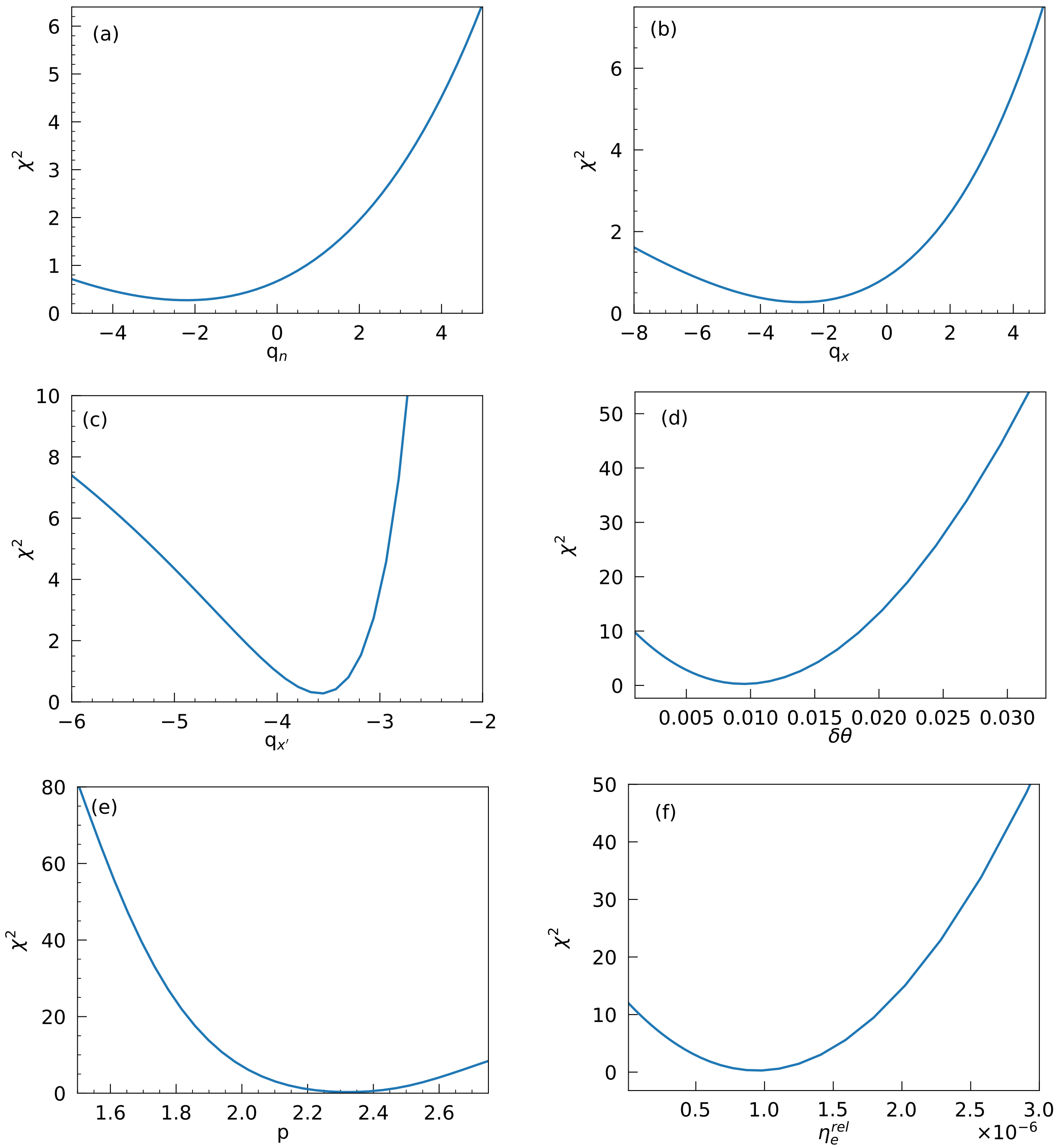

Figure 4.4: χ^2 value plots of the model HH80/2016 for parameters (a) q$_n$, (b) q$_x$, (c) q$'_x$, (d) $\delta\theta$, (e) p, and (f) η_e^{rel}, calculated by varying each parameter while the other best-fitting parameters are held constant.

Similar to the central region of the jet, multiple epochs of observational data were available for this knot as well, but we have chosen to fit models separately to only two epochs (1989 and 2016) of data. The data from other epochs were not considered

Table 4.4: Best fit model parameters of the observed jets.

Model	$\epsilon^{a\,*}$	$n_0 x_0^{b\,\dagger}$	q_n^c	q_x^d	$q_x'^{e}$	$\delta\theta^f$	p^g	$\eta_e^{rel\;h}$	$\chi^{2\;i}$	References‡
			(cm^{-3})				(°)			
18162/2016	2/3	4.5×10^4	-1.0	-0.2	0.0*	0.10	1.7	1×10^{-4}	0.87	1
18162/2009	2/3	3×10^5	-2.0	-0.5	0.0*	0.10*	1.7	1×10^{-4}	0.60	2
HH80/2016	2/3	200	-2.0	-2.5	-3.5	0.01	2.3	1×10^{-6}	0.30	1
HH80/1989	2/3	200	-3.0	-0.2	-3.0	0.01*	1.7	1×10^{-6}	1.07	3
HH81/2016	2/3	10^3	-3.0	-5.0	-4.5	0.01	2.2	1×10^{-7}	0.14	1
HH81/1989	2/3	10^3	-2.0	-0.2	-4.0	0.01*	2.4	1×10^{-6}	0.96	3
G114.0835+02.8568-B/2015	3/4	10^3	-1.5	-5.0	0.0*	0.50	1.8	1×10^{-6}	0.01	4
DG-Tau/2012-2013	3/4	500	-1.5	-1.0	-0.5	0.06	2.25	1×10^{-4}	1.31	5

[†] (1) Vig et al. (2018) (2) Masqué et al. (2012) (3) Marti et al. (1993) (4) Obonyo et al. (2019) (5) Feeney-Johansson et al. (2019)

[a] Power-law index of radial variation in jet width

[b] Ionized number density of the jet at r_0

[c] Power-law index of radial variation in jet number density

[d] Power-law index of radial variation in ionization fraction

[e] Power-law index of lateral variation in ionization fraction

[f] The thickness of the outer shocked region in degrees

[g] Power-law index of non-thermal electron distribution

[h] Fraction of relativistic electrons in the shocked region

[i] Chi-square value of the best fit model

[*] assumed parameter

for reasons similar to the case of IRAS 18162-2048 region.

The best-fit model for the low frequency observational data of Vig et al. (2018) designated as HH80/2016, is shown in Fig. 4.2 (b) as the solid black curve, along with the data. The datapoints used for the fitting are shown in black. The model spectrum peaks at a frequency of 171 MHz with a flux density of 1.20 mJy. The spectral index of the model between $0.3 - 1.3$ GHz is -0.52. The best-fit model provides a reasonably good fit to the observational data. The χ^2 plots for the model parameters q$_n$, q$_x$, q$'_x$, $\delta\theta$, p and η_e^{rel} are shown in Fig. 4.4.

The best-fit model for the high frequency observational data of Marti et al. (1993) designated as HH80/1989, is shown in Fig. 4.2 (b) as the dashed grey curve, along with the data. The datapoints used for the fitting are shown in green. For this epoch, we have assumed the same thickness of shocked shell ($\delta\theta = 0.01°$) as obtained for the low frequency case. The model spectrum peaks at a frequency of 13 MHz with a flux density of 6.97 mJy. The spectral index of the model between $1.5 - 15.0$ GHz is -0.32. The observing frequencies are different in the two epochs leading to different spectral indices for the two models.

The flux densities measured across three decades apart show that the emission from this knot displays variability. We find a difference of $0.5 - 1.8$ mJy in flux densities between 300 MHz to 30 GHz for the models HH80/2016 and HH80/1989. Therefore we have been able to reproduce the variability in observations using models that have a minor difference in jet parameters. The best-fit parameters for the models are listed in Table. 4.4. For the two models, we have used the same electron number densities for the fitting procedure and obtained the best-fit values for the parameters to be similar, except for q_x and p. These two parameters vary significantly between the two models, and this accounted for the flux density variation between the two epochs. The best fit value of $\delta\theta$ shows that the shocked region comprises 0.5% of the jet opening angle.

4.1.1.3 HH81

The HH81 knot is located at a projected distance of $3.7'$ from the central protostar. The projected size of the bright HH81 knot is taken as 0.7×10^{17} cm (Heathcote et al., 1998), with an opening angle of $2.5°$. Similar to HH80, we find best-fit models for HH81 corresponding to two epochs (1989 and 2016) of observations to account for variability. The electron density in HH81 knot is assumed to be 1000 cm^{-3} which is similar to the densities obtained from the [SII] line ratios observed towards this region (Heathcote et al., 1998).

For this knot as well, although multiple epochs of observational data were available, we have chosen to fit models separately to only two epochs of data. The data from other epochs were not considered for reasons similar to the previous cases.

The best-fit model for the low frequency observational data of Vig et al. (2018) designated as HH81/2016, is shown in Fig. 4.2 (c) as the solid black curve, along with the data. The datapoints used for the fitting are shown in black. The model spectrum peaks at a frequency of 147 MHz with a flux density of 1.36 mJy. The spectral index of the model between $0.3 - 1.3$ GHz is -0.15. The χ^2 plots for the model parameters q$_n$, q$_x$, q$'_x$, $\delta\theta$, p and η_e^{rel} are shown in Fig. 4.5.

The best-fit model for the high frequency observational data of Marti et al. (1993) designated as HH81/1989, is shown in Fig. 4.2 (c) as the dashed grey curve, along with the data. The datapoints used for the fitting is shown in green. For this epoch, we have assumed the same thickness of shocked shell ($\delta\theta = 0.01°$) as obtained for

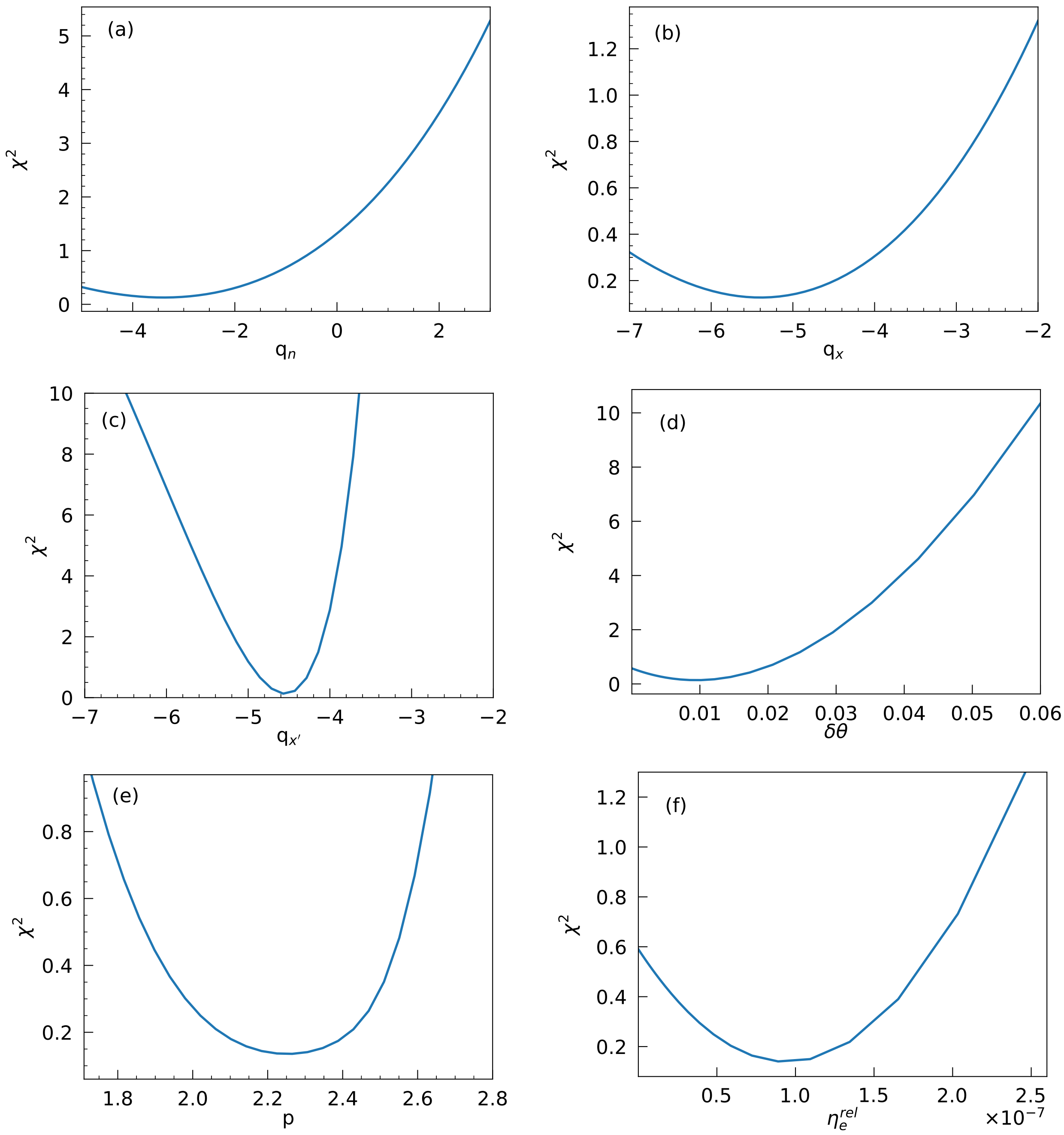

Figure 4.5: χ^2 value plots of the model HH81/2016 for parameters (a) q$_n$, (b) q$_x$, (c) q$'_x$, (d) $\delta\theta$, (e) p, and (f) η_e^{rel}, calculated by varying each parameter while the other best-fitting parameters are held constant.

the low frequency case. The model spectrum peaks at a frequency of 486 MHz with a flux density of 3.10 mJy. The spectral index of the model between $1.5 - 15.0$ GHz is -0.24.

Table 4.5: Spectral features of the best-fit models of the observed jets.

Source	Peak Flux (mJy)	Peak Frequency (MHz)	Spectral index*
IRAS 18162-2048[1]	2.75	762	+0.13
IRAS 18162-2048[2]	4.18	5311	+0.11
HH80[1]	1.20	171	-0.52
HH80[3]	6.97	13	-0.32
HH81[1]	1.36	147	-0.15
HH81[3]	3.10	486	-0.24
G114.0835+02.8568-B/2015[4]	0.52	94	-0.39
DG-Tau/2012-2013[5]	1.24	486	-0.60

† (1) Vig et al. (2018) (2) Masqué et al. (2012) (3) Marti et al. (1993) (4) Obonyo et al. (2019) (5) Feeney-Johansson et al. (2019)

* Calculated in the frequency range of observations.

Similar to the case of HH80 knot, the HH81 knot also displays variability as evident from the flux densities measured across three decades apart. We find a difference of $0.5 - 1.9$ mJy in flux densities between 300 MHz to 30 GHz for the models HH81/2016 and HH81/1989. Using models with a minor difference in the jet parameters, we have been able to replicate the variability for this knot as well. The best-fit parameters for the models are listed in Table. 4.4. For the two models, we have used the same electron number densities for the fitting procedure and obtained the best-fit values for the parameters to be similar, except for q_x which varies in the range -0.2 to -5. This is accounted to the flux density variation between the two epochs. The best fit value of $\delta\theta$ shows that the shocked region comprises 0.5% of the jet opening angle.

4.1.2 G114.0835+02.8568

This jet is taken from a sample of Massive Young Stellar Objects (MYSOs) investigated by Obonyo et al. (2019). The MYSO G114.0835+02.8568 is located at a distance of 4.2 kpc and the lobe G114.0835+02.8568-B towards this MYSO has multiple measurements of flux densities and exhibits signatures of non-thermal emission. The L-band map of the lobe, overlaid with L- and C-band contours is shown in Fig. 4.6 (a). The measured spectral index of lobe B is -0.39. The lobe is located at a (projected) distance of $1.64''$ away from the central source which is used to estimate the radial distance r_0 from the source. The major axis of the lobe, $\theta_{maj} = 2.5''$ which we assume as the projected length of the lobe. For an observed θ_{min} of $1.2''$, we estimate the opening angle θ_0 of the knot to be $23.4°$.

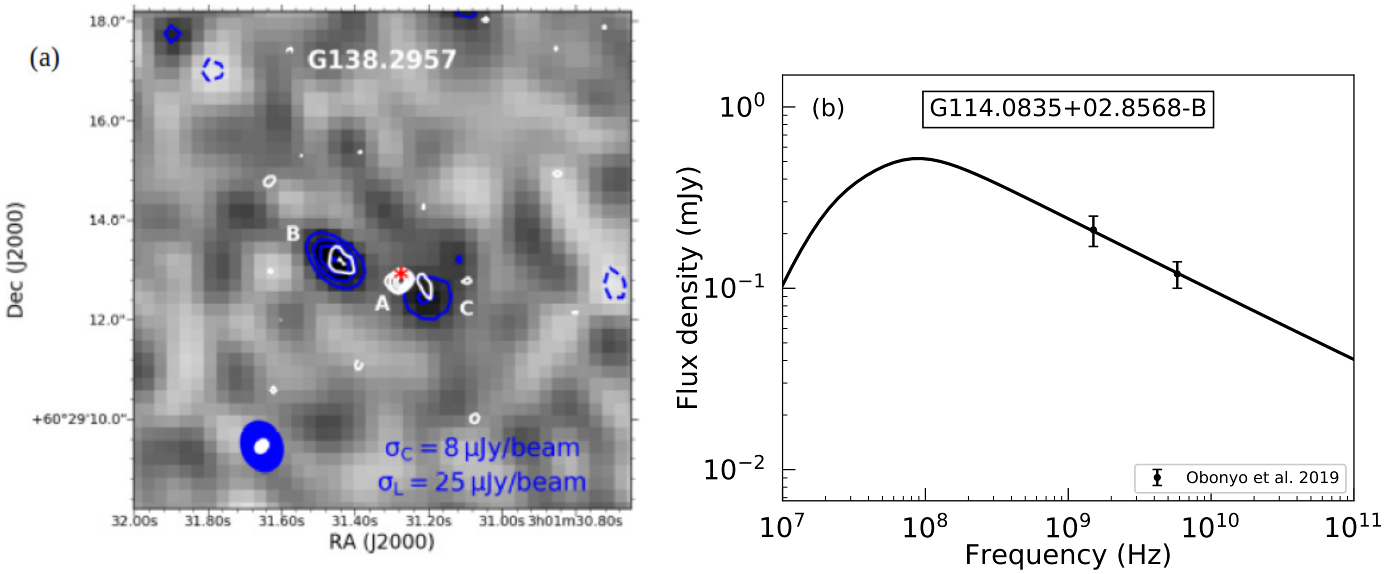

Figure 4.6: (a) L-band map of the lobe G114.0835+02.8568-B overlaid with L- and C-band map contours as adopted from Obonyo et al. (2019). The asterisk marked in red indicates the Q-band location of the core of MYSO. (b) Comparison of best fit-model spectra with observational data for G114.0835+02.8568-B. The data points shown in black are used for fitting and the solid black curve represent the best-fit model G114.0835+02.8568-B/2015.

We note that we have observational data at only two frequencies, as obtained from Obonyo et al. (2019) to constrain the model. Since there are many parameters in the model, we have assumed few parameters to be constant, these include $q'_x = 0$, $\epsilon = 3/4$ and those listed in Table. 4.2. The best-fit model, designated as G114.0835+02.8568-B/2015, is shown in Fig. 4.6 (b) plotted along with observational data. The best-fit variable parameters along with the chi-square value are listed in Table. 4.4. The best-fit spectrum peaks at a frequency of 94 MHz with a flux density of 0.52 mJy. The spectral index of the model between $1.5 - 6$ GHz is -0.39. The spectral index indicates the presence of a combination of thermal and non-thermal emission processes in the knot. The χ^2 plots for the model parameters q$_n$, q$_x$, q$'_x$, $\delta\theta$, p and η_e^{rel} are shown in Fig. 4.7.

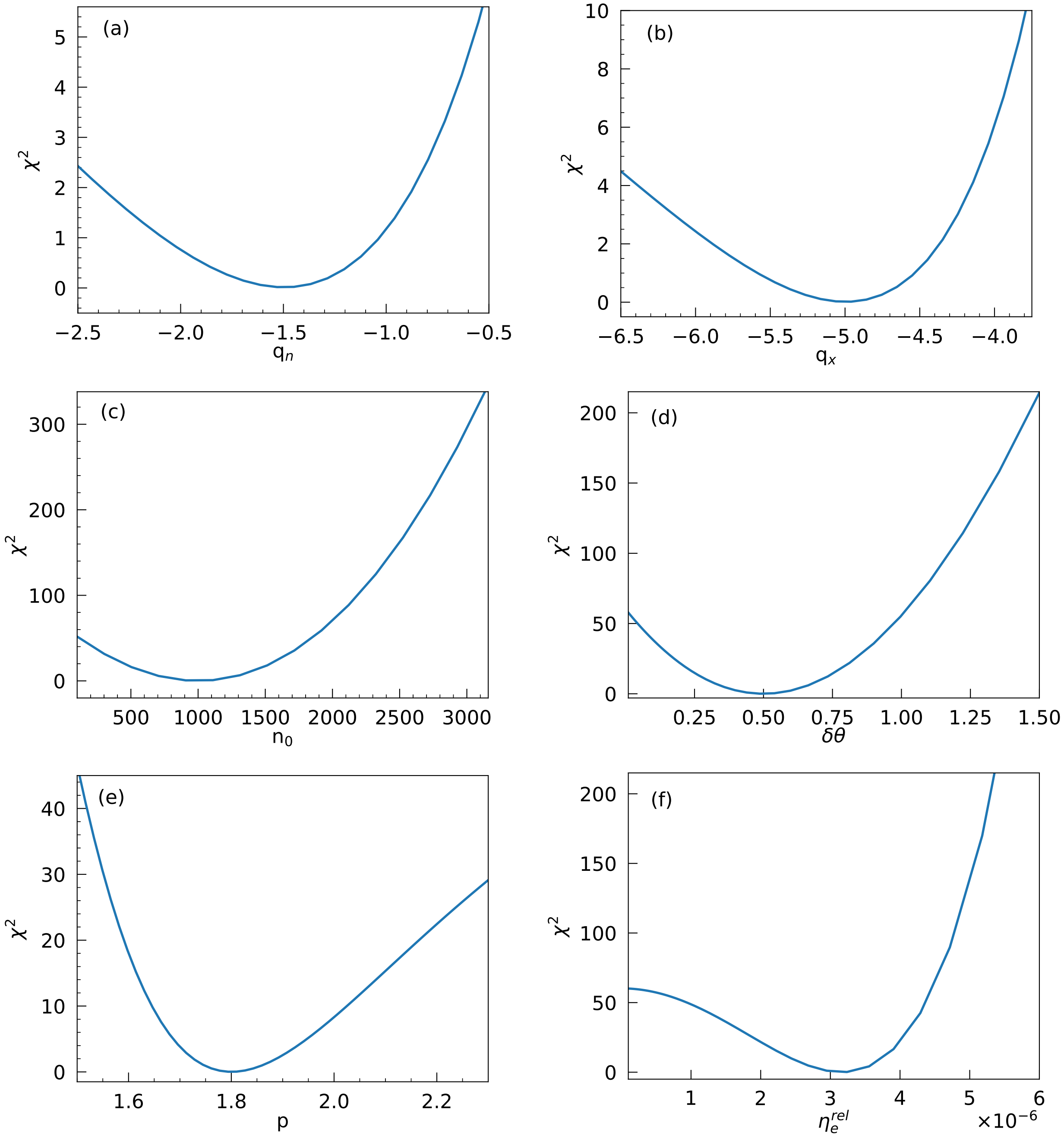

Figure 4.7: χ^2 value plots of the model G114.0835+02.8568-B/2015 for parameters (a) q$_n$, (b) q$_x$, (c) n_0, (d) $\delta\theta$, (e) p, and (f) η_e^{rel}, calculated by varying each parameter while the other best-fitting parameters are held constant.

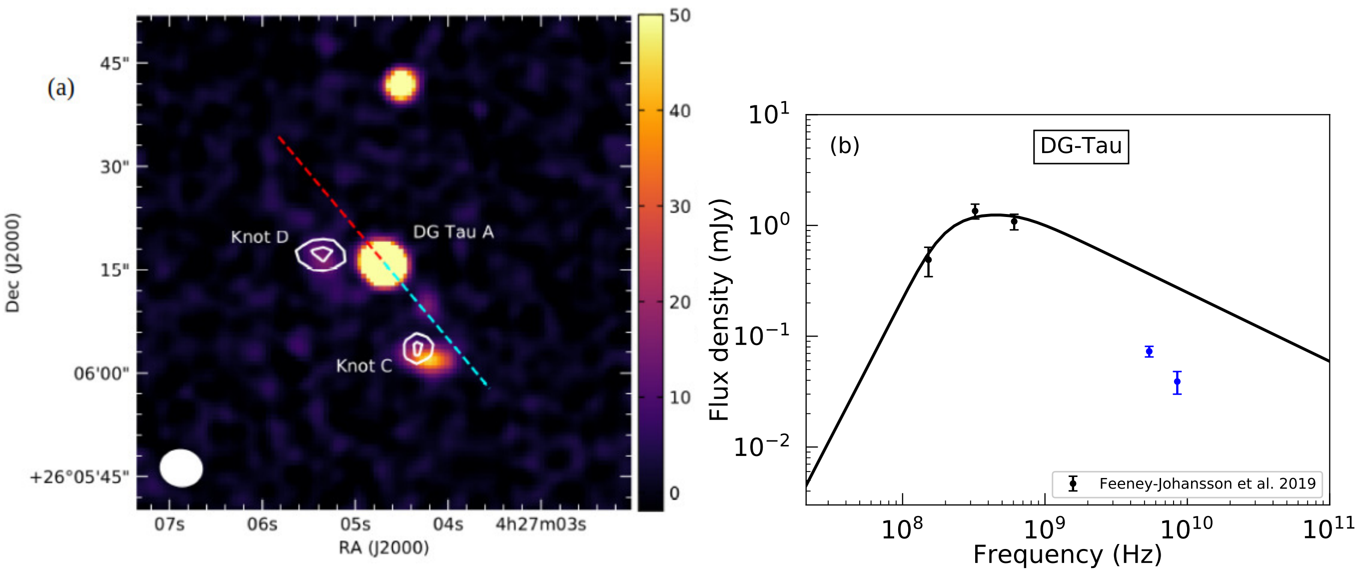

Figure 4.8: (a) Image of DG-Tau A jet showing the overlay of contour plot at 152 MHz on the color image at 6 GHz, as adopted from Feeney-Johansson et al. (2019), (b) Comparison of best fit-model spectra with observational data for DG-Tau A. The data points shown in black are used for fitting and the remaining data shown in blue, obtained from the same reference, are plotted only for representation. The solid black curve represent the best-fit model DG-Tau/2012-2013.

4.1.3 DG-Tau A

DG-Tau A is a classical T-Tauri star, located in the Taurus molecular cloud at a distance of 120.8 pc (Gaia Collaboration et al., 2016), with a bipolar jet lying at an inclination angle of $37.7°$ (Eislöffel & Mundt, 1998). Very low frequency observations (152 MHz) of this low mass YSO by Feeney-Johansson et al. (2019) resulted in the detection of synchrotron emission from knot C of the jet. The contour plot of DG-Tau A jet at 152 MHz overlaid on the color image at 6 GHz, as adopted from Feeney-Johansson et al. (2019) is shown in Fig. 4.8 (a), with knot C labeled in the figure. We attempt to reproduce the low frequency turnover observed in the spectrum of knot C from through our model. The angular separation of knot C from the YSO is $12.5''$, its size is assumed to be $5.3''$ (Purser et al., 2018) and opening angle estimated as $\theta_0 = 20.6°$.

A comparison of the spectrum generated by the best-fit model, designated as DG-Tau/2012-2013, with observational data is shown in Fig. 4.8 (b) and the best-fit parameters are listed in Table. 4.4. Our model spectrum shows that the contribution of

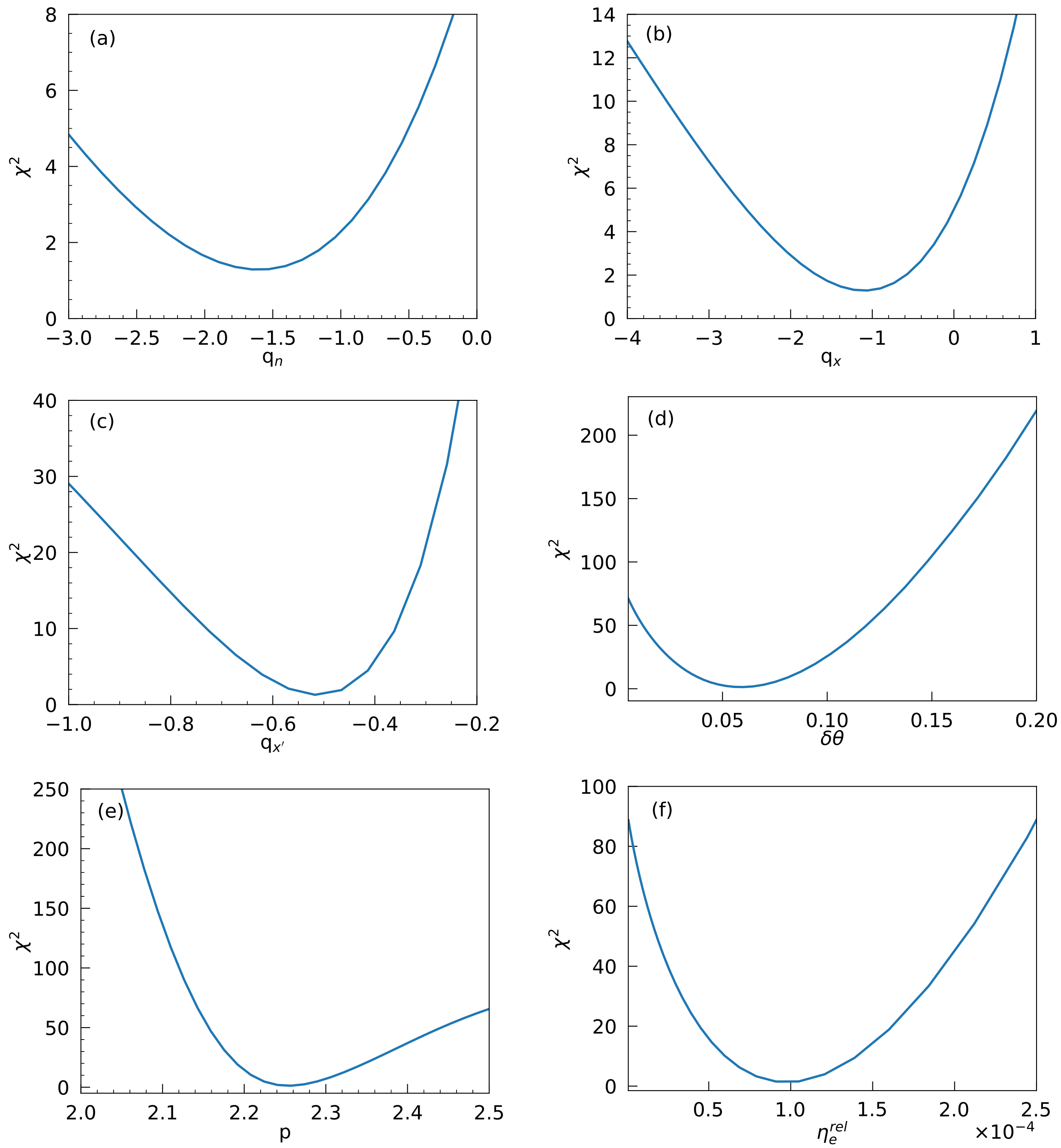

Figure 4.9: χ^2 value plots of the model DG-Tau/2012-2013 for parameters (a) q$_n$, (b) q$_x$, (c) q$'_x$, (d) $\delta\theta$, (e) p, and (f) η_e^{rel}, calculated by varying each parameter while the other best-fitting parameters are held constant.

synchrotron emission is larger than free-free emission. The spectrum peaks at a frequency of 486 MHz with a flux density of 1.24 mJy. For the optically thin domain of the spectrum, the spectral index of the total emission is -0.60 between $0.6-8.5$ GHz.

The emission at lower frequencies are well-reproduced by the model flux-densities, including the turn-over. However, for the data at higher frequencies (5 and 8.5 GHz), the model flux densities are higher than the observed data (see explanation in next paragraph). Therefore, while fitting the model, we have excluded the high frequency data, and the χ^2 values shown in the table are calculated by considering only the low frequency data. The χ^2 plots for each of the model parameters q_n, q_x, q'_x, $\delta\theta$, p and η_e^{rel} are shown in Fig. 4.9.

The spectral index of this source as estimated from the observational data (including the data shown in blue; Fig. 4.8 (b)) is steeper than what is explicable by synchrotron emission. The spectral index of -1.4 between 1 and 8 GHz is steep and is a factor of two higher than what has been observed from other protostellar jets. Feeney-Johansson et al. (2019) attribute this behavior to Razin effect which comes into play when the non-thermal emission is assumed to be surrounded by a thermal plasma. The turnover frequency for Razin effect is given by ν_R below which the flux density decreases exponentially with frequency. In order to account for this effect, a factor of $e^{-\nu_R/\nu}$ can be multiplied to the optically thin spectrum in Dougherty et al. (2003). However, it is difficult to incorporate the same in our model as the synchrotron emitting region also has thermal emission emanating from it. We have therefore not incorporated Razin effect in our model.

4.2 Implications of the best-fit parameter values

The physical interpretations of the best-fit values of various model parameters for the sources investigated here are discussed in this section. For all the sources, the best-fit values obtained for the power-law index of number density profiles range from $\mathrm{q}_n = -1$ to -3, with HH80 and HH81 knots having steeper profiles compared to other sources. Previous observational studies and models have predicted a density profile with q_n in the range -1 to -2 for the circumstellar material observed around YSOs (Hogerheijde et al., 1999; van der Tak et al., 1999). However, for HH80 and HH81 knots, a steeper profile for number density ($\mathrm{q}_n = -3$), is also reasonable due to the fact that these knots are located much farther away ($\sim 2-3$ pc; Marti et al., 1993) from the driving source, where the ambient density will be significantly lower than the immediate neighborhood of the central YSO. In addition, it was also observed that the corresponding knot in the northern lobe of the jet, which is at similar radial distances from the driving source, has moved out of the molecular cloud (Marti et al., 1993) into a region of lower density. Given this, we believe that the q$_n$ value obtained for these farther knots are reasonable, while for the rest of the knots the values are consistent with the previous predictions.

The jet material is primarily ionized in the radial direction due to internal shocks resulting from variations in the flow velocity and this is determined by the parameter q_x. The best-fit values of q_x for all the knots range from -0.2 to -5. Large values of q_x (~ -5), therefore imply that the degree of ionization is significantly lower at farther radial distances from the driving source, indicating a reduction in the strength of internal shocks which are capable of ionizing the jet material. This is seen in the case of G114.0835+02.8568-B, HH81 and HH81 knots. For the knots HH80 and HH81, the best-fit values of q_x show a significant variation between the model for two epochs, implying that it is an important parameter in deciding the nature of the spectrum.

The parameter q_x' indicates the degree of ionization resulting from shocks on the lateral edges of the jet where it impacts the ambient medium. For HH80-81 jet, this is seen to weaken with radial distance from the driving source as inferred from the large values of q_x' (-4.5 to -3) for HH80 and HH81 knots, compared to IRAS 18162-2048. For the majority of the other knots, we have assumed this parameter to be 0, in order to reduce the number of fitting parameters compared to the available data.

The most significant attribute of the radio spectra of HH80, HH81, G114.0835+02.8568-B and DG-Tau jet is that they are dominated by synchrotron emission. The model parameters that strongly determine the relative contribution of synchrotron emission in the overall radio spectrum are η_e^{rel} and p, which are representative of the efficiency of shock in generating a relativistic electron population and the density distribution of the non-thermal electron population in energy space, respectively. The best-fit values of η_e^{rel} for these jets, are in the range $10^{-7} - 10^{-4}$ which are comparable to the values obtained from the results of simulation studies in the context of diffusive shock acceleration (Berezhko & Ellison, 1999; Padovani et al., 2016). This provides sufficient evidence to reinforce the assertion that the shocks present in these knots are efficient in generating relativistic electron population. The best-fit values of p are in the range of $1.7 - 2.4$, which are typical of shocks that are capable of generating non-thermal electron population in YSO jets (Araudo et al., 2021). Given that this parameter p is the power-law index of the number density distribution of the relativistic electron population in energy space, $p \leq 2.4$ could imply that the majority of the particle kinetic energy is carried by those particles with energies significantly higher than the average.

G114.0835+02.8568-B, HH80 and HH81 knots further demonstrate that, despite having steeply decreasing power-law profiles for ionization fraction in the lateral direction ($q_{x'} = -3$ to -4.5) and a thin shocked region ($\frac{\delta\theta}{\theta} < 5\%$), the shock acceleration mechanism is highly efficient at generating non-thermal emission that dominates the total radio emission from these knots. This is evident from the best-fit values of the knot spectral indices which range from -0.15 to -0.52 (Table. 4.5). For the central knot of the HH80-81 jet, we also observe that although η_e^{rel} is much higher than HH80 and HH81 knots, the small fraction of shocked region with respect to the total opening angle ($\frac{\delta\theta}{\theta} \sim 0.8\%$) and the high number density (n_0) towards this region together results in higher contribution of thermal emission in the frequency window that was considered in this study.

4.3 Summary

To summarize, in this chapter, we have generated grids of models within a finite parameter space for three prominent protostellar jets which exhibit non-thermal emission in their radio spectra and estimated the best-fit model for their available observational data. The χ^2 values were estimated for each model within the grid and the best-fit model was obtained using χ^2 minimization. Through this, we have calculated the best-fit values for the model parameters q_x, q_x', p, η_e^{rel}, $\delta\theta$ and q_n for various protostellar jets. For the best-fit models, we obtained the thickness of the jet edges, non-thermal electron density distribution index and fraction of relativistic electrons that contribute to non-thermal emission in the range $0.01° - 0.5°$, $1.7 - 2.4$ and $10^{-7} - 10^{-4}$, respectively. For the best-fit parameter sets, the model spectral indices lie in the range of -0.60 to +0.11 within the observed frequency windows.

Chapter 5

Understanding of the massive protostellar jet HH80-81 in NIR shock tracers

In this chapter, our primary goal is to carry out a morphological characterization of the shocks associated with different knots of the HH80-81 jet and to estimate the physical properties of the jet by utilizing the molecular H_2 and atomic [Fe II] emission lines. In addition, here we also investigate the immediate neighborhood of the driving source of the jet in molecular H_2 line and broad-band emission in NIR and MIR.

5.1 HH80-81 protostellar jet

The HH80-81 jet is associated with IRAS 18162-2048 which is identified as a B-type protostar (Carrasco-González et al., 2012) located at a distance of 1.4 kpc (Añez-López et al., 2020). The protostar is associated with the IR reflection nebula known as GGD 27 (Yamashita et al., 1987), an ultra-compact HII region and numerous OH and H_2O masers (Rodriguez et al., 1980). Towards the neighborhood of the central protostar, 25 millimetre cores have been detected by Busquet et al. (2019) using the Atacama Large Millimetre Array (ALMA). Of these, MM1 and MM2 have been found to be the most massive and drivers of outflows in the region, with the HH80-81 jet being excited by MM1 (Busquet et al., 2019).

The HH80-81 jet is one of the largest known protostellar jets, which is also highly collimated extending up to 18.7 pc (Masqué et al., 2012). Proper motion studies of the jet in radio wavelengths have measured velocities as high as 1000 km s^{-1} (Marti et al., 1995). The bipolar jet consists of numerous knots and the projected direction of the jet lobes lie along the north-east and south-west of the protostar in the sky plane (Rodriguez et al., 1989b; Girart et al., 2001). The jet extends up to HH80 in the south-west, and up to HH80N in the north-east. The morphology and kinematics of the HH80-81 jet have been well studied in optical wavelengths by Heathcote et al. (1998). These studies show that the knots showcase high-excitation conditions due to the presence of strong shocks as seen in Hα and [SII] emission lines (which produce the HH objects) whose line-width are $\sim 600 - 700$ kms^{-1}. The HH80N on the other hand, is only detected in FIR and radio wavelengths due to the high extinction it suffers due to a dense cloud that this arm has encountered along its path. The jet is oriented such that the northern arm is blue-shifted and the southern arm is red-shifted.

UV radiation, generated by the dissociative head of the strong shocks, was observed to induce a photodissociation region in association with the outflow cavity walls (Molinari et al., 2001). Spitzer observations at 8μm have identified a bi-conical outflow cavity towards the inner radio jet (Qiu et al., 2008). Multiple molecular outflows were also detected towards this region indicating active star formation (Yamashita et al., 1989; Qiu & Zhang, 2009; Fernández-López et al., 2013; Qiu et al., 2019).

Radio polarization investigation towards this region have shown the presence of linearly polarized emission from knots located at $\sim$0.5 pc from the protostar, inferring that the high collimation of this jet is due to the presence of a helical magnetic field (Carrasco-González et al., 2010). These results have also confirmed the existence of synchrotron emission in protostellar jets, indicating the presence of relativistic particles at the lateral and terminal shocks of the jet. Motivated by this, a search for γ-ray emission from these relativistic particles have found a significant γ-ray excess towards this jet consistent with previous particle acceleration studies (Yan et al., 2022).

5.2 NIR imaging observations using UKIRT

We imaged the IRAS 18162-2048 region using the Wide-Field Camera (WFCAM; Casali et al., 2007) mounted on the 3.8 m United Kingdom Infrared Telescope (UKIRT).

The WFCAM has four 2048×2048 HgCdTe Hawaii-II arrays with an optical system that provides a pixel scale of 0.4″. This provides a total field of view of 13.5′×13.5′ per array and 0.21 deg^2 for all four arrays together. The target was located in the center of one of the four arrays and the data from only that array was used in the current study. The observations were performed by dithering the target to 9 positions on the array and a $2{\times}2$ micro-stepping was done. The resulting mosaics have an image scale of 0.2″/pix. Observations were carried out using the NIR broad-band J, H, K filters and the narrow-band H_2 and [Fe II] filters. The narrow-band H_2 filter is centered at $\lambda = 2.122$ μm and the [Fe II] line filter at $\lambda = 1.644$ μm with a full width at half maximum (FWHM) of 0.021 μm and 0.028 μm, respectively.

We have obtained imaging observations of H_2 in four epochs and those of [Fe II] in six epochs. The total integration time for J, H, K, H_2 and [Fe II] filters were 720 s, 360 s, 180 s, 1440 s and 1440 s, respectively, for each epoch of observation. The observations were conducted between 20200220 UT and 20210920 UT.

In addition to this, the L′ (3.678 μm) and M′ (4.686 μm) band imaging observations were carried out using the UKIRT 1-5 μm Imager Spectrometer (UIST; Ramsay Howat et al., 2004). UIST has a 1024 × 1024 InSb array. The observations were carried out using the 0.12″ pixel^{-1} camera. The object was dithered to four positions along the corners of a square of 40″ side. The total integration time for the L′ and M′ band observations were 160 s and 280 s, respectively.

5.2.1 Data Reduction and Continuum subtraction

The preliminary reduction including the creation of mosaics was carried out by the Cambridge Astronomical Survey Unit (CASU) and the details of the data reduction procedure followed by the pipeline are described in Quinn & Bridger (2004). For the narrow-band H_2 and [Fe II] filters, further reduction including continuum subtraction was carried out using the Starlink software (Currie et al., 2014). The procedure followed and Starlink tasks used for continuum subtraction are given below and the flowchart for the same is shown in Fig. 5.1.

(a) For each epoch, the H_2 and [Fe II] images were aligned with K and H-band images, respectively, using `WCSALIGN`.

(b) Due to variations in the seeing conditions between the narrow-band and broad-band observations, images with smaller point-spread function (PSF) were smoothed to match with the FWHM of the images with larger PSF using the task `GAUSMOOTH`.

(c) For the subtraction of continuum emission from the narrow-band emission, sufficient number of isolated bright point sources were selected and photometry was carried out on them using the task `AUTOPHOTOM`, in both the narrow-band and broad-band sky-subtracted images.

(d) The broad-band to narrow-band flux ratio was then computed.

(e) For each imaging observation in an epoch, the broad-band image was scaled using the average value of the ratio of these fluxes and subtracted from the narrow-band image to obtain the continuum-subtracted image for that epoch.

(f) The continuum-subtracted images of all the epochs/exposures were averaged to obtain the final image.

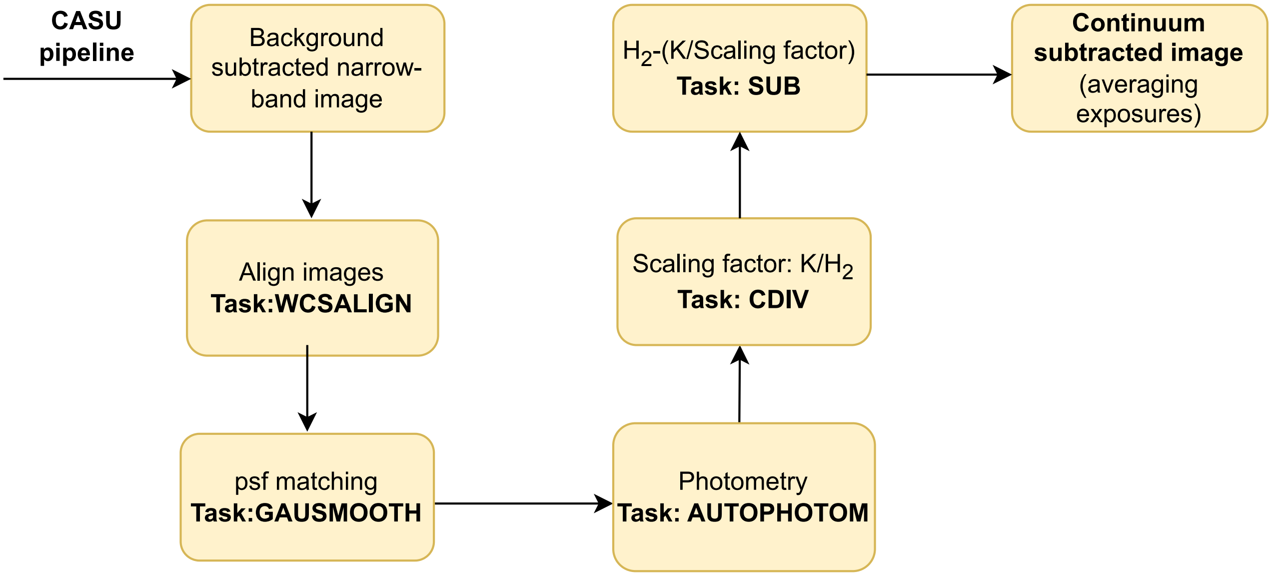

Figure 5.1: Schematic illustrating the sequence of steps for continuum subtraction of the NIR data.

In the case of L′ and M′ band observations, for each setting, a dark observation was done, which was followed by the science observations. The dark subtracted science frames were median combined to create sky flats. Frames in individual pairs were subtracted from each other and divided by the flats. This resulted in a positive and negative beam in the mutually subtracted, flat fielded image. The final mosaic was constructed by combining the positive and negative beams.

5.2.2 Flux calibration: Narrow-band filters

The flux calibration of the continuum-subtracted images was carried out using the H and K band flux densities of isolated point sources in the field. The sequence of steps followed for flux calibration are given below and the flowchart for the same is shown in Fig. 5.2.

(a) We first interpolated the broad-band H and K filter flux densities of a few isolated point sources to the central wavelength of the narrow-band filters.

(b) These flux densities were multiplied by the FWHM of the narrow-band filters to obtain the total fluxes.

(c) We then derived the photometry of the point sources on the normalized narrow-band images to obtain the counts in ADU.

(d) This was used to estimate the flux/ADU and this is used to scale the counts in ADU obtained from the continuum-subtracted narrow-band images to estimate the fluxes. The fluxes are not corrected for extinction as the extinction value towards each knot is not known.

5.3 Archival datasets

In addition to the NIR observations, we have used archival data in the MIR and optical to investigate the HH80-81 jet and its environment. The emission from warm dust associated with this region was studied using the MIR Spitzer Space Telescope and the MSX data. The optical emission towards the knots of the jet was studied using the HST data. The photometry data of two YSOs in the neighborhood of the jet was obtained from the catalog of Yale Southern Observatory.

5.3.0.1 Spitzer Space Telescope

The warm dust emission towards the driving source of HH80-81 jet was examined at 8μm using the MIR map from the Spitzer Space Telescope. The primary mirror size of the telescope is 85 cm. The Infrared Array Camera (IRAC) is one of the three scientific instruments aboard the telescope, with a focal plane arrangement and a four-channel camera designed to acquire broadband images at 3.6, 4.5, 5.8 and 8

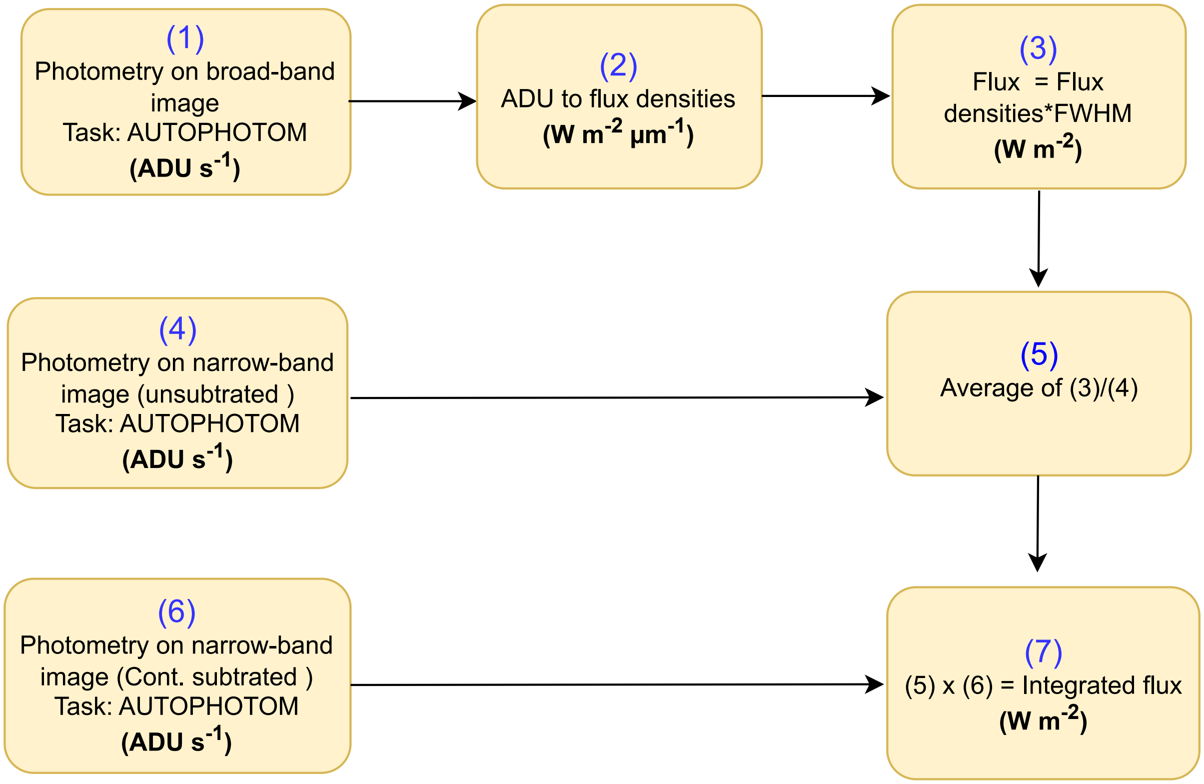

Figure 5.2: Schematic illustrating the sequence of steps for flux calibration of the narrow-band line images.

μm simultaneously. All four detector arrays in the IRAC camera have a size of 256 × 256 pixels, and a pixel size of 1.2″. For 3.6, 4.5, 5.8 and 8 μm bands, the resolutions achieved are 1.7″, 1.7″, 1.9″, and 2″, respectively (Fazio et al., 2004). In this work, we have used the Level-2 Post Basic Calibrated data (PBCD) image at 8μm generated by the Galactic Legacy Infrared Mid-Plane Survey Extraordinaire 3D (GLIMPSE 3D; Benjamin et al., 2006). The image was extracted from the NASA/IPAC Infrared Science Archive, which is operated by the Jet Propulsion Laboratory, California Institute of Technology, under contract with the National Aeronautics and Space Administration. We use this map to correlate the MIR diffuse emission with the observed NIR features towards the driving source of the HH80-81 and its immediate environment.

5.3.0.2 HST

The optical emission from the HH80-81 jet in the filters Hα + [NII], [SII] and [OIII] has been imaged using the Wide Field and Planetary Camera 2 (WFPC2) on-board the HST. WFPC2 is located at the center of the telescope's focal plane and operates across a wavelength range of $1150 - 11000$ Å. For this study, we have used the high angular resolution images which have been published by Heathcote et al. (1998). We have extracted these images from the Hubble Legacy Archive. We have employed these images to compare the morphologies of HH80 and HH81 with those from our NIR observations, in order to characterize the nature of shocks.

5.3.0.3 MSX Survey

The MSX Galactic Plane Survey has mapped the Galactic plane covering $|\mathrm{b}| < 5°$ and $0 < |\,\mathrm{l}\,| < 360$. This operates in four wavelength bands: 8.3, 12.1, 14.7 and 21.3 μm and has a resolution of $\sim$18.3$''$ (Price et al., 2001). We have extracted the catalog data from MSX archive provided by NASA/IPAC Infrared Science Archive service.

5.3.0.4 Yale Southern Observatory

The catalog data for two YSOs in the neighborhood of HH80-81 jet, were extracted from the Yale/San Juan Southern Proper Motion Catalog (SPM4). This catalog is based on photographic and charge-coupled device observations obtained with the Yale Southern Observatory's double-astrograph at Cesco Observatory in El Leoncio, Argentina. The SPM4 database includes absolute proper motions, celestial coordinates, and B, V photometry for more than 10^3 million stars and galaxies located between the celestial south pole and declination of -20°. This catalog is approximately complete up to V = 17.5.

5.4 HH80-81 main jet: NIR emission features

The full length of HH80-81 jet as observed in H_2 emission is shown in the central panel of Fig. 5.3. The surrounding panels display the emission towards the jet in H_2, [Fe II] and the optical Hα + [NII] filters in red, green and blue, respectively, revealing the morphologies of individual knots. The details of the sizes and locations of the sub-images are listed in Table. 5.1. We observe that in the $12'$ image obtained by us, the jet displays a chain of knots extending up to 1.9 pc in the north-east and 2 pc in the south-west directions, as projected on the sky plane. Considering the inclination angle of the jet to be $56°$ (Heathcote et al., 1998) from the sky plane, the

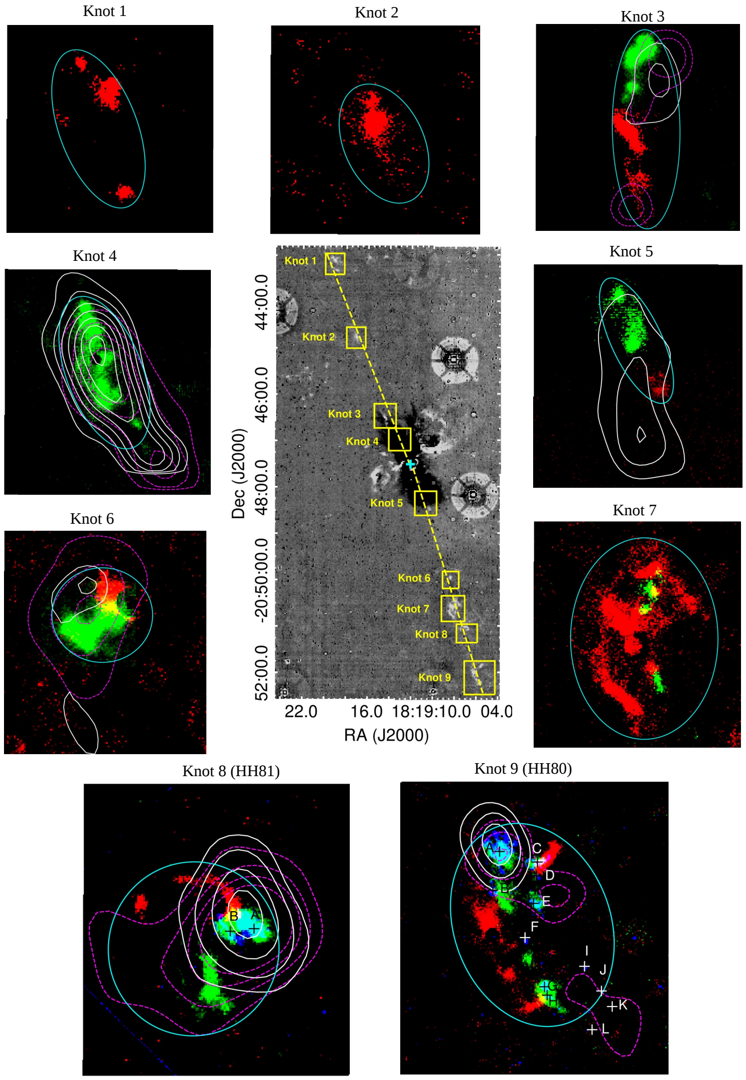

Figure 5.3: [Central panel]: Continuum subtracted H_2 image of the full length of HH80-81 jet, and [surrounding panels]: color composite image of the individual knots of the jet in the NIR H_2 emission (red), [Fe II] emission (green) and HST optical Hα+[NII] (blue). The HST observations were carried out only towards the knots HH81 and HH80. Various knots are enclosed in yellow boxes in the central image to show their locations. The details of the locations and sizes of the sub-images are listed in Table. 5.1. The cyan ellipses show the apertures used for the calculation of fluxes of each of the knots. The white contours in the enlarged images of the knots represent VLA 20 cm data obtained from Marti et al. (1993). The magenta contours (dashed lines) show the GMRT 610 MHz emission from (Vig et al., 2018). The cyan cross between knots 4 and 5 in the central figure indicates the driving source of the jet (MM1). Sub-knots towards HH80 and HH81 are shown as crosses and labeled according to Heathcote et al. (1998).

true extent of the bipolar jet as imaged in NIR is $\sim$ 7 pc. It is possible that there are additional knots extending farther away from this towards HH80N. We identify a total of nine new knots along the HH80-81 main jet direction and multiple arcs in H_2 emission. Four knots are in the northern arm and five are in the southern arm of the jet. We assign numbers 1-9 to the knots as seen in our NIR images from north to south. The Knots 8 and 9 correspond to HH81 and HH80, respectively. We describe a few morphological features of the knots below:

(a) Knots 1 and 2 exhibit only H_2 emission, Knot 4 is revealed in only [Fe II] emission, while the remaining knots exhibit emission in both [Fe II] and H_2 transitions.

(b) Knots 1-6 are elongated along the direction of the jet. Knots 7-9 appear broken and have complex morphologies.

(c) In none of the knots, the regions corresponding to [Fe II] and H_2 emission completely overlap. In Knots 3 and 6, the [Fe II] emission clearly lies ahead of the H_2 emission along the outward jet direction; whereas, in the case of Knot 5, the reverse is seen.

(d) The NIR line emission for Knots 8 and 9 do not coincide with optical line emission. For other knots, the optical data is not available due to the high visual extinction.

Table 5.1: Details of the coordinates of the center as well as the sizes of sub-images shown in Fig. 5.3.

Source name	RA(J2000) (α)	Dec(J2000) (δ)	δRA ($''$)	δDec ($''$)
Knot 1	18:19:19.10	-20:43:11.4	27.2	24.4
Knot 2	18:19:17.13	-20:44:47.2	27.2	24.4
Knot 3	18:19:14.37	-20:46:30.0	32.9	31.2
Knot 4	18:19:12.97	-20:47:02.4	32.4	39.5
Knot 5	18:19:10.62	-20:48:27.4	32.7	35.4
Knot 6	18:19:08.45	-20:50:03.9	24.0	27.7
Knot 7	18:19:08.13	-20:50:37.6	33.1	30.0
Knot 8 (HH81)	18:19:06.91	-20:51:06.6	28.2	32.8
Knot 9 (HH80)	18:19:05.70	-20:52:02.4	41.7	45.4

5.4.1 Morphology of knots

We have identified nine knots along the HH80-81 jet: four on the northern side and five on the southern side of the driving source, as shown in Fig. 5.3. The morphology of the individual knots are outlined in Appendix A. It is to be noted that in the case of HH80-81 jet, the H_2 emission is observed at large distances from the central stellar source (up to 2 pc in projection on each side). Therefore, we suggest that the shock origin is a more plausible scenario than the fluorescence phenomenon. The NIR emission lines of the Fe atom are also tracers of jets (Reipurth et al., 2000; Pyo et al., 2003; Giannini et al., 2013; White et al., 2014) since these excitations can be readily achieved in shocks as already discussed in Chapter 1.

We examine and compare the morphologies of the nine knots in H_2 and [Fe II] emission here.

Knot 1: We have detected solely molecular H_2 emission towards this knot, [Fe II] emission has not been detected. The morphology of the H_2 emission appears elongated and the emission appears to trace the edges of the jet with a lack of emission in the central region. The eastern edge appears to demonstrate a broken morphology. We do not observe any radio emission towards this knot.

Knot 2: Similar to the case of Knot 1, we detect only molecular H_2 emission from this knot. The morphology of this knot is also elongated. However, unlike the case of Knot 1, the emission appears to emanate from the jet itself, although we do see hints of emission towards the edges. It is possible that we are viewing the front-edge of the cavity in H_2 towards us. Similar to the case of Knot 1, we do not observe any radio emission towards this knot.

Knot 3: We detect both H_2 and [Fe II] emission at distinct locations in this knot. The morphology of emission in both lines is very different. There are two [Fe II] knots and two H_2 knots here. A comparison with radio emission towards this knot suggests that [Fe II] knots trace the radio emission, while the H_2 knots lie to the south of the radio and [Fe II] emission.

Knot 4: This is the knot in the jet closest to the exciting source in the northern side. We detect only [Fe II] emission towards this knot. The emission appears to have an elongated morphology along the jet axis with at least six [Fe II] knot structures aligned almost linearly. The [Fe II] emission traces the ionized gas distribution in this case while the H_2 features appear to trace the cooler edges.

Knot 5: This is the knot in the jet that is closest to the exciting source in the southern side. Here we observe two [Fe II] and three H_2 knots, lying at distinct locations. The H_2 knots are located in the outer direction of the propagating jet. We observe that the knots appear to be aligned along the jet direction. Here, ionized gas emission is detected at 20 cm (Marti et al., 1993), overlapping with [Fe II] and H_2 emission. The radio emission appears to be more extended than the NIR emission due to the difference in spatial resolution in these observations. However, radio emission is not detected at low radio frequencies of 610 and 325 MHz. This suggests that the 20 cm radio emission can plausibly be attributed to thermal excitation rather than non-thermal emission.

Knot 6: We observe both [Fe II] and H_2 emission towards this knot, with an overlapping region of emission. The [Fe II] emission morphology resembles an arc with the head pointing in the outward jet direction while the H_2 emission is located towards the western wing of the arc with a region of overlap. Here the ionized gas emission overlaps with [Fe II] and H_2 emission.

Knot 7: We observe both H_2 and [Fe II] emission towards this knot, which displays a complex morphology. The H_2 emission appears to resemble a broken bow morphology. Towards the north, we notice two arc-shaped structures with no emission in the center, which could be part of a broken bubble. Elongated emission is observed towards the south-east of the bubble-like structure. Two faint knots of [Fe II] emission are located towards the interior of the H_2 emission. No radio emission is detected towards this knot.

Knot 8: This knot corresponds to HH81 and we observe [Fe II] as well as H_2 emission towards this knot. For comparison, we have included optical emission from HST in the filter $H\alpha$+[NII]. We note that there is an overlap between the optical and [Fe II] emission, visible as cyan in Fig. 5.3 where optical emission is represented in blue. This emission reveals the presence of various sub-knots within the main knot. We observe an elongated emission and a compact knot in [Fe II] towards the south of the optical emission. Heathcote et al. (1998) have identified two sub-knots structures namely A and B in the optical emission and both of these overlap with two of the [Fe II] knots in the north. The other two [Fe II] knots and the two H_2 knots do not have any corresponding optical emission. Towards the north and east of the optical emission, we observe two arcs in the H_2 emission. There is a marginal overlap between the H_2 and [Fe II]/optical emission. The orientation of the [Fe II]/optical bow as well as the northern H_2 bow are in a direction that is opposite to the jet propagation. There is no overlap between the [Fe II] and H_2 emission. The associated ionized gas emission has spatial overlap with [Fe II] and optical emission, but no overlap with H_2 emission. A comparison with soft X-ray emission towards this knot as discussed by Pravdo et al. (2004) in their Fig. 3 suggests that the X-ray emission lies in the vicinity of Knot A to the south-west.

Knot 9: This knot corresponds to HH80 and we observe [Fe II] as well as H_2 emission towards this knot. Similar to the case of HH81 we include the optical emission from HST for a comparative study. Heathcote et al. (1998) have identified 12 sub-knots in the optical emission and labeled them in the order from A to L, shown in Fig. 5.3. For sub-knots A to E, G and H, the optical emission and [Fe II] emission overlap, which is visible as cyan in the figure. Knot F is located above the corresponding optical sub-knot. For sub-knots I, J, K and L, we do not detect associated [Fe II] emission. The H_2 emission, on the other hand, has a distinct location compared to both [Fe II]/optical emission without any overlap. We observe four H_2 sub-knots, of which three are linearly arranged along the direction of jet propagation. However, this arrangement is outward of the [Fe II]/optical emission towards the east and appears to be tracing the walls of the jet cavity. One H_2 sub-knot is located towards the north-eastern edge of the sub-knot C. However, this extends outwards farther than the [Fe II]/optical emission. Similar to HH81, there is no overlap of ionized gas emission in radio with H_2 emission. There appears to be an overlap of [Fe II] emission with radio towards sub-knots A to E, however, we cannot comment on the exact correspondence with sub-knots due to the relatively large beam-size of radio observations. For sub-knots F, G and H which display [Fe II] emission, there is no associated ionized gas emission. Soft X-ray emission has also been detected towards sub-knots A, C and G by Rodríguez-Kamenetzky et al. (2019). This suggests the presence of hard shocks traveling at speeds greater than 300 km s^{-1} (Bally et al., 2002).

Among the knots observed in NIR, all knots other than Knots 7, 8 and 9 show an elongated morphology along the jet axis. This is explicable on the basis of excitation in the immediate vicinity of the jet. Knots 7, 8 and 9, on the other hand, display a complex fragmented morphology.

5.4.2 Emission lines and the associated shock nature

In this section, we qualitatively characterize the nature of shocks at play in each of the knots. Depending on the strength, structure and nature of the shock generated by jets, the shocked plasma can cool via emission of atomic, molecular or ionic lines. Thus the emission line features can be utilized to uncover the type and nature of shocks that give rise to these emissions. While spectroscopy is ideal for probing the intensities of excitation lines and hence the nature of shock at a specific location, the spatial distribution of the different excitation lines through a morphological study is equally important as it provides strong clues about jet propagation in the ambient medium.

We utilize the H_2 and [Fe II] line images to comment on the possible nature of shocks in different knots of the HH80-81 jet. Molecular H_2 is a good tracer of low-velocity ($10 - 50$ km s^{-1}) weak molecular shocks associated with protostellar jets, i.e. shocks at low velocities (Draine, 1980). In such cases, the dissociation of H_2 molecule does not occur. However, in regions of low densities, the H_2 molecule remains undissociated even up to 80 km s^{-1} (Le Bourlot et al., 2002). IR H_2 emission could occur either in non-dissociative C-shocks or low velocity J-shocks. This is corroborated by the fact that numerous HH flows (Schwartz et al., 1988; Lane, 1989) and several CO outflows have exhibited H_2 emission features tracing weaker regions of shocks with low excitation levels. J-shocks with speeds greater than 25 km s^{-1} are found to dissociate H_2 (Kwan et al., 1977), whereas C-shocks are capable of accelerating H_2 to velocities up to 50-80 km s^{-1} without dissociating it (Draine, 1980; Le Bourlot et al., 2002). [Fe II] emission is widely used to understand fast and dissociative J-shocks caused by jets with velocities larger than 50 km s^{-1}. At these velocities, the head of the bow shock can destroy the grain in which iron is locked up (Lorenzetti et al., 2002). The grain destruction releases iron in the gas phase and this is followed by ionization of the neutral iron through charge transfer reactions with ions. It is possible that J-shocks can have cooler wings, where H_2 molecules are excited behind the [Fe II] emitting region. Alternately, J-shocks with magnetic precursors can give rise to a geometry in which H_2 emission is seen in front of the [Fe II] emission (Draine, 1980). The morphology of emission in shock tracers can provide a resourceful gauge to examine the interaction of the jet with the ambient medium.

5.4.2.1 Nature of shocks in HH80-81 jet knots

In the HH80-81 jet, from the observed morphology of knots aligned along the jet, we attempt to segregate strong and weak shocks and correlate this information with signatures of C-shocks, J-shocks as well J-shocks with magnetic precursors. In Knot 1, the elongated cavity like H_2 emission and the absence of [Fe II] and radio emission towards this distant knot could be explicable by the weakening of the shock strength with radial distance as it moves outwards from the central source. The absence of [Fe II] and radio emission helps to exclude J-shock as the exciting mechanism at this knot location, and hence we propose that the shock in this knot could be a C-type shock. For Knot 2, although its morphology is different from that of Knot 1, strong H_2 emission and the absence of [Fe II] and radio emission again points towards the possibility of a C-type shock due to weakening of the shock with radial distance from the central source. The filled morphology could suggest the presence of a stronger shock. Compared to Knot 1, this shock is possibly stronger due to smaller radial distance from the driving source. Alternatively, the emission could be from the front side of the wall-cavity as mentioned earlier.

In Knot 3 the [Fe II] emission appears to arise from the head of the bow shock and the H_2 emission corresponds to the cooler wing of the bow shock i.e interior to that of [Fe II] emission in the post-shock cooling zone. The fast dissociative shock head of the J-shock results in the generation of Fe^+ ions in the immediate post-shock region which undergoes collisional excitation and emission of forbidden [Fe II] transition. Behind the shock front, molecular re-formation occurs due to which H_2 emission is observed (Hollenbach & McKee, 1989). For the H_2 molecule to remain undissociated, the angle between the direction of the oblique planar shock responsible for the emission and the jet direction is expected to be less than 5-7° for a J-type shock and 10-15° for a C-type shock (Davis et al., 2000). In Knot 3, we find that the angle between the H_2 knot and the flow direction is $\sim 16^\circ$ and between the [Fe II] knot and jet is $\sim 42^\circ$. This strongly suggests the C-type nature of the cooler wings and J-type nature of the shock head where H_2 emission is missing. A similar case is observed towards Knot 6. The [Fe II] emission is located at the bow head and H_2 emission is at the cooler wings behind the shock front. This again points to the possibility of a strong dissociative J-shock with cooler wings. In Knot 4, only [Fe II] emission is present due to the highly dissociative nature of the shock.

We observe the presence of H_2 emission exterior to the [Fe II] emission in Knot 5, and it is possible that a J-shock with a magnetic precursor can account for this scenario. The magnetic precursor causes heating and compression of the materials upstream of the shock front when the shock wave travels in a weakly ionized gas in the presence of a transverse magnetic field (Hartigan et al., 1989; Flower et al., 2003). However, here the neutrals undergo a discontinuous change of physical conditions across the shock. A low ionization fraction reduces the rate of ion-neutral collisions resulting in weaker compression of the magnetic field. Under these low-ionization conditions, if the magnetic field is strong enough the shock will possess a magnetic precursor which compresses the magnetic field even before the shock front crosses a region. This happens because in this scenario because the magnetosonic waves can propagate faster than the actual shock front (Draine, 1980). Hence, the arrival of shock compression before the shock front at each location along the path of the jet flow provides favorable conditions for excitation of H_2 molecules without dissociating it. This could explain the observed H_2 emission in this knot. Furthermore, behind the shock compression, at the dissociating shock front, we observe [Fe II] emission in accordance with predictions from the theory.

The HH80 and HH81 knots display complex morphologies. For HH81 (Knot 8), the H_2 and [Fe II]/optical emission appears to arise from bow shocks which are arched in a direction that is opposite to the jet propagation. The arching of the bow shock opposite to the direction of the flow can be explained by a scenario where the jet encounters a small and dense clump of material on its path (Stapelfeldt et al., 1991). The bow shock then curves in the direction opposite to the direction of the jet flow. Towards HH80 (Knot 9), multiple knot-like structures are observed. The presence of elongated H_2 emission towards the eastern lateral edge of the [Fe II] emitting region could have an origin in the wiggling or sideways motion of the jet flow (Marti et al., 1993; Eisloffel et al., 1994). An alternative explanation is provided by Noriega-Crespo et al. (1996) which introduces the grazing jet/cloud core collision scenario. This states that when the jet impacts on the molecular core at an angle, it gets deflected and moves away from the surface of impact. As the jet deflects away, the external pressure forces it back causing the outflow to bounce back and forth while some gas slides closer to the core. This is the zone of interaction between the atomic and molecular gas, and the H_2 excitation is most likely to be arising from this region. We suggest that the back-and-forth motion of the jet could create internal shocks that are substantiated by the presence of elongated [Fe II] emission, located closer to the jet-axis than the H_2 emission. The complex morphology of the entire knot could arise from a scenario where thermal instabilities develop in an optically thin jet which ultimately fragments and breaks up the shocked material (Field, 1965; Hunter, 1970). Proper motion studies aimed at understanding the kinematics of these HH80-81 knots have measured velocities for all the sub-knots, and these lie in the range $74-916$ km/s (Heathcote et al., 1998). The direction of velocity is different for different sub-knots, which supports our claim regarding fragmentation of these knots as a result of thermal instabilities. For HH80 and HH81, it is difficult to conclude the nature of shock that explains the entire complex morphology of knots using the NIR and optical emission alone, and it is possible that one or multiple types of shocks could be generated in the sub-knots.

We, next, utilize the location of soft X-ray emission to discuss the plausible nature of shocks in these regions. The highly dissociative head of a J-shock being the strongest section of the shock is believed to be rich in UV and X-ray emissions. X-ray emission has been detected towards HH80 (sub-knots A, C and G) and HH81 (sub-knots A) by Rodríguez-Kamenetzky et al. (2019) that has overlap with the optical emission. In addition, a scrutiny of the [Fe II]/optical and soft X-ray images (Fig. 2; Rodríguez-Kamenetzky et al., 2019) suggest the X-ray emission to be marginally ahead of the [Fe II]/optical emission in the outward propagating jet direction. This points towards the likely presence of a J-type shock at these locations. For the other sub-knots, the shock mechanisms are difficult to disentangle.

The displacement in the position of [Fe II] and H_2 emission (see Fig. 5.3) for various knots along the jet hints at a possible wiggling motion of the jet. Similar variations in flow direction or wiggling morphologies at smaller scales have been observed towards other massive collimated jets as well (Davis et al., 2004; Gredel, 2006; Caratti o Garatti et al., 2008). For this jet, however, we are unable to clearly identify the wiggling at regions closer to the YSO (< 0.2 pc) due to strong continuum emission in the region, plausibly from the cavity. Therefore, further observations in jet tracers need to be carried out to confirm and model this small scale wiggling.

5.4.2.2 Variation of shock strength across jet length

The $\mathcal{R}$ value of each knot is representative of the strength of the shock generated. The Hollenbach & McKee (1989) model predicts that a [Fe II]/H_2 ratio greater than 0.5 is indicative of high-velocity dissociative shocks. The $\mathcal{R}$ values of the HH80-81 jet knots are greater than 0.5 (Table. 5.2) thereby indicating the presence of J-type shocks throughout the length of the jet. In the case of Knot 5 which is located in the southern arm of the jet, the $\mathcal{R}$ value is significantly high, due to its close proximity to the driving source. Here, the shocks are very strong and highly dissociative, thereby, favoring [Fe II] emission over H_2. Similarly, the corresponding closest knot in the northern arm, Knot 4, is much stronger and dissociative resulting in only [Fe II] emission.

Although we have tried to understand the nature of shocks, i.e. strong (J), weak (C), or intermediate (J with magnetic precursor), based on the spatial distribution and overlap of H_2 and [Fe II] lines, it is possible that extinction effects could also play a role in regions where H_2 is detected but [Fe II] is not detected as the former suffers lower ($\sim 50\%$) extinction compared to the latter.

5.4.3 HH80-81 jet propagation

A comprehensive view of the jet reveals that towards the northern arm, the knots closer to the driving source display solely [Fe II] and radio emission or a combination of [Fe II], radio and molecular H_2 emission, whereas H_2 emission dominates in the farther knots. The H_2 emission is believed to trace the diffuse regions in outflow lobes which are not well-collimated whereas [Fe II] and radio emission reveals the compact jet where the fast moving jet ejecta produces stronger shocks (Lorenzetti et al., 2002). This implies that [Fe II] and radio emission traces the ejecta accelerated directly by the exciting source, whereas H_2 emission might also arise from shocked ambient gas where the ejecta interacts with it. The [Fe II] emission gradually diminishes with radial distance from the exciting source towards this arm. From this, we can infer that at smaller radial distances from the driving source, shocks are stronger J-type, and they appear to gradually weaken farther along the jet length.

In the southern arm, all the knots show both [Fe II] and H_2 emission. HH81 and HH80, located towards the southern extremity of the jet are complex in nature which we attribute to thermal instabilities associated with low densities. Overall, the nature of shocks in the knots would suggest that densities of the ambient medium are relatively lower towards the southern arm as compared to the northern arm. This is validated by the fact that optical emission from HH81 and HH80 is visible due to lower extinction. This is also in accordance with conclusions of Marti et al. (1993) that the knots in the northern arm interact with the molecular cloud unlike the southern knots HH80 and HH81, which lie beyond the edge of the molecular cloud. A comparison of fields towards the northern and southern regions of the jet in the *JHK* three-color composite image shown in Fig. 5.4 of Appendix 5.4.7 indicates that the northern field displays a lower number of sources which are redder as compared to the southern field.

In view of the fact that we detect both [Fe II] and H_2 emissions in all the knots in the southern arm, we carefully analyze the variation of the corresponding $\mathcal{R}$ values with radial distance. The $\mathcal{R}$ values for all the knots are tabulated in Table 5.2. One can discern that with an increase in radial distance from the central YSO, $\mathcal{R}$ decreases from Knot 5 to Knot 9 with a sharp decline in the value at Knot 7. The decrease in $\mathcal{R}$ with radial distance is likely to be due to a decrease in the strength of dissociative shocks. Such a decrease in $\mathcal{R}$ with radial distance has also been observed in other jet systems (Davis et al., 2000; Nisini et al., 2002; Lorenzetti et al., 2002). In addition, the lower densities towards Knots 8 and 9 could also result in a decrease in H_2 emission in these knots compared to the ones at smaller radial distances.

For each knot, we compare the NIR narrow-line observations with the radio emission from ionized gas, wherever available. We note that the knots giving rise to ionized gas emission are associated with [Fe II] emission. However, the converse is not true, and the exceptions are Knot 5 (no 610 MHz emission) and Knot 7 where the [Fe II] emission does not have a corresponding ionized gas emission. This is consistent with our assertion that the shock in this knot is J-type with a magnetic precursor. This is weaker than the strong J-type shock and it is highly likely that ionization of Fe is favorable against the ionization of hydrogen, as the former has lower ionization potential than the latter. This would explain the lack of ionized gas emission as well as the presence of [Fe II] towards this knot.

5.4.4 Large scale jet geometry

The overall geometry of the jet on a large scale shows a curved S-shape centered on the MM1 core in IRAS 18162-2048. This S-shape in the distribution of knots was first noted in radio by Marti et al. (1993). We have used NIR emission from multiple knots including those that emit in radio to confirm the curved morphology of the knot train. In addition, we note that a direct evidence of wiggling is seen in HH80 (Marti et al., 1993), where H_2 is linearly elongated along the lateral edge of the jet, which provides support for a wiggling jet scenario. Similar geometries have been observed before in various other jets (Gomez et al., 1997; Eisloffel & Mundt, 1997; Lorenzetti et al., 2002). Two possible scenarios can be considered (i) the jet interacting with dense ambient medium (Lorenzetti et al., 2002), or (ii) the wiggling of jet (Raga et al., 1993). The symmetric shape is believed to result from the wiggling of jet due to precession (Bachiller et al., 2001; Lorenzetti et al., 2002; Takami et al., 2011). The jet precession, in turn, can be attributed to (A) the presence of a companion, or to (B) asymmetry in the accretion of envelope into the disk. The presence of a companion could lead to (a) the precession of the accretion disk due to the tidal interactions with a non-coplanar companion or to (b) the orbital motion of the jet source around a companion in orbit with the core. In case (B), the asymmetry could be due to a large difference in the orientation of magnetic and rotation axes of the core as demonstrated by simulations (Hirano & Machida, 2019). ALMA studies at a resolution of 40 mas (~ 56 au) did not reveal the presence of a binary companion within MM1 core at these separations (Busquet et al., 2019). This means that the companion must be closer or could be much less massive that the protostar itself. Therefore higher resolution studies are required to draw valid conclusions regarding the presence of a binary companion.

5.4.5 Estimation of jet properties

5.4.5.1 Knot Fluxes and Luminosities

We have estimated the integrated fluxes of knots in the narrow-band H_2 and [Fe II] filters by using elliptical apertures for each of the knots, which are marked in cyan in Fig. 5.3. The knot fluxes along with the sizes of apertures (semi-major × semi-minor) used for the flux calculation are tabulated in Table. 5.2. The H_2 and [Fe II] fluxes of the knots are in the range $0.4 - 5.2{\times}10^{-14}$ erg s^{-1} cm^{-2} and $3.1 - 13.6{\times}10^{-14}$ erg s^{-1} cm^{-2}, respectively. Knots 1 and 2 do not have any associated [Fe II] emission. We have also calculated the ratio of [Fe II]/H_2 emission towards knots where both are detected. This ratio is represented as $\mathcal{R}$, and estimated in order to understand the nature of shock across different knots. These values are also tabulated in Table 5.2 and are comparable with those obtained from observational studies conducted towards other YSO jet sources (Lorenzetti et al., 2002; McCoey et al., 2004; Garcia Lopez et al., 2010). It is worthwhile to note that the extinction can be quite non-uniform along the length of the jet, and will also be affected by the inclination of the jet with respect to the line-of-sight (LOS). However, having stated this, we observe that $\mathcal{R}$ varies widely across the knots, from 0.6 in Knot 7 suggesting relatively low excitation of [Fe II] emission to 12.1 in Knot 5 where [Fe II] emission clearly dominates over the H_2 emission. This clearly indicates that there is a considerable difference in the excitation conditions of the knots.

Table 5.2: Fluxes of HH80-81 jet knots in the narrow-band H_2 and [Fe II] filters, the sizes of apertures (semi-major × semi-minor) used for the flux calculation, and the [Fe II]/H_2 line ratios ($\mathcal{R}$) for the HH80-81 main jet knots in which both H_2 and [Fe II] emission were detected.

Source name	H_2 flux (10^{-14} erg s^{-1} cm^{-2})	[Fe II] flux (10^{-14} erg s^{-1} cm^{-2})	Aperture size	$\mathcal{R}$ = [Fe II]/H_2
Knot 1	1.7	– †	$10.7'' \times 4.7''$	–
Knot 2	1.3	– †	$8.1'' \times 4.7''$	–
Knot 3	2.6	4.6	$14.8'' \times 5.5''$	1.8
Knot 4	– ‡	11.7	$13.9'' \times 6.0''$	–
Knot 5	0.4	4.6	$10.7'' \times 3.9''$	12.1
Knot 6	0.9	5.2	$5.9'' \times 5.8''$	6.0
Knot 7	5.2	3.1	$14.6'' \times 10.7''$	0.6
Knot 8	1.5	7.0	$9.6'' \times 9.1''$	4.7
Knot 9	4.3	13.6	$16.2'' \times 12.1''$	3.2

† [Fe II] emission is not detected in these knots, ‡ H_2 emission is not detected in this knot.

The luminosities of knots in H_2 (2.122 μm) and [Fe II] (1.644 μm) lines are calculated using dereddened fluxes and are in the range $10^{31} - 10^{33}$ erg s^{-1}, tabulated in Table 5.3. For this, we have assumed $A_v = 30$ mag (Davis et al., 2001) for the knots close to the central region and in the northern arm (Knots 1, 2, 3, 4 and 5). Rodríguez-Kamenetzky et al. (2019) had calculated A$_v$ $= 2.8$ mag and 3.4 mag for HH80 and HH81 (Knots 8 and 9), respectively. For the knots at intermediate distances (Knots 6 and 7), we have assumed A$_v$ $= 15$ mag. We note that the ratio of [Fe II] and H$_2$ luminosities $\left(\frac{L_{[Fe\ II]}}{L_{H_2}}\right)$ are in the range $1.4 - 70.0$. This is higher than the values obtained for low mass Class 0 and Class I YSOs for which $\frac{L_{[Fe\ II]}}{L_{H_2}} \sim 10^{-2} - 10^{-1}$ (Davis et al., 2003; Caratti o Garatti et al., 2006). A thorough literature survey has also revealed that in the case of massive YSOs, there exist only one example of such ratio, which is estimated to be in the range of ∼0.6−0.8 (Caratti o Garatti et al., 2015). We attempt to understand the observed $\frac{L_{[Fe\ II]}}{L_{H_2}}$ ratio obtained from our study, in terms of the dynamical age and evolutionary stage of the YSO driving the jet. The dynamical timescales of the HH80-81 radio jet is $\sim 10^4$ yr (Masqué et al., 2012) while the associated outflows provide an estimate of $\sim 10^6$ yr (Benedettini et al., 2004). As massive objects have shorter evolutionary timescales compared to their lower mass counterparts, this would suggest that the driving source is at a later evolutionary phase when compared to the low mass Class 0/I sources of similar dynamical ages (Barsony & Kenyon, 1992; Andre et al., 2000). This indicates that the difference in $\frac{L_{[Fe\ II]}}{L_{H_2}}$ is plausibly the effect of evolutionary phase of the driving source which manifests its influence on the jet physical properties. This is also corroborated by the large extent of the jet ~ 18 pc. Another noteworthy point is that the ratio $\frac{L_{[Fe\ II]}}{L_{H_2}} > 1$ implies a weakening of molecular line emission with the age of the driving source. This is expected because the clearing of the ambient medium by the previous mass-loss activities would result in lower densities and thus weak ambient magnetic field (Hollenbach, 1997) thereby favoring the dominance of dissociative J-type shocks over non-dissociative C-type shocks.

5.4.6 Mass-loss and accretion rates

We also compute the mass-loss rates ($\dot{M}_{\text{jet}}$) of the knots using the mass (M_{jet}), tangential velocity ($v_\perp$) and sky-projected length ($l_\perp$), by using the following formula.

$$\begin{aligned} \dot{M}_{\text{jet}} &= M_{jet}\frac{v_\perp}{l_\perp} \\ &= \mu m_H L_{\text{[Fe II]}}\left(h\nu A_i f_i \frac{Fe^+}{Fe}\left[\frac{Fe}{H}\right]\right)^{-1}\frac{v_\perp}{l_\perp} \end{aligned} \tag{5.1}$$

Table 5.3: Physical parameters of HH80-81 jet knots and, mass-loss and momentum rates for the knots in which [Fe II] emission was detected.

Source name	L_{H_2} (10^{31} erg s^{-1})	$L_{[Fe\ II]}$ (10^{32} erg s^{-1})	$v_\perp$ km s^{-1}	$l_\perp$ (°)	$\dot{M}_{jet}$ (10^{-5} M$_\odot$ yr^{-1})	$\dot{P}$ (10^{-2} M$_\odot$ yr^{-1} km s^{-1})
Knot 1	8.9	–†	–†	–†	–†	–†
Knot 2	6.8	–†	–†	–†	–†	–†
Knot 3	13.2	13.7	1000	11.5	4.3	4.3
Knot 4	–‡	34.5	1000	24.0	5.2	5.2
Knot 5	2.0	13.6	1000	14.0	3.5	3.5
Knot 6	1.0	1.4	500	6.5	0.4	0.2
Knot 7	5.7	0.8	500	17.5	0.1	0.04
Knot 8	0.5	0.3	500	11.5	0.04	0.02
Knot 9	1.3	0.5	500	30.0	0.03	0.02

† [Fe II] emission is not detected in these knots, ‡ H_2 emission is not detected in this knot

Here, $\mu = 1.24$, $m_H = 1.67 \times 10^{-27}$ kg and $A_i = 0.00465$ s^{-1} (Nussbaumer & Storey, 1988) are mean atomic weight, proton mass and radiative rate of the considered transition, respectively. We assume that the knot temperatures are $\sim 10^4$ K since radio emission is detected in the majority of our knots. For this temperature and electron densities of $\sim 10^4$ cm^{-3} which is typical of protostellar jets (Nisini et al., 2005; Takami et al., 2006; Giannini et al., 2013), the fractional population of upper level of the transition $f_i = 0.01$ (Hamann et al., 1994) and $\frac{Fe^+}{Fe} \sim 0.25$ (Hamann, 1994). We assume a gas phase abundance of iron $\left[\frac{Fe}{H}\right] = 3.09 \times 10^{-5}$ which is the solar abundance (Asplund et al., 2021) assuming that there is no dust depletion.

To get estimates of the velocities of knots, we utilize proper motion studies of HH80-81 from literature. Radio observations have shown that the tangential velocities of knots close to the YSO can be as high as 1000 km s^{-1} (Marti et al., 1993, 1995). Optical proper motion study by Heathcote et al. (1998) had revealed a range of velocities for the sub-knots of HH81 and HH80, and here we adopt an average velocity of 500 km s^{-1} for both these knots. We also assume $v_\perp = 500$ km s^{-1} for the knots at intermediate distances. The extent of [Fe II] emission along the jet in each knot is adopted as the projected length ($l_\perp$).

The inferred mass-loss rates for the knots are in the range $3.0 \times 10^{-7} - 5.2 \times 10^{-5}$ M$_\odot$ yr^{-1}, tabulated in Table 5.3. For the knots close to the YSO, the values are consistent with those obtained from other tracers: 3×10^{-5} M$_\odot$ yr^{-1} from molecular gas using CO (Qiu et al., 2019), and $\sim\ 10^{-5}$ M$_\odot$ yr^{-1} using radio emission from ionized gas (Carrasco-González et al., 2012) towards the central region of the jet system. The mass-loss rates of HH80-81 jet are larger than those from jets of low-mass YSOs, $10^{-10} - 10^{-7}$ M$_\odot$ yr^{-1} (Davis et al., 2003; Garcia Lopez et al., 2008; Dionatos et al., 2009; Reiter et al., 2016), but comparable to the [Fe II] mass-loss rate from few massive YSOs, $10^{-7} - 10^{-4}$ M$_\odot$ yr^{-1} (Caratti o Garatti et al., 2008; Fedriani et al., 2018, 2019). Assuming $\frac{\dot{M}_{\text{jet}}}{\dot{M}_{\text{acc}}} \sim 10\%$ (Cabrit, 2007; Antoniucci et al., 2008), we obtain $\dot{M}_{\text{acc}}$ of $\sim\ 10^{-6} - 10^{-4}$ M$_\odot$ yr^{-1} from the knots. The accretion rates obtained from the knots close to the YSO are consistent with the observational and modeling estimates obtained towards the central region of this source (Carrasco-González et al., 2012; Añez-López et al., 2020) and is higher than the accretion rates observed towards low-intermediate mass protostars (Calvet et al., 2004; Evans et al., 2009; Ellerbroek et al., 2013; Antoniucci et al., 2014; Lee, 2020).

5.4.7 Possibility of variation in extinction across jet length

Fig. 5.4 shows the three-color *JHK* composite image of the HH80-81 jet region. In the figure, the K band emission is shown in red, the H band emission in green and the J band in blue. Knots $1 - 9$ are marked with cyan crosses. The regions enclosed in boxes with green outline and marked as Field 1 and 2 represents two fields of sizes $3' \times 3'$. These boxes have been used to compare the overall source density and reddening towards the northern arm and southern arm of the jet, respectively. We note that there are fewer sources in Field 1 as compared to Field 2. In addition, the sources in Field 1 are more reddened sources in comparison to those in Field 2. This implies the presence of a dense molecular cloud towards the northern arm. This is also consistent with the conclusions of Marti et al. (1993) that the knots in the northern arm interact with the molecular cloud unlike the southern knots HH80 and HH81, which are detected in optical as they lie beyond the edge of the molecular cloud.

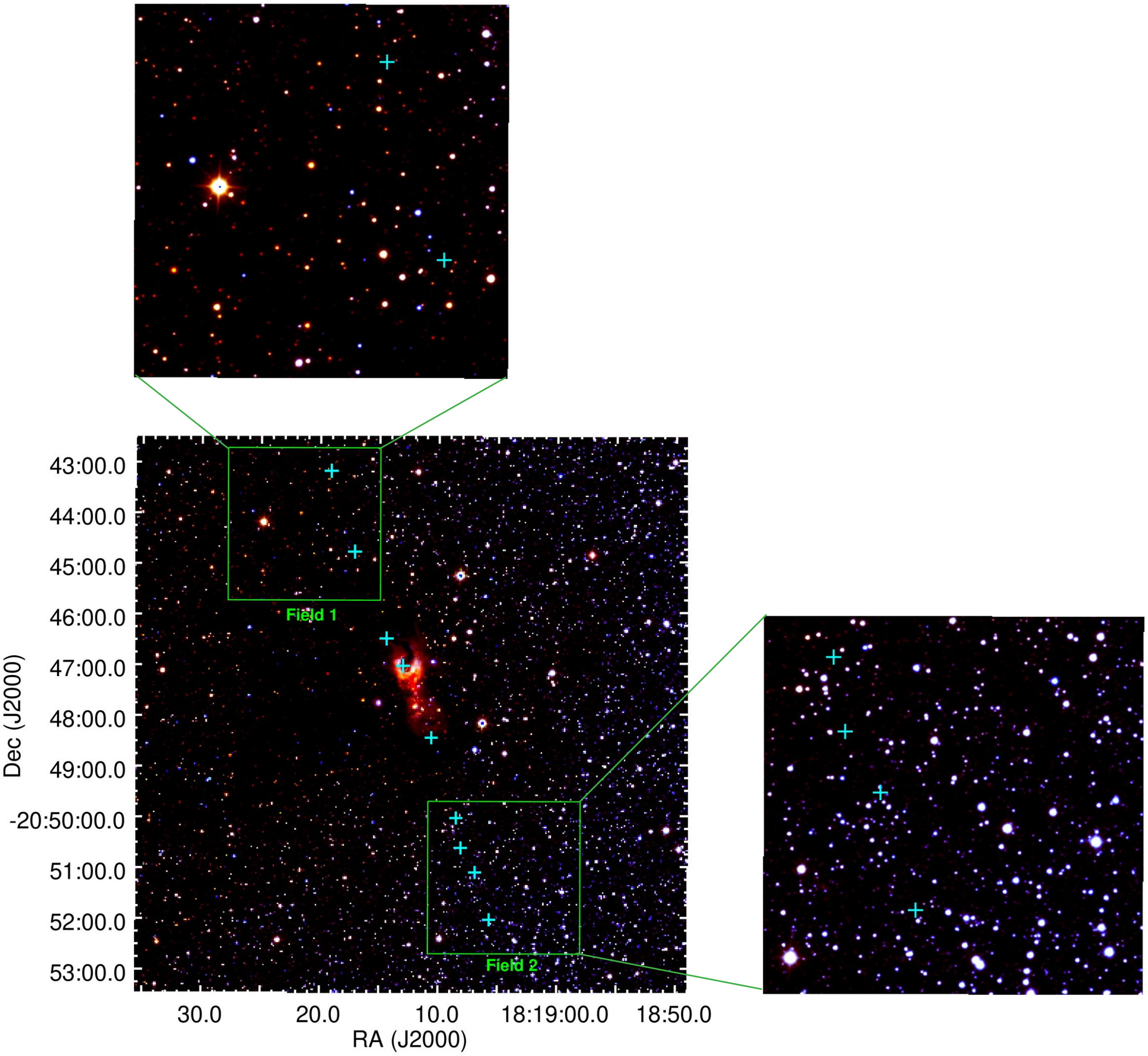

Figure 5.4: *JHK* color-composite image of the HH80-81 jet, with K band emission shown in red, H band emission in green and J band in blue. Knots 1 − 9 are marked with cyan crosses. The green boxes marked as Fields 1 and 2 show two regions towards the northern and southern arms of the jet, respectively.

5.5 The central region

5.5.1 Narrow-band emission in NIR

In this section, we examine the region close to the driving source and its immediate surroundings.

The central region close to the driving source of the jet is shown in Fig. 5.5. The Spitzer 8 μm broad-band image is shown in red and the H_2 emission is depicted in green. The maps are overlaid with the contours of [Fe II] emission in orange. The association with radio emission is illustrated by contours (cyan) corresponding to the 610 MHz emission (Vig et al., 2018). We observe that the emission in H_2 is widely distributed across the image, unlike the [Fe II] emission. It is also evident that the [Fe II] emission arises from the highly ionized inner jet close to the axis while the MIR emission delineates the outflow cavity. Multiple bow shocks and knots are observed in H_2 and the majority of this emission appears to be distributed in directions away from the HH80-81 jet axis. The radio jet is well delineated by the [Fe II] emission.

The prominent H_2 features in the region are:

(a) The HH80-81 main jet: This extends along the north-east – south-west direction. The emission is seen as knots extending along the jet as well as arcs close to the central region. The catalog number of the knots associated with this jet in the Catalog of Molecular Hydrogen Emission-Line Objects (MHOs) in Outflows from Young Stars (Davis et al., 2010) is MHO 2354.

(b) Reg 1: This comprises a chain of 5 H_2 knots towards the eastern side, that are enclosed within a dashed ellipse shown in Fig. 5.5.

(c) Reg 2: This includes two distinct H_2 knots to the north-east of Reg 1.

(d) Reg 3: This region includes arcs of H_2 emission along the east and west directions on either side of a YSO (Qiu et al., 2008), as shown in Fig. 5.5, facing inwards of the dashed ellipse of size $0.5' \times 0.4'$. The arc towards the east is very strong in emission and with overlapping emission at 8 μm, it is seen as yellow in the figure. We note that the nebulosity at 8 μm appears well enclosed within the defined ellipse.

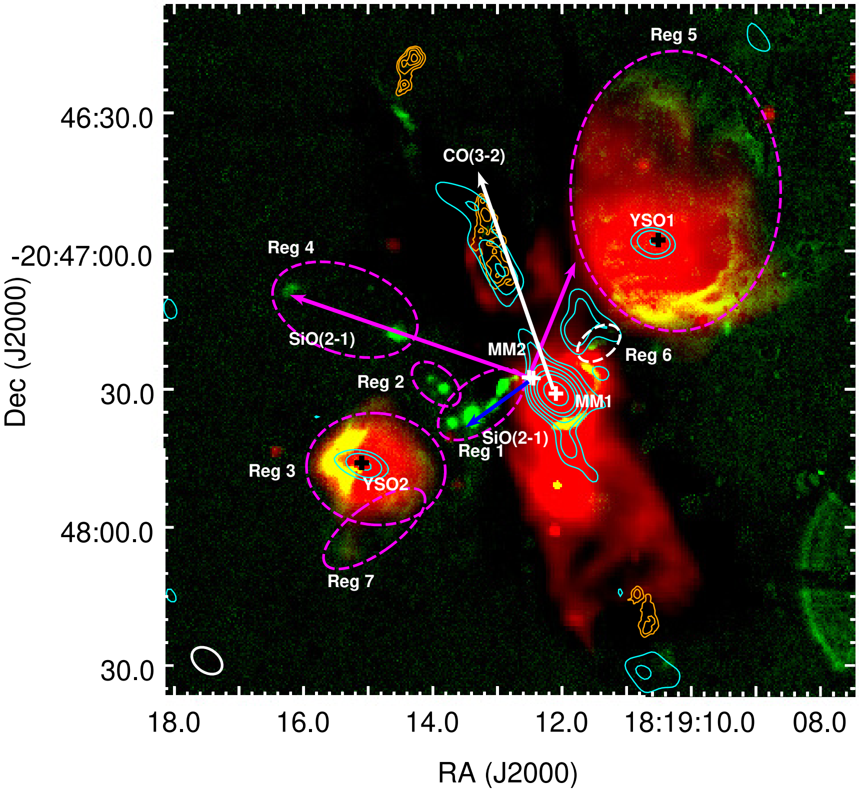

Figure 5.5: Two color-composite image of the central region of HH80-81 jet. The Spitzer 8 μm broad-band image is shown in red and the NIR H_2 emission is shown in green. The NIR [Fe II] emission is overlaid as orange contours, and the arrows depict outflows detected in this region by Fernández-López et al. (2013) and Qiu et al. (2019). The white crosses indicate two mm cores which are believed to drive some of the detected outflows. The cyan contours show ionized gas at 1300 MHz (Vig et al., 2018) and the beam is shown towards the bottom left of the image as a white ellipse. The dashed ellipses (magenta) labeled as Reg $1-7$ are discussed in the text. The black crosses indicate two YSOs of interest in the region.

(e) Reg 4: This region shows two knots aligned north-east with respect to the central region.

(f) Reg 5: The H_2 emission shows arc-shaped patterns over a region of size $1.0' \times 0.7'$. The arcs appear to surround the nebulosity observed at 8 μm. The emission to the south of the enclosed ellipse shows strong H_2 emission, overlapping with 8 μm emission.

(g) Reg 6: This region includes a knot towards the west of the central region.

(h) Reg 7: Two faint arcs in H_2 are observed facing each other within the region enclosed by the ellipse in this region.

The MHO catalog numbers of Regs 1-7 are MHO $2355-2361$.

5.5.2 Broad-band emission in NIR and MIR

In this section, we describe the emission from the central region in NIR and MIR broad-band filters. The emission through the NIR J, H and K bands can be seen in Fig. 5.6. The J, H and K band emission towards the northern extension of the jet is up to $\sim 1' = 0.4$ pc. On the other hand, towards the southern arm, the NIR J and H band emission is observed up to 0.2 pc whereas the K band emission is seen to extend up to 0.3 pc. We identify a sharp bend in the jet cavity towards the northern arm, where it is initially directed westwards but veers towards the east, see Fig. 5.6. This could be either due to a large scale precession or small scale wiggle in the jet. The most massive mm cores observed in this region are MM1 and MM2 (Busquet et al., 2019), which are marked in the figure. In addition, the knots and arcs which are discussed in Sect. 3.1 are also shown in the figure.

The emission towards the central region in the L$'$ and M$'$ bands can be viewed in Fig. 5.7. We note that the cavity is not seen very clearly in these images and we attribute this to the low signal-to-noise ratio of these images. While the L$'$ band image shows hints of emission towards the jet cavity near the center (see Fig. 5.7(a)), this is not detected in the M$'$ image. A comparison with MIR IRAC images from the space-based *Spitzer* mission shows the presence of strong MIR emission from the cavity walls (Fig. 5.5). Cavities around jets in MIR have been observed earlier and the emission has been attributed to thermal dust which is directly heated by the central source that drives the outflow (De Buizer, 2006). We observe a few point-like sources in our moderately high resolution L$'$ and M$'$ images, and we identify a few of them as cores that have been observed using mm ALMA emission (Busquet et al., 2019). The brightest emission in L$'$ image is observed at $\sim$2000 au to the north-east of MM1 and this emission is very likely from the outflow cavity. The lack of associated mm emission gives credence to the outflow cavity hypothesis. MM1 is brighter in the M$'$ band compared to L$'$ band, indicating that it is indeed young. We have not detected any emission associated with MM2(E) and MM2(W) in the M$'$ band.

The driving source of the jet, MM1 is not visible in the NIR J, H and K or the narrow-band images implying the highly embedded nature of the exciting YSO. A molecular

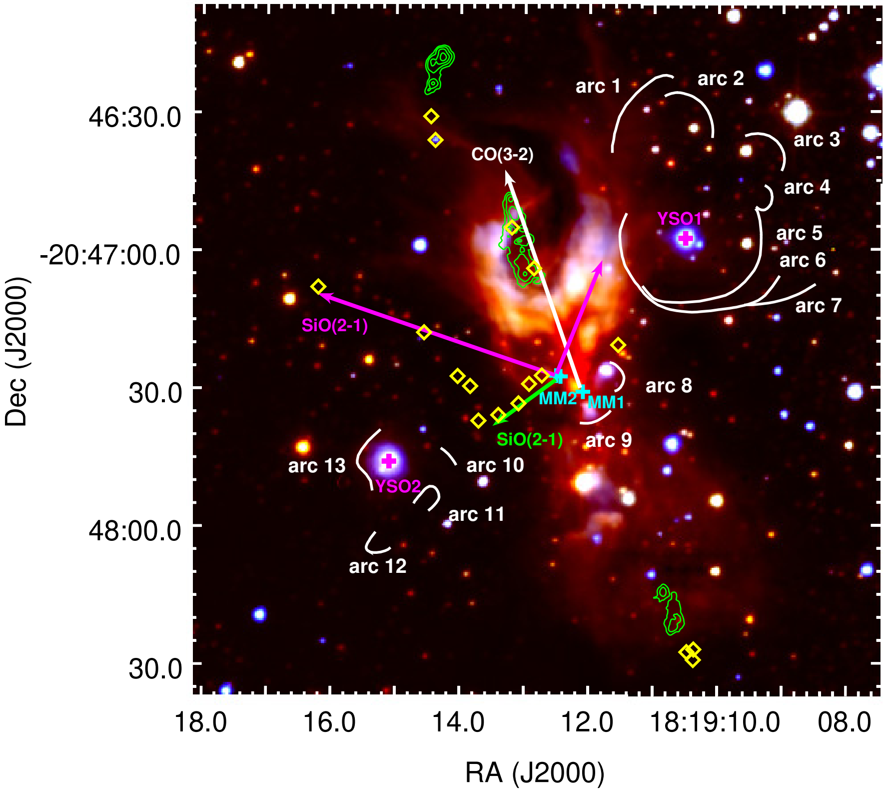

Figure 5.6: *JHK* color-composite image of the central region of HH80-81 jet. K is shown in red, H in green and J in blue. The NIR [Fe II] emission is overlaid as green contours, the arrows depict outflows detected in this region by Fernández-López et al. (2013) and Qiu et al. (2019). The cyan crosses indicate two mm cores which are believed to drive some of the detected outflows, the magenta crosses indicate two YSOs of interest in the region, the white arcs represent the bow shocks identified in the H_2 image of the central region shown in Fig. 5.5 and the yellow diamonds show H_2 knots.

outflow has been observed to be originating from MM1 with a position angle (PA) of 19° (Qiu et al., 2019) and is found to be associated with the radio jet. Molecular line observations using CO (2-1), (3-2), (6-5) and (7-6) lines by them have revealed the red- and blue-shifted components of this outflow aligned along the direction of the radio jet. The outflow is marked as a white arrow pointing in the direction of the blue-shifted emission in Fig. 5.6. In the vicinity of MM1, we also observe two arc-shaped structures in the west and south-west which resemble bow shocks; arcs 8 and 9 in the figure. These arcs appear to surround MM1 towards the western side and we believe that these could be bow-shocks associated with the walls of wind-swept wide angle cavities of strong winds (Davis et al., 2002) ejected by MM1.

Additional outflow components have been detected from the central region emanat-

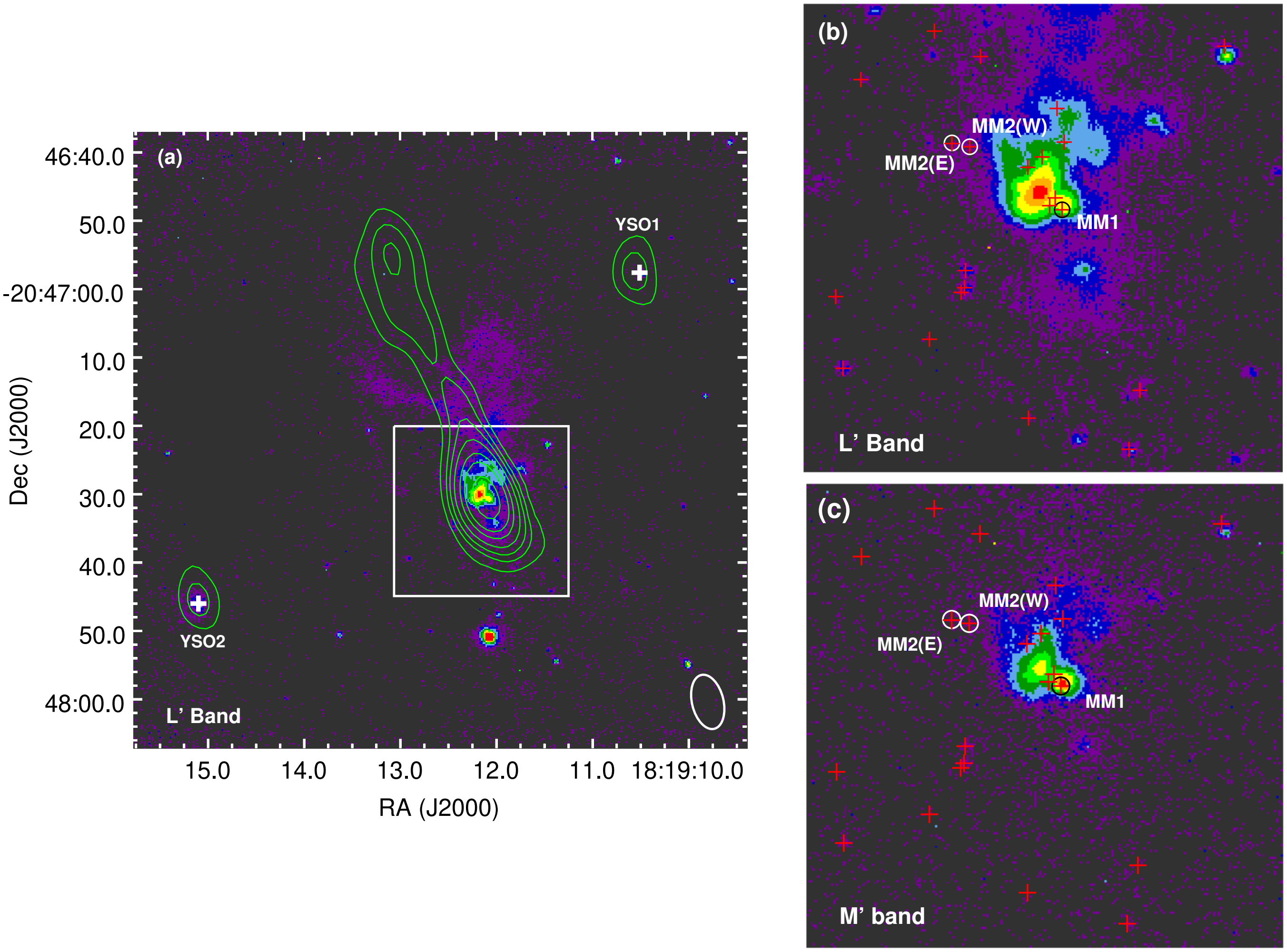

Figure 5.7: (a) L′-band image of the central region of HH80-81 jet system obtained with UIST. The white box encloses the region of size 0.4′ × 0.4′ shown in (b) L′-band emission and, (c) M′-band emission. The green contours represent the 20 cm radio continuum emission (Marti et al., 1993), with the beam shown as a white ellipse towards the right corner. The crosses in (b) mark the locations of mm cores in the central region identified by Busquet et al. (2019). The massive cores MM1 and MM2 are labeled.

ing towards north-east, north-west and south-east using sub-mm SiO(2-1), HCO$^+$(1-0), HCN(1-0) and CO(3-2) lines (Fernández-López et al., 2013). These outflows are shown as magenta and green arrows in Fig. 5.6. The lengths of the arrows indicate the approximate extent of the detected emission from the outflows. These outflows are believed to originate from MM2, which is $\sim 10^4$ au from MM1. MM2 comprises two cores, towards the east MM2(E) and west MM2(W) (Busquet et al., 2019). The string of H_2 knots, in Reg 1 are aligned with the outflow in the south-east direction and we believe that these H_2 knots are shock-excited by the associated jet. The extent of the knots matches the extent of the detected outflow lobe. We note that these 5 knots trace a curve indicating precession of the outflow.

There is a H_2 knot in Reg 6 which appears to lie on the opposite side of this outflow. Although no outflow lobe has been detected in this direction, we believe that this knot could plausibly be due to the other lobe of the same outflow that give rise to knots in Reg 1. Reg 4 has two H_2 knots that are aligned along the north-east SiO(2-1) outflow lobe. Again, we note a correspondence between the location of the knots and the extent of the outflow detected. Reg 2 has two H_2 knots which are located to the north of Reg 1 and south of Reg 4. It is difficult to comment on the likely outflow or exciting source responsible for this knot due to the cluster of sources present in the region. We also note arcs 11 and 12 facing inwards within the ellipse of Reg 7 appear to extend farther along the south-east of Reg 1. It is possible that they are bow-shocks associated with the same outflow. Davis et al. (2001) had previously probed the central region (within $40''$) using echelle spectroscopy and identified two bright H_2 knots and faint diffuse emission within the slit. The knots identified by the authors coincide with H_2 emission arcs that we discern towards the central region.

5.6 YSOs in the neighborhood

We also observe a number of H_2 arcs in Regs 3 and 5. These are located about the 8 μm nebulous regions about $\sim 20''$ from MM1. While it is possible that few of these maybe associated with outflows discussed above, we explore the possibility of other YSOs in the vicinity as the source of excitation of these bow-shocks. We employ the NIR *JHK* color-color diagram to identify YSOs. The NIR color-color diagram is an efficient tool to identify the physical properties of YSOs and their evolutionary classes. Using our WFCAM-UKIRT observations, we have carried out photometry of sources in the region. We find a total of 86 sources in a circular region of radius $1'$ about MM1 that are detected in all the three bands. Their distribution on the NIR color-color diagram is shown in Fig. 5.8(a). The loci of the main-sequence stars, giants, classical T-Tauri stars (Meyer et al., 1997) and Herbig Ae/Be stars (Lada & Adams, 1992) are shown. The reddening vectors of the main-sequence stars, giants, T-Tauri stars are also depicted.

There are a total of 45 IR-excess sources in the color-color diagram, shown as red points in Fig. 5.8[Left]. These are the objects lying to the right of the reddening

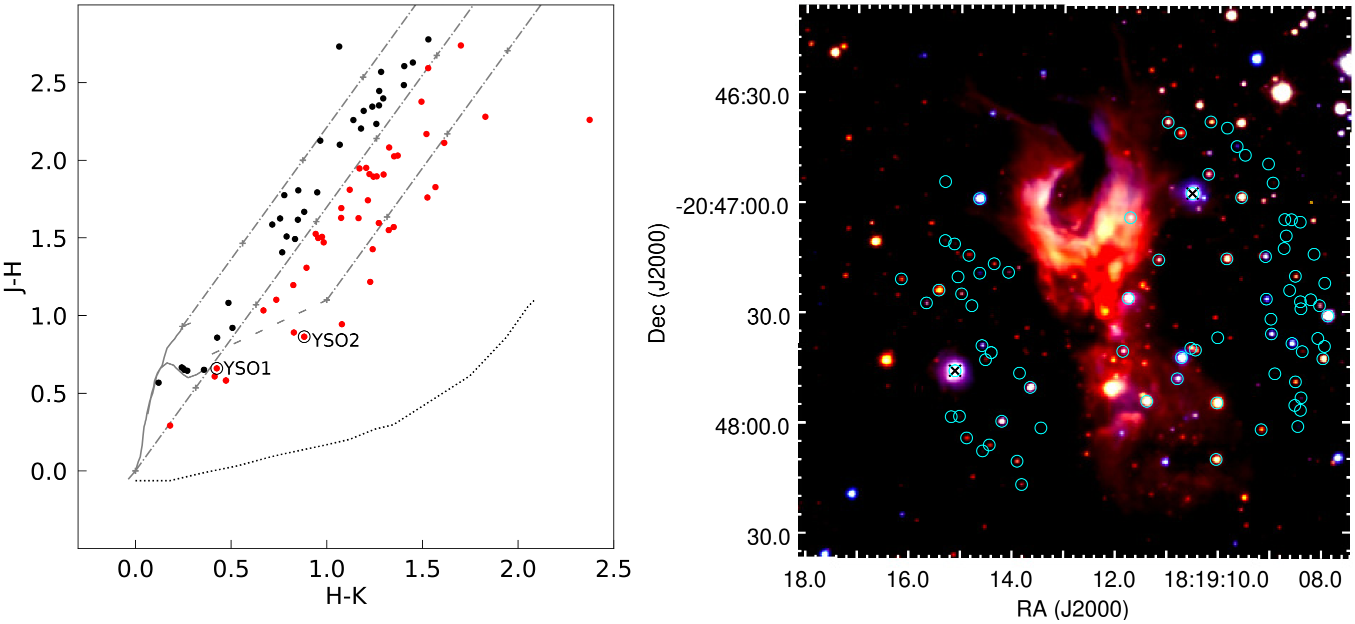

Figure 5.8: [Left] NIR color-color diagram depicting the colors of the sources in the central region including YSO 1 and 2. Of these, the IR-excess sources are marked in red points. The two solid curves represent the loci of giant (thick lines) and reddened main-sequence stars (thin lines) as obtained from Bessell & Brett (1988). The dashed lines represents the loci of classical T-Tauri stars (Meyer et al., 1997). The parallel dash-dotted lines show the reddening vectors with crosses located at intervals of 5 mag of visual extinction. Here, the reddening law of (Rieke & Lebofsky, 1985) has been adopted. The black dotted line represents the locus of Herbig AeBe stars (Lada & Adams, 1992). [Right] *JHK* color-composite image of the central region of HH80-81 jet. The IR-excess sources identified in this region are shown in cyan circles, with YSO 1 and 2 marked as black crosses within cyan circles.

vector drawn from the bottom of the main-sequence curve as well as those lying in the T-Tauri and HeAeBe zones in the color-color diagram. The location of these sources can be viewed in Fig. 5.8[Right]. Of these IR-excess YSOs, we find that two YSOs namely YSO1 and YSO2 are associated with MIR nebulosity as well as radio emission, see Fig. 5.5. In the color-color diagram, YSO1 and YSO2 lie close to the loci of T-Tauri stars and HeAeBe zone suggesting the youth of these objects. For the present study, we exclusively focus on these two YSOs.

Reg 5 envelopes the H_2 arcs 1-7 and 8 μm nebulosity around YSO1 as seen in Fig. 5.3. On the other hand, Reg 3 encloses H_2 arcs 10-13 and 8 μm nebulosity around YSO2. YSO1 and YSO2 have 2MASS designations J18191051-2046578 and J18191510-2047460, respectively. They have been identified as intermediate to massive YSOs by Qiu et al. (2008) based on NIR and MIR color-color diagrams.

Radio emission has been observed towards both these objects by Marti et al. (1993) and Vig et al. (2018), see Fig. 5.5. The radio spectral indices obtained by Marti et al. (1993) using the Very Large Array (VLA) in 1989 using 1.5, 5 and 15 GHz emission indicated that YSO1 displays a negative spectral index of -0.8 ± 0.2, while YSO2 shows a flat spectral index of 0.0 ± 0.1. We note that both objects were detected at low-frequencies of 1300 and 610 MHz by Vig et al. (2018) in 2016. We have extracted the flux densities of the two YSOs from images taken in 2016 using the Giant Metrewave Radio Telescope (GMRT) and estimated the spectral indices using these two bands. We infer non-thermal spectral indices for both these YSOs: -0.3 for YSO1 and -0.6 for YSO2. The difference in spectral indices from VLA and GMRT could be due to different frequency ranges considered as well as the outcome of measurements at different epochs. In the former, we anticipate that the contribution of thermal vis-a-vis non-thermal emission could result in different spectral indices as the frequency ranges are different. We also believe that variability could lead to differing flux densities and spectral index measurements in the two epochs. We note that both these sources display negative spectral indices characteristic of non-thermal emission at low radio frequencies, which is plausibly due to radio jets.

YSO1 is also associated with soft X-ray emission with X-ray luminosity of $(0.52-1.8)\times10^{31}$ ergs s^{-1} as demonstrated by Pravdo et al. (2004). These authors conclude that YSO1 is a high X-ray luminosity pre-main sequence star. It is surrounded by a multitude of arcs, extending up to a distance of 0.2 pc in north and 0.1 pc in south. This appears to outline the nebulous emission seen towards this YSO in MIR 8 μm band, which has been attributed to a reflection nebula (Aspin et al., 1991). We believe this nebula is associated with YSO1. The north-south elongation of the cavity leads us to speculate this as the direction of the jet/outflow from YSO1. Such bipolar outflow cavities have been observed around sources in previous studies conducted at different wavelengths (Bally et al., 2002; Quillen et al., 2005; Drozdovskaya et al., 2015; Fedriani et al., 2020). YSO2 does not show any associated X-ray emission. We note that the high-resolution 1300 MHz emission towards YSO2 is elongated along the E-W direction. From Fig. 5.5, we observe that this emission is elongated with the direction matching the H_2 bow-shocks corresponding to arcs 13 and 10 in Reg 3. We observe diffuse nebulosity around this YSO in MIR and the arcs appear at the eastern edge of the nebulosity. In fact, the eastern edge of the elongation matches the shape of H_2 arc 13 like a piece of jigsaw puzzle, see Fig. 5.5. This strongly suggests that the

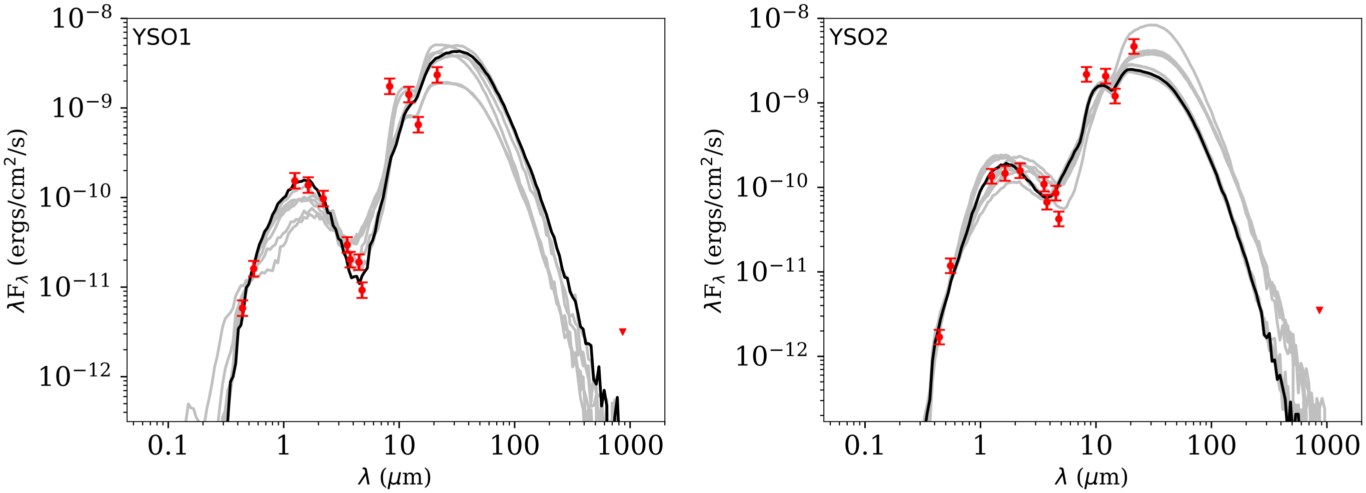

Figure 5.9: IR SEDs of YSO1 (left) and YSO2 (right) fitted with the SED models of Robitaille et al. (2007). The red solid circles indicate flux densities while the red triangle indicates upper limit. The black line shows the best fit model while the grey lines show the next nine good fits.

non-thermal emission from YSO2 is from the associated east-west jet of YSO2.

We further examine the nature of YSO1 and YSO2 by constructing the spectral energy distributions (SEDs) of YSO1 and YSO2 to understand their probable evolutionary phase using the radiative transfer models of Robitaille et al. (2007). The SEDs have been created using Optical, NIR and MIR flux densities. The optical B and V filter flux densities were taken from the Yale/San Juan Southern Proper Motion Catalog, SPM4 (Girard et al., 2011). The NIR and MIR flux densities were taken from WFCAM-UKIRT and UIST-UKIRT observations along with Spitzer-IRAC (Qiu et al., 2008) and MSX (Egan et al., 2003) archival data. We have applied upper limits to the sub-mm flux densities based on measurements by Di Francesco et al. (2008). We have fitted the observed NIR to sub-mm SED of YSO 1 and 2 with the Robitaille models assuming a distance of 1.4 kpc. The SEDs with ten best-fit models are shown in Fig. 5.9. The range of parameters corresponding to these models are shown in Table. 5.4. It is to be noted that values of A_V shown in the table correspond to the external foreground extinction and in the case of YSO1 for which the orientation of the disk is edge-on, A_V goes up to $\sim 10^3$ mags if we include extinction from the circumstellar material.

For the characterization of the nature of these sources we use the parameters such as mass, luminosity, effective temperature etc. obtained from the best-fit models.

Table 5.4: Parameters of the models shown in Fig 5.9. The rows corresponding to column 1 give chi-square value of the fit, mass, effective temperature, luminosity, inclination angle, envelope accretion rate, disk mass, extinction and age, respectively. Columns 2 and 3 list the range of parameters of YSO1 and YSO2, respectively, with the best fit values given in brackets.

Parameter Name	Range of parameters (best fit)	
	YSO1	YSO2
χ^2	110.9 – 179.6 (110.9)	68.1 – 96.4 (68.1)
Mass ($M_\odot$)	6.1 – 7.1 (7.1)	5.7 – 9.6 (5.7)
T_{eff} (K)	5569 – 20530 (5569)	5569 – 7558 (7558)
Luminosity (10^2 $L_\odot$)	3.3 – 16.9 (7.5)	3.8 – 24.0 (3.8)
Inc. Angle (°)	81.4 – 87.1 (87.1)	18.2 – 87.1 (18.2)
Env. Accretion Rate ($M_\odot$ yr^{-1})	3.9×10^{-6} – 2.1×10^{-5} (2.1×10^{-5})	8.8×10^{-6} – 3.6×10^{-5} (8.8×10^{-6})
Disk Mass ($M_\odot$)	4.3×10^{-3} – 2.1×10^{-1} (2.1×10^{-1})	2.3×10^{-4} – 2.1×10^{-1} (2.3×10^{-4})
A_V (mag)	1.3 – 2.9 (1.3)	2.3 – 6.8 (4.0)
Age (10^5 Yrs)	1.1 – 6.5 (1.1)	0.4 – 3.5 (3.5)

The central protostellar objects are inferred to be intermediate-mass to massive with best-fit values of 7.1 and 5.7 $M_\odot$, respectively. The best-fit effective temperatures are ~ 5500 and ~ 7500 K. The best-fit model luminosities of YSO1 and YSO2 are similar, 7500 and 3800 $L_\odot$. We note that this is consistent with the inferences in Aspin & Geballe (1992) and Qiu et al. (2008). Robitaille et al. (2006) models provide a classification scheme for YSOs based on the best fit parameters obtained. The classification is based on the parameters: (i) Central object mass ($M_\star$), (ii) Envelope accretion Rate ($\dot{M}_{env}$), and (iii) disk mass (M_{disk}). An $\dot{M}_{env}/M_\star > 10^{-6}$ yr^{-1} implies the object is a Stage 0/1 object with infalling envelope, with a possibility of a disk component. A stage II source is one with $\dot{M}_{env}/M_\star < 10^{-6}$ yr^{-1} and $M_{disk}/M_\star > 10^{-6}$. In this case, the source has an optically thick disk with a remnant infalling envelope. A stage III source is one with $\dot{M}_{env}/M_\star < 10^{-6}$ yr^{-1} and $M_{disk}/M_\star < 10^{-6}$. This has an optically thin disk. Based on this classification scheme, we note that both YSO 1 and 2 are Stage 0/I objects having contribution of a disk component in the SED. We also note with caution that these parameters are derived for an assumed distance of 1.4 kpc. Depending on the actual distance, the mass and other parameters would get scaled.

Although the stage classification followed by this model is analogous to the YSOs classes (Lada, 1987; Adams et al., 1987), stages are decided based on physical properties such as disk mass, envelope accretion rate etc., whereas classes are based on the NIR slope of the observed SED. Although this model classifies YSO1 and YSO2 as Stage 0/1 objects (with infalling envelope and a disk component), we cannot rule out the possibility that these are Class II objects as they exhibit optical emission. In this context, it is important to take into account the caveats faced by the model. The major caveats are: (i) stars of all masses are assumed to be formed via disk and envelope accretion (ii) the model assumes that only one source is present even if multiple sources could be illuminating the envelope, (iii) PAH emission or continuum emission from small grains are not considered although this could contribute significantly in MIR (iv) flared disk geometry is assumed, which may not be applicable to very high mass sources. More caveats of this model are discussed in detail in Robitaille et al. (2006) and Robitaille et al. (2007).

5.7 Summary

In this chapter, we present the first time detection of NIR H_2 and [Fe II] emission lines and a comprehensive NIR/MIR view of shock formation associated with the HH80-81 jet. We discuss the knots generated by the HH80-81 jet in the context of strong, intermediate and weak shocks. We have utilized NIR H_2 and [Fe II] emission lines to characterize the nature of the shocks at play in various knots. In the northern arm of the jet, we find that the knots closer to the central YSO show only [Fe II] emission, the knots at intermediate distance show a combination of [Fe II] and H_2 emission and the farther knots show only H_2 emission. From this, we infer that the shock strength is highest close to the driving source which gradually weakens with an increase in radial distance. In the southern arm, the shocks do not show such a transition but rather remain strong enough to excite [Fe II] even in the farther knots of the jet, and thus all the knots in this direction show both H_2 and [Fe II] emission. The knots in the southern arm have complex morphologies compared to the north and we attribute it to lower ambient density in the southern side. We determine the H_2 (2.122 μm) and [Fe II] (1.644 μm) luminosities of all the knots to be in the range $0.5 - 13.2 \times 10^{31}$ erg s^{-1} and $0.3 - 34.5 \times 10^{32}$ erg s^{-1}, respectively. For those knots in which [Fe II] emission is detected, we obtain mass-loss rates of $\sim 3.0 \times 10^{-7} - 5.2 \times 10^{-5}$ M$_\odot$ yr^{-1} which are consistent with the estimates from other massive protostars. We correlate the arcs and knots in H_2 emission towards the central region with multiple outflows detected as well as with YSOs in the vicinity.

Chapter 6

Conclusions and Future Scope

6.1 Conclusions

The primary objective of this thesis has been to improve our understanding of various physical properties of protostellar jets for which we have undertaken a study of theoretical and observational aspects of these jets. For this, we have primarily modeled the radio emission from protostellar jets and have carried out NIR imaging along with detailed shock analysis of a prominent massive protostellar jet. The following summarizes the main results and conclusions from each of the chapters.

In Chapter 2, we have presented the details of the numerical model which we have formulated to explain the observed radio spectral indices of protostellar jets using thermal and non-thermal emission mechanisms. The model flux densities include contribution from an inner thermal jet, and a combination of emission from thermal and non-thermal distributions along the edges and extremities, where the jet interacts with the interstellar medium. Additionally, the effect of varying ionization fraction laterally across the jet was also incorporated while estimating the flux densities. In this chapter, we have first demonstrated the dependence of model geometry on the value of the parameter ϵ which characterizes the radial profile of the jet. The geometry, that results from different values of ϵ, shows that, $\epsilon = 1$ represents the case of a conical jet with a constant opening angle, and $\epsilon = 0$ would imply a constant width throughout the jet, suggesting a highly collimated nature of the jet. Values with $\epsilon > 1$ would lead to increase in opening angle with radial distance. In addition to the model geometry, we have also described in detail the other input model parameters and the emission mechanisms incorporated. We have then demonstrated that, although the number density which is contributing to the emission in Reynolds model is different from that of our numerical model for a given LOS, the flux difference is not considerable. In the rest of the chapter, we have discussed in detail the emission mechanisms, their relative geometry and the estimation of model flux densities.

In Chapter 3, we have generated sample model spectra for typical values of jet parameters. We have then explored the effect of the major improvements and generalizations of our model on the overall flux densities by comparing our model spectrum with that of the Reynolds model. Compared to the Reynolds model, the significant improvements of our model include the following.

(a) We incorporate a more general geometry and do not assume a small opening angle for the jet.

(b) A significant addition is the inclusion of non-thermal synchrotron emission. In order to include this, we take insights from observations of protostellar jets where the synchrotron emission is observed from the edges and termination regions of the jet (Rodríguez-Kamenetzky et al., 2016, 2017).

(c) We have also added the lateral variation of ionization fraction across the jet cross-section. At any given length, the jet has maximum ionization fraction along the long central-axis and the fraction of ionized gas decreases with distance from the axis outwards to the cross-sectional edge.

(d) We have accommodated intermediate optical depth values corresponding to intermediate radial distances.

Given these aspects, a comparison of our model with the Reynolds model leads us to the conclusion that as a consequence of the approximations assumed in the calculation of geometry and emission mechanisms, the Reynolds model over-estimates the flux densities of jets. Our generalized model can therefore predict the spectra of protostellar jets more accurately and can be applied to jets with wide as well as narrow opening angles.

Further, an investigation of radio emission and spectra along the jet also shows the dependence of the emission process and optical depth along the line of sight. The model can be used to estimate the spectrum of a fully thermal jet as well as a jet with thermal and non-thermal emission. This can be achieved by assigning the value of either of the parameters η_e^{rel} or $\delta\theta$ to be 0. In this chapter, we have chosen η_e^{rel} for this purpose. We have shown the influence of η_e^{rel} on the dominant emission mechanism of the jet and it is seen that as η_e^{rel} increases, the spectrum transforms from thermal emission dominated to a non-thermal dominated one. We have also demonstrated the variation in the behavior of radio emission as a function of projected length of the jet. The resulting spectra exhibit a transition from free-free to synchrotron dominated flux as one moves from the base to the top of the jet. We have then analyzed the spectra generated by the model by examining the dependence of the major spectral features such as turnover frequencies and spectral indices (between 10 MHz and 300 GHz) on the different physical parameters of the radio jet. A careful inspection of the behavior of the turnover frequencies with the parameter values show that the turnover from fully optically thick to optically thin jet occurs at higher frequencies when the amount of particles contributing to the emission increases, which could be brought about by an increase in any of the parameters, such as, n_0, r_0, x_0, η_e^{rel}, B_0, p, $\delta\theta$, or a decrease in either of $|q_n|$, $|q_x|$, $|q'_x|$. We have also examined the relative contribution of different regions of the jet to the total flux density, and the results indicate that emission from the base of the jet dominates the overall emission.

In Chapter 4, we have applied our toy model to the observational data of a few prominent protostellar jets which include the HH80-81 jet, a jet driven by the massive YSO G114.0835+02.8568 and the DG-Tau jet. For the case of HH80-81 jet, we have considered the emission towards the central region of the jet, and towards HH80 and HH81 knots. For each of these knots, we have generated best fit models for two epochs corresponding to two frequency windows. For the remaining jets studied in this chapter, we have generated best fit models for single epoch of observations. Through this, we obtained various physical parameters of the knots which are otherwise difficult to be solely determined from observations. The parameters obtained from the fitting include q_n, q_x, q'_x, $\delta\theta$, p, η_e^{rel} and n_0 depending on whichever parameter is not available from previous studies and needs to be constrained. Using electron number densities of $200 - 10^5$ cm^{-3} for these knots, we find the absolute values of power-law indices for ionization fraction profile in the radial ($|q_x|$) and lateral ($|q'_x|$) direction to be in the range $0.2 - 5$ and $0 - 4.5$, respectively. The jet edges that contribute to synchrotron emission contains non-thermal electron population with η_e^{rel} in the range $10^{-7} - 10^{-4}$ which is consistent with the typical values observed in jet shocks. For the best-fit parameter sets, the model spectral indices of all the knots lie in the range -0.60 to +0.13 within the corresponding observed frequency windows. For all the sources, we have also generated the χ^2 plots for each parameter by keeping that particular parameter fixed at its best-fit value and varying the remaining parameters. These plots, exhibiting minimum χ^2 at the best-fit values of each parameter, show the robustness of the fitting procedure.

In Chapter 5, we present new NIR line imaging observations of the HH80-81 jet in the H_2 (2.122 μm) and [Fe II] (1.644 μm) lines. These emission lines have enabled us to trace not only the jet close to the exciting source but also the knots located farther away. We have detected nine groups of knot-like structures in the jet including HH80 and HH81 spaced $0.2 - 0.9$ pc apart. The knots in the northern arm of the jet show only [Fe II] emission closer to the exciting source, a combination of [Fe II] and H_2 at intermediate distances, and solely H_2 emission farther outwards. Towards the southern arm, all the knots exhibit both H_2 and [Fe II] emission. The nature of the shocks is inferred by assimilating the NIR observations with radio and X-ray observations from literature. In the northern arm, we infer the presence of strong dissociative shocks (J-type shocks) in the knots located close to the exciting source. The knots in the southern arm, that include HH80 and HH81, are explicable as a combination of strong and weak (C-type shocks) shocks. In general, the emission resulting from rovibrational transition of H_2 molecule originate in slow C-type shocks or in the cooler wings of J-type shocks, since molecular H_2 requires slow and weak shocks for it to be sustained in molecular form without being dissociated. [Fe II] line emission, on the other hand, will be prevalent in strong dissociative shocks that are capable of grain destruction which releases the Fe atoms in gas phase trapped within them, indicating the need for J-type shocks shocks in those regions. For the knots towards which both emission lines were detected, we estimated the ratio of [Fe II] and H_2 fluxes. This ratio, represented by $\mathcal{R}$ is found to decrease with radial distance from the central driving source indicating the weakening of shocks as they move further out into the ambient medium. Assuming a variable extinction along the length of the jet, we have calculated the knot luminosities in both the narrow-band images. These luminosities are comparable to that of other high mass YSOs. The mass-loss rates of the knots determined from [Fe II] luminosities are in the range $\sim 3.0 \times 10^{-7} - 5.2 \times 10^{-5}$ $M_\odot$ yr^{-1}, consistent with those from massive protostars and higher than typical values seen in low mass YSOs.

In addition to examining the HH80-81 main jet, we have also investigated the molecular H_2 emission and the broad-band NIR emission in the neighborhood of the driving source. Close to the driving source of the jet, we have identified, for the first time, seven new MHOs, which are oriented in directions different from that of the HH80-

81 jet. These appear as various arcs in H_2 emission which resemble bow shocks, and strings of H_2 knots which reveal traces of multiple outflows. Further, we have examined the nature of two YSOs, namely YSO 1 and 2, in the central region by constructing their SEDs and identifying their probable evolutionary phase using radiative transfer models. Through this we conclude that both YSO 1 and 2 are Stage 0/I objects having contribution of a disk component in the SED.

6.2 Future scope

We have developed the numerical model for the radio spectra of protostellar jets by accommodating a simplistic geometry. However in realistic scenarios, the jet dynamics would result in a more complex morphology for which magneto-hydrodynamics need to be considered in predicting the jet geometry more accurately. Sophisticated time dependent simulations, that can take into account the knot structure and evolution, jet collimation etc., will be suitable for more precise estimation of their radio fluxes. We next intend to carry out simulations that could assist us in enabling a more realistic jet geometry and also help in reducing the number of free parameters that could make the application of our model to the observed data of protostellar jets more effective. Additionally, the modeling study will benefit from lower frequency observations (eg. low frequency array (LOFAR)), since synchrotron emission is stronger at these frequencies. Higher resolution observations with the help of telescopes such as square kilometer array (SKA) can also provide more details about the structure and morphology of these jets and enable us to locate the exact regions of the jet that give rise to synchrotron emission.

In the second part of this thesis, we have carried out a detailed imaging study of the largest known protostellar jet in the Galaxy, the HH80-81 jet, using the NIR emission lines to morphologically characterize the nature of shocks in the jet knots and to estimate relevant physical parameters of the jet. However, imaging observations cannot provide certain parameters such as velocity information, electron density, ionization fraction etc. and also cannot assist in the identification of the exact the excitation mechanism of ro-vibrational transition of molecular H_2. This will only be possible with the help of spectroscopic analysis. It is therefore instructive to carry out spectroscopic observations to utilize the diagnostic capabilities of the NIR emission lines and a follow-up study of the HH80-81 jet and other jets from massive protostars for generalizing the results. Through a morphological analysis and numerical estimation we have identified a dominance of dissociative J-type shocks in HH80-81 jet. Extending this study to a larger sample of high and low mass stars, followed by a comparison between the two cases could help us generalize our understanding of the influence of parameters such as mass of the driving source, its environment, magnetic field strength etc., on the nature of shocks associated with protostellar jets. Furthermore, the estimation and comparison of parameters such as mass-loss rates and accretion rates for a sample of high and low mass protostellar jets could help in answering the question of whether high mass star formation is a scaled-up version of lower mass counterparts. These can be efficiently achieved with high resolution, high sensitivity, broad spectrum and wide field-of-view observations by instruments on-board space based telescopes as well as adaptive optics in ground based telescopes. This along with techniques such as integral field spectroscopy, can be provided by the current and upcoming telescopes such as the James Webb Space Telescope (JWST), the Thirty Meter Telescope (TMT), the Giant Magellan Telescope (GMT) etc.

Bibliography

Añez-López, N., Osorio, M., Busquet, G., Girart, J. M., Macías, E., Carrasco-González, C., Curiel, S., Estalella, R., Fernández-López, M., Galván-Madrid, R., Kwon, J., & Torrelles, J. M. 2020, APJ, 888, 41

Adams, F. C. & Gregory, S. G. 2012, APJ, 744, 55

Adams, F. C., Lada, C. J., & Shu, F. H. 1987, APJ, 312, 788

Afflerbach, A., Churchwell, E., Acord, J. M., Hofner, P., Kurtz, S., & Depree, C. G. 1996, ApJS, 106, 423

Agra-Amboage, V., Dougados, C., Cabrit, S., & Reunanen, J. 2011, A& A, 532, A59

Ainsworth, R. E., Scaife, A. M. M., Ray, T. P., Taylor, A. M., Green, D. A., & Buckle, J. V. 2014, ApJ, 792, L18

Andre, P., Ward-Thompson, D., & Barsony, M. 1993, APJ, 406, 122

Andre, P., Ward-Thompson, D., & Barsony, M. Protostars and Planets IV, ed. , V. ManningsA. P. Boss & S. S. Russell, 59

Anglada, G., Rodríguez, L. F., & Carrasco-González, C. 2018, A&A Rev., 26, 3

Antoniucci, S., García López, R., Nisini, B., Caratti o Garatti, A., Giannini, T., & Lorenzetti, D. 2014, A& A, 572, A62

Antoniucci, S., Nisini, B., Giannini, T., & Lorenzetti, D. 2008, A& A, 479, 503

Araudo, A. T., Padovani, M., & Marcowith, A. 2021, MNRAS, 504, 2405

Araudo, A. T., Romero, G. E., Bosch-Ramon, V., & Paredes, J. M. 2007, A& A, 476, 1289

Arce, H. 2003, Revista Mexicana de Astronomía y Astrofísica, 15, 123

Arce, H. G., Shepherd, D., Gueth, F., Lee, C. F., Bachiller, R., Rosen, A., & Beuther, H. Protostars and Planets V, ed. , B. ReipurthD. Jewitt & K. Keil, 245

Aspin, C. & Geballe, T. R. 1992, A& A, 266, 219

Aspin, C., McCaughrean, M. J., Casali, M. M., & Geballe, T. R. 1991, A& A, 252, 299

Asplund, M., Amarsi, A. M., & Grevesse, N. 2021, A& A, 653, A141

Axford, W. I., Leer, E., & Skadron, G. 1977, in International Cosmic Ray Conference, Vol. 11, International Cosmic Ray Conference, 132

Bacciotti, F. Revista Mexicana de Astronomia y Astrofisica Conference Series, ed. , W. J. HenneyW. SteffenL. Binette & A. Raga, 8–15

Bacciotti, F., Chiuderi, C., & Oliva, E. 1995, A& A, 296, 185

Bacciotti, F. & Eislöffel, J. 1999, A& A, 342, 717

Bachiller, R., Pérez Gutiérrez, M., Kumar, M. S. N., & Tafalla, M. 2001, A& A, 372, 899

Bally, J. 2016, Annual Review of Astronomy and Astrophysics, 54, 491 [LINK]

Bally, J. 2016, ARA&A, 54, 491

Bally, J., Heathcote, S., Reipurth, B., Morse, J., Hartigan, P., & Schwartz, R. 2002, AJ, 123, 2627

Bally, J., Heathcote, S., Reipurth, B., Morse, J., Hartigan, P., & Schwartz, R. 2002, The Astronomical Journal, 123, 2627 [LINK]

Bally, J., Morse, J., & Reipurth, B. Science with the Hubble Space Telescope - II, ed. , P. BenvenutiF. D. Macchetto & E. J. Schreier, 491

Bally, J., Reipurth, B., & Davis, C. J. 2007, Protostars and Planets V, 215

Bally, J., Reipurth, B., & Davis, C. J. Protostars and Planets V, ed. , B. ReipurthD. Jewitt & K. Keil, 215

Bally, J. & Zinnecker, H. 2005, AJ, 129, 2281

Barsony, M. & Kenyon, S. J. 1992, ApJ, 384, L53

Beck, T. L., Riera, A., Raga, A. C., & Reipurth, B. 2007, AJ, 133, 1221

Beckwith, S., Persson, S. E., Neugebauer, G., & Becklin, E. E. 1978, APJ, 223, 464

Bellan, P. M., You, S., & Hsu, S. C. 2005, Simulating Astrophysical Jets in Laboratory Experiments, ed. G. Kyrala (Dordrecht: Springer Netherlands), 203–209 [LINK]

Benaglia, P. 2011, in Revista Mexicana de Astronomia y Astrofisica Conference Series, Vol. 40, Revista Mexicana de Astronomia y Astrofisica Conference Series, 211–216

Benedettini, M., Molinari, S., Testi, L., & Noriega-Crespo, A. 2004, Monthly Notices of the Royal Astronomical Society, 347, 295 [LINK]

Benjamin, R., Churchwell, E., Meade, M., Babler, B., Whitney, B., Merrifield, M., Cohen, M., Watson, C., & Blommaert, J. 2006, GLIMPSE 3D: The Vertical Stellar and Interstellar Structure of the Inner Galaxy, Spitzer Proposal ID 30570

Berezhko, E. G. & Ellison, D. C. 1999, APJ, 526, 385

Bessell, M. S. & Brett, J. M. 1988, PASP, 100, 1134

Beuther, H., Churchwell, E. B., McKee, C. F., & Tan, J. C. Protostars and Planets V, ed. , B. ReipurthD. Jewitt & K. Keil, 165

Beuther, H., Leurini, S., Schilke, P., Wyrowski, F., Menten, K. M., & Zhang, Q. 2007b, A& A, 466, 1065

Beuther, H., Schilke, P., Menten, K. M., Motte, F., Sridharan, T. K., & Wyrowski, F. 2002a, APJ, 566, 945

Beuther, H., Schilke, P., Sridharan, T. K., Menten, K. M., Walmsley, C. M., & Wyrowski, F. 2002b, A& A, 383, 892

Beuther, H., Walsh, A., Schilke, P., Sridharan, T. K., Menten, K. M., & Wyrowski, F. 2002c, A& A, 390, 289

Biermann, P. L. & Strittmatter, P. A. 1987, APJ, 322, 643

Birkinshaw, M. 1997, in Advanced Topics on Astrophysical and Space Plasmas, 17

Bjerkeli, P., Liseau, R., Nisini, B., Tafalla, M., Benedettini, M., Bergman, P., Dionatos, O., Giannini, T., Herczeg, G., Justtanont, K., Larsson, B., McOey, C., Olberg, M., & Olofsson, A. O. H. 2011, A& A, 533, A80

Bjerkeli, P., Ramsey, J. P., Harsono, D., Calcutt, H., Kristensen, L. E., van der Wiel, M. H. D., Jørgensen, J. K., Muller, S., & Persson, M. V. 2019, A& A, 631, A64

Bjerkeli, P., van der Wiel, M. H. D., Harsono, D., Ramsey, J. P., & Jørgensen, J. K. 2016, Natur, 540, 406

Blandford, R. & Eichler, D. 1987, , 154, 1

Blandford, R., Meier, D., & Readhead, A. 2019, Annual Review of Astronomy and Astrophysics, 57, 467 [LINK]

Blandford, R. D. & Ostriker, J. P. 1978, ApJ, 221, L29

Blandford, R. D. & Payne, D. G. 1982, MNRAS, 199, 883

Blitz, L. & Shu, F. H. 1980, APJ, 238, 148

Böhm, K.-H. 1995, , 233, 11

Bonnell, I. A., Bate, M. R., & Price, N. M. 1996, Monthly Notices of the Royal Astronomical Society, 279, 121 [LINK]

Bontemps, S., Andre, P., Terebey, S., & Cabrit, S. 1996, A& A, 311, 858

Bosch-Ramon, V., Romero, G. E., Araudo, A. T., & Paredes, J. M. 2010, A& A, 511, A8

Brand, P. W. J. L. 2006, The Observatory, 126, 62

Bronfman, L., Cohen, R. S., Alvarez, H., May, J., & Thaddeus, P. 1988, APJ, 324, 248

Brugel, E. W. 1990, High Velocity Interstellar Shocks: Herbig-Haro Objects in Cepheus A, and HH-34, IUE Proposal ID HHLEB

Burton, M. G. 1987, PhD thesis, University of Edinburgh, UK

Busquet, G., Girart, J. M., Estalella, R., Fernández-López, M., Galván-Madrid, R., Anglada, G., Carrasco-González, C., Añez-López, N., Curiel, S., Osorio, M., Rodríguez, L. F., & Torrelles, J. M. 2019, A& A, 623, L8

Cabrit, S. in , Star-Disk Interaction in Young Stars, ed. J. BouvierI. Appenzeller, Vol. 243, 203–214

Calvet, N., Muzerolle, J., Briceño, C., Hernández, J., Hartmann, L., Saucedo, J. L., & Gordon, K. D. 2004, The Astronomical Journal, 128, 1294 [LINK]

Caratti o Garatti, A., Froebrich, D., Eislöffel, J., Giannini, T., & Nisini, B. 2008, A& A, 485, 137

Caratti o Garatti, A., Giannini, T., Nisini, B., & Lorenzetti, D. 2006, A& A, 449, 1077

Caratti o Garatti, A., Stecklum, B., Linz, H., Garcia Lopez, R., & Sanna, A. 2015, A& A, 573, A82

Carey, S. J., Clark, F. O., Egan, M. P., Price, S. D., Shipman, R. F., & Kuchar, T. A. 1998, APJ, 508, 721

Carrasco-González, C., Galván-Madrid, R., Anglada, G., Osorio, M., D'Alessio, P., Hofner, P., Rodríguez, L. F., Linz, H., & Araya, E. D. 2012, ApJ, 752, L29

Carrasco-González, C., Rodríguez, L. F., Anglada, G., Martí, J., Torrelles, J. M., & Osorio, M. 2010, Science, 330, 1209

Casali, M., Adamson, A., Alves de Oliveira, C., Almaini, O., Burch, K., Chuter, T., Elliot, J., Folger, M., Foucaud, S., Hambly, N., Hastie, M., Henry, D., Hirst, P., Irwin, M., Ives, D., Lawrence, A., Laidlaw, K., Lee, D., Lewis, J., Lunney, D., McLay, S., Montgomery, D., Pickup, A., Read, M., Rees, N., Robson, I., Sekiguchi, K., Vick, A., Warren, S., & Woodward, B. 2007, A& A, 467, 777

Casali, M. M. & Eiroa, C. 1996, A& A, 306, 427

Cerqueira, A. H. & de Gouveia Dal Pino, E. M. 2001, The Astrophysical Journal, 550, L91 [LINK]

Cesaroni, R., Moscadelli, L., Neri, R., Sanna, A., Caratti o Garatti, A., Eisloffel, J., Stecklum, B., Ray, T., & Walmsley, C. M. 2018, A& A, 612, A103

Chandler, C. J. & Richer, J. S. 2000, APJ, 530, 851

Cheng, Y., Qiu, K., Zhang, Q., Wyrowski, F., Menten, K., & Güsten, R. 2019, APJ, 877, 112

Chernoff, D. F. 1987, APJ, 312, 143

Codella, C., Cabrit, S., Gueth, F., Cesaroni, R., Bacciotti, F., Lefloch, B., & McCaughrean, M. J. 2007, A& A, 462, L53

Coffey, D., Bacciotti, F., & Podio, L. 2008, APJ, 689, 1112

Cranmer, S. R. 2008, APJ, 689, 316

—. 2009, APJ, 706, 824

Curiel, S., Ho, P. T. P., Patel, N. A., Torrelles, J. M., Rodríguez, L. F., Trinidad, M. A., Cantó, J., Hernández, L., Gómez, J. F., Garay, G., & Anglada, G. 2006, APJ, 638, 878

Curiel, S., Rodriguez, L. F., Moran, J. M., & Canto, J. 1993, APJ, 415, 191

Currie, M. J., Berry, D. S., Jenness, T., Gibb, A. G., Bell, G. S., & Draper, P. W. in , Astronomical Society of the Pacific Conference Series, Vol. 485, Astronomical Data Analysis Software and Systems XXIII, ed. N. MansetP. Forshay, 391

Dame, T. M., Elmegreen, B. G., Cohen, R. S., & Thaddeus, P. 1986, APJ, 305, 892

Davis, C. J. & Eisloeffel, J. 1995, A& A, 300, 851

Davis, C. J., Froebrich, D., Stanke, T., Megeath, S. T., Kumar, M. S. N., Adamson, A., Eislöffel, J., Gredel, R., Khanzadyan, T., Lucas, P., Smith, M. D., & Varricatt, W. P. 2009, A& A, 496, 153

Davis, C. J., Gell, R., Khanzadyan, T., Smith, M. D., & Jenness, T. 2010, A& A, 511, A24

Davis, C. J., Nisini, B., Takami, M., Pyo, T. S., Smith, M. D., Whelan, E., Ray, T. P., & Chrysostomou, A. 2006, APJ, 639, 969

Davis, C. J., Ray, T. P., Desroches, L., & Aspin, C. 2001, MNRAS, 326, 524

Davis, C. J., Scholz, P., Lucas, P., Smith, M. D., & Adamson, A. 2008, MNRAS, 387, 954

Davis, C. J., Smith, M. D., & Eislöffel, J. 2000, MNRAS, 318, 747

Davis, C. J., Stern, L., Ray, T. P., & Chrysostomou, A. 2002, A& A, 382, 1021

Davis, C. J., Varricatt, W. P., Todd, S. P., & Ramsay Howat, S. K. 2004, A& A, 425, 981

Davis, C. J., Whelan, E., Ray, T. P., & Chrysostomou, A. 2003, A& A, 397, 693

De Buizer, J. M. 2006, ApJ, 642, L57

de Gouveia dal Pino, E. M. & Birkinshaw, M. 1996, APJ, 471, 832

de Gouveia dal Pino, E. M., Birkinshaw, M., & Benz, W. 1996, ApJ, 460, L111

de Valon, A., Dougados, C., Cabrit, S., Louvet, F., Zapata, L. A., & Mardones, D. 2020, A& A, 634, L12

del Valle, M. V., Araudo, A., & Suzuki-Vidal, F. 2022, A& A, 660, A104

Dhawan, V., Mirabel, I. F., & Rodríguez, L. F. 2000, APJ, 543, 373

Di Francesco, J., Johnstone, D., Kirk, H., MacKenzie, T., & Ledwosinska, E. 2008, ApJS, 175, 277

Dinerstein, H. in , The Analysis of Emission Lines: A Meeting in Honor of the 70th Birthdays of D. E. Osterbrock & M. J. Seaton, ed. R. WilliamsM. Livio, 134

Dionatos, O., Nisini, B., Cabrit, S., Kristensen, L., & Pineau Des Forêts, G. 2010, A& A, 521, A7

Dionatos, O., Nisini, B., Garcia Lopez, R., Giannini, T., Davis, C. J., Smith, M. D., Ray, T. P., & DeLuca, M. 2009, APJ, 692, 1

Dobbs, C. L., Krumholz, M. R., Ballesteros-Paredes, J., Bolatto, A. D., Fukui, Y., Heyer, M., Low, M. M. M., Ostriker, E. C., & Vázquez-Semadeni, E. H. Beuther, R. S. KlessenC. P. Dullemond & T. Henning, 3

Dougados, C., Cabrit, S., Lavalley, C., & Ménard, F. 2000, A& A, 357, L61

Dougherty, S. M., Pittard, J. M., Kasian, L., Coker, R. F., Williams, P. M., & Lloyd, H. M. 2003, A& A, 409, 217

Draine, B. T. 1980, APJ, 241, 1021

—. 2011, Physics of the Interstellar and Intergalactic Medium

Draine, B. T. & McKee, C. F. 1993, ARA&A, 31, 373

Draine, B. T. & Woods, D. T. 1989, in Infrared Spectroscopy in Astronomy, ed. E. Böhm-Vitense, 155

Drozdovskaya, M. N., Walsh, C., Visser, R., Harsono, D., & van Dishoeck, E. F. 2015, Monthly Notices of the Royal Astronomical Society, 451, 3836 [LINK]

Duarte-Cabral, A., Bontemps, S., Motte, F., Hennemann, M., Schneider, N., & André, P. 2013, A& A, 558, A125

Dunham, M. M., Arce, H. G., Allen, L. E., II, N. J. E., Broekhoven-Fiene, H., Chapman, N. L., Cieza, L. A., Gutermuth, R. A., Harvey, P. M., Hatchell, J., Huard, T. L., Kirk, J. M., Matthews, B. C., Merín, B., Miller, J. F., Peterson, D. E., & Spezzi, L. 2013, The Astronomical Journal, 145, 94 [LINK]

Egan, M. P., Price, S. D., Kraemer, K. E., Mizuno, D. R., Carey, S. J., Wright, C. O., Engelke, C. W., Cohen, M., & Gugliotti, M. G. 2003, VizieR Online Data Catalog, V/114

Egan, M. P., Shipman, R. F., Price, S. D., Carey, S. J., Clark, F. O., & Cohen, M. 1998, ApJ, 494, L199

Eisloffel, J., Davis, C. J., Ray, T. P., & Mundt, R. 1994, ApJ, 422, L91

Eisloffel, J. & Mundt, R. 1997, AJ, 114, 280

Eislöffel, J. & Mundt, R. 1998, AJ, 115, 1554

Eislöffel, J., Smith, M. D., & Davis, C. J. 2000, A& A, 359, 1147

Ellerbroek, L. E., Podio, L., Kaper, L., Sana, H., Huppenkothen, D., de Koter, A., & Monaco, L. 2013, A& A, 551, A5

Ellingsen, S. P., Breen, S. L., Caswell, J. L., Quinn, L. J., & Fuller, G. A. 2010, Monthly Notices of the Royal Astronomical Society, 404, 779 [LINK]

Evans, Neal J., I., Dunham, M. M., Jørgensen, J. K., Enoch, M. L., Merín, B., van Dishoeck, E. F., Alcalá, J. M., Myers, P. C., Stapelfeldt, K. R., Huard, T. L., Allen, L. E., Harvey, P. M., van Kempen, T., Blake, G. A., Koerner, D. W., Mundy, L. G., Padgett, D. L., & Sargent, A. I. 2009, ApJS, 181, 321

Fazio, G. G., Hora, J. L., Allen, L. E., Ashby, M. L. N., Barmby, P., Deutsch, L. K., Huang, J. S., Kleiner, S., Marengo, M., Megeath, S. T., Melnick, G. J., Pahre, M. A., Patten, B. M., Polizotti, J., Smith, H. A., Taylor, R. S., Wang, Z., Willner, S. P., Hoffmann, W. F., Pipher, J. L., Forrest, W. J., McMurty, C. W., McCreight, C. R., McKelvey, M. E., McMurray, R. E., Koch, D. G., Moseley, S. H., Arendt, R. G., Mentzell, J. E., Marx, C. T., Losch, P., Mayman, P., Eichhorn, W., Krebs, D., Jhabvala, M., Gezari, D. Y., Fixsen, D. J., Flores, J., Shakoorzadeh, K., Jungo, R., Hakun, C., Workman, L., Karpati, G., Kichak, R., Whitley, R., Mann, S., Tollestrup, E. V., Eisenhardt, P., Stern, D., Gorjian, V., Bhattacharya, B., Carey, S., Nelson, B. O., Glaccum, W. J., Lacy, M., Lowrance, P. J., Laine, S., Reach, W. T., Stauffer, J. A., Surace, J. A., Wilson, G., Wright, E. L., Hoffman, A., Domingo, G., & Cohen, M. 2004, ApJS, 154, 10

Fedriani, R., Caratti o Garatti, A., Coffey, D., Garcia Lopez, R., Kraus, S., Weigelt, G., Stecklum, B., Ray, T. P., & Walmsley, C. M. 2018, A& A, 616, A126

Fedriani, R., Caratti o Garatti, A., Koutoulaki, M., Garcia-Lopez, R., Natta, A., Cesaroni, R., Oudmaijer, R., Coffey, D., Ray, T., & Stecklum, B. 2020, A& A, 633, A128

Fedriani, R., Caratti o Garatti, A., Purser, S. J. D., Sanna, A., Tan, J. C., Garcia-Lopez, R., Ray, T. P., Coffey, D., Stecklum, B., & Hoare, M. 2019, Nature Communications, 10, 3630

Feeney-Johansson, A., Purser, S. J. D., Ray, T. P., Eislöffel, J., Hoeft, M., Drabent, A., & Ainsworth, R. E. 2019, ApJ, 885, L7

Felli, M., Massi, F., Robberto, M., & Cesaroni, R. 2006, A& A, 453, 911

Fermi, E. 1949, Physical Review, 75, 1169

Fernandes, A. J. L. & Brand, P. W. J. L. 1998, , 261, 179

Fernández-López, M., Girart, J. M., Curiel, S., Zapata, L. A., Fonfría, J. P., & Qiu, K. 2013, APJ, 778, 72

Fernández-López, M., Girart, J. M., Curiel, S., Zapata, L. A., Fonfría, J. P., & Qiu, K. 2013, The Astrophysical Journal, 778, 72 [LINK]

Fernández-López, M., Girart, J. M., Curiel, S., Gómez, Y., Ho, P. T. P., & Patel, N. 2011, The Astronomical Journal, 142, 97 [LINK]

Ferrari, A., Massaglia, S., & Trussoni, E. 1982, MNRAS, 198, 1065

Ferreira, J., Dougados, C., & Cabrit, S. 2006, A& A, 453, 785

Ferreira, J., Pelletier, G., & Appl, S. 2000, MNRAS, 312, 387

Field, G. B. 1965, APJ, 142, 531

Flower, D. R., Le Bourlot, J., Pineau des Forêts, G., & Cabrit, S. 2003, MNRAS, 341, 70

Flower, D. R. & Pineau des Forêts, G. 2003, MNRAS, 343, 390

Fontani, F., Cesaroni, R., & Furuya, R. S. 2010, A& A, 517, A56

Froebrich, D., Davis, C. J., Ioannidis, G., Gledhill, T. M., Takami, M., Chrysostomou, A., Drew, J., Eislöffel, J., Gosling, A., Gredel, R., Hatchell, J., Hodapp, K. W., Kumar, M. S. N., Lucas, P. W., Matthews, H., Rawlings, M. G., Smith, M. D., Stecklum, B., Varricatt, W. P., Lee, H. T., Teixeira, P. S., Aspin, C., Khanzadyan, T., Karr, J., Kim, H. J., Koo, B. C., Lee, J. J., Lee, Y. H., Magakian, T. Y., Movsessian, T. A., Nikogossian, E. H., Pyo, T. S., & Stanke, T. 2011, MNRAS, 413, 480

Fukui, Y., Iwata, T., Mizuno, A., Bally, J., & Lane, A. P. in , Protostars and Planets III, ed. E. H. LevyJ. I. Lunine, 603

Gaia Collaboration, Brown, A. G. A., Vallenari, A., Prusti, T., de Bruijne, J. H. J., Mignard, F., Drimmel, R., Babusiaux, C., Bailer-Jones, C. A. L., Bastian, U., Biermann, M., Evans, D. W., Eyer, L., Jansen, F., Jordi, C., Katz, D., Klioner,

S. A., Lammers, U., Lindegren, L., Luri, X., O'Mullane, W., Panem, C., Pourbaix, D., Randich, S., Sartoretti, P., Siddiqui, H. I., Soubiran, C., Valette, V., van Leeuwen, F., Walton, N. A., Aerts, C., Arenou, F., Cropper, M., Høg, E., Lattanzi, M. G., Grebel, E. K., Holland, A. D., Huc, C., Passot, X., Perryman, M., Bramante, L., Cacciari, C., Castañeda, J., Chaoul, L., Cheek, N., De Angeli, F., Fabricius, C., Guerra, R., Hernández, J., Jean-Antoine-Piccolo, A., Masana, E., Messineo, R., Mowlavi, N., Nienartowicz, K., Ordóñez-Blanco, D., Panuzzo, P., Portell, J., Richards, P. J., Riello, M., Seabroke, G. M., Tanga, P., Thévenin, F., Torra, J., Els, S. G., Gracia-Abril, G., Comoretto, G., Garcia-Reinaldos, M., Lock, T., Mercier, E., Altmann, M., Andrae, R., Astraatmadja, T. L., Bellas-Velidis, I., Benson, K., Berthier, J., Blomme, R., Busso, G., Carry, B., Cellino, A., Clementini, G., Cowell, S., Creevey, O., Cuypers, J., Davidson, M., De Ridder, J., de Torres, A., Delchambre, L., Dell'Oro, A., Ducourant, C., Frémat, Y., García-Torres, M., Gosset, E., Halbwachs, J. L., Hambly, N. C., Harrison, D. L., Hauser, M., Hestroffer, D., Hodgkin, S. T., Huckle, H. E., Hutton, A., Jasniewicz, G., Jordan, S., Kontizas, M., Korn, A. J., Lanzafame, A. C., Manteiga, M., Moitinho, A., Muinonen, K., Osinde, J., Pancino, E., Pauwels, T., Petit, J. M., Recio-Blanco, A., Robin, A. C., Sarro, L. M., Siopis, C., Smith, M., Smith, K. W., Sozzetti, A., Thuillot, W., van Reeven, W., Viala, Y., Abbas, U., Abreu Aramburu, A., Accart, S., Aguado, J. J., Allan, P. M., Allasia, W., Altavilla, G., Álvarez, M. A., Alves, J., Anderson, R. I., Andrei, A. H., Anglada Varela, E., Antiche, E., Antoja, T., Antón, S., Arcay, B., Bach, N., Baker, S. G., Balaguer-Núñez, L., Barache, C., Barata, C., Barbier, A., Barblan, F., Barrado y Navascués, D., Barros, M., Barstow, M. A., Becciani, U., Bellazzini, M., Bello García, A., Belokurov, V., Bendjoya, P., Berihuete, A., Bianchi, L., Bienaymé, O., Billebaud, F., Blagorodnova, N., Blanco-Cuaresma, S., Boch, T., Bombrun, A., Borrachero, R., Bouquillon, S., Bourda, G., Bouy, H., Bragaglia, A., Breddels, M. A., Brouillet, N., Brüsemeister, T., Bucciarelli, B., Burgess, P., Burgon, R., Burlacu, A., Busonero, D., Buzzi, R., Caffau, E., Cambras, J., Campbell, H., Cancelliere, R., Cantat-Gaudin, T., Carlucci, T., Carrasco, J. M., Castellani, M., Charlot, P., Charnas, J., Chiavassa, A., Clotet, M., Cocozza, G., Collins, R. S., Costigan, G., Crifo, F., Cross, N. J. G., Crosta, M., Crowley, C., Dafonte, C., Damerdji, Y., Dapergolas, A., David, P., David, M., De Cat, P., de Felice, F., de Laverny, P., De Luise, F., De March, R., de Martino, D., de Souza, R., Debosscher, J., del Pozo, E., Delbo, M., Delgado, A., Delgado, H. E., Di Matteo, P., Diakite, S., Distefano, E., Dolding, C., Dos Anjos, S., Drazinos, P., Duran, J., Dzigan, Y., Edvardsson, B., Enke, H., Evans, N. W., Eynard Bontemps, G., Fabre, C., Fabrizio, M., Faigler, S., Falcão, A. J., Farràs Casas, M., Federici, L., Fedorets, G., Fernández-Hernández, J., Fernique, P., Fienga, A., Figueras, F., Filippi, F., Findeisen, K., Fonti, A., Fouesneau, M., Fraile, E., Fraser, M., Fuchs, J., Gai, M., Galleti, S., Galluccio, L., Garabato, D., García-Sedano, F., Garofalo, A., Garralda, N., Gavras, P., Gerssen, J., Geyer, R., Gilmore, G., Girona, S., Giuffrida, G., Gomes, M., González-Marcos, A., González-Núñez, J., González-Vidal, J. J., Granvik, M., Guerrier, A., Guillout, P., Guiraud, J., Gúrpide, A., Gutiérrez-Sánchez, R., Guy, L. P., Haigron, R., Hatzidimitriou, D., Haywood, M., Heiter, U., Helmi, A., Hobbs, D., Hofmann, W., Holl, B., Holland , G., Hunt, J. A. S., Hypki, A., Icardi, V., Irwin, M., Jevardat de Fombelle, G., Jofré, P., Jonker, P. G., Jorissen, A., Julbe, F., Karampelas, A., Kochoska, A., Kohley, R., Kolenberg, K., Kontizas, E., Koposov, S. E., Kordopatis, G., Koubsky, P., Krone-Martins, A., Kudryashova, M., Kull, I., Bachchan, R. K., Lacoste-Seris, F., Lanza, A. F., Lavigne, J. B., Le Poncin-Lafitte, C., Lebreton, Y., Lebzelter, T., Leccia, S., Leclerc, N., Lecoeur-Taibi, I., Lemaitre, V., Lenhardt, H., Leroux, F., Liao, S., Licata, E., Lindstrøm, H. E. P., Lister, T. A., Livanou, E., Lobel, A., Löffler, W., López, M., Lorenz, D., MacDonald, I., Magalhães Fernandes, T., Managau, S., Mann, R. G., Mantelet, G., Marchal, O., Marchant, J. M., Marconi, M., Marinoni, S., Marrese, P. M., Marschalkó, G., Marshall, D. J., Martín-Fleitas, J. M., Martino, M., Mary, N., Matijevič, G., Mazeh, T., McMillan, P. J., Messina, S., Michalik, D., Millar, N. R., Mirand a, B. M. H., Molina, D., Molinaro, R., Molinaro, M., Molnár, L., Moniez, M., Montegriffo, P., Mor, R., Mora, A., Morbidelli, R., Morel, T., Morgenthaler, S., Morris, D., Mulone, A. F., Muraveva, T., Musella, I., Narbonne, J., Nelemans, G., Nicastro, L., Noval, L., Ordénovic, C., Ordieres-Meré, J., Osborne, P., Pagani, C., Pagano, I., Pailler, F., Palacin, H., Palaversa, L., Parsons, P., Pecoraro, M., Pedrosa, R., Pentikäinen, H., Pichon, B., Piersimoni, A. M., Pineau, F. X., Plachy, E., Plum, G., Poujoulet, E., Prša, A., Pulone, L., Ragaini, S., Rago, S., Rambaux, N., Ramos-Lerate, M., Ranalli, P., Rauw, G., Read, A., Regibo, S., Reylé, C., Ribeiro, R. A., Rimoldini, L., Ripepi, V., Riva, A., Rixon, G., Roelens, M., Romero-Gómez, M., Rowell, N., Royer, F., Ruiz-Dern, L., Sadowski, G., Sagristà Sellés, T., Sahlmann, J., Salgado, J., Salguero, E., Sarasso, M., Savietto, H., Schultheis, M., Sciacca, E., Segol, M., Segovia, J. C., Segransan, D., Shih, I. C., Smareglia, R., Smart, R. L., Solano, E., Solitro, F., Sordo, R., Soria Nieto, S., Souchay, J., Spagna, A., Spoto, F., Stampa, U., Steele, I. A., Steidelmüller, H., Stephenson, C. A., Stoev, H., Suess, F. F., Süveges, M., Surdej, J., Szabados, L., Szegedi-Elek, E., Tapiador, D., Taris, F., Tauran, G., Taylor, M. B., Teixeira, R., Terrett, D., Tingley, B., Trager, S. C., Turon, C., Ulla, A., Utrilla, E., Valentini, G., van Elteren, A., Van Hemelryck, E., van Leeuwen, M., Varadi, M., Vecchiato, A., Veljanoski, J., Via, T., Vicente, D., Vogt, S., Voss, H., Votruba, V., Voutsinas, S., Walmsley, G., Weiler, M., Weingrill, K., Wevers, T., Wyrzykowski, Ł., Yoldas, A., Žerjal, M., Zucker, S., Zurbach, C., Zwitter, T., Alecu, A., Allen, M., Allende Prieto, C., Amorim, A., Anglada-Escudé, G., Arsenijevic, V., Azaz, S., Balm, P., Beck, M., Bernstein, H. H., Bigot, L., Bijaoui, A., Blasco, C., Bonfigli, M., Bono, G., Boudreault, S., Bressan, A., Brown, S., Brunet, P. M., Bunclark, P., Buonanno, R., Butkevich, A. G., Carret, C., Carrion, C., Chemin, L., Chéreau, F., Corcione, L., Darmigny, E., de Boer, K. S., de Teodoro, P., de Zeeuw, P. T., Delle Luche, C., Domingues, C. D., Dubath, P., Fodor, F., Frézouls, B., Fries, A., Fustes, D., Fyfe, D., Gallardo, E., Gallegos, J., Gardiol, D., Gebran, M., Gomboc, A., Gómez, A., Grux, E., Gueguen, A., Heyrovsky, A., Hoar, J., Iannicola, G., Isasi Parache, Y., Janotto, A. M., Joliet, E., Jonckheere, A., Keil, R., Kim, D. W., Klagyivik, P., Klar, J., Knude, J., Kochukhov, O., Kolka, I., Kos, J., Kutka, A., Lainey, V., LeBouquin, D., Liu, C., Loreggia, D., Makarov, V. V., Marseille, M. G., Martayan, C., Martinez-Rubi, O., Massart, B., Meynadier, F., Mignot, S., Munari, U., Nguyen, A. T., Nordlander, T., Ocvirk, P., O'Flaherty, K. S., Olias Sanz, A., Ortiz, P., Osorio, J., Oszkiewicz, D., Ouzounis, A., Palmer, M., Park, P., Pasquato, E., Peltzer, C., Peralta, J., Péturaud, F., Pieniluoma, T., Pigozzi, E., Poels, J., Prat, G., Prod'homme, T., Raison, F., Rebordao, J. M., Risquez, D., Rocca-Volmerange, B., Rosen, S., Ruiz-Fuertes, M. I., Russo, F., Sembay, S., Serraller Vizcaino, I., Short, A., Siebert, A., Silva, H., Sinachopoulos, D., Slezak, E., Soffel, M., Sosnowska, D., Straižys, V., ter Linden, M., Terrell, D., Theil, S., Tiede, C., Troisi, L., Tsalmantza, P., Tur, D., Vaccari, M., Vachier, F., Valles, P., Van Hamme, W., Veltz, L., Virtanen, J., Wallut, J. M., Wichmann, R., Wilkinson, M. I., Ziaeepour, H., & Zschocke, S. 2016, A& A, 595, A2

Garay, G., Ramirez, S., Rodriguez, L. F., Curiel, S., & Torrelles, J. M. 1996, APJ, 459, 193

Garcia Lopez, R., Nisini, B., Eislöffel, J., Giannini, T., Bacciotti, F., & Podio, L. 2010, A& A, 511, A5

Garcia Lopez, R., Nisini, B., Giannini, T., Eislöffel, J., Bacciotti, F., & Podio, L. 2008, A& A, 487, 1019

Gatley, I., Hasegawa, T., Suzuki, H., Garden, R., Brand, P., Lightfoot, J., Glencross, W., Okuda, H., & Nagata, T. 1987, ApJ, 318, L73

Giannini, T., McCoey, C., Caratti o Garatti, A., Nisini, B., Lorenzetti, D., & Flower, D. R. 2004, A& A, 419, 999

Giannini, T., Nisini, B., Antoniucci, S., Alcalá, J. M., Bacciotti, F., Bonito, R., Podio, L., Stelzer, B., & Whelan, E. T. 2013, The Astrophysical Journal, 778, 71 [LINK]

Giannini, T., Nisini, B., Antoniucci, S., Alcalá, J. M., Bacciotti, F., Bonito, R., Podio, L., Stelzer, B., & Whelan, E. T. 2013, APJ, 778, 71

Girard, T. M., van Altena, W. F., Zacharias, N., Vieira, K., Casetti-Dinescu, D. I., Castillo, D., Herrera, D., Lee, Y. S., Beers, T. C., Monet, D. G., & López, C. E. 2011, AJ, 142, 15

Girart, J. M., Estalella, R., Fernández-López, M., Curiel, S., Frau, P., Galvan-Madrid, R., Rao, R., Busquet, G., & Juárez, C. 2017, APJ, 847, 58

Girart, J. M., Estalella, R., Viti, S., Williams, D. A., & Ho, P. T. P. 2001, ApJ, 562, L91

Girart, J. M., Fernández-López, M., Li, Z. Y., Yang, H., Estalella, R., Anglada, G., Áñez-López, N., Busquet, G., Carrasco-González, C., Curiel, S., Galvan-Madrid, R., Gómez, J. F., de Gregorio-Monsalvo, I., Jiménez-Serra, I., Krasnopolsky, R., Martí, J., Osorio, M., Padovani, M., Rao, R., Rodríguez, L. F., & Torrelles, J. M. 2018, ApJ, 856, L27

Gnedin, N. Y., Glover, S. C., Klessen, R. S., Springel, V., Klessen, R. S., & Glover, S. C. 2016, Star Formation in Galaxy Evolution: Connecting Numerical Models to Reality: Saas-Fee Advanced Course 43. Swiss Society for Astrophysics and Astronomy, 85

Gomez, M., Kenyon, S. J., & Whitney, B. A. 1997, AJ, 114, 265

Gomez, Y., Rodriguez, L. F., & Marti, J. 1995, APJ, 453, 268

Goodson, A. P. & Winglee, R. M. 1999, APJ, 524, 159

Govoni, F. & Feretti, L. 2004, International Journal of Modern Physics D, 13, 1549

Gredel, R. 2006, A& A, 457, 157

Gredel, R., Reipurth, B., & Heathcote, S. 1992, A& A, 266, 439

Greenhill, L. J., Goddi, C., Chandler, C. J., Matthews, L. D., & Humphreys, E. M. L. 2013, ApJ, 770, L32

Greenhill, L. J., Gwinn, C. R., Schwartz, C., Moran, J. M., & Diamond, P. J. 1998, Natur, 396, 650

Gregory, S. G., Donati, J. F., Morin, J., Hussain, G. A. J., Mayne, N. J., Hillenbrand, L. A., & Jardine, M. 2012, APJ, 755, 97

Güdel, M., Eibensteiner, C., Dionatos, O., Audard, M., Forbrich, J., Kraus, S., Rab, C., Schneider, C., Skinner, S., & Vorobyov, E. 2018, A& A, 620, L1

Güdel, M., Telleschi, A., Audard, M., Skinner, S. L., Briggs, K. R., Palla, F., & Dougados, C. 2007, A& A, 468, 515

Guillet, V., Pineau Des Forêts, G., & Jones, A. P. 2011, A& A, 527, A123

Gusdorf, A., Cabrit, S., Flower, D. R., & Pineau Des Forêts, G. 2008, A& A, 482, 809

Gutermuth, R. A., Pipher, J. L., Megeath, S. T., Myers, P. C., Allen, L. E., & Allen, T. S. 2011, APJ, 739, 84

Hamann, F. 1994, ApJS, 93, 485

Hamann, F., Simon, M., Carr, J. S., & Prato, L. 1994, APJ, 436, 292

Hansen, E. C., Frank, A., Hartigan, P., & Lebedev, S. V. 2017, APJ, 837, 143

Haro, G. 1950, AJ, 55, 72

—. 1952, APJ, 115, 572

Harris, D. E. & Krawczynski, H. 2006, ARA&A, 44, 463

Hartigan, P., Curiel, S., & Raymond, J. 1989, ApJ, 347, L31

Hartigan, P., Morse, J. A., & Raymond, J. 1994, APJ, 436, 125

Hayashi, C. & Nakano, T. 1965, Progress of Theoretical Physics, 34, 754 [LINK]

Heathcote, S., Reipurth, B., & Raga, A. C. 1998, AJ, 116, 1940

Hennebelle, P., Pérault, M., Teyssier, D., & Ganesh, S. 2001, A& A, 365, 598

Herbig, G. H. 1951, APJ, 113, 697

Hirano, N., Liu, S.-Y., Shang, H., Ho, P. T. P., Huang, H.-C., Kuan, Y.-J., McCaughrean, M. J., & Zhang, Q. 2006, ApJ, 636, L141

Hirano, N., Liu, S. Y., Shang, H., Ho, P. T. P., Qizhou, Z., Huang, H. C., Kuan, Y. J., & McCaughrean, M. J. 2005, in Protostars and Planets V Posters, 8334

Hirano, S. & Machida, M. N. 2019, Monthly Notices of the Royal Astronomical Society, 485, 4667 [LINK]

Hoare, M. G., Kurtz, S. E., Lizano, S., Keto, E., & Hofner, P. Protostars and Planets V, ed. , B. ReipurthD. Jewitt & K. Keil, 181

Hogerheijde, M. R., van Dishoeck, E. F., Salverda, J. M., & Blake, G. A. 1999, APJ, 513, 350

Hollenbach, D. in , Herbig-Haro Flows and the Birth of Stars, ed. B. ReipurthC. Bertout, Vol. 182, 181–198

Hollenbach, D. & McKee, C. F. 1989, APJ, 342, 306

Hollenbach, D. J., Chernoff, D. F., & McKee, C. F. 1989, in Infrared Spectroscopy in Astronomy, ed. E. Böhm-Vitense, 245

Hosokawa, T. & Omukai, K. 2009, APJ, 691, 823

Hugoniot, H. 1889, J. Ec. Polyt. Paris, 57, 1

Hugoniot, P. 1887, Mémoire sur la propagation du mouvement dans les corps et plus spécialement dans les gaz parfaits, 2e Partie, 58

Hunter, James H., J. 1970, APJ, 161, 451

Hunter, T. R., Churchwell, E., Watson, C., Cox, P., Benford, D. J., & Roelfsema, P. R. 2000, AJ, 119, 2711

Koenigl, A. 1986, Annals of the New York Academy of Sciences, 470, 88

KOO, B.-C. & LEE, Y.-H. 2015, Publication of Korean Astronomical Society, 30, 145

Kurtz, S. R. Cesaroni, M. FelliE. Churchwell & M. Walmsley, Vol. 227, 111–119

Kurtz, S., Cesaroni, R., Churchwell, E., Hofner, P., & Walmsley, C. M. Protostars and Planets IV, ed. , V. ManningsA. P. Boss & S. S. Russell, 299–326

Kwan, J. H., Gatley, I., Merrill, K. M., Probst, R., & Weintraub, D. A. 1977, APJ, 216, 713

Lada, C. J. in , Star Forming Regions, ed. M. PeimbertJ. Jugaku, Vol. 115, 1

Lada, C. J. & Adams, F. C. 1992, APJ, 393, 278

Lane, A. P. 1989, in European Southern Observatory Conference and Workshop Proceedings, Vol. 33, European Southern Observatory Conference and Workshop Proceedings, 331–348

Larson, R. B. 1969, MNRAS, 145, 271

—. 2003, Reports on Progress in Physics, 66, 1651

Larson, R. B. & Starrfield, S. 1971, A& A, 13, 190

Launhardt, R., Pavlyuchenkov, Y., Gueth, F., Chen, X., Dutrey, A., Guilloteau, S., Henning, T., Piétu, V., Schreyer, K., & Semenov, D. 2009, A& A, 494, 147

Lavalley, C., Cabrit, S., Dougados, C., Ferruit, P., & Bacon, R. 1997, A& A, 327, 671

Le Bourlot, J., Pineau des Forêts, G., Flower, D. R., & Cabrit, S. 2002, MNRAS, 332, 985

Lee, C.-F. 2020, A&A Rev., 28, 1

Lee, C.-F., Ho, P. T. P., Hirano, N., Beuther, H., Bourke, T. L., Shang, H., & Zhang, Q. 2007, The Astrophysical Journal, 659, 499 [LINK]

Lee, C.-F., Ho, P. T. P., Li, Z.-Y., Hirano, N., Zhang, Q., & Shang, H. 2017, Nature Astronomy, 1, 0152

Lee, C.-F., Li, Z.-Y., Codella, C., Ho, P. T. P., Podio, L., Hirano, N., Shang, H., Turner, N. J., & Zhang, Q. 2018a, APJ, 856, 14

Lee, C.-F., Li, Z.-Y., Hirano, N., Shang, H., Ho, P. T. P., & Zhang, Q. 2018b, APJ, 863, 94

Lee, C.-F., Li, Z.-Y., Shang, H., & Hirano, N. 2022, ApJ, 927, L27

Lee, H.-T., Takami, M., Duan, H.-Y., Karr, J., Su, Y.-N., Liu, S.-Y., Froebrich, D., & Yeh, C. C. 2012, ApJS, 200, 2

Lee, J.-J., Koo, B.-C., Lee, Y.-H., Lee, H.-G., Shinn, J.-H., Kim, H.-J., Kim, Y., Pyo, T.-S., Moon, D.-S., Yoon, S.-C., Chun, M.-Y., Froebrich, D., Davis, C. J., Varricatt, W. P., Kyeong, J., Hwang, N., Park, B.-G., Lee, M. G., Lee, H. M., & Ishiguro, M. 2014, MNRAS, 443, 2650

Lehmann, A. & Wardle, M. 2016, arXiv e-prints, arXiv:1612.09383

Leurini, S., Wyrowski, F., Wiesemeyer, H., Gusdorf, A., Güsten, R., Menten, K. M., Gerin, M., Levrier, F., Hübers, H. W., Jacobs, K., Ricken, O., & Richter, H. 2015, A& A, 584, A70

Li, Z.-Y. & Nakamura, F. 2006, ApJ, 640, L187

Lightfoot, J. F., Cudlip, W., Furniss, I., Glencross, W. M., Jennings, R. E., King, K. J., & Poulter, G. 1983, MNRAS, 205, 653

Liu, M. C., Graham, J. R., Ghez, A. M., Meixner, M., Skinner, C. J., Keto, E., Ball, R., Arens, J. F., & Jernigan, J. G. 1996, APJ, 461, 334

Livio, M. The Formation Of Astrophysical Jets, ed. , D. T. WickramasingheG. V. Bicknell & L. Ferrario, 845

Livio, M. in , American Institute of Physics Conference Series, Vol. 522, American Institute of Physics Conference Series, ed. S. S. HoltW. W. Zhang, 275–297

Livio, M. American Institute of Physics Conference Series, Vol. 1358, , Gamma Ray Bursts 2010, ed. J. E. McEneryJ. L. Racusin & N. Gehrels, 329–333

Lorenzetti, D., Giannini, T., Vitali, F., Massi, F., & Nisini, B. 2002, APJ, 564, 839

Louvet, F., Dougados, C., Cabrit, S., Mardones, D., Ménard, F., Tabone, B., Pinte, C., & Dent, W. R. F. 2018, A& A, 618, A120

Lovelace, R. V. E., Wang, J. C. L., & Sulkanen, M. E. 1987, APJ, 315, 504

Lynden-Bell, D. 1996, MNRAS, 279, 389

—. 2003, MNRAS, 341, 1360

Mac Low, M.-M. & Klessen, R. S. 2004, Rev. Mod. Phys., 76, 125 [LINK]

Mac Low, M.-M., Klessen, R. S., Burkert, A., & Smith, M. D. 1998, Phys. Rev. Lett., 80, 2754 [LINK]

Machida, M. N. 2014, ApJ, 796, L17

Machida, M. N., Inutsuka, S.-i., & Matsumoto, T. Protostellar Jets in Context, ed. , K. TsinganosT. Ray & M. Stute (Berlin, Heidelberg: Springer Berlin Heidelberg), 405–410

Macquorn Rankine, W. J. 1870, Philosophical Transactions of the Royal Society of London Series I, 160, 277

Marti, J., Rodriguez, L. F., & Reipurth, B. 1993, APJ, 416, 208

—. 1995, APJ, 449, 184

Masqué, J. M., Girart, J. M., Estalella, R., Rodríguez, L. F., & Beltrán, M. T. 2012, ApJ, 758, L10

Masqué, J. M., Rodríguez, L. F., Araudo, A., Estalella, R., Carrasco-González, C., Anglada, G., Girart, J. M., & Osorio, M. 2015, APJ, 814, 44

Masunaga, H. & ichiro Inutsuka, S. 2000, The Astrophysical Journal, 531, 350 [LINK]

Masunaga, H. & Inutsuka, S.-i. 2000, APJ, 531, 350

Matthews, L. D., Greenhill, L. J., Goddi, C., Chandler, C. J., Humphreys, E. M. L., & Kunz, M. W. 2010, APJ, 708, 80

McCoey, C., Giannini, T., Flower, D. R., & Caratti o Garatti, A. 2004, MNRAS, 353, 813

McKee, C. F., Chernoff, D. F., & Hollenbach, D. J. in , Astrophysics and Space Science Library, Vol. 108, Galactic and Extragalactic Infrared Spectroscopy, ed. M. F. KesslerJ. P. Phillips, 103–131

McKee, C. F. & Ostriker, E. C. 2007, Annual Review of Astronomy and Astrophysics, 45, 565 [LINK]

McKee, C. F. & Ostriker, E. C. 2007, ARA&A, 45, 565

Meier, D. L., Koide, S., & Uchida, Y. 2001, Science, 291, 84 [LINK]

Meyer, M. R., Calvet, N., & Hillenbrand, L. A. 1997, AJ, 114, 288

Mezger, P. G., Altenhoff, W., Schraml, J., Burke, B. F., Reifenstein, E. C., I., & Wilson, T. L. 1967, ApJ, 150, L157

Micono, M., Massaglia, S., Bodo, G., Rossi, P., & Ferrari, A. 1998, A& A, 333, 1001

Mirabel, I. F. & Rodríguez, L. F. 1999, Annual Review of Astronomy and Astrophysics, 37, 409 [LINK]

Molinari, S., Noriega-Crespo, A., & Spinoglio, L. 2001, APJ, 547, 292

Monnier, J. D. & Millan-Gabet, R. 2002, APJ, 579, 694

Monnier, J. D., Tuthill, P. G., Ireland, M., Cohen, R., Tannirkulam, A., & Perrin, M. D. 2009, APJ, 700, 491

Moriarty-Schieven, G. H. & Snell, R. L. 1988, APJ, 332, 364

Moriarty-Schieven, G. H., Wannier, P. G., Mangum, J. G., Tamura, M., & Olmsted, V. K. 1995, APJ, 455, 190

Motte, F., Bontemps, S., & Louvet, F. 2018, ARA&A, 56, 41

Motte, F., Bontemps, S., Schilke, P., Schneider, N., Menten, K. M., & Broguière, D. 2007, A& A, 476, 1243

Mouri, H., Kawara, K., & Taniguchi, Y. 2000, APJ, 528, 186

Mullan, D. J. 1971, MNRAS, 153, 145

Mundt, R., Buehrke, T., Solf, J., Ray, T. P., & Raga, A. C. 1990, A& A, 232, 37

Murdin, P. 2000, Encyclopedia of Astronomy and Astrophysics

Murphy, T., Cohen, M., Ekers, R. D., Green, A. J., Wark, R. M., & Moss, V. 2010, MNRAS, 405, 1560

Myers, P. C. & Ladd, E. F. 1993, ApJ, 413, L47

Nakamura, F. & Li, Z.-Y. 2007, APJ, 662, 395

Nisini, B. Jets from Young Stars II, ed. , F. BacciottiL. Testi & E. Whelan, Vol. 742, 79

Nisini, B., Bacciotti, F., Giannini, T., Massi, F., Eislöffel, J., Podio, L., & Ray, T. P. 2005, A& A, 441, 159

Nisini, B., Caratti o Garatti, A., Giannini, T., & Lorenzetti, D. 2002, A& A, 393, 1035

Noriega-Crespo, A. Revista Mexicana de Astronomia y Astrofisica Conference Series, ed. , W. J. HenneyW. SteffenL. Binette & A. Raga, 71–78

Noriega-Crespo, A., Garnavich, P. M., Raga, A. C., Canto, J., & Boehm, K. H. 1996, APJ, 462, 804

Nussbaumer, H. & Storey, P. J. 1988, A& A, 193, 327

Obonyo, W. O., Lumsden, S. L., Hoare, M. G., Purser, S. J. D., Kurtz, S. E., & Johnston, K. G. 2019, MNRAS, 486, 3664

Oh, H., Pyo, T.-S., Yuk, I.-S., & Park, B.-G. 2015, Journal of Korean Astronomical Society, 48, 113

Oliva, E., Moorwood, A. F. M., & Danziger, I. J. 1989, A& A, 214, 307

Omont, A., Gilmore, G. F., Alard, C., Aracil, B., August, T., Baliyan, K., Beaulieu, S., Bégon, S., Bertou, X., Blommaert, J. A. D. L., Borsenberger, J., Burgdorf, M., Caillaud, B., Cesarsky, C., Chitre, A., Copet, E., de Batz, B., Egan, M. P., Egret, D., Epchtein, N., Felli, M., Fouqué, P., Ganesh, S., Genzel, R., Glass, I. S., Gredel, R., Groenewegen, M. A. T., Guglielmo, F., Habing, H. J., Hennebelle, P., Jiang, B., Joshi, U. C., Kimeswenger, S., Messineo, M., Miville-Deschênes, M. A., Moneti, A., Morris, M., Ojha, D. K., Ortiz, R., Ott, S., Parthasarathy, M., Pérault, M., Price, S. D., Robin, A. C., Schultheis, M., Schuller, F., Simon, G., Soive, A., Testi, L., Teyssier, D., Tiphène, D., Unavane, M., van Loon, J. T., & Wyse, R. 2003, A& A, 403, 975

Osorio, M., Díaz-Rodríguez, A. K., Anglada, G., Megeath, S. T., Rodríguez, L. F., Tobin, J. J., Stutz, A. M., Furlan, E., Fischer, W. J., Manoj, P., Gómez, J. F., González-García, B., Stanke, T., Watson, D. M., Loinard, L., Vavrek, R., & Carrasco-González, C. 2017, APJ, 840, 36

Pacholczyk, A. G. 1970, Radio astrophysics. Nonthermal processes in galactic and extragalactic sources

Padovani, M., Hennebelle, P., Marcowith, A., & Ferrière, K. 2015, A& A, 582, L13

Padovani, M., Marcowith, A., Hennebelle, P., & Ferrière, K. 2016, A& A, 590, A8

Palau, A., Ho, P. T. P., Zhang, Q., Estalella, R., Hirano, N., Shang, H., Lee, C. F., Bourke, T. L., Beuther, H., & Kuan, Y. J. 2006, ApJ, 636, L137

Palau, A., Zapata, L. A., Rodríguez, L. F., Bouy, H., Barrado, D., Morales-Calderón, M., Myers, P. C., Chapman, N., Juárez, C., & Li, D. 2014, Monthly Notices of the Royal Astronomical Society, 444, 833 [LINK]

Perault, M., Omont, A., Simon, G., Seguin, P., Ojha, D., Blommaert, J., Felli, M., Gilmore, G., Guglielmo, F., Habing, H., Price, S., Robin, A., de Batz, B., Cesarsky, C., Elbaz, D., Epchtein, N., Fouque, P., Guest, S., Levine, D., Pollock, A., Prusti, T., Siebenmorgen, R., Testi, L., & Tiphene, D. 1996, A& A, 315, L165

Persson, M. V. 2014 [LINK]

Pillai, T., Wyrowski, F., Carey, S. J., & Menten, K. M. 2006, A& A, 450, 569

Plunkett, A. L., Arce, H. G., Mardones, D., van Dokkum, P., Dunham, M. M., Fernández-López, M., Gallardo, J., & Corder, S. A. 2015, Natur, 527, 70

Podio, L., Bacciotti, F., Nisini, B., Eislöffel, J., Massi, F., Giannini, T., & Ray, T. P. 2006, A& A, 456, 189

Pravdo, S. H., Tsuboi, Y., & Maeda, Y. 2004, APJ, 605, 259

Pravdo, S. H., Tsuboi, Y., & Maeda, Y. 2004, The Astrophysical Journal, 605, 259 [LINK]

Price, S. D., Egan, M. P., Carey, S. J., Mizuno, D. R., & Kuchar, T. A. 2001, AJ, 121, 2819

Pudritz, R. E. & Norman, C. A. 1983, APJ, 274, 677

Purser, S. J. D., Ainsworth, R. E., Ray, T. P., Green, D. A., Taylor, A. M., & Scaife, A. M. M. 2018, MNRAS, 481, 5532

Purser, S. J. D., Lumsden, S. L., Hoare, M. G., Urquhart, J. S., Cunningham, N., Purcell, C. R., Brooks, K. J., Garay, G., Gúzman, A. E., & Voronkov, M. A. 2016, MNRAS, 460, 1039

Pyo, T.-S., Hayashi, M., Kobayashi, N., Terada, H., & Tokunaga, A. T. 2009, APJ, 694, 654

Pyo, T.-S., Hayashi, M., Kobayashi, N., Tokunaga, A. T., Terada, H., Goto, M., Yamashita, T., Itoh, Y., Takami, H., Takato, N., Hayano, Y., Gaessler, W., Kamata, Y., Minowa, Y., & Iye, M. 2003, , 287, 21

Qiu, K., Wyrowski, F., Menten, K., Zhang, Q., & Güsten, R. 2019, APJ, 871, 141

Qiu, K. & Zhang, Q. 2009, ApJ, 702, L66

Qiu, K., Zhang, Q., Megeath, S. T., Gutermuth, R. A., Beuther, H., Shepherd, D. S., Sridharan, T. K., Testi, L., & De Pree, C. G. 2008, APJ, 685, 1005

Quillen, A. C., Thorndike, S. L., Cunningham, A., Frank, A., Gutermuth, R. A., Blackman, E. G., Pipher, J. L., & Ridge, N. 2005, The Astrophysical Journal, 632, 941 [LINK]

Quinn, P. J. & Bridger, A. 2004, Optimizing Scientific Return for Astronomy through Information Technologies, 5493

Raga, A., Cabrit, S., Dougados, C., & Lavalley, C. 2001, A& A, 367, 959

Raga, A. C., Canto, J., Binette, L., & Calvet, N. 1990, APJ, 364, 601

Raga, A. C., Cantó, J., & Biro, S. 1993, Monthly Notices of the Royal Astronomical Society, 260, 163 [LINK]

Raga, A. C. & Kofman, L. 1992, APJ, 386, 222

Ragan, S. E., Bergin, E. A., & Gutermuth, R. A. 2009, APJ, 698, 324

Ramsay Howat, S. K., Todd, S., Leggett, S., Davis, C., Strachan, M., Borrowman, A., Ellis, M., Elliot, J., Gostick, D., Kackley, R., & Rippa, M. in , Society of Photo-Optical Instrumentation Engineers (SPIE) Conference Series, Vol. 5492, Ground-based Instrumentation for Astronomy, ed. A. F. M. MoorwoodM. Iye, 1160–1171

Rathborne, J. M., Jackson, J. M., & Simon, R. 2006, APJ, 641, 389

Ray, T., Dougados, C., Bacciotti, F., Eislöffel, J., Chrysostomou, A., Reipurth, B., Jewitt, D., & Keil, K. 2007, Reipurth, D

Ray, T. P. & Ferreira, J. 2021, , 93, 101615

Reid, M. J., Argon, A. L., Masson, C. R., Menten, K. M., & Moran, J. M. 1995, APJ, 443, 238

Reid, M. J., Menten, K. M., Zheng, X. W., Brunthaler, A., Moscadelli, L., Xu, Y., Zhang, B., Sato, M., Honma, M., Hirota, T., Hachisuka, K., Choi, Y. K., Moellenbrock, G. A., & Bartkiewicz, A. 2009, APJ, 700, 137

Reipurth, B. & Bally, J. 2001, Annual Review of Astronomy and Astrophysics, 39, 403 [LINK]

Reipurth, B. & Bally, J. 2001, ARA&A, 39, 403

Reipurth, B. & Raga, A. C. in , NATO Advanced Study Institute (ASI) Series C, Vol. 540, The Origin of Stars and Planetary Systems, ed. C. J. LadaN. D. Kylafis, 267

Reipurth, B., Rodrguez, L. F., Anglada, G., & Bally, J. 2004, The Astronomical Journal, 127, 1736 [LINK]

Reipurth, B., Yu, K. C., Heathcote, S., Bally, J., & Rodríguez, L. F. 2000, AJ, 120, 1449

Reiter, M., Smith, N., & Bally, J. 2016, Monthly Notices of the Royal Astronomical Society, 463, 4344 [LINK]

Reynolds, S. P. 1982, APJ, 256, 13

—. 1986, APJ, 304, 713

Rieke, G. H. & Lebofsky, M. J. 1985, APJ, 288, 618

Robitaille, T. P., Whitney, B. A., Indebetouw, R., & Wood, K. 2007, ApJS, 169, 328

Robitaille, T. P., Whitney, B. A., Indebetouw, R., Wood, K., & Denzmore, P. 2006, The Astrophysical Journal Supplement Series, 167, 256 [LINK]

Rodgers, S. D. & Charnley, S. B. 2003, APJ, 585, 355

Rodríguez, L. F. Jets at All Scales, ed. , G. E. RomeroR. A. Sunyaev & T. Belloni, Vol. 275, 367–373

Rodriguez, L. F., Curiel, S., Moran, J. M., Mirabel, I. F., Roth, M., & Garay, G. 1989a, ApJ, 346, L85

Rodriguez, L. F., Curiel, S., Moran, J. M., Mirabel, I. F., Roth, M., & Garay, G. 1989b, in , Vol. 21, 792

Rodriguez, L. F., Garay, G., Curiel, S., Ramirez, S., Torrelles, J. M., Gomez, Y., & Velazquez, A. 1994, ApJ, 430, L65

Rodriguez, L. F., Moran, J. M., Ho, P. T. P., & Gottlieb, E. W. 1980, APJ, 235, 845

Rodríguez, L. F. & Reipurth, B. 1989, Revista Mexicana de Astronomia y Astrofisica, 17, 59

Rodríguez-Kamenetzky, A., Carrasco-González, C., Araudo, A., Romero, G. E., Torrelles, J. M., Rodríguez, L. F., Anglada, G., Martí, J., Perucho, M., & Valotto, C. 2017, APJ, 851, 16

Rodríguez-Kamenetzky, A., Carrasco-González, C., Araudo, A., Torrelles, J. M., Anglada, G., Martí, J., Rodríguez, L. F., & Valotto, C. 2016, APJ, 818, 27

Rodríguez-Kamenetzky, A., Carrasco-González, C., González-Martín, O., Araudo, A. T., Rodríguez, L. F., Vig, S., & Hofner, P. 2019, Monthly Notices of the Royal Astronomical Society, 482, 4687

Rybicki, G. B. & Lightman, A. P. 2008, Radiative processes in astrophysics (John Wiley & Sons)

Sacco, G. G., Flaccomio, E., Pascucci, I., Lahuis, F., Ercolano, B., Kastner, J. H., Micela, G., Stelzer, B., & Sterzik, M. 2012, The Astrophysical Journal, 747, 142 [LINK]

Sanna, A., Moscadelli, L., Goddi, C., Krishnan, V., & Massi, F. 2018, A& A, 619, A107

Saraceno, P., Andre, P., Ceccarelli, C., Griffin, M., & Molinari, S. 1996, A& A, 309, 827

Sargent, A. I., van Duinen, R. J., Aalders, J. W. G., Fridlund, C. V. M., & Nordh, H. L. 1981, APJ, 249, 607

Sari, R., Piran, T., & Narayan, R. 1998, ApJ, 497, L17

Schmid-Burgk, J., Guesten, R., Mauersberger, R., Schulz, A., & Wilson, T. L. 1990, ApJ, 362, L25

Schulz, N. S. 2005, From Dust To Stars Studies of the Formation and Early Evolution of Stars

Schwartz, R. D., Williams, P. M., Cohen, M., & Jennings, D. G. 1988, ApJ, 334, L99

Seifried, D., Banerjee, R., Klessen, R. S., Duffin, D., & Pudritz, R. E. 2011, MNRAS, 417, 1054

Seifried, D., Pudritz, R. E., Banerjee, R., Duffin, D., & Klessen, R. S. 2012, MNRAS, 422, 347

Sewilo, M., Churchwell, E., Kurtz, S., Goss, W. M., & Hofner, P. 2004, APJ, 605, 285

Shang, H., Krasnopolsky, R., & Liu, C.-F. 2023, arXiv e-prints, arXiv:2301.08512

Shang, H., Lizano, S., Glassgold, A., & Shu, F. 2004, The Astrophysical Journal, 612, L69 [LINK]

Shimajiri, Y., Takahashi, S., Takakuwa, S., Saito, M., & Kawabe, R. 2008, APJ, 683, 255

Shu, F. H., Adams, F. C., & Lizano, S. 1987, Annual Review of Astronomy and Astrophysics, 25, 23 [LINK]

Shu, F. H., Lizano, S., Ruden, S. P., & Najita, J. 1988, ApJ, 328, L19

Simon, R., Jackson, J. M., Rathborne, J. M., & Chambers, E. T. 2006, APJ, 639, 227

Simon, R., Schneider, N., Bigiel, F., Ossenkopf-Okada, V., Okada, Y., Johnstone, D., Schilke, P., Stacey, G., Roellig, M., Sanchez-Monge, A., Seifried, D., Stutzki, J., Bertoldi, F., Buchbender, C., Fich, M., Herter, T., Higgins, R., & Nikola, T. 2019, , 51, 367

Skinner, S. L., Audard, M., & Güdel, M. 2011, APJ, 737, 19

Smith, M. D. 1994, A& A, 289, 256

Smith, M. D. & Mac Low, M. M. 1997, A& A, 326, 801

Stahler, S. W. D. Rouan, T. SpohnS. Tirard & M. Viso, 2076–2085

Stahler, S. W. & Palla, F. 2004, The Formation of Stars

Stapelfeldt, K. R., Beichman, C. A., Hester, J. J., Scoville, N. Z., & Gautier, Thomas N., I. 1991, APJ, 371, 226

Stecklum, B., Caratti o Garatti, A., Davis, C., Linz, H., Stanke, T., & Zinnecker, H. 2009, in Protostellar Jets in Context, Springer, 619–621

Stone, J. M. & Norman, M. L. 1993, APJ, 413, 198

Strom, S. E., Strom, K. M., & Grasdalen, G. L. 1975, ARA&A, 13, 187

Suzuki-Vidal, F., Lebedev, S. V., Ciardi, A., Pickworth, L. A., Rodriguez, R., Gil, J. M., Espinosa, G., Hartigan, P., Swadling, G. F., Skidmore, J., Hall, G. N., Bennett, M., Bland, S. N., Burdiak, G., de Grouchy, P., Music, J., Suttle, L., Hansen, E., & Frank, A. 2015, APJ, 815, 96

Tabone, B., Cabrit, S., Bianchi, E., Ferreira, J., Pineau des Forêts, G., Codella, C., Gusdorf, A., Gueth, F., Podio, L., & Chapillon, E. 2017, A& A, 607, L6

Takami, M., Chrysostomou, A., Ray, T. P., Davis, C. J., Dent, W. R. F., Bailey, J., Tamura, M., Terada, H., & Pyo, T. S. 2006, The Astrophysical Journal, 641, 357 [LINK]

Takami, M., Karr, J. L., Nisini, B., & Ray, T. P. 2011, The Astrophysical Journal, 743, 193 [LINK]

Tan, J. C., Beltrán, M. T., Caselli, P., Fontani, F., Fuente, A., Krumholz, M. R., McKee, C. F., & Stolte, A. H. Beuther, R. S. KlessenC. P. Dullemond & T. Henning, 149–172

Tielens, A. G. G. M. 2005, The Physics and Chemistry of the Interstellar Medium

Tychoniec, Ł., Tobin, J. J., Karska, A., Chandler, C., Dunham, M. M., Harris, R. J., Kratter, K. M., Li, Z.-Y., Looney, L. W., Melis, C., Pérez, L. M., Sadavoy, S. I., Segura-Cox, D., & van Dishoeck, E. F. 2018, ApJS, 238, 19

Ustyugova, G. V., Koldoba, A. V., Romanova, M. M., Chechetkin, V. M., & Lovelace, R. V. E. 1995, ApJ, 439, L39

van der Tak, F. F. S., van Dishoeck, E. F., Evans, Neal J., I., Bakker, E. J., & Blake, G. A. 1999, APJ, 522, 991

Varricatt, W. P., Davis, C. J., Ramsay, S., & Todd, S. P. 2010, MNRAS, 404, 661

Varricatt, W. P., Davis, C. J., Ramsay, S., & Todd, S. P. 2010, Monthly Notices of the Royal Astronomical Society, 404, 661

Vig, S., Veena, V. S., Mandal, S., Tej, A., & Ghosh, S. K. 2018, MNRAS, 474, 3808

Vorobyov, E. I., Elbakyan, V. G., Plunkett, A. L., Dunham, M. M., Audard, M., Guedel, M., & Dionatos, O. 2018, A& A, 613, A18

Wardle, M. 1990, MNRAS, 246, 98

Whelan, E. M., Ray, T., Bacciotti, F., Rand ich, S., & Natta, A. 2009, Astrophysics and Space Science Proceedings, 13, 259

Whelan, E. T., Ray, T. P., & Davis, C. J. 2004, A& A, 417, 247

White, M. C., Bicknell, G. V., McGregor, P. J., & Salmeron, R. 2014, Monthly Notices of the Royal Astronomical Society, 442, 28 [LINK]

Wijers, R. A. M. J. & Galama, T. J. 1999, APJ, 523, 177

Wilgenbus, D., Cabrit, S., Pineau des Forêts, G., & Flower, D. R. 2000, A& A, 356, 1010

Wilner, D. J., Reid, M. J., & Menten, K. M. 1999, APJ, 513, 775

Woitas, J., Ray, T. P., Bacciotti, F., Davis, C. J., & Eislöffel, J. 2002, APJ, 580, 336

Wood, D. O. S. & Churchwell, E. 1989, ApJS, 69, 831

Wu, Y., Wei, Y., Zhao, M., Shi, Y., Yu, W., Qin, S., & Huang, M. 2004, A& A, 426, 503

Yamashita, T., Sato, S., Nagata, T., Suzuki, H., Hough, J. H., McLean, I. S., Garden, R., & Gatley, I. 1987, A& A, 177, 258

Yamashita, T., Suzuki, H., Kaifu, N., Tamura, M., Mountain, C. M., & Moore, T. J. T. 1989, APJ, 347, 894

Yan, D.-H., Zhou, J.-N., & Zhang, P.-F. 2022, Research in Astronomy and Astrophysics, 22, 025016

Yorke, H. W. 1979, A& A, 80, 308

Zanni, C. 2014, in European Physical Journal Web of Conferences, Vol. 64, European Physical Journal Web of Conferences, 05005

Zanni, C., Ferrari, A., Massaglia, S., Bodo, G., & Rossi, P. 2004, Astrophysics and Space Science, 293, 99

Zanni, C. & Ferreira, J. 2011, ApJ, 727, L22

Zapata, L. A., Lizano, S., Rodríguez, L. F., Ho, P. T. P., Loinard, L., Fernández-López, M., & Tafoya, D. 2015, APJ, 798, 131

Zinnecker, H., McCaughrean, M. J., & Wilking, B. A. in , Protostars and Planets III, ed. E. H. LevyJ. I. Lunine, 429

Zinnecker, H. & Yorke, H. W. 2007, Annual Review of Astronomy and Astrophysics, 45, 481 [LINK]

List of Publications

(a) **Radio spectra of protostellar jets: Thermal and non-thermal emission**, S. Mohan, S. Vig, and S. Mandal, 2022, Monthly Notices of Royal Astronomical Society, vol. 514, no. 3, pp. 3709−3724.

(b) **Imaging of HH80-81 Jet in the Near-infrared Shock Tracers $\mathbf{H_2}$ and [Fe II]**, S. Mohan, S. Vig, W. P. Varricatt, and A. Tej, 2023, The Astrophysical Journal, vol. 942, no. 2, 76, p. 76.

(c) **Modeling of thermal and non-thermal radio emission from HH80-81 jet**, S. Mohan, S. Vig, and S. Mandal, 2023, Journal of Astrophysics and Astronomy, Vol. 44, no. 2, 57.